Part 4

Physics Scope

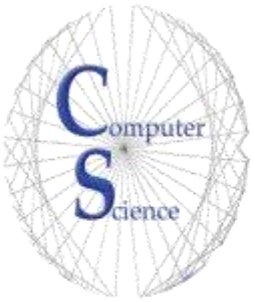

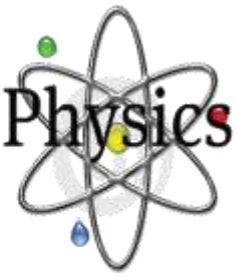

Content Table

Seq.	Title	Researchers
12.	Study the Structural and Optical Properties Pure Copper Sulfide (CuS) Films Prepared by Pulsed Laser Deposition (PLD)	Meriam K Chloob1, Saleem A Hussain1
13.	Next Generation of High-Speed Optical Communications Networks Using OFDM Technology	Atta Takhum Jaber[1], Soudad S. Ahmed[2], and Shehab Ahmed Kadhim[3]
14.	Thermal analysis for stability the nanocrystals ZnSe(diamantane)	H A T Al-Ogaili 1* and R. A. Al-Wardy2
15.	Electrical Characterization of Thin Films $(TiO_2: ZnO)_{1-x}$ $(GO)_x$ / FTO Heterojunction Prepared by Spray Pyrolysis Technique	M J Alsultani[1] , H H Abed[2] , R A Ghazi[3] and M A Mohammed[4]
16.	Experimental investigation of uranium content in urine samples of cancer patients in Al-Diwaniyah Governorate, Iraq	Zahraa Q. Rahman1, Anees A. Al-Hamzawi1*
17.	Structural, Morphological and Electrical properties of PVDF/lithium Iron Oxide nano-composites	Ruqaya Fouad Kadhim and Zainab Raheem Muslim
18.	Structural Properties and Characterization of Lithium Olivine Compounds	Z R Muslim[1] and A Q Kadhum[2]
19.	Structural,Optical and Sensing Properties of ZnO:Cu Films Prepared by Pulsed Laser Deposition	Saleem A Hussain1 , Awatif J Radi1,2 , Firas A Najim1 , Mohamed A Shaheed1
20.	Distribution of Radon Concentration in Farmland Soil Samples in Al-Shamiyah City, Al-Qadisiyah, Iraq	Amer Y. Kadhim[1, 2], Khalid H. Al-Ataya1, Murtadha Sh. Aswood[*2]

Synthesis and characterization of PVA-Graphene-Ag nanocomposite by using laser ablation technique

Musaab Khudhur Mohammed1, Ghaleb Al-Dahash2 and Amer Al-Nafiey2

1University of Babylon, College of Education for Pure Sciences, Department of Physics, Iraq
2University of Babylon, College of science for women, Department of Laser Physics, Iraq
*musabali33@yahoo.com

Abstract: The PVA-G-Ag nanocomposite have been synthesized effectively by pulsed laser ablation liquid (PLAL) as a considered to be environmentally friendly and free of residues from chemical reactions. The high excellence silver plate (99.99%) and graphite plate (99.99%) was immersed in the polyvinyl alcohol (PVA) solution and irradiated with the Nd-YAG laser at wavelength 1064 nm, power 160 mJ for the silver plate and 80mJ for graphite plate, reiteration rate 6 Hz, 10 ns pulse width and 300 pules for graphite plate and 700 pulse for silver plate. The pure of PVA, PVA-Graphene and PVA-Graphene-Ag nanocomposite were investigated using UV-VIS spectroscopy, FTIR and SEM. The absorption spectra of PVA-Graphene-Ag nanocomposite show the presence of two peaks one 0.4 at 272 and second 0.47 at 403 nm. The optical energy gap (Eg) decreased from 5eV of a pure PVA to 4.6eV of a PVA-G-Ag for indirect allowed transition and therefore, decreased from 4.4eV of a pure PVA to 4.1eV of a PVA-G-Ag for indirect forbidden transition. The transmittance and absorption coefficient have been determined. The SEM images confirmed that homogenous composite without aggregation of the components. The average size of nanoparticles of GNPs and AgNPs for PVA-G and PVA-G-Ag nanocomposite was 130 and 115 nm respectively. The FTIR has demonstrated that the connection between the graphene, silver and polymer network was enough to have stable nanocomposite. This investigation demonstrates that the pulse laser ablation decent instrument to decorated metals on the graphene with the presence of the polymer.

Keywords: graphene, AgNPs, PVA-G-Ag nanocomposite, Laser ablation

1. Introduction

The graphene structure has been one of the remarkable discovery in modern physics over the past 14 years. The graphene has been prepared for the first time by the Geim A. K in 2004 which opened many application [1]. Since that time, there has been a lot of research on this discovery [2]. Because the graphene has been discovered as a result, Geim A. K. and et. al. acquired the Nobel Prize in Physics in 2010 [3-4].

Graphene is define as a monolayer of sp^2-hybridized carbon atoms structured in a honeycomb lattice. The hybridized orbitals form strong σ-bonds in the plane and un-hybridized p-orbitals overlap with neighboring atoms to form π-bond. While the σ-bond is responsible for the most of the structural integrity of graphene, the π-bond determines optical and electronic properties. The interaction of graphene with electromagnetic wave is attractive because of the excellent band structure of graphene and the two-dimensional confinement of electrons [5]. It has other fundamental highlights, comprising of wonderful optical transmittance (≈ 97.3%)[6]. Graphene has been prepared in several methods like, chemical vapor deposition CVD [7], micro-mechanical exfoliation [8], epitaxial growth of silicon carbide pyrolysis [9], and reduction of the oxidized graphite [10], graphite intercalation [11] and electrochemical technique [12]. These techniques aren't eco-friendly, including multi-steps and needed strong reducing agents. On the opposite hand, the pulsed laser ablation liquid (PLAL) it's a few benefits like cleanness, simplicity, and easily synthesis particle in nanoscale [13].

In view of low Young's modulus esteem, that a few polymers show can be expanded essentially upon the homogeneous joining of graphene, in this manner making polymer/graphene nanocomposites

appealing for a scope of utilizations. Polymer- graphene (reduced graphene oxide) nanocomposites as an important materials form for photonic and optoelectronic devices, like graphene-polyvinyl alcohol (PVA) nanocomposite films were fabricated by different techniques like, solution cast method [14], simple solution method [15], a facial aqueous solution[16], while many efforts have been accomplished, which include graphene and diverse metallic nanoparticles, like gold(Au) [17], silver(Ag) [18] and copper (Cu) [19].

In this paper, we proposition a novel method to fabrication PVA-G-Ag nanocomposite by the pulsed laser ablation in liquid (PLAL) with the less pulse laser energy and short ablation time.

2. Experiment

2.1 Preparation of graphite (G) plate

The measure of graphite powder (5g) (99.99% quality; Interchimiques SA, France) it was a compressed with a hydraulic piston after cleaning the cylinder with ethanol, under pressure 20 MPa with width 2 cm and thickness (2 mm), after that it was annealing for 4 hours at 450°C, for strengthening. A graphite plate was cleaned utilizing a cleaned paper, to evacuate the debasements and afterward washed with ethanol and refined water.

2.2 Preparation of silver (Ag) plate

The measure of silver powder (5g) (99.99% quality; Sigma Aldrich, St. Louis, MO) was pressured with a hydraulic piston after cleaning the cylinder with ethanol, under pressure 22 MPa with width 2 cm and thickness (2 mm), after that it was annealing for one hour at 500°C, for strengthening. A silver plate was cleaned utilizing a cleaned paper, to evacuate the debasements and afterward washed with ethanol and refined water.

2.3 Preparation of solvent of Poly (vinyl alcohol) (PVA)

0.5 g of Polyvinyl alcohol that (molecular weight 18000 g/mol, temperature of glass 75^{o} C and density 1.18g/cm^{3}) has been solvent in 30 ml of deionized water with magnetic stirrer and temperature 50^{o} C for 30 minute.

2.4 Syntheses of PVA-G-Ag nanocomposite by laser ablation in liquid

The prepared graphite plate was immersed in 2 mm under the liquid surface on a bracket in a glass vessel filled with 5 ml of the PVA solution and then, the graphite plate was exposed by (300) pulses using a pulsed Q-Switched Nd:YAG laser. The pulse duration of 10 ns and 6 Hz repetition rate at wavelength 1064 nm with an energy of 80 mJ per pulse as shown in Figure.1. This colloid solutions PVA-G nanocomposite will redecorate with Ag NPs by immersed Ag target in this nanocomposite solution and exposed by (700) pulses and energy of 160 mJ from the same Q-Switched Nd:YAG laser..

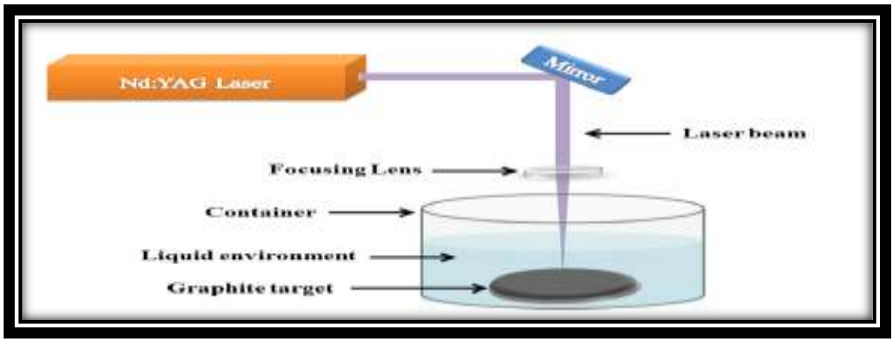

Figure.1 Laser ablation setup

The optical properties have been determined by utilizing a UV-VIS-NIR (UV/1800/Shimadzu spectrophotometer) in the wavelength range of (200-1100) nm for the colloid straight and for the scanning electron microscope (SEM) and Fourier transform infrared spectroscopy (FTIR) analyses the samples were prepared as a thin film by spin coating method with speed 500 rpm/sec for 20 seconds on a silicon wafer.

3. Result and discussion

The absorption spectra of a pure PVA, PVA-Graphene and PVA-Graphene-Ag nanocomposite are shown in Figure.2. The figure shows that the absorption peak 0.29 at 274nm for the PVA-G nanocomposite due to π–π* transition of C=C band [20]. These absorption peaks are observed due to Surface Plasmon Resonance (SPR) in the free electron cloud of carbonaceous material π electrons [21]. The absorption peak at 274 nm in oxidized graphite is a characteristic feature of graphene [22], while PVA-Graphene-Ag nanocomposite displays two peaks, one 0.4 at 272 nm and another 0.48 at 403 nm. The main peak of graphene (G) has a violet shift 2 nm, this shift of absorption peak toward shorter wavelength (violet shift) indicates the decreased particle size and vice versa [23]. This result agree with the authors [24].

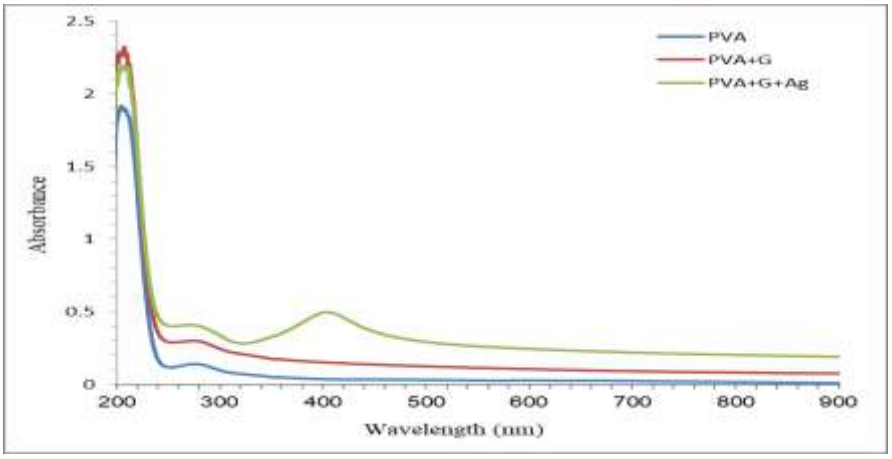

Figure.2 the absorption spectra of a pure PVA, PVA-G and PVA-G-Ag nanocomposite

The optical transmittance of a pure PVA, PVA-Graphene and PVA-Graphene-Ag nanocomposite, has been determined by using the relation (1) [25]:

$$T = 10^{-A} \quad (1)$$

where A: is the absorbance

The transmittance are appeared in Figure 3. The figures show that the transmittance decreased from 98% of a pure PVA to 94% of PVA-G nanocomposite. This decreased was attributed to the presence of the monolayer graphene, while the transmittance decreased to 88% for the PVA-G-Ag nanocomposite. This influence due to some absorption in that wavelength range (272 and 403nm). This result is agreement with the authors [26].

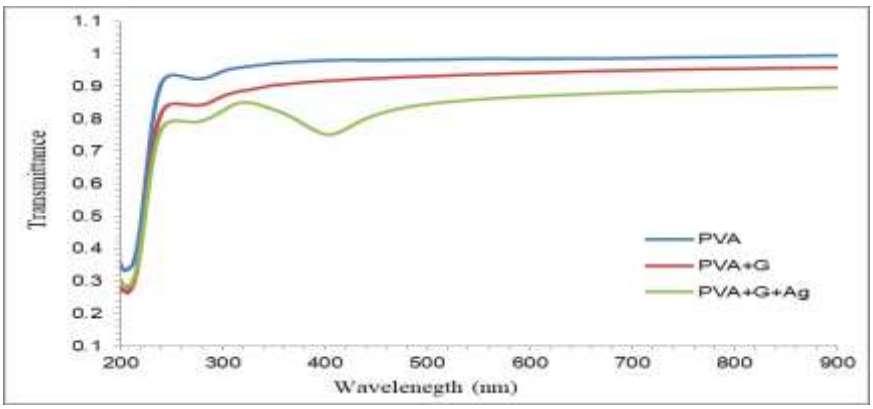

Figure.3 the transmittance spectra of a pure PVA, PVA-G and PVA-G-Ag nanocomposite

To determine the absorption coefficient spectra (α) for the three samples by using the relation (2) [27]:

$$\propto = 2.303 \frac{A}{t} \qquad (2)$$

Where A: is absorbance and t: is film thickness.

So, Figure.4 show that the absorption coefficient of the three samples. This figure show that the absorption coefficient of PVA-G and PVA-G-Ag nanocomposite increased compared to the pure of PVA. The values of α is less than 10^4 cm^{-1}, this indicate that the composites have indirect energy gap [28].

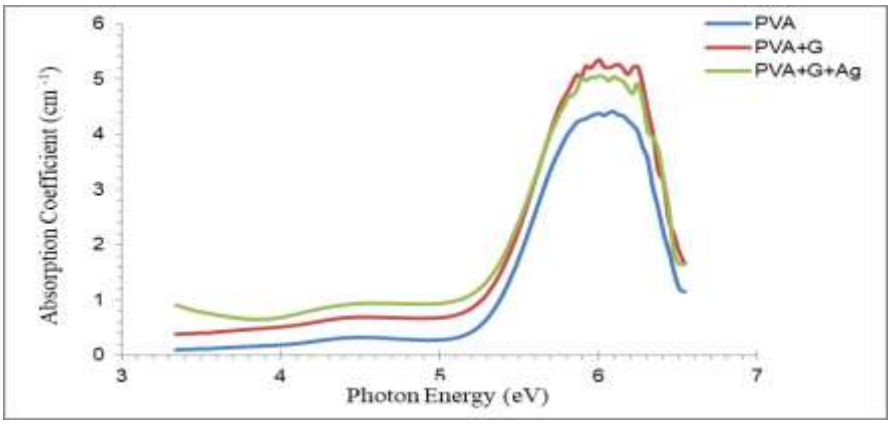

Figure.4 the absorption coefficient of a pure PVA, PVA-G and PVA-G-Ag nanocomposite

By using the following relation (3) to calculated optical energy gap (E_g) [29].

$$\alpha = A(h\nu - E_g)^r/h\nu \qquad (3)$$

To determine the (E_g) is to scheme a chart between $(\alpha h\nu)^r$ and photon energy ($h\nu$) and find the value of the r which provides the best line diagram are shown in Figure.5. The estimations of optical band hole are chosen by extrapolating the straight pieces of these relations to the hν axis and recorded in Table.1. The (E_g)` decreased with the increasing of graphene and graphene-silver respectively. The variety of the determined estimation of the energy hole may reflect the role of graphene and graphene-silver in a variable the electronic structure of the polymeric grid because of the presence of different polaronic and defect levels. Expansion the graphene and graphene-silver substance may bring about the restricted conditions of different shading communities to stretching out in the versatility hole. This association may demonstrate the decline in the energy hole when the including graphene and graphene-silver respectively to the PVA. This result is agreement with the authors [30]

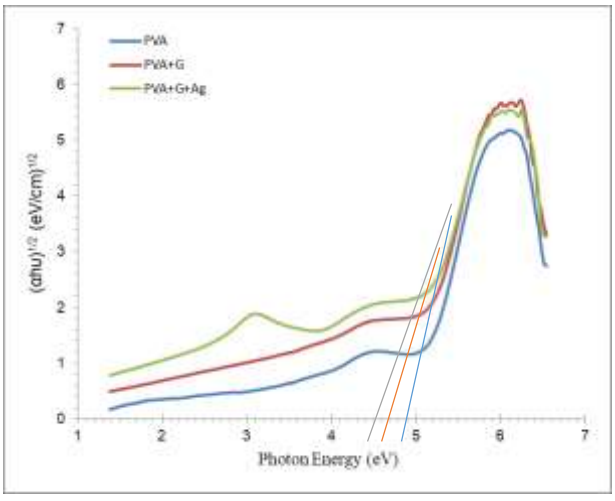

(a)

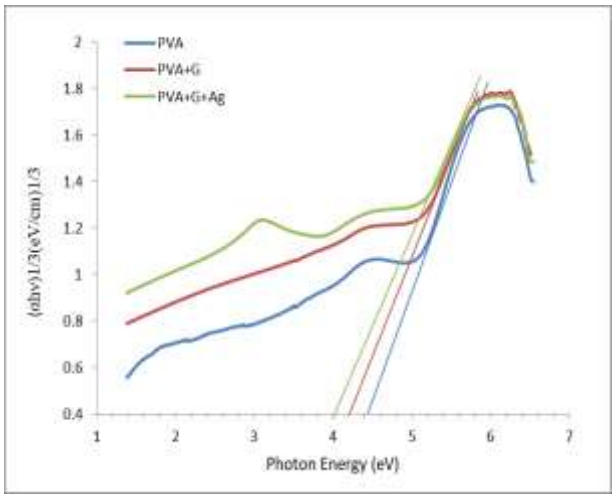

(b)

Figure.5 (a) and (b)The plot of $(\alpha h\upsilon)^{1/2}$ and $(\alpha h\upsilon)^{1/3}$ as a function of photon energy respectively

Table 1. The value of energy gap for a pure PVA, PVA-G and PVA-G-Ag nanocomposite

Component	Allowed E_g(eV)	Forbidden E_g(eV)
Pure PVA	5	4.4
PVA-G	4.8	4.2
PVA-G-Ag	4.7	4.1

Scanning electron microscopic (SEM) used to show the morphologies for a pure PVA, PVA-Graphene and PVA-Graphene-Ag nanocomposite are appeared in Figure.6. This Figure. a show that the image for a pure PVA was homogenous due to the spin coating method. The SEM images of PVA-G and PVA-G-Ag nanocomposite in Figure. b show that the GNPs are uniformly spread inside the PVA matrix and the average size nanoparticle was 130 nm, while the adding of AgNPs and GNPs to the PVA matrix was apparently noticeable from Figure. c and the average size nanoparticle was 115 nm. From this images of the SEM has been confirmed the incorporation for the PVA-G-Ag nanocomposite that deal with the result of the absorption spectra of this nanocomposite. The microstructural attributes of their materials demonstrated that the G was fairly scattered consistently in the grid even at higher focus because of the solid interfacial communications with the lattice and the turn drying strategy which was utilized during their answer mixing system are appeared in Figure.7

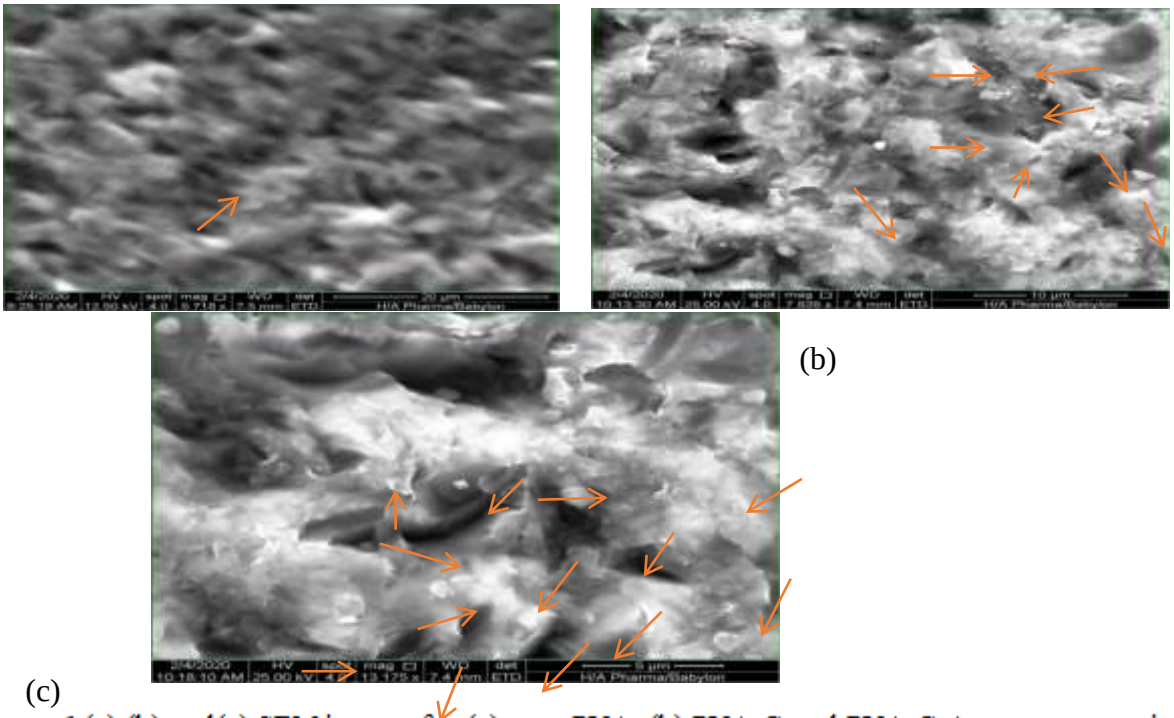

(a) (b) (c)

Figure.6 (a) (b) and(c) SEM images for (a) pure PVA, (b) PVA-G and PVA-G.Ag nanocomposite

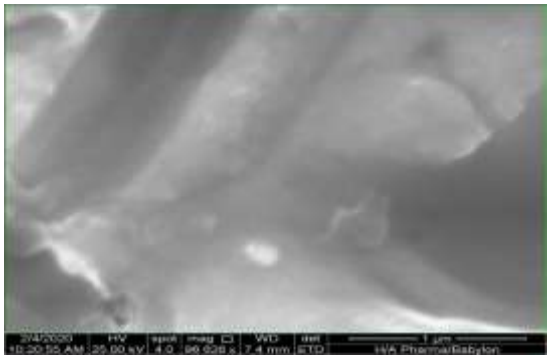

(a)

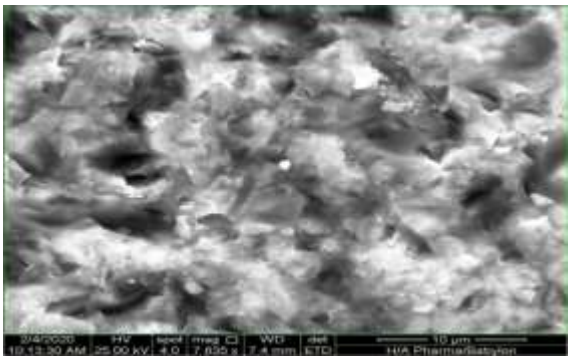

(b)

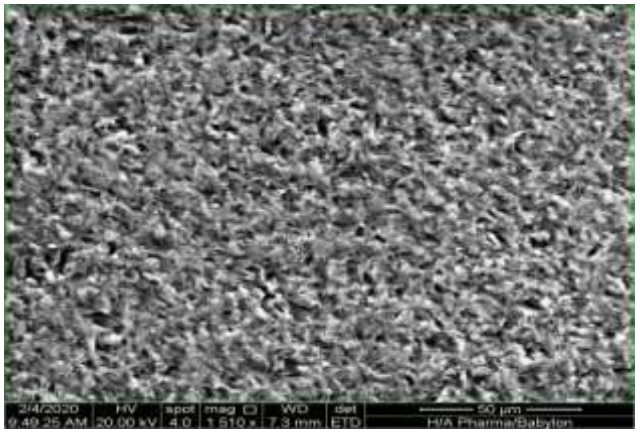

(c)

Figure.7 (a) (b) and (c) SEM for PVA-G-Ag nanocomposite

Fourier transform infrared (FTIR) spectroscopy was utilized to show data about the compound holding in the recently created nanomaterials. Figure.8 shows FTIR for pure PVA, pure graphite and PVA-G-Ag nanocomposite individually.

In the pure PVA, there are peaks at (3295, 2937, 1713,1240,1140,1086 and 832) cm^{-1} clearly observed, but is missing in the graphite spectra that have only strong peak at 1086 cm-1 has observed and for PVA-G-Ag nanocomposite spectrum, peaks at (3292, 2895,2359,1660,1200 and 1086) cm^{-1} observed without four peaks are missing (1713, 1240, 1140 and 832) cm^{-1}, additionally, the peaks 3295 cm^{-1} and 2937 cm^{-1} had been shifted for lower wavenumber and new peaks at (2359, 1660 and 1200) cm^{-1} has been established.

In all spectrums, the 3295 cm^{-1} and 3292 cm^{-1} due to O–H stretching vibration of carboxyl groups and the absorbed water this absorption peak is shifted to 3292 cm^{-1}[31], a lower wavenumber with the addition of graphene. Meanwhile, the stretching vibration at 2937 cm^{-1} and 2895 cm^{-1} belonging to C–H_2 [32,33]. The vibration at 1660 cm^{-1}, 1200 cm^{-1} and 1086 cm^{-1} are allocated to C=C stretching, and C–O stretching[34,35], respectively with higher intensity in the PVA-G-Ag nanocomposite spectrum than in pure PVA and graphite spectrums, indicating that carbon bond between C, C and O has been established.

The above results prove the strong interfacial interaction between graphene and PVA.

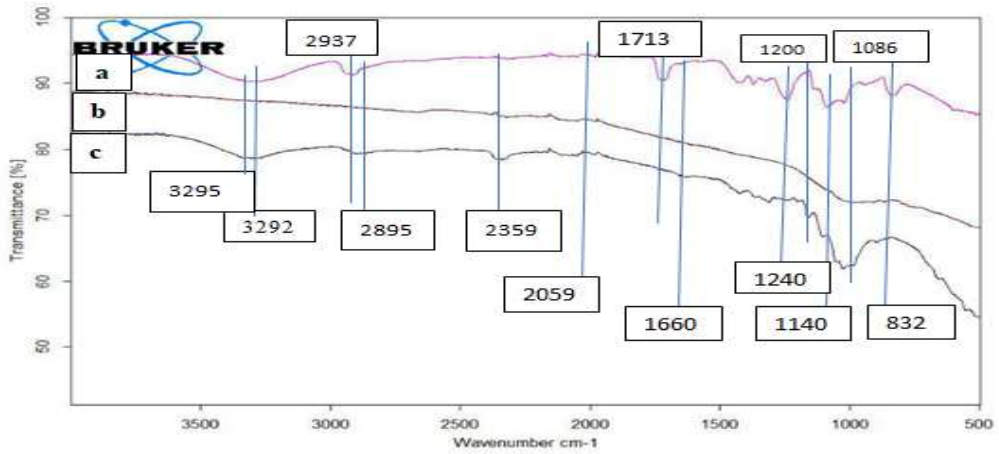

Figure.8 FTIR spectrum for (a) pure PVA, b)pure graphite and (c) PVA-G-Ag nanocomposite respectively

Conclusion

In summary, we have utilized pulsed laser ablation liquid technique to fabricate PVA-G-Ag nanocomposite using with less laser power and small laser beam spot sizes and less time ablation close to 2 minutes. The UV-Vis spectrum of PVA-Graphene-Ag nanocomposite show that two main peaks one 0.4 around 272 nm for G and second 0.48 around 403 nm for AgNPs which indicates that the formation PVA-G-Ag nanocomposite. The energy gap decreased from 5 to 4.6 eV for allowed indirect transition and also decreased from 4.4 to 4.1eV for forbidden indirect transition. The optical parameters such as transmittance and absorption coefficient have been calculated. The SEM images confirmed the homogenous shape without aggregations of prepared samples for pure PVA, PVA-Graphene, and PVA-Graphene-Ag nanocomposite. The FTIR studies also gave the evidence regarding the formation of the nanocomposites, where, FTIR has shown that the interaction between the graphene, silver and polymer matrix. This investigation demonstrates that the pulse laser ablation a good instruments to decorated metals on graphene.

Acknowledgments

Praise be to Allah Lord of the World, and best prayers and peace upon him best messenger Mohammed, his pure descendants, and his noble companions. Then, I would like to express my deep gratitude and appreciation to my supervisors, Dr. Ghaleb Al-Dahash, Dr. Amer Al-Nafiey for their guidance, suggestions, and encouragement throughout the research work.

References

[1] Novoselov and K S. “Nobel lecture: Graphene: Materials in the flatland” 2011 *Reviews of Modern physics* **83** 837

[2] Geim and A K “Nobel Lecture: Random walk to graphene” 2011 *Reviews of Modern Physics* **83** 851.

[3] Wei J, Atif R, Vo T and Inam F “Graphene nanoplatelets in epoxy system: dispersion, reaggregation, and mechanical properties of nanocomposites” 2015 *J. of Nanomaterials* **16** 374.

[4] Slonczewski J C and Weiss P R “Band structure of graphite” 1958 *Physical Review* **109** 272 (1958).

[5] Zhu Y, Murali S, Cai W, Li X, Suk J W, Potts J R and Ruof R S “Graphene and graphene oxide: synthesis, properties, and applications” 2010 *Advanced materials* **22** 3906-3924.

[6] Tiwari A and Syväjärvi M "Graphene Materials: Fundamentals and Emerging Applications" 2015 *John Wiley & Sons*.
[7] Dedkov Y S, Fonin M, Rudiger U and Laubschat C " Effect in the Graphene/Ni(111) System" 2008 *Phys. Rev. Lett*. **100** 602.
[8] Novoselov K S, Geim A K, Morozov S V, Jiang D, Zhang Y, Dubonos S V, Grigorieva V and Firsov A A " Electric Field Effect in Atomically Thin Carbon Films" 2004 *Science* **306** 666.
[9] Sadowski M L, Martinez G, Potemski M, Berger C and de Heer W A"Landau Level Spectroscopy of Ultrathin Graphite Layers" 2006 *Phys. Rev. Lett* **97** 405.
[10] He H .Y, Klinowski J, Forster M, Michael, Lerf and Anton"A new structural model for graphite oxide" 1998 *Chemical Physics Letters* **287** 266.
[11] Li X, Zhang G, Bai X, Sun X, Wang X, Wang E and Dai H" Highly conducting graphene sheets and Langmuir-Blodgett films" 2008 *Nat. Nanotechnol* **3** 538.
[12] Liu N., Fang L, Haoxi W, Yinghui L, Chao Z, Ji C "One-Step Ionic-Liquid-Assisted Electrochemical Synthesis of Ionic-Liquid-Functionalized Graphene Sheets Directly from Graphite" 2008 *Adv. Funct. Mater.* **18** 1518.
[13] Russo P, Hu A M, Compagnini G, Duley W W, Zhou N Y "Femtosecond. Laser Ablation of Highly Oriented Pyrolytic Graphite: a Green Route for Large-Scale Production of Porous Graphene and Graphene Quantum Dots" 2014 *Nanoscale* **6** 2381−2389.
[14] Yanyan F, Ningning D, Gaozhong W, Yuanxin L, Saifeng Z, Kangpeng W, Long Z, Werner J B and Jun W " Saturable absorption behavior of free-standing graphene polymer composite films over broad wavelength and time ranges" 2015 *Optics Express* **23** 559-569.
[15] Abu Hannifa A, Zulhelmi I, Anis S Z A, Fadwa S I and Kamal Y" PVA/Graphene Nanocomposite: Morphology and its Thermal Properties" 2018 *IOP Conf. Series: Materials Science and Engineering* **319**.
[16] Chenlu B, Yuqiang G, Lei S, and Yuan H" Poly (vinyl alcohol) nanocomposites based on graphene and graphite oxide: A comparative investigation of property and mechanism" 2011 *J. of Materials Chemistry* **21** 13942-13950.
[17] Chang-Jie G, Fen-Ying K, Zhi-Dong C, Da-He F, Hai-Lin F and Wei W " Reduced graphene oxide-Hemin-Au nanohybrids: Facile one-pot synthesis and enhanced electro catalytic activity towards the reduction of hydrogen peroxide"2016 *Biosensors and Bioelectronics* **78** 300-307.
[18] Anamt M N, Muhammad M S, Perumal R and Nay M H " A glassy carbon electrode modified with graphene oxide and silver nanoparticles for amperometric determination of hydrogen peroxide" 2016 *J. of springer* **183** 911–916.
[19] Ke-Jing H, Lan W, Jing L, Tian G and Yan-Ming L " Glassy carbon electrode modified with glucose oxidase–graphene–nano-copper composite film for glucose sensing" 2013 *Science direct* **46** 378-383.
[20] Chen J L and Yan X P "A dehydration and stabilizer free approach to production of stable water dispersions of graphene nanosheets" 2010 *J. Mater. Chem.* **20** 4328–4332.
[21] Kumar V, Singh S, Umrao V, Parashar S, Abraham A K, Singh G Nath, Saxena P S and Srivastava A "Facile, rapid and up scaled synthesis of green luminescent functional graphene quantum dots for bioimaging" 2014 *RSC Adv.* **4** 21101–21107.
[22] Ghavidel E, Sari A H, and Dorranian D "Experimental investigation of the effects of different liquid environments on the graphene oxide produced by laser ablation method" 2018 *Opt. Laser Technol.* **103** 155–162.
[23] Ghanbari H, Sarraf-Mamoory R, Sabbaghzadeh J, Chehrghani A and Malekfar R "Nonlinear optical absorption of carbon nanostructures synthesized by laser ablation of highly oriented pyrolytic graphite in organic solvents" 2013 *Int. J. Opt. Photonics* **7** 113–124.
[24] Amer Al, Palaniappan S, Ahmed A, Brigitte S, Sabine S and Rabah B "Green synthesis of reduced graphene oxide-silver nanoparticles using environmentally friendly L-arginine for H_2O_2 detection" 2016 *ECS Journal of Solid State Science and Technology* **5** 3060-3066.

[25] Yanyan F, Ningning D, Gaozhong W, Yuanxin L, Saifeng Z, Kangpeng W, Long Z, Werner J B and Jun W ”Saturable absorption behavior of free-standing graphene polymer composite films over broad wavelength and time ranges” 2015 *Optics Express* **23**.

[26] Streetman B G, Bonerjee S “Solid state electronic devices, 5th ed.”2000 *Engle Wood cliffs, N. J. Prenticeilall*.

[27] Hua D, Zhaoxin W, Yaqiu J, Weihua L, Xin L, Bo J, Waseem A and Xun H “Flexible and Thin Graphene/Silver Nanowires/Polymer Hybrid Transparent Electrode for Optoelectronic Devices” 2016 *ACS Appl. Mater. Interfaces* **8** 31212−31221.

[28] Sami S C, Khalid H A, Tahseen H M, Nadir F H, Musaab K M and Abdulhussain A K “Fabrication and Study the Structure, Optical and Dispersion Parameters of PMMA with $InCl_3$ Additive” 2019 *J. of Global Pharma Technology* **11** 369-374.

[29] Abdulhussain A k, Khalid H A, Sami S C, Musaab K M , Nadir F H, Taghreed K H and Ismaeel A. A.,”Study the Influence of Antimony Trioxide (Sb_2O_3) on Optical Properties of (PVAPVP) Composites" 2018 *J. of engineering and applied* **13** 9689-9692.

[30] Hamdy M Z , Elmetwally M A, Amr M A, Ahmed E T ”Article Characterization and some physical studies of PVA/PVP filled with MWCNTs" 2018 *J. mater res technol*. **8** 904-913.

[31] He, Hui, Wang, Haibo, Li, Kai1, Zhu, Jun, Liu, Jianshuang, Meng, Xiangdong, Shen, Xiaoshuang, Zeng, Xianghua, Cai and Weiping “Green and tunable decoration of graphene with spherical nanoparticles based on laser ablation in water: A case of Ag nanoparticle/graphene oxide sheet composites.” 2016 *Langmuir*, **32** 1667-1673.

[32] Karthikeyan B “Spectroscopic studies on Ag-polyvinyl alcohol nanocomposite films” 2005 *Physica B* **364** 328–332.

[33] Kutsenko A S and Granchak V M “Photochemical synthesis of silver nanoparticles in polyvinyl alcohol matrices” 2009 *Theoretical and Experimental Chemistry* **45** 313–318.

[34] Matveev S, Portnyagin M, Ballhaus C, Brooker R and Geiger C A ”FTIR spectrum of phenocryst olivine as an indicator of silica saturation in magmas” 2005 *J. of Petrology* **46** 603-614.

[35] Okuno D, Iwase T, Shinzawa-Itoh K, Yoshikawa S and Kitagawa T ”FTIR detection of protonation/deprotonation of key carboxyl side chains caused by redox change of the CuA-heme a moiety and ligand dissociation from the heme a 3-CuB center of bovine heart cytochrome c oxidase” 2003 *J. of the American Chemical Society* **125** 7209-7218.

Investigation of Mixed Symmetry States in 170-178Yb isotopes

Heiyam Najy Hady[1*] and Mohsin Kadhim Muttal[2]

[1]University of Kufa, Education College for girls, physics department
[2]University of Babylon, Science College, physics department
[*] E-mail : heiyam_najy@yahoo.com

Abstract: low-lying positive parity states, dynamic symmetries, mixed symmetry states (MSS), reducing electric quadrupole transition probabilities B(E2), branching ratio, reducing magnetic dipole transition probabilities B(M1), and mixing ratios δ(E2/M1) for $^{170\text{-}178}$Yb have been investigated by applied IBM-1 and IBM-2 program package. The software package IBM-1 and IBMT computer code for IBM-1 and Neutron Proton Boson NPBOS and Neutron Proton Boson Electromagnetic NPBEM software package have been used. The Ytterbium nuclei with the $(170-178)$ mass number considered as rotational nuclei after applying the first and second interacting boson model with studying dynamic symmetry and energy ratios $(E4_1^+/E2_1^+)$, $(E6_1^+/E2_1^+)$ and $(E8_1^+/E2_1^+)$ that approximated to (3.33,7 and 12). The reducing transition probability for electric quadruple $B(E2)$ and branching ratios that state the small values of the ratios R' and R'' as having rotational characteristics. A study of the mixed symmetry state of these nuclei shows that the lower energy mixing level is the first 1^+ level, which distinguishes the rotational determination nuclei. The energy levels values for the states $2_2^+, 3_1^+, 5_1^+, 1_1^+$ have a clear mixed symmetry state (MSS) directly proportional with Majorana parameters ζ_2 , while $2_{3,}^+$ and $2_{4,}^+$ tend to be approximately more conservative.

1. Introduction

The interacting bosons model is an effective method to describe the behavior of nuclei and knowing their characteristics, as it is considered one of the most flexible models in nuclear structure to describe a wide range of nuclei have the medium and heavy mass number, with its three rotational, vibratory, unstable, γ unstable limits and transitional regions. The medium heavy rare-earth Ytterbium nuclei with the neutron number between 100 and 108 have decay scheme characterized by small and nearby energy levels in the ground band which generally as rotational nuclei. $^{170\text{-}178}$Yb isotopes have Z=70, then 6 hole bosons the number of protons and neutrons lying between 50 , 82 and 82, 126 magic shells, respectively. The ^{170,172}Yb isotopes have 100,102 neutrons which mean (9,10) particle neutron bosons with total boson numbers 15,16 respectively. The $^{176\text{-}178}$Yb isotopes have 106 and 108 neutrons which mean (10,9) hole neutron bosons, the nucleons, and 16,15 boson numbers respectively. There are many studies and research that attempted to understand and explain the behavior of $^{170\text{-}178}$Yb nuclei by using different models[1-5]. in the present research the low –lying positive party states , dynamic symmetries, mixed symmetry states (MSS), and reducing transition probabilities for electric quadrupole $B(E2)$, branching ratio, magnetic dipole $B(M1)$,and mixing ratios $\delta(E2/M1)$ $^{170\text{-}178}$Yb have been investigated by applying $IBM-1$ and $IBM-2$ program package.

2.Theoretical Part

The IBM is built on a closed shell i.e., the total number of bosons (N) depends on the number of active nucleon particle (or hole) pairs outside a closed shell. Each type of bosons, the s- and d-boson, has its binding energy with regard to the closed shell [6]. The IBM-1 dose not distinguish between proton and neutron bosons; the total number of bosons $(N = n_{\pi} + n_{\nu})$ is finite and conserved in a given nucleus. The s $(L=0)$ and d $(L=2)$ bosons of the IBM-I have six sub- states; therefore, it define a six-dimensional space, so that one can describe it in terms of the unitary group in six dimensions, $U(6)$. This leads to drive many of the characteristic properties of the IBM-1 by group theoretical methods and express it analytically[7-9]. The Hamiltonian operator according to IBM-1 describes the system of s and d boson can be written as [10-13]:-

$$H = \varepsilon n_d + a_0 P^{\dagger} P + a_1 L.L + a_2 Q.Q + a_3 T_3 T_3 + a_4 T_4 T_4 \quad (1)$$

where $\varepsilon = \varepsilon_d - \varepsilon_s$ is the boson energy, for simplicity ε_s is set equal to zero only $\varepsilon = \varepsilon_d$ appears a_0, a_1, a_2, a_3, a_4 $a_4$designate the strengths of the quadrupole, angular momentum, pairing, octupole and hexadecapole interacting between bosons respectively. The electromagnetic transition operators has been given as [6-13]:-

$$T_m^l = \alpha_2 \delta_{l2} [d^{\dagger} s + s^{\dagger} d]_m^{(2)} + \beta_l [d^{\dagger} d]_m^{(l)} + \gamma_0 \delta_{l0} \delta_{m0} [s^{\dagger} s]_0^{(0)} \quad (2)$$

where $\alpha_2, \beta_l, \gamma_0$ are the coefficients of the various terms in the operators. The $M1$ operator has been given by [12,14]:-

$$T^{M1} = \beta_1 [d^{\dagger} d]_m^{(1)} \quad (3)$$

The magnetic transition will occur only for d-boson since the s-d interaction will vanish. The angular momentum operator and $g-$ factor have been written as [13,15]

$$T_m^{M1} = \sqrt{3/4\pi}\, g_B L,\ g_B = \beta_1/10\sqrt{4\pi/3}\, L \quad (4)$$

where g_B is the effective boson $g-$factor, the factor $\sqrt{3/4\pi}$ has been introduced to conform with standard notation since the operator L is diagonal in any basis no $M1$ transition can occur in this approximation, the diagonal matrix element depends only on L and is the same for all three cases they given by[12,16]:-

$$\langle L' \| T^{M1} \| L \rangle = \sqrt{3/4\pi}\, g_B \sqrt{[L(L+1)(2L+1)]} \quad (5)$$

In terms of magnetic moment (μL) [14,17]

$$g_B = \mu_L \,/\, L \quad (6)$$

The states $g-$factor defined as [18]:-

$$g_L = \mu_L \,/\, L, \text{ where } g_L = g_B \quad (7)$$

The magnetic dipole transition probability can be given by the form [18]:-

$$B(M1; L' \to L) = \frac{1}{2L+1} |\langle L' \| T^{M1} \| L \rangle|^2 \quad (8)$$

The electric quadrupole $T(E2)$ operator can be taken from equation (2) as [6]:-

$$T_m^{E2} = \alpha_2 [d^{\dagger} s + s^{\dagger} d]_m^{(2)} + \beta_2 [d^{\dagger} d]_m^{(2)} \quad (9)$$

where α_2 is the effective charge of s and d boson , β_2 is the effective charge of d- boson. The selection rules of the electric quadrupole operator for three dynamical symmetries (Chain I, II, and III) are as follows [6-13].

Chain I ; SU(5) : $\Delta nd = 0, \pm 1$;
Chain II; SU(3): $\Delta\lambda = 0, \Delta\mu = 0$;
Chain III; O(6) : $\Delta\sigma = 0, \Delta\tau = \pm 1$.

The electric quadrupole transition rates are governed by $B(E2)$ values, defined as [8]

$$B(E2; L_i \to L_f) = \frac{1}{2L_f+1} \left| \langle L_f \| T^{M1} \| L_i \rangle \right|^2 \quad (10)$$

where L_i is the initial angular momentum and L_f is the final angular momentum. The (Branching Ratios) of the reduced transition probabilities for electric quadrupole transition of the dynamical symmetry SU(5), SU(3), and O(6) obey the following relations [6-10]:-

$$R = \frac{B(E2; 4_1^+ \to 2_1^+)}{B(E2; 2_1^+ \to 0_1^+)} \quad (11)$$

$$R' = \frac{B(E2; 2_2^+ \to 2_1^+)}{B(E2; 2_1^+ \to 0_1^+)} \quad (12)$$

$$R'' = \frac{B(E2; 0_2^+ \to 2_1^+)}{B(E2; 2_1^+ \to 0_1^+)} \quad (13)$$

they can be written in terms of the total boson number N [13]:-

$$R = R' = R^{"} = \frac{2(N-1)}{N} < 2; SU(5) \quad (14)$$

$$R \approx \frac{10}{7}; R' = R^{"} = 0 \ ; SU(3) \quad (15)$$

$$R = R' < \frac{10}{7}; R^{"} = 0; O(6) \quad (16)$$

The Hamiltonian operator in $IBM-2$ will have three parts: one parts for each of proton and neutron bosons and a third part for describing the proton-neutron interaction, i.e.

$$H = H_\pi + H_\nu + V_{\pi\nu} \quad (17)$$

A simple schematic Hamiltonian guided by microscopic consideration is given by [12]:-

$$H = \varepsilon(n_{d\pi} + n_{d\nu}) + \kappa Q_\pi . Q_\nu + V_{\pi\pi} + V_{\nu\nu} + M_{\pi\nu} \quad (18)$$

where

$$Q_\rho = (d_\rho^\dagger s_\rho + s_\rho^\dagger d_\rho)_\rho^2 + \chi_\rho (d_\rho^\dagger d_\rho)_\rho^2 \ \ \rho = \pi, \nu \quad (19)$$

$$V_{\rho\rho} = \sum_{L=0,2,4} \frac{1}{2}(2L+1)^{\frac{1}{2}} C_L^\rho \left[(d_\rho^\dagger d_\rho^\dagger)^{(L)} . (d_\rho d_\rho)^{(L)}\right]^{(0)} \quad (20)$$

and $\varepsilon_\pi, \varepsilon_\nu$ are proton and neutron energies respectively and they assumed equal $\varepsilon_\pi = \varepsilon_\nu = \varepsilon$. The last term in Eq.(18) contains the Majorana operator $M_{\pi\nu}$ and it is usually added to remove states of mixed proton neutron symmetry. This term can be written as[13,18]

$$M_{\pi\nu} = \zeta_2 (s_\nu^\dagger d_\pi^\dagger - d_\nu^\dagger s_\pi^\dagger)^{(2)} . (s_\nu d_\pi - d_\nu s_\pi)^{(2)} + \sum_{k=1,3} \zeta_k (d_\nu^\dagger d_\pi^\dagger)^{(k)} - (d_\nu d_\pi)^{(k)} \quad (21)$$

If there is an experimental evidence for the so called "mixed symmetry" state, then the Majorana parameters are varied to fix the location of these states in the spectrum. The energy levels are obtained by diagonalizing the Hamiltonian Eq.(18) and allowing the parameters $\varepsilon, \kappa, \chi_\pi, \chi_\nu$ and C_L to vary until one obtains the beast fit to the experimental spectrum.

Using Eq. (18), it is possible to obtain spectra that are similar to those of the IBM-1 with only one kind of boson [18]. The $U(5)$ limit when $\varepsilon \gg \kappa$, the $SU(3)$ limit when $\varepsilon \ll \kappa$ and $\chi_\pi = \chi_\nu = -\sqrt{7}/2$, and $O(6)$ limit when $\varepsilon \ll \kappa$ and $\chi_\nu = -\chi_\pi$. Most nuclei do not strictly belong to any of these three limiting cases, but are somewhere between two of them. In the IBM, it is possible to make a smooth transition between the limiting cases for a series of isotopes. The general single boson transition operator of angular momentum ℓ has the same form as in Eq.(2) in IBM-1 except for the fact that in each term one has to consider π, ν degree of freedom and this can be written as[12]

$$[d^\dagger s + s^\dagger d]_\rho^{(2)} + \beta_{\ell\rho}[d^\dagger d]_\rho^{(\ell)} + \gamma_{0\rho}\delta_{\ell 0}[s^\dagger s]_\rho^{(0)} \ldots \rho = \pi \ or \ \nu \quad (22)$$

This equation yield transition operators for $E0, M1, E2, M3$, and $E4$, For $E2$ operator[13]

$$T^{E2} = e_\pi Q_\pi + e_\nu Q_\nu \quad (23)$$

Where $Q_\rho$is the same as in Eq. (19) and e_π , e_ν are boson effective charges depending on the boson number N and they can take any value to fit the experimental result .The values of effective charge are sensitive to the nuclear structure while the ratio e_ν/e_π depends only on the assumption of maximal F − spin for 0_1^+ and 2_1^+states .The two effective charges e_π and e_ν can obtained[19] by using boson number N_π , N_ν and experimental $B(E2; 2_1^+ \to 0_1^+)$ values for a series of isotopes to produce a plot between N_ν/N_π and M where defined as [18-21]

$$M = N_\pi \left[N . B(E2; 2_1^+ \to 0_1^+)\right]^{1/2} \quad eb \ in \ U(5) \quad (24)$$

$$M = N_\pi \left[5N(2N+3)^{-1} . B(E2; 2_1^+ \to 0_1^+)\right]^{1/2} eb \quad in \ SU(3) \quad (25)$$

$$M = N_\pi \left[5N(N+4)^{-1} . B(E2; 2_1^+ \to 0_1^+)\right]^{1/2} \quad eb \ in \ O(6) \quad (26)$$

The best straight line through the experimental point is obtained with slope $e_\pi$and intercept e_ν. The $M1$ operator obtained by letting $\ell = 1$ in Eq. (22) [18,19] as:-

$$T^{(M1)} = [\frac{3}{4\pi}]^{\frac{1}{2}}(g_\pi L_\pi^{(1)} + g_\nu L_\nu^{(1)}) \quad (27)$$

Where g_π , g_ν are the boson g-factor in unit μ_N and $L_\rho^{(1)} = \sqrt{10}(d^\dagger d)_\rho^{(1)}$,then

$$T^{(M1)} = [\frac{3}{4\pi}]^{\frac{1}{2}}[\frac{1}{2}(g_\pi + g_\nu)(L_\pi^{(1)} + L_\nu^{(1)}) + \frac{1}{2}(g_\pi - g_\nu)(L_\pi^{(1)} - L_\nu^{(1)})] \quad (28)$$

The first term on the right hand side of this equation is diagonal; therefore, for $M1$ transition the previous equation may be written as

$$T^{(M1)} = 0.77[(d^\dagger d)_\pi^{(1)} - (d^\dagger d)_\nu^{(1)}](g_\pi - g_\nu) \quad (29)$$

Few experimental absolute $B(M1)$ transition are available to test IBM predictions, the total g- factor is defined by [21,22]:

$$g = \frac{g_\pi N_\pi}{(N_\pi + N_\nu)} + \frac{g_\nu N_\nu}{(N_\pi + N_\nu)} \Rightarrow g = \frac{(g_\pi N_\pi + g_\nu N_\nu)}{(N_\pi + N_\nu)};\ g = Z/A \quad (30)$$

where Z is the atomic number ,and A is the mass number , g_π and g_ν are obtained by using the same method which used to calculate the effective charges e_π and e_ν.The $M1$ strength many be expressed in terms of the multipole mixing

$$\delta\left(\frac{E2}{M1}\right) = 0.835E_\gamma(MeV).\Delta;\ \ \Delta = \frac{\langle J_f \| T^{(E2)} \| J_i \rangle}{\langle J_f \| T^{(M1)} \| J_i \rangle} \quad (31)$$

by having fitted $E2$ matrix elements, one can then use them with $\delta(E2/M1)$ to obtain $M1$ matrix element and compare them with the matrix elements predicted by the model using the operator eq.(31). An important property of this new version is that the proton-neutron symmetry character of each state is specified in terms of a new quantum number called F −spin [23]. The F −spin raising , lowering, and F −component operators given in.[24]as:-

$$F_+ = d_\pi^\dagger d_\nu + s_\pi^\dagger s_\nu\ ;\quad F_- = d_\nu^\dagger d_\pi + s_\nu^\dagger s_\pi \quad (32)$$

Proton boson have an intrinsic quantity, $F = 1/2$ which can be introduced in a formalism similar to that used for isotopic spin[23,24]. Then proton bosons will have a Z −projection $F_Z = +1/2$ while neutron bosons have $F_Z = -1/2$, thus one can write an F −spin multiple as

$$|\pi\rangle = \left|\frac{1}{2}, +\frac{1}{2}\right\rangle,\ |\nu\rangle = \left|\frac{1}{2}, -\frac{1}{2}\right\rangle \quad (33)$$

The total symmetric states have the maximum value F −spin $F_{max} = |(N_\pi + N_\nu)|/2$ while the mixed symmetry states characterized by decreasing F −spin value $F_{max} = |N_\pi + N_\nu|/2 \rightarrow |N|/2\,, F = F_{max} - 1, F_{max} - 2, \dots, F_{min} = |N_\pi - N_\nu|/2$,bosons is fully symmetric under the interchange of neutron and proton boson if it has maximal F −spin $F_{max} = N/2$ .A state with only s- boson is naturally fully symmetric and has $F = N/2$ it should be noted that the state of maximum F − spin are in one to one correspondence with the states of IBM-1 while the states with F −spin less than the maximum value of $N/2$ having no counterparts in IBM-1. They have mixed proton-neutron symmetry character, thus they are called mixed symmetry states. These states are considered as the main interest in studying the IBM-2 [23]. Mixed symmetry states have been observed in many even -even nuclei between the mass numbers 50 and 240. This urges when the movement of protons and neutrinos forming collective excitation are not in one phase, it has been observed in the three limits of collective excitations in vibrational rotational and γ −unstable nuclei the lowest energy to mixed symmetry states is first 1^+ level at about 3Mev in rotational nuclei while lowest energy mixed symmetry states in vibrational and γ unstable is around 2 MeV[23].

3.Results and discussion

IBM-1 and IBM-2 software package have been used to estimate a set of parameters described in the Hamiltonian operator as it is shown in equations (1) and (17). The parameters estimated for the low- lying calculations of the excited energy levels for Ytterbium isotopes are given in table (1)

Table 1: The parameters have been used in the IBM-1 and IBM-2 Hamiltonian for even-even $^{170\text{-}178}$Yb isotopes (in MeV) except χ , $\chi\nu$ and $\chi\pi$ were unit less.

Isotopes	IBM-1 parameters in MeV unless χ							
	N_{tot}	ε	a_0	a_1	a_2	a_3	a_4	χ
^{170}Yb	15	0.0	0.0	0.009	-0.0122	0.0	0.0	-1.31
^{172}Yb	16	0.0	0.0	0.008	-0.0112	0.0	0.0	-1.31
^{176}Yb	16	0.0	0.0	0.009	-0.012	0.0	0.0	-1.31
^{178}Yb	15	0.0	0.0	0.008	-0.0142	0.0	0.0	-1.31
Isotopes	IBM-2 parameters in MeV unless χ , χ_π= -1.24 , N_π =6							
	N	ε_d	κ	χ_ν	ζ_2	$\zeta_{1,3}$	C_ν^L	C_π^L
^{170}Y	9	0.61	-0.07	-	0.01	0.01	0.08,0.08,0.0	0.4,0.08 ,0.0
^{172}Y	1	0.6	-0.064	-	-0.01	0.01	0.08,0.06,0.0	0.4,0.08 ,0.0
^{176}Y	1	0.61	-0.067	-	-0.01	0.01	0.08,0.08,0.0	0.4,0.08 ,0.0
^{178}Y	9	0.61	-0.075	-	-0.001	0.02	0.08,0.08,0.0	0.4,0.08 ,0.0

One of the most important tests have been carried out on the nuclei is the calculation of energy ratios that are a good indication and a guide for the determination symmetries region that the isotope belongs. ($E4_1^+/E2_1^+$), ($E6_1^+/E2_1^+$) and ($E8_1^+/E2_1^+$) have been calculated for $^{170\text{-}178}$Yb isotopes put in Figure (1), That leads to guessing the nearest dynamic symmetries which correspond to the characterizes of $^{170\text{-}178}$Yb isotopes [12].

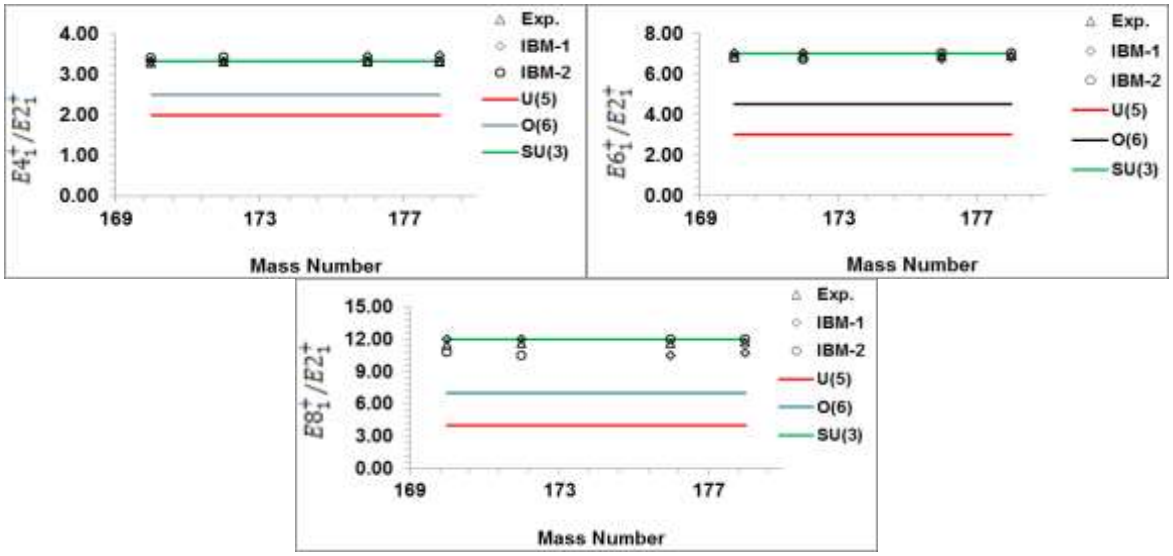

Figure 1: The experimental[25-29], theoretical and standard[18] energy ratios ($E4_1^+/E2_1^+$, $E6_1^+/E2_1^+$, and $E8_1^+/E2_1^+$) respectively as a function of mass numbers for $^{170\text{-}178}$Yb isotopes.

The calculated energy levels compared with experimental data [24-29] $^{170\text{-}178}$Yb isotopes have been shown in Figure (2) .

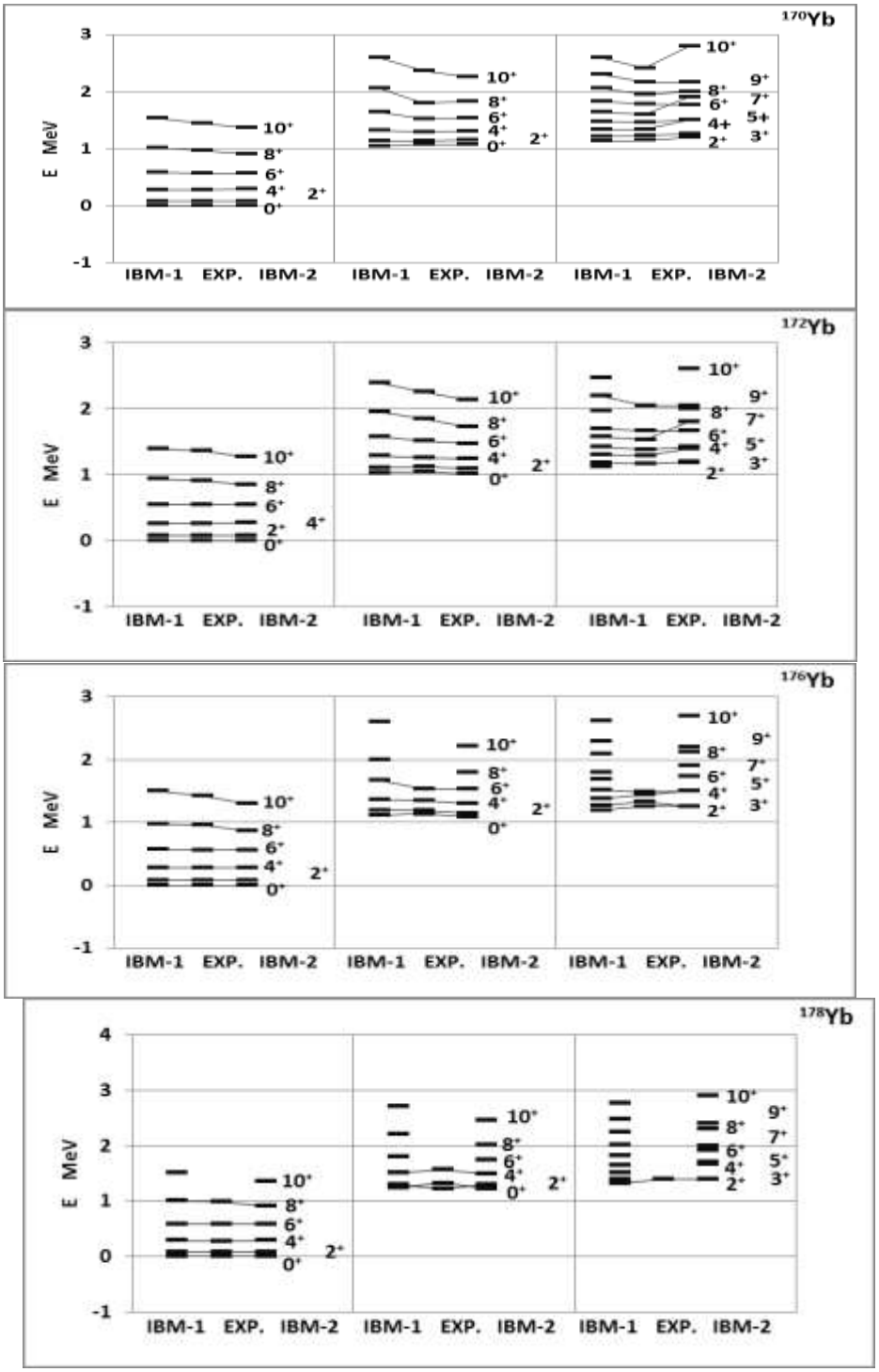

Figure 2: Comparison between experimental [25-29] and calculated energy levels for $^{170\text{-}178}$Yb isotope.

The most important features of IBM-2 was the possibility of clarification of mixed symmetry states in even-even nuclei which made up from mix up of the protons and neutrons waves functions. In more vibrational and gamma soft nuclei the lowest MS states with $J = 2^+$, in the rotational nuclei observed as

the $J = 1^+$ states .The effect of Majorana parameters (ζ_2) on the calculated excitation energy levels for $^{170\text{-}178}$Yb isotopes has been investigated by vary the ζ_2 around the best-fitted with experimental data as shown in figure (3).

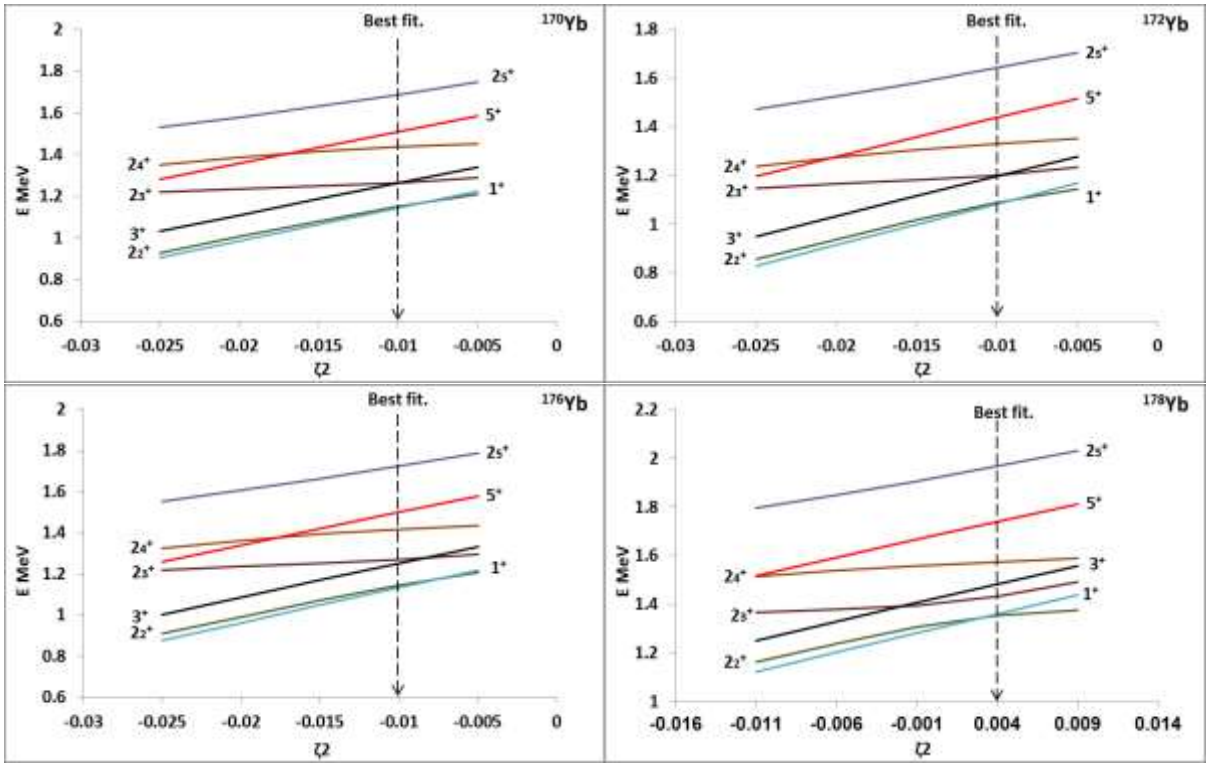

Figure 3: Mixed symmetry states Mss as a function ζ_2 for $^{170\text{-}178}$Yb isotopes.

The effective boson charges have been estimated from equations (9) and (23) to calculate $B(E2)$ transition probabilities , theoretical branching ratios. $B(E2)$ compression with the experimental values [25-31] for $^{170\text{-}178}$Yb isotopes were listed in tables (2) and (3).

Table 2: The used effective boson charges used in IBM-1and IBM-2 to calculate B(E2) transition probabilities for $^{170\text{-}178}$Yb isotopes and branching ratios.

Isotopes	The effective boson charges (eb)			
	IBM-1		IBM-2	
	E2SD	E2DD	e_ν	e_π
^{170}Yb	0.107	-0.1398	0.06	0.22
^{172}Yb	0.104	-0.137	0.061	0.22
^{176}Yb	0.099	-0.127	0.049	0.22
^{178}Yb	0.11	-0.143	0.06	0.22

Isotopes	R			R'			R''		
	Exp.	IBM-1	IBM-	Exp.	IBM-1	IBM-2	Exp.	IBM-1	IBM-2
^{170}Yb	--	1.414	1.428	--	$8.5\times10^{-}$	0.0014	--	0	0.0022
^{172}Yb	1.42	1.412	1.41	--	$1.9\times10^{-}$	0.0009	--	0	0.0019
^{176}Yb	1.445	1.412	1.414	--	$3.5\times10^{-}$	0.0029	--	$2.7\times10^{-}$	0.0014
^{178}Yb	--	1.41	1.407	--	$1.4\times10^{-}$	0.0011	--	$3.3\times10^{-}$	0.00138

*$E2SD$ and $E2DD$ are $IBMT$ parameters where α_2 and β_2 are the boson effective charge for $IBM1$ $E2SD = \alpha_2, E2DD = \sqrt{5}\beta_2$ where $\beta_2 = -\frac{0.7}{\sqrt{5}}\alpha_2, -\frac{\sqrt{7}}{2}\alpha_2$, $\beta_2 = 0$ in $U(5), SU(3)$, and $O(6)$ limits respectively.

Table 3: Calculated reduced electric quadrupole transitions probability $B(E2)$ values in (e^2b^2) unit compression with experimental data [24-30] for $^{170\text{-}178}$Yb isotopes.

Isotopes	^{170}Yb			^{172}Yb		
$J_i^+ \to J_f^+$	Exp.	IBM-1	IBM-2	Exp.	IBM-1	IBM-2
$2_1 \to 0_1$	1.124	1.124	1.126	1.204	1.208	1.203
$4_1 \to 2_1$	--	1.59	1.6	1.71	1.71	1.697
$6_1 \to 4_1$	--	1.719	1.74	1.818	1.853	1.843
$8_1 \to 6_1$	1.697	1.75	1.693	2.27	1.893	1.896
$10_1 \to 8_1$	1.678	1.73	1.68	2.1	1.883	1.958
$0_2 \to 2_1$	--	0.0	0.0025	--	0.0	0.0022
$2_2 \to 0_2$	--	0.0076	0.201	--	0.0072	0.265
$2_2 \to 2_1$	--	0.0000096	0.00163	--	0.0000023	0.0011
$4_2 \to 2_2$	--	0.542	0.57	--	0.59	0.609
$6_2 \to 4_2$	--	1.048	1.147	--	1.144	1.385
$8_2 \to 6_2$	--	1.229	1.272	--	1.346	1.385
$10_2 \to 8_2$	--	1.285	1.331	--	1.415	1.478
$3_1 \to 2_2$	--	1.64	1.446	--	1.786	1.444
$5_1 \to 3_1$	--	0.859	0.982	--	0.937	1.032
$7_1 \to 5_1$	--	1.154	1.168	--	1.263	1.232
$9_1 \to 7_1$	--	1.253	1.287	--	1.379	1.373
$4_3 \to 2_3$	--	1.293	0.994	--	1.411	1.306
$6_3 \to 4_3$	--	1.388	1.267	--	1.519	1.404
$8_3 \to 6_3$	--	1.397	1.423	--	1.538	1.5
$10_3 \to 8_3$	--	1.36	1.517	--	1.509	1.622
$3_1 \to 1_1$	--	--	0.842	--	--	0.875
$1_1 \to 2_1$	--	--	0.032	--	--	0.033
$2_1 \to 0_1$	--	--	1.0001	--	--	0.989
Isotopes	^{176}Yb			^{178}Yb		
$J_i \to J_f$	Exp.	IBM-1	IBM-2	Exp.	IBM-1	IBM-2
$2_1 \to 0_1$	1.072	1.076	1.074	--	1.184	1.182
$4_1 \to 2_1$	1.55	1.524	1.565	--	1.675	1.66
$6_1 \to 4_1$	1.71	1.651	1.706	--	1.811	1.796
$8_1 \to 6_1$	1.72	1.687	1.723	--	1.844	1.839
$10_1 \to 8_1$	--	1.677	1.74	--	1.825	1.882
$0_2 \to 2_1$	--	0.0	0.0016	--	0.0	0.0016
$2_2 \to 0_2$	--	0.0064	0.198	--	0.008	0.267
$2_2 \to 2_1$	--	0.000038	0.0031	--	0.000017	0.00137
$4_2 \to 2_2$	--	0.526	0.531	--	0.571	0.585
$6_2 \to 4_2$	--	1.021	1.202	--	1.021	1.188
$8_2 \to 6_2$	--	1.201	1.225	--	1.201	1.235
$10_2 \to 8_2$	--	1.263	1.309	--	1.263	1.298
$3_1 \to 2_2$	--	1.593	1.176	--	1.593	1.427

$5_1 \rightarrow 3_1$	--	0.836	0.909	--	0.836	1.01
$7_1 \rightarrow 5_1$	--	1.127	1.221	--	1.127	1.36
$9_1 \rightarrow 7_1$	--	1.23	1.34	--	1.23	1.329
$4_3 \rightarrow 2_3$	--	1.256	1.135	--	1.256	1.086
$6_3 \rightarrow 4_3$	--	1.352	1.233	--	1.352	1.297
$8_3 \rightarrow 6_3$	--	1.369	1.35	--	1.369	1.45
$10_3 \rightarrow 8_3$	--	1.343	1.453	--	1.343	1.548
$3_1 \rightarrow 1_1$	--	--	0.789	--	--	0.878
$1_1 \rightarrow 2_1$	--	--	0.039	--	--	0.036
$2_1 \rightarrow 0_1$	--	--	0.954	--	--	0.989

Magnetic properties of nuclear states are effective probes of nuclear wave functions the nuclei near closed shells mainly determined $g-$ factors by single particle motion and configuration mixing ,in the deformation nuclei the collective motion of protons and neutrons is responsible for $g-$factors values. $B(M1)$transition probability has been calculated using the effective $g-$factors for proton g_π and neutron g_ν. for $^{170\text{-}178}$Yb isotopes $g_\pi = (0.51\mu_N)$ and $g_\nu = (0.28\mu_N)$. Eq. (28,31*)* have been used in IBM-2 to calculate the $B(M1)$ transition probabilities and $\delta(E2/M1)$ as shown in table (4). The calculated values for $B(M1)$ and the mixing ratio $\delta(E2/M1)$ have been compared with the available experiments data[25-29].

Table 4: Comparison between calculated magnetic transitions $B(M1)$ in unit (μ_N^2) and mixing ratio $\delta(E2/M1)$ with the experimental data [25-29,31] for $^{170\text{-}178}$Yb isotopes.

Isotopes	^{170}Yb				^{172}Yb			
$J_i \rightarrow J_f$	B(M1) μ_N^2		$\delta(E2/M1)$		B(M1) μ_N^2		$\delta(E2/M1)$	
	Exp.	IBM-2	Exp.	IBM-2	Exp.	IBM-2	Exp.	IBM-2
$2_1 \rightarrow 1_1$	--	0.0171	--	--	--	0.0176	--	--
$2_2 \rightarrow 1_1$	--	1.0729	--	--	--	9.83×10^{-9}	--	--
$2_3 \rightarrow 1_1$	--	0.00069	--	--	--	0.00062	--	--
$2_2 \rightarrow 2_1$	--	0.03288	--	--	--	0.032	--	+0.16
$2_2 \rightarrow 2_3$	--	0.0003	--	--	--	0.00014	--	--
$2_1 \rightarrow 2_3$	--	0.0073	--	--	--	0.009	--	--
$3_1 \rightarrow 2_1$	--	0.0207	--	--	--	0.021	$+14.6^{+2}_{-2}$	-0.59
$3_1 \rightarrow 2_2$	--	0.000327	--	--	--	0.0003	--	--
$4_1 \rightarrow 3_1$	--	0.0193	--	+1.17	--	0.019	,-2.71+	+1.15
$4_2 \rightarrow 4_1$	--	0.04559	--	+0.19	--	0.045	$+13^{+76}_{-6}$	+1.0049
$5_1 \rightarrow 4_1$	--	0.0209	--	--	0.001	0.021	+1.43	-0.078
$5_1 \rightarrow 4_2$	--	3.064E-	--	--	--	1.61×10^{-5}	--	--
$4_2 \rightarrow 3_1$	--	--	--	--	--	2.33×10^{-5}	--	-86.4
Isotopes	^{176}Yb				^{178}Yb			
$J_i \rightarrow J_f$	B(M1) μ_N^2		$\delta(E2/M1)$		B(M1) μ_N^2		$\delta(E2/M1)$	
	Exp.	IBM-2	Exp.	IBM-2	Exp.	IBM-2	Exp.	IBM-2
$2_1 \rightarrow 1_1$	--	0.0179	--	--	--	0.0177	--	--

$2_2 \rightarrow 1_1$	--	3.3×10^{-6}	--	--	--	3.76×10^{-6}	--	--
$2_3 \rightarrow 1_1$	--	0.00061	--	--	--	0.000715	--	--
$2_2 \rightarrow 2_1$	--	0.0348	$+11^{+5}_{-3}$	+0.27	--	0.032	--	--
$2_2 \rightarrow 2_3$	--	0.000199	--	--	--	0.00018	--	--
$2_1 \rightarrow 2_3$	--	0.0073	+1.6	+1.74	--	0.01005	--	--
$3_1 \rightarrow 2_1$	--	0.0217		-0.8	--	0.0216	--	--
$3_1 \rightarrow 2_2$	--	0.00028	--	--	--	0.00051	--	--
$4_1 \rightarrow 3_1$	--	0.019	-6^{+9}_{-5}	+1.4	--	0.0197	--	--
$4_2 \rightarrow 4_1$	--	0.046	-0.26	+0.23	--	0.0469	--	--
$5_1 \rightarrow 4_1$	--	0.021	--	--	--	0.0214	--	--
$5_1 \rightarrow 4_2$	--	1.79×10^{-5}	--	--	--	5.9×10^{-5}	--	--

4.Conclusion

The Ytterbium nuclei with the (170-178) mass number exhibit rotational properties. The first and second interacting boson model have been studied dynamic symmetry and energy ratios ($E4_1^+/E2_1^+$), ($E6_1^+/E2_1^+$) and ($E8_1^+/E2_1^+$). The ratios approximate to (3.33,7 and 12).The reducing transition probability for electric quadruple B(E2) and branching ratio have small values for R' and R'' as in rotational limit, because of selection rules for this limit consider that the transitions $B\ (E2;\ 2_2^+ \rightarrow 2_1^+)$, $B\ (E2;\ 0_2^+ \rightarrow 2_1^+)$ are equal to zero which means forbidden transitions as we see in tables (2&3) and equation (15). The Majorana parameter effect (ζ_2) for $^{170\text{-}178}$Yb isotopes, has been investigated by vary ζ_2 around the best-fitted with experimental data. The energy levels values for the states $2_2^+, 3_1^+, 5_1^+, 1_1^+$ have clear mixed symmetry state (MSS) directly proportional with the Majorana parameters ζ_2, while $2_{3,}^+$and $2_{4,}^+$ tend to be more conservative . A study of the mixed symmetry state of these nuclei shows that the lower energy mixing level is the first 1^+ level, that distinguishes the rotational determination nuclei. The collective states location of mixed proton-neutron symmetry is one of the most remarkable open experimental difficulties in the study of collective features of nuclei. The experimental values of the first 1^+ for $^{170-176}$Yb isotopes are (1.634, 2.009 and 1.819) MeV respectively somewhat higher than the values in the best fitting (1.143,1.082 and 1.132) MeV while no experimental value for ^{178}Yb and the best fitting was 1.279 MeV. The results of the reduced electrical transitions probability $B(E2)$ that obtained from the IBM-1 & IBM-2 program package have been compared with the experimental values and the results are satisfactory. The reduced magnetic transitions probability ($M1$) and the $\delta(E2/M1)$ ratio have been calculated using the second program and have been compared with the few available experimental values they are considered to be compatibility acceptable. All results have been shown that $^{170\text{-}178}$Yb nuclei as deformation nuclei they obey rotational limit perfectly.

References

[1] Barfield A Wood J and Barrett B 1986 *Physical Review C* **34** 5
[2] Minkov N Drenska S Raychev P Roussev R and Bonatsosy D 1997 *Physical Review C* **55** 5
[3] Sharrad F Abdullah H AL-Dahan N Mohammed-Ali A Okhunov A Abu Kassim H 2012 *Romanian Journal of Physics* **57** 9
[4] Okhunov A Al-Sammarrae A and Turaeva G 2014 *Conference Series* **553** 012011
[5] Abed Al-Jubbori M 2017 *Ukr. J. Phys* **62** 11
[6] Arima A and Iachello F 1975 *Review Letters* **35** 16
[7] Arima A and Iachello F 1976 *Ann. Phys. NY* **99** 253

[8] Arima A and Iachello F 1978 *Ann. Phys* **111** 201
[9] Arima A and Iachello F 1979 *Ann.Phys* **123** 468
[10] Arima A Otsuka T Iachello F and Talmi I 1977 *Physics Letters* **B 66** 205
[11] Iachello F 1979 *Interacting Boson in Nuclear Physics* (New York :Plenum)
[12] Iachello F and Arima A 1987 *The Interacting Boson Model* (England:The Syndicate Press of the University of Cambridge)
[13] Casten R and Warner D 1988 *Rev. Mod. Phys.* **60** 389
[14] Caprio M 2003 *Structure of collective modes in transitional and deformed nuclei* (Yale University: PhD)
[15] Bohr A and Mottelson B 1977 *Nuclear Structure* **2** 59
[16] Deshalit A and Feshbach H 1974 *Theortical Nuclear Physics I* (New York: John Wiley and Sons)
[17] Eisenberg J and Greiner W 1970 *Nuclear Model I* (North-Holland)
[18] Ameer A 1991 *Investigations of Nuclear Energy Levels in ^{82}Kr, ^{76}Se and ^{194}Pt* (London University Ph. D Thesis)
[19] Scholten O Heyde K Van Isacker P Jolie J Moreau J Waroquier M and Sau J 1985 *Nuclear PhysicsA* **438** 41
[20] Hamilton W 1990 *J. Phys. G: Nucl. Part. Phys.* **16** 745
[21] Wolf A Casten R and Warner D *Physics Letters B* **190** 19
[22] Bijker R Dieperink A and Scholten O *J. Nuclear. Phys.* **334** 207
[23] Al-Khudair F and Gui-Lu L 2002 *Theor. Phys. Beijing,China* **37** 699
[24] Otsuka T. 1993 Algebraic Approaches to Nuclear Structure (NewYork Brookhaven National Laboratory)
[25] Baglin C 2002 *NDS* **96** 611
[26] Singh B 1995 *NDS* **75** 199
[27] Basunia M 2006 *NDS* **107** 791
[28] Achterberg E Capurro O and Mrti G 2009 *NDS* **110** 1473
[29] Subbert A Hamilton W Van Isacker P Schreckenbach K and Colvint G 1988 *J. Phys.G:Nucl. Phys.* **14** 87
[30] Raman S Nestor C JR and Tikkanen P 2001 *At. Data Nucl. Data Tables* **78** 1
[31] Stone N 2005 *At. Data Nucl. Data Tables* **90** 75

Preparation and characterization of hydroxyapatite powder and study of hydroxyapatite - alumina Composite

Ghazi K. Saeed1 , Abbas F. Essa2 and Saja Abdul-Ammer Said2

1 Science Department – College of Basic Education /University of Waist
2 Physics Department – College of Science/ University of Waist
Email: phyghazi@ymail.com

Abstract. Hydroxyapatite powder $Ca_{10}(PO_4)_6(OH)_2$ was prepared locally from Iraqi beef bones, and characterization the powder as well as studied purity. A composite of hydroxyapatite-alumina was also prepared with a ratio of alumina 0,5,10,15,20,25% wt .Use polyethylene glycol as a binder with 1% wt by dissolving polyethylene glycol with ethanol (1g: 100ml) at 40 °C and using a magnetic stirrer to obtain a homogeneous solution for the material. Then drying the powder and pressing to prepare compound samples, after that heat treatment at 1350°C for three hours. The physical and mechanical properties studied such as density, porosity, water absorption ratio, hardness and compression resistance, as well as X-ray diffraction and X-ray florescence. X-ray diffraction analysis showed that the hydroxyapatite phase was stabilized for all prepared samples before and after heat treatment with chemical form $Ca_{10}(PO_4)_6(OH)_2$, the hydroxyapatite showed a stabilization in phase before and after heat treatment without decomposition into different components.

Keywords: Hydroxyapatite, Alumina, Composite and Medical applications

1. Introduction

The importance of hydroxyapatite (HA) used in the many applications, especially in medical applications. Hydroxyapatite is a natural mineral form of calcium apatite, the chemical formula $Ca_5 (PO_4)_3 (OH)$, but it is usually written $Ca_{10} (PO_4)_6 (OH)_2$ to indicate that the crystal unit cell of two entities. Molecular weight has 502.31g/mol and hexagonal crystalline structure with dimensions a = 9.41 Å, c = 6.88 Å as shown in Figure (1). It can take several colors including white, milky, colorless, gray, yellow and yellowish green. The main components of human bones are organics, mostly collagen fibers and inorganic materials known as hydroxyapatite, which accounts for 65-70% by weight of natural bone as shown in Figure (2). Collagen fibers are responsible for bone flexibility, while the metal component (hydroxyapatite) is responsible for bone stiffness, and the molecular ratio of calcium to phosphorus ratio (Ca/P) within hydroxyapatite in bone tissue is around 1.67 [1-3].

Calcium Phosphate (CaP) is widely used directly in solid tissues (eg bone) and in various medical applications, which can be used as compensation for solid tissues. There are many types of calcium phosphate such as hydroxyapatite (HA), tetra- calcium phosphate (TTCP), tri-calcium phosphate (TCP), anhydrous dia-calcium phosphate (DCP), amorphous- calcium phosphate (ACP), binary-calcium phosphate (BCP). Hydroxyapatite (HA) is the most promising and good material for bone replacement for its consistency and biocompatibility [4]. Several methods were used to prepare hydroxyapatite, including precipitation, sol-gel, hydrothermal technique, biomimetic deposition, electro deposition, Animal bones directly, and other methods [5]. When the samples are formed in any way and the thermal treatment is performed, and after the temperature exceeds 1100°C, hydroxyapatite breaks up into several compounds such as β-$Ca_3 (PO_4)_2$, called β-TCP [6-9]. It can dissolve according to the following reactions [10, 11].

$$Ca_{10}(PO_4)_6(OH)_2 \rightarrow Ca_4P_2O_9 + 2Ca_3(PO_4)_2 + H_2O \quad \ldots\ldots (1)$$

$$Ca_{10}(PO_4)_6(OH)_2 \leftrightarrow 3Ca_3(PO_4)_2 + CaO + H_2O \quad \ldots\ldots\ldots (2)$$

Hydroxyapatite can be used as a coating for all parts of the human body. Complete parts of the human body can also be prepared as parts of the bone, teeth, face, jaws and skull. It also enters the cosmetic processes of many parts of the body. In addition can enter a large proportion in the preparation of animal feed [12].

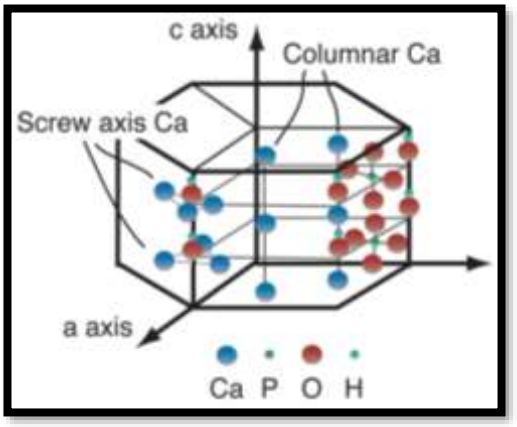

Figure (1) crystalline structure of hydroxyapatite [2]

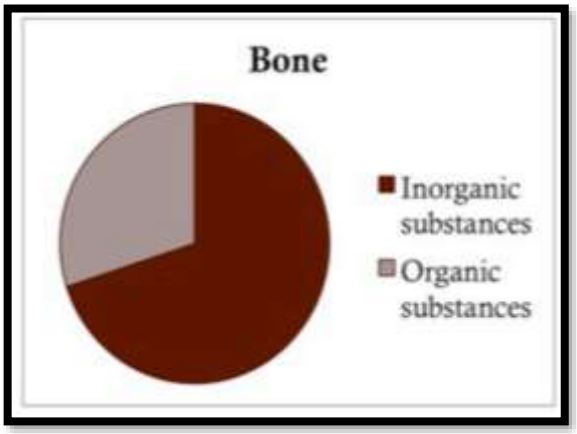

Figure (2) The proportions of organic and inorganic substances [3]

2. Experimental Work

2.1. For the purpose of preparing the hydroxyapatite powder locally, follow the following steps:

Iraqi beef bones were prepared from local markets and first cleaned from the meat and fat residues, boiling the bones with water for five hours and more than once to remove the fat, drying the bones with the electric dryer at 75 ° C for 24 hours, cracking bones into small pieces using an iron hammer , putting the broken bones in a ceramic package and conduct the process of heat treatment through calcinations at 750°C for four hours, and make sure that all broken bones lost organic materials and became a pure white milky black color, after thermal treatment, the bone was milled using a rotary mill with iron blades, sifting the powder with a particle size of less than 150μm using sieves. Conducting analysis for the diagnosis of the substance and phase using the XRD diffraction system. Materials and impurities introduced in the structure of hydroxyapatite verified through the XRD for American hydroxyapatite powder was used for comparison purposes, in addition to the standard spectra, which is included with the system within the x-ray diffraction library.

2.2. Preparation of samples:

To Preparation of a composite of hydroxyapatite-alumina with alumina ratios 0,5,10,15,20,25% wt, the alumina used from ALM-41-SUMITO-CHEMICAL-COMPANY-UK, which screening the powder with a particle size of less than 150μm using sieves , using following steps.

Polyethelenglycol (SIGMA-ALDRICH-WG) with a molecular weight of 6000 was used as a bond material by dissolving polyethelenglycol with alcohol ethanol (1g: 100ml) and at 40°C. Using a magnetic stirrer, the magnet movement moves the solution continuous to obtain a homogeneous solution. The ratio of the polyethylene solution was used for the preparation of mixtures of hydroxyapatite - 99% wt against the bonding material by 1% wt and by using the magnetic mixer for the purpose of obtaining a homogeneous solution. Drying the solution containing the materials using a dryer at 75°C heat for 24 hours. Compressing the samples using a 9mm metal mold and a pressure of 2.75Ton to compress the samples in a semi-dry form. Special program for thermal treatment to samples as shown in Figure (3).

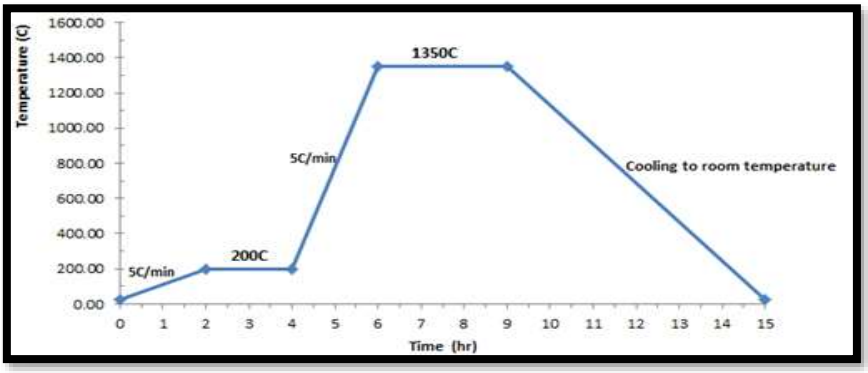

Figure (3) Thermal treatment program

2.3. Analysis:

X-ray diffraction tests for the purpose of determining the type and phase of the material. Figure (4) shows that the material is hydroxyapatite with phase is hexagonal by comparing to the USA-spectra and the standard spectra with the card number (34-0010). There is almost perfect match between the three spectra. In addition, X-ray diffraction tests were conducted for one of the samples prepared at the thermal treatment at 1350°C for three hours. The tests showed that the material is hydroxyapatite without any disintegration into other components as shown in Figure (5). XRF tests show that the main materials in the analysis are phosphorus oxides (P_2O_5) and calcium oxides (CaO). This confirms that the predominant material is hydroxyapatite and other substances with low ratios, and this is expected in bone components as in Table (1). The molecular ratio of calcium to phosphorus ratio (Ca/P) was found 1.71 which approximately compatible to references [1-3]. Green density measured with pressure to choose the best pressure for forming the samples as shown in Figure (6). Density tests with the temperature of the different thermal treatment at a time of three hours as in Figure (7). The following tests were performed: radial shrinkage (diameter contraction), hardness of Vickers, compressive strength, apparent density, porosity and water absorption ratio as shown in Figures (8-13).

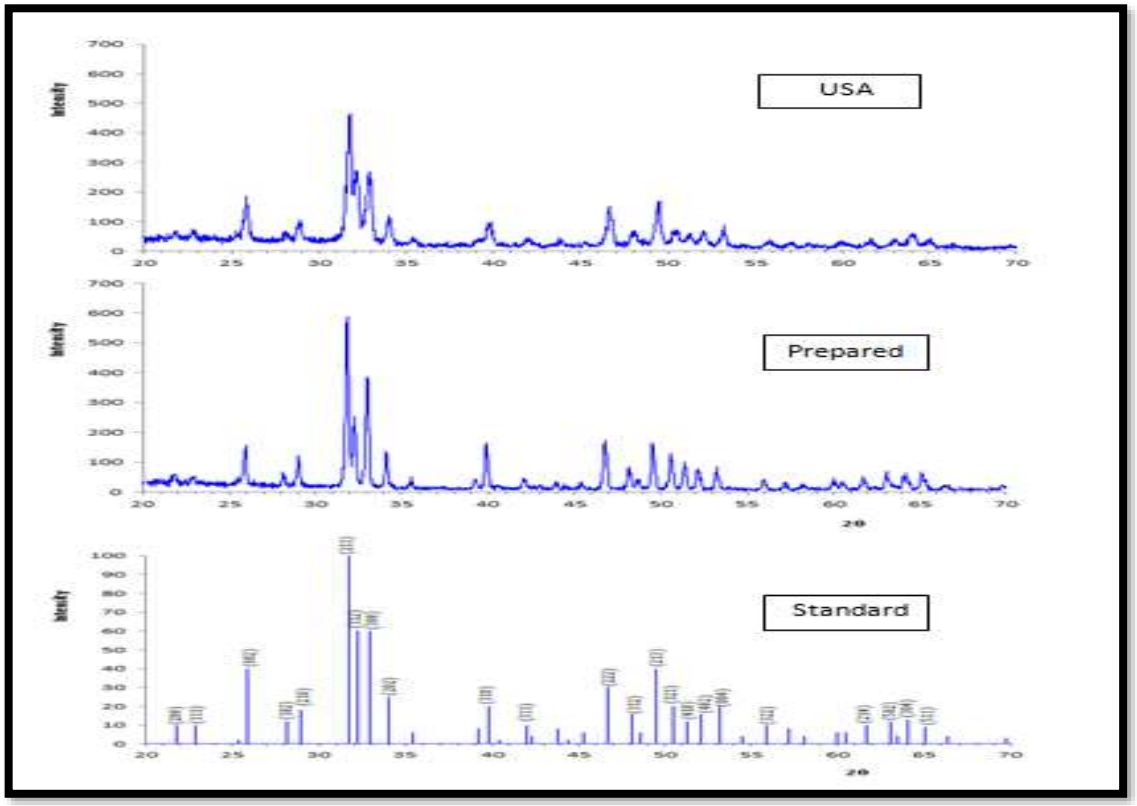

Figure (4) X-ray diffraction spectra of HA-powder USA- powder, prepared and standard

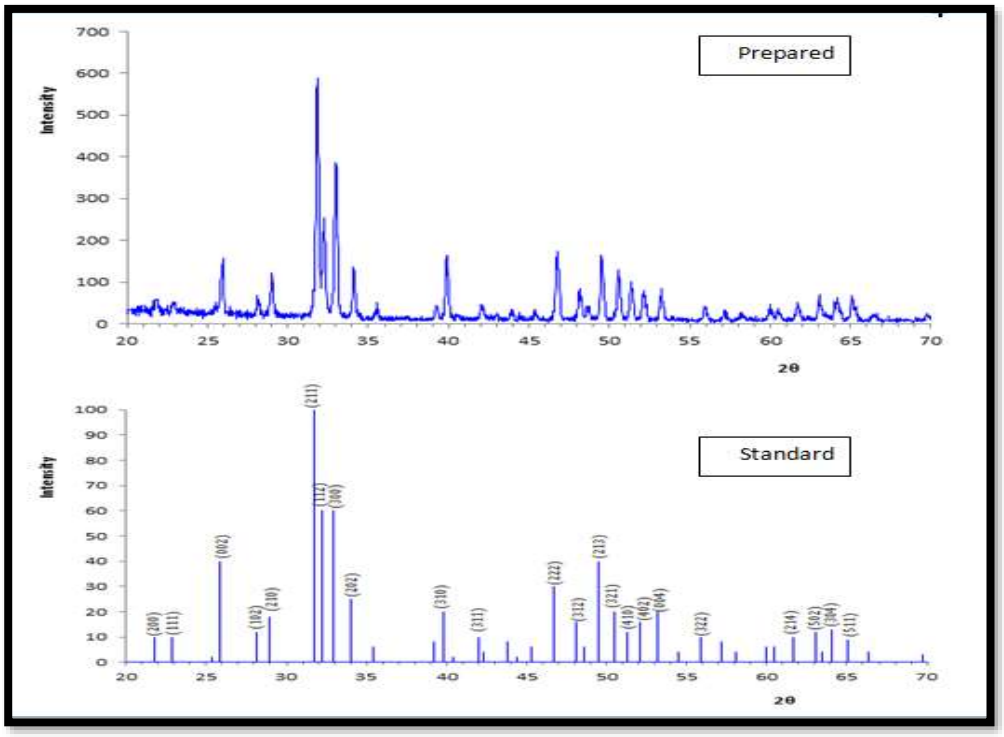

Figure (5) Represent the X-ray diffraction spectra of the hydroxyapatite sample alone at heat treatment 1350^{o}C for three hours

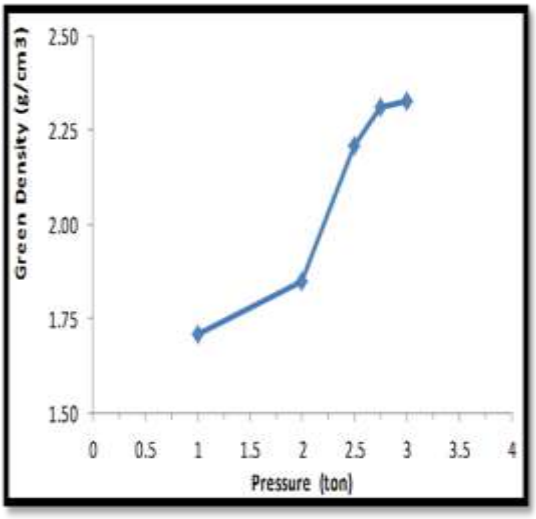

Figure (6) Change green density with pressure

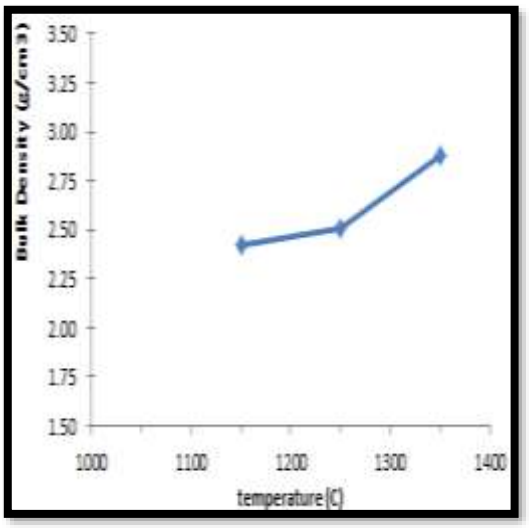

Figure (7) bulk density with the temperature

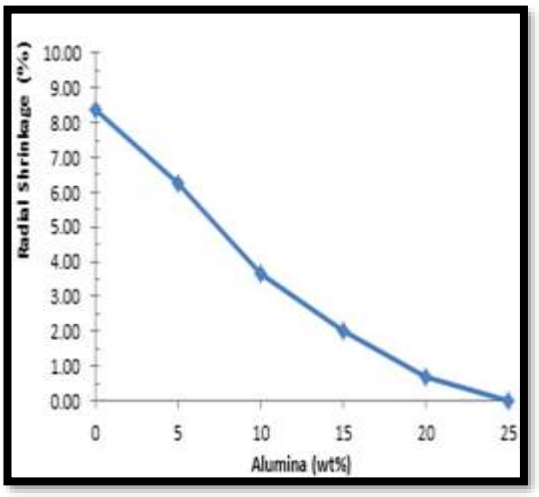

Figure (8) Change radial shrinkage with alumina

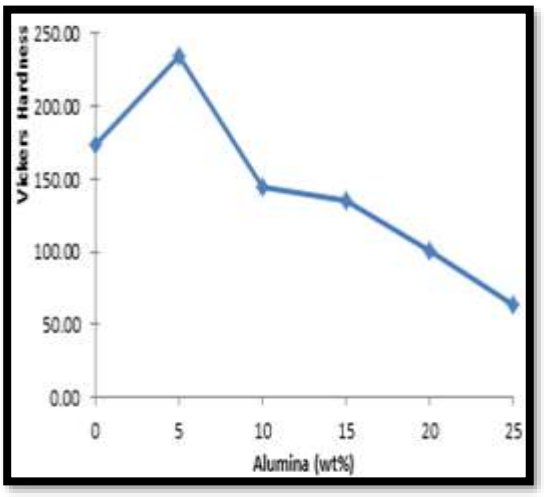

Figure (9) Vickers hardness with alumina

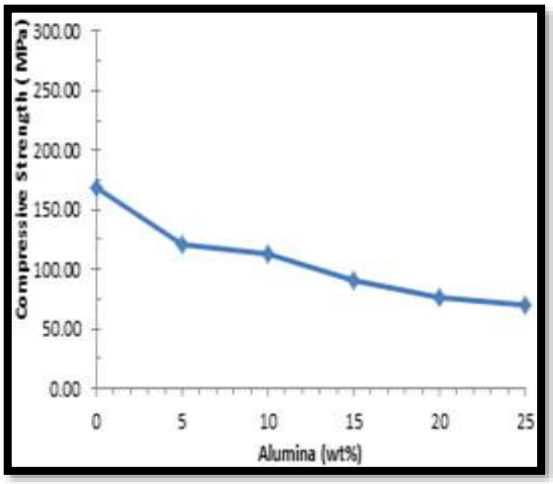

Figure (10) Change compressive strength with alumina

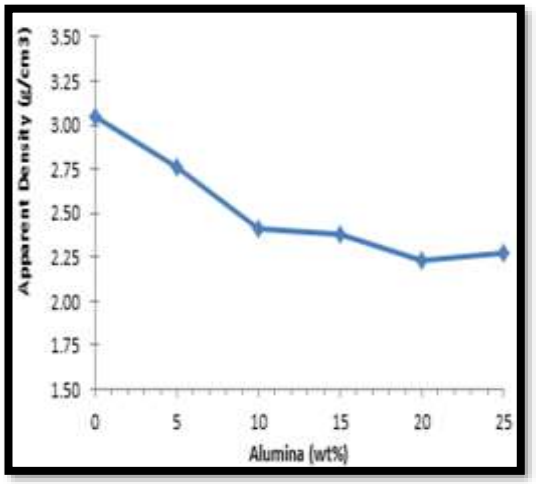

Figure (11) apparent density with alumina

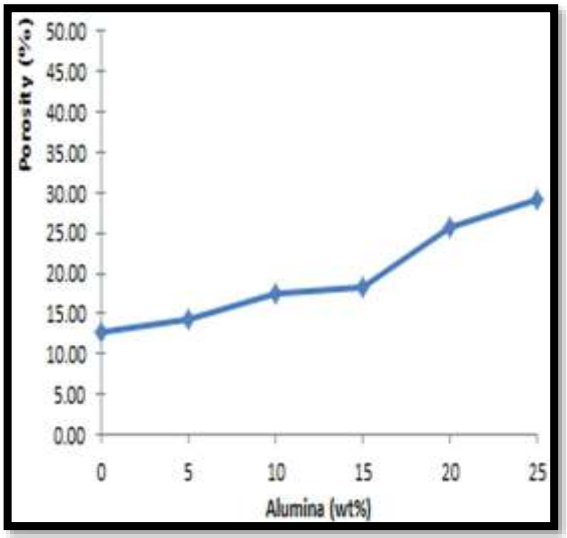

Figure (12) Change porosity with alumina

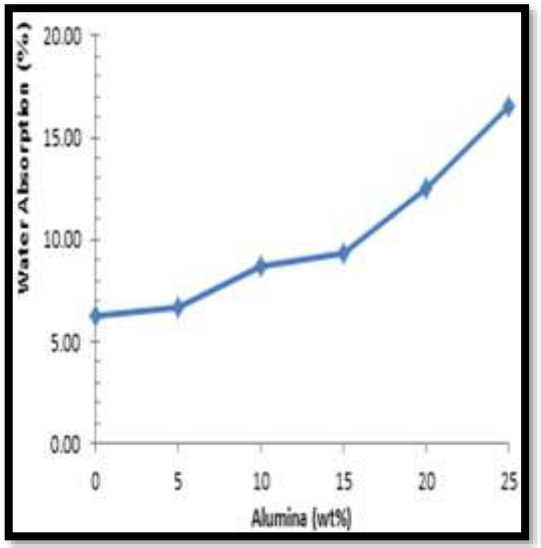

Figure (13) Change water absorption with alumina

Table (1) shows the results of the x-ray fluorescence of the hydroxyapatite

Sample Name	Saja		Date of Receipt	11/13/2017 14:40:56
Description			Method	TurboQuant-Powders

Z	Symbol	Element	Norm. Int.	Concentration	Abs. Error
12	MgO	Magnesium	113.8379	3.131 %	0.046 %
13	Al2O3	Aluminum	0.0000	< 0.0038 %	(0.0) %
14	SiO2	Silicon	0.0000	< 0.0011 %	(0.0) %
15	P2O5	Phosphorus	31550.8606	31.37 %	0.02 %
16	SO3	Sulfur	624.2428	0.3879 %	0.0013 %
17	Cl	Chlorine	708.2183	0.07756 %	0.00023 %
19	K2O	Potassium	0.0000	< 0.0012 %	(0.0) %
20	CaO	Calcium	12892.4394	53.90 %	0.04 %
22	TiO2	Titanium	1.4561	0.0085 %	0.0021 %
23	V2O5	Vanadium	0.4519	< 0.0061 %	(0.0060) %
24	Cr2O3	Chromium	4.1424	< 0.00015 %	(0.0) %
25	MnO	Manganese	0.6879	0.00068 %	0.00030 %
26	Fe2O3	Iron	97.8309	0.03731 %	0.00032 %
27	CoO	Cobalt	0.0803	< 0.00039 %	(0.0) %
28	NiO	Nickel	13.9385	0.00331 %	0.00012 %
29	CuO	Copper	21.9924	0.00441 %	0.00013 %
30	ZnO	Zinc	181.5375	0.02709 %	0.00016 %
31	Ga	Gallium	5.5232	0.00052 %	0.00006 %
32	Ge	Germanium	0.0000	< 0.00005 %	(0.0) %
33	As2O3	Arsenic	0.0000	< 0.00007 %	(0.0) %
34	Se	Selenium	0.0000	< 0.00005 %	(0.0) %
35	Br	Bromine	9.5250	0.00043 %	0.00002 %
37	Rb2O	Rubidium	4.0470	0.00012 %	0.00002 %
38	SrO	Strontium	2621.3861	0.07414 %	0.00012 %
39	Y	Yttrium	916.2336	0.02117 %	0.00006 %
40	ZrO2	Zirconium	908.6147	0.4376 %	0.0011 %
41	Nb2O5	Niobium	0.0000	< 0.00014 %	(0.0) %
42	Mo	Molybdenum	0.0000	< 0.00010 %	(0.0) %
47	Ag	Silver	0.0000	< 0.00020 %	(0.0) %
48	Cd	Cadmium	0.7717	< 0.00020 %	(0.0) %
50	SnO2	Tin	9.7564	0.00274 %	0.00014 %
51	Sb2O5	Antimony	8.8373	0.00329 %	0.00018 %
52	Te	Tellurium	10.6952	0.00229 %	0.00012 %
53	I	Iodine	0.0000	< 0.00030 %	(0.0) %
55	Cs	Cesium	0.0000	< 0.00040 %	(0.0) %
56	Ba	Barium	12.1451	0.00942 %	0.00076 %
57	La	Lanthanum	0.0000	< 0.00020 %	(0.0) %
58	Ce	Cerium	0.0000	< 0.00020 %	(0.0) %
68	Er	Erbium	0.0000	< 0.00051 %	(0.0) %
70	Yb	Ytterbium	0.0552	< 0.00020 %	(0.0) %
72	Hf	Hafnium	19.4467	0.00649 %	0.00018 %
73	Ta2O5	Tantalum	22.0777	0.00898 %	0.00026 %
74	WO3	Tungsten	1.4712	< 0.00018 %	(0.0) %
80	Hg	Mercury	0.4720	< 0.00010 %	(0.0) %
81	Tl	Thallium	2.0335	0.00014 %	0.00003 %
82	PbO	Lead	7.0797	0.00075 %	0.00005 %
83	Bi	Bismuth	0.0000	< 0.00010 %	(0.0) %
90	Th	Thorium	5.7943	0.00041 %	0.00004 %
92	U	Uranium	4.9709	< 0.00010 %	(0.0) %
		Sum of concentration		89.52 %	

3. Discussion

The X-ray diffraction in Figure (4) shows that the prepared samples is hydroxyapatite and the phase is hexagonal phase by comparing with USA spectrum and the standard spectra of card number (34-0010). And its color is milky white and its purity is high through the results of the XRF tests shown in Table (1). When the percentage of loss (loi) of 10.48%wt was left, the ratio of calcium oxide was 59.92%wt and the ratio of phosphorus oxide was 35.04% wt and the total ratio became 94.96% wt. The remaining percentage is for other substances. These results indicate that the main components of hydroxyapatite are calcium

oxide and phosphorus oxide and this is consistent with the hydroxyapatite compound $Ca_{10}(PO_4)_6(OH)_2$. Figure 5 shows that the X-ray diffraction spectra of the sample prepared at 1350 °C for three hours preserves the hydroxyapatite phase by comparing with the standard spectra, this is due to the thermal treatment program chosen, and this is very useful in the various applications of hydroxyapatite. Most of the literature refers to the breakdown of hydroxyapatite when conducting heat transactions that exceed 1100ºC [6-8]. Figure (6) represents the change of green density with the different values of pressing; the pressure of 2.75ton was selected for preparing the samples. Figure (7) represents the change in density with temperature; the results showed that the best temperature was 1350°C for three hours. Figure (8) represents the change in the radial shrinking with the alumina ratios and shows a linear decrease with the ratios due to the fact that by increasing the alumina ratio, we need a temperature higher than 1350°C for which the material granules are combined to complete the sintering process. Figure (9) represents the change in Vickers hardness with alumina ratios, the highest hardness value is shown in 5%wt of alumina ratio, there was a decrease in the hardness values for the same reason, which is not enough for the sintering temperature, and the hardness values are consistent with reference values [8]. Figure (10) represents the compression strength with alumina ratios and through the form shows a decrease in values with increased alumina ratios due to low temperature of sintering and results consistent with reference values [6]. Figure (11) represents the change in the apparent density with the alumina ratios; the results show a decrease in the density ratios as the other properties, the reason is the same as mentioned above despite the increase in the alumina ratios, whose theoretical density of alumina is higher than the density of hydroxyapatite. The Figures (12) and (13) represent the change in porosity and water absorption rate and their behavior as expected to reverse the behavior of the apparent density. The shapes show that the less porosity and absorption of water is at the hydroxyapatite alone to achieve the appropriate degree of sintering.

4. Conclusion

The powder is characterized as hexagonal hydroxyapatite, milky white, high purity, can be easily grinded and sieving (screened) to obtain the desired particle size, stable with time and weather conditions. The best properties were pure hydroxyapatite, except for the Vickers hardness, which had the highest value at 5% wt of alumina. Also, phase-hydroxyapatite was preserved before and after thermal treatment by selecting the heat treatment program.

5. References

[1] Sobczak-Kupiec A , Malina D, Kijkowska R and Wzorek Z. 2012 Comparative Study of Hydroxyapatite Prepared by the Authors With Selected Commercially Available Ceramics, *Digest Journal of Nanomaterials and Biostructures, Vol. 7, No* **1**, *January - March,* pp. 385 – 391.

[2] Uddin M H , Matsumoto T, Okazaki M , Nakahira A and Sohmura T 2010 Biomimetic fabrication of apatite related biomaterials, *book edited by Amitava Mukhergee, ISBN 978-953-307-025-4, Published: under CC BY-NC-SA-3.0 license.*

[3] Azmat O and Nagtode P P 2015 Hydroxyapatite Crystal Deposition Disease-An Indepth Analysis to Improve Understanding and Facilitate Symptomatic Relief, *DOI: 10.1594/essr2015/P-0106.*

[4] Pal S, Roy S and Bag S 2005 Hydroxyapatite Coating over Alumina -Ultra High Molecular Weight Polyethylene Composite Biomaterials, *Trends Biomater. Artif. Organs, Vol* **18** *(2), January,* pp. 106-109.

[5] Nayak A K 2010 Hydroxyapatite Synthesis Methodologies: An Overview . *International Journal of ChemTech Research, Vol.2, No.***2**, *April-June, pp 903-907.*

[6] Hannora A E 2014 Preparation and Characterization of Hydroxyapatite/ Alumina anocomposites by High-Energy Vibratory Ball Milling. *J. Ceram. Sci. Tech.*, 05 [**04**], pp 293-298.

[7] Shekhar N, Krishanu B, Kaishi W, Rajendra K B and Bikramjit B 2010 Sintering, Phase Stability, and Properties of Calcium Phosphate-Mullite Composites, *J. Am. Ceram. Soc., 93* [**6**], pp1639–1649.

[8] Bulut B , Demirkol N, Erkmen Z E and Kayali E S 2015 Comparison of Microstructural and Mechanical Properties of Hydroxyapatite-Al_2O_3 Composites with Commercial Inert Glass (CIG) Addition, *ACTA PHYSICA POLONICA A Vol. 127, No.* **4**, pp1094-1096.

[9] Pujiyanto E , Tontowi1 A E , Wildan M W and Siswomihardjo W 2012 Porous Hydroxyapatite–Zirconia Composites Prepared by Powder Deposition and Pressureless Sintering, *Advanced Materials Research Vol. 445* pp 463-468.

[10] Aminzare M, Eskandarib A, Baroonian M H, Berenov A, RazaviHesabi Z, Taheria M and Sadrnezhaad S K 2013 Review paper: Hydroxyapatite nanocomposites: Synthesis, sintering and mechanical properties, *Ceramics International 39* pp 2197–2206.

[11] Mohsen E , Touradj E and Esmail S 2012 Effect of Sintering Atmosphere on Phase Evolution of Hydroxyapatite Nanocomposite Powders, *PROCEEDINGS OF THE INTERNATIONAL CONFERENCE NANOMATERIALS: APPLICATIONS AND PROPERTIES,* Vol. 1 No **2**, 02NNBM05(3pp).

[12] Mohamaddoost F, Yusoff H M, Matori K A, Ostovan F and Vahedi G R 2014 Bio Ceramic Zirconia/Hydroxyapatite Nano Composite Extracted from Bovine Bone, *Australian Journal of Basic and Applied Sciences, 8(***15***) Special,* pp 302-306.

[13] Pertti A 1996 Mechanical and Physical Properties of Engineering Alumina Ceramic, *VTT TIEDOTTEITA – MEDDELANDEN – RESEARCH NOTES 1792 , ,TECHNICAL RESEARCH CENTER OF FINLAND ESPOO,* PP 1-26.

Study the kinetic of Acridin orange dye adsorption by ZnO/GO nanocomposite

Baydaa A. Kadhim[1] ,Asmhan A. Muhmood[2], Liwaa H. Mahdi[3]

1 University of Alkafeel/Iraq /Najaf
2 Physics Department / Faculty of Science /Kufa university / Iraq
3 Pathology Department / Faculty of medicine / Kufa University / Iraq
*Corresponding Author Email: Baydaa.Awad @alkafeel.edu.iq

Abstract: Found of dyes in water bodies because of industrialization has prompted genuine medical problems. In the present investigation, an adsorbent ZnO/GO nanopartical was utilized for the removal of Acridine orange dye from watery that containing dyes. The adequacy of this adsorbent was read in group reads for different size portions of adsorbent at various pH, convergence of dye, measure of adsorbent, contact time and temperature. The seudo-first-request, pseudo-second-request and Elovich models were applied to test the motor test information. Pseudo first request model best fitted the adsorption of dye, The maximum adsorption rate was found to be 47% by 0.2 g of ZnO/GO nanocomposite in wastewater at a temperature of 25 °C dyes.

Introduction

Pollution is any harmful or hostile change in the environment that results from the physical, chemical, or biological side-effects of human industrial or social activities[1]. Contamination can affect the atmosphere, streams, oceans, and the earth. Water contaminants include those that are *biodegradable*, such as manure sewage, which reason no lasting damage if sufficiently preserved and discrete, as well as those which are *non-biodegradable*,for e xample chlorinated hydrocarbon insecticides, convinced industrial colors, organic composites (such as phenol and phenol derivatives)[2] . When these collect in the environment they can become very focused in food chains. In the sea, oil spilling from transporters and the inadequate release of sewage effluent are the main problems. Pollution of water with toxic substances is of major concern for human health as well as for the environmental quality [3].

Dye is the first pollutant to be standard in water and has to be removed from wastewater before clearing it into water bodies. Remaining colors are the main suppliers to dye in wastewater produced from fabric, elastic, paper, flexible, makeups and dye industrial industries, etc[4]. Release of these colors in water river is appealingly unwanted and has severe environmental influence[5].

- Due to forceful colours, dyes obstruct light diffusion, delay photosynthetic activity, constrain the growth of biota and also has a tendency to chelate metal ions which result in micro-toxicity to creature. In adding, most of colours are mutagenic and oncogenic[6]. As most of colours are steady to photodegradation, bio-degradation and oxidizing agents, they cannot be simply removed by conventional wastewater treatment processes owin g to their complex construction and synthetic origins[7].

- **Graphene oxide**

In a past few years, more focus is given to graphene especially for its facile synthesis, novel hybrids materials and applications. Graphene oxide (GO) contains a grasp of reactive oxygen functional groups, which make it a strong nominee for use in lots of applications through chemical[8].

In addition, controlled oxidation provides tunability of the electronic and mechanical properties including the possibility of accessing zero-band gap graphene via complete removal of the C-O bonds[9]. Various functionalities on the surface of GO make it an ideal platform for chemical modification, which may generate materials with amazing properties[10].

Material and methods

Acridine dye [λ_{max} = 521 nm] were obtained from Al-Hilla¸ Textile Company (Babylon, Iraq). The chemical structures of Acridine orange are shown in Fig 1 . Concentrations of dyes were determined by finding out the absorbance at the characteristic wavelength using a double beam UV/Vis spectrophotometer (UV–Visible spectrophotometer, Shimadzu 1650) and Fig 2 is Lamda max to acridine orange dye

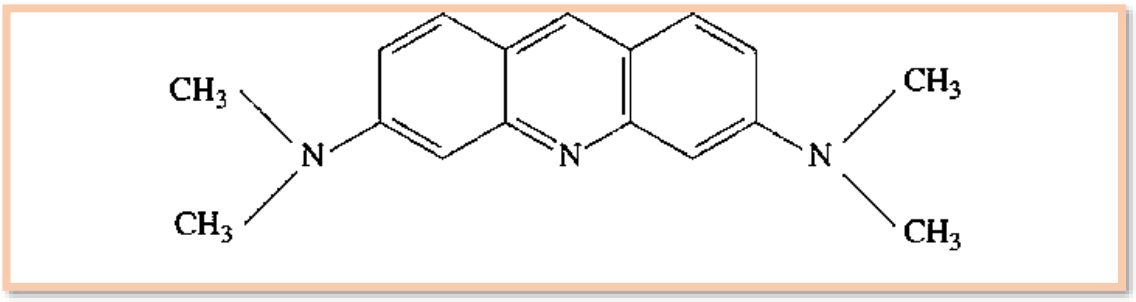

Figure (1): Structure of acridine orange dye

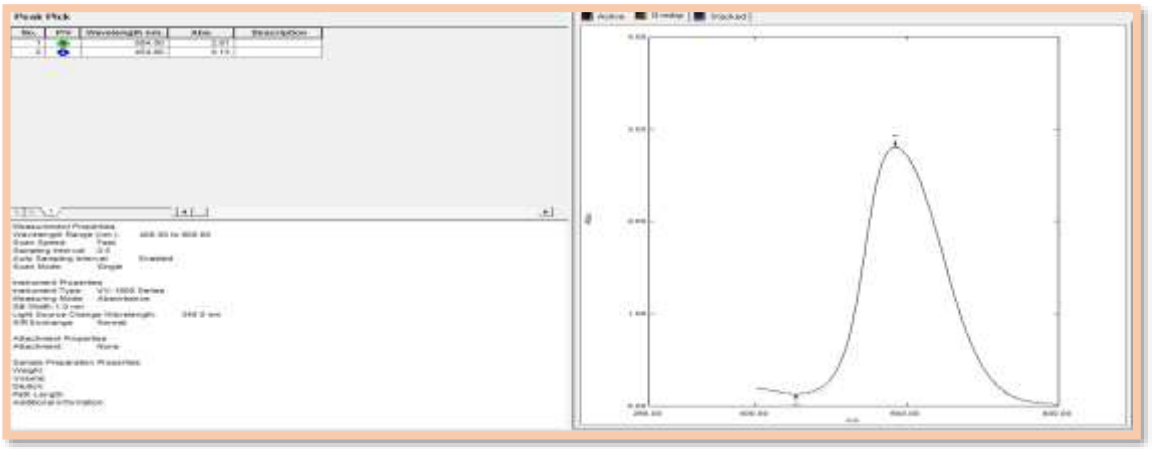

Figure (2):Lamda max to acridine orange dye

Stock Solution

Analytical mark acridine orange dye was used to prepare stock solution. Double distilled water was used to prepare stock solution. Lighter concentration solutions of essential concentrations were prepared using stock solution. 0.1 N HCl and 0.1N NaOH solutions were used to adjust the pH of the solutions. Industrial effluent (before treatment) from a local industry was collected, filtered using centrifuge and stored in air tight containers.

Batch Adsorption Studies

Batch adsorption studies were accompanied to determine the balance time requisite to reach saturation. Adsorption kinetics were carried out using acridine dye solutions of 10 to 40 ppm, pH in the range 2 to 12, 0.01 to 0.2g adsorbent , a contact time up to 60 min, constant agitation of 200 rpm and temperature of 25^{O}C. The parameters were diverse one at a time and samples composed at predetermined intervals, filtered, centrifuged and analyzed by UV. visible (Shimadzu). The amount of dye uptake by the bark was found. All experiments were carried out in duplicate and mean values are presented. The maximum deviation was 5.0 %. The percentage removal of dye from the solution was calculated using (1),

$$\%Removal = \frac{C_0 - C_i}{C_0} * 100 \quad \text{..... (1)}$$

Where C_0 is initial concentration of dye, C_i is final concentration of dye. The adsorption capacity q_e (mg/g) after reaching equilibrium was calculated using (2).[11]

$$q_e = (C_0 - C_e)\frac{V}{W} \quad \text{..... (2)}$$

Where V is the volume (L) of solution and W is the mass (g) of adsorbate used[11].

Adsorption kinetics of Acridine dye removal

In order to examine the order of adsorption process, several kinetic models were used to test the experimental data. In the present work following kinetics models were applied to check the applicability of the equations.

Pseudo-First Order Model

In 1898, Lagergren presented the first-order rate equation for the adsorption of solutes from a liquid solution on charcoal. Lagergren's equation was the first kinetic equation for the sorption of liquid/solid system based on solid capacity and was used extensively to describe the sorption kinetics [12].

This model assumes that the rate of change of solute uptake with time is directly proportional to difference in saturation concentration and the amount of solid uptake with time. In order to distinguish a kinetic equation based on the adsorption capacity of a solid from one based on the concentration of a solution, Lagergren's first-order rate equation has been also called pseudo-first order equation (3) [13].

$$\frac{dq_t}{dt} = K_1 (q_e - q_t) \quad (3)$$

Where: q_t and q_e are the amount adsorbed at time t and at equilibrium (mg.g^{-1}), respectively and $K_1$is the pseudo-first order rate constant for the adsorption process (min^{-1}) .

After integration and applying boundary conditions t = 0 to t = t and $q_t = 0$ to $q_t = q_t$ the integrated form of equation (3) becomes:

$$\ln(q_e - q_t) = \ln q_e - K_1 t \quad (4)$$

The plot of $\ln(q_e - q_t)$ versus t gives a straight line for first order kinetics, which allows computation of the adsorption rate constant, K_1.

Pseudo-Second Order Model

The sorption kinetics may be described by a pseudo-second order model. The differential equation is the following [14].

$$\frac{dq_t}{dt} = K_2(q_e - q_t)^2 \quad (5)$$

K_2 is the equilibrium rate constant of pseudo-second order sorption (g.mg^{-1}.min^{-1})

Integrating equation(1-15) for the boundary conditions t =0 to t = t and $q_t = 0$ to $q_t = q_t$ gives:

$$\frac{1}{q_e - q_t} = \frac{1}{q_e} + K_2 t \quad (6)$$

Equation(6) can be rearranged to obtain the following linear form:

$$\frac{t}{q_t} = \frac{1}{K_2 q^2{}_e} + \left[\frac{1}{q_e}\right] t \quad (7)$$

If the initial adsorption rate (h) is:

$$h = K_2 q^2{}_e \quad (8)$$

Then equation(8) becomes:

$$\frac{t}{q_t} = \frac{1}{h} + \left[\frac{1}{q_e}\right] t \quad (9)$$

The rate parametersK_2, h and $q_e$can be directly obtained from the intercept and slope of the plot of t/q_t versus t.

Results and Discussion

Parameters Removal of Acridin orange by batch experiments.

The experiments were accompanied in batches in 100 mL conical flask with stopper. The studies were passed out at ambient temperature of 25 ± 0.5 °C excepting the study accompanied to identify the influence of temperature. All the experiments were carried out at their natural pH and no adjustments were made excepting the study carried out to know the effect of pH.

Effect of contact time

The percentage of dye adsorbed at variable contact time keeping other parameters constant is presented in Fig 3. Removal of Acridin dyes be contingent on its contact time with the adsorbents. Adsorption of dye at different contact time was studied for initial dye concentration of 10 mg/L.Adsorption experiments were conducted with nanomaterial at ambient temperature (25 ± 0.5 °C) by varying the stirring time from 5 to 60 minutes (5, 10, 15, 20, ….. 60 min). It is apparent from the figure (3) to Acridin dye that almost 12.1% removal to ZnO/GO took place within first 5 minutes and equilibrium was established after 50 minutes.

Decrease in removal rate with time, may be due to the detail that initially all the active sites of nanoparticle contains Zn ion, which are exchanged by dye ion and initially the adsorbate concentration gradient was also high. Later, the dye approval rate by adsorbent was decreased knowingly, due to the decrease in amount of active sites as well as dye concentration[15].

Table (1) : Contact time versus percentage removal of Acridin dye by ZnO/GO nanocomposite.

Time(mint)	Concentration (Ce)	Removal (%)
5	0.334	12.10526
10	0.328	13.68421
15	0.318	16.31579
20	0.296	22.10526
25	0.283	25.52632
30	0.272	28.42105
35	0.263	30.78947
40	0.252	33.68421
45	0.242	36.31579
50	0.228	40
55	0.2	47.36842
60	0.2	47.36842

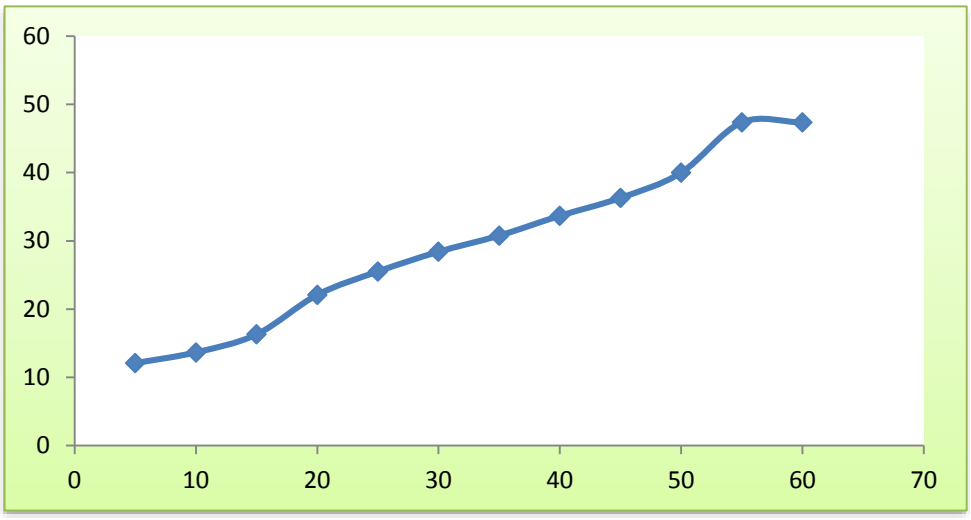

Figure (4): Contact time versus percentage removal of Acridin dye by ZnO/GO nanocomposite

Effect of adsorbent dosage on dye removal

The effect of variation of adsorbent dose on percentage removal of dye from aqueous solution with layered double hydroxide used in this study is graphically shown in fig 4**,** It is well evident that the removal of dye Acridine increased with increase in the adsorbent dosage, for ZnO/GO nanocomposite . It is evident that the removal of Acridin dye increased from **21.05% to 47.37** for 0.01 to 0.2 g in 100mL of reaction solution of initial dye concentration, 10 mg/L. There is increase in percentage removal with increase in adsorbent dose because for a fixed initial solute concentration, increase in total adsorbent doses provides a greater surface area or adsorption sites and increases the adsorption potential[16].

best percentage removal of dye by ZnO/GO was found to be **47.37% t0 0.2 g** for initial concentration of l0mg/L. The initial and final pH of the solution after adsorption were measured and it was observed that there was almost no change in the pH of the solution because the conversation of dye occurs by the anion present in the interlayer spaces.

Table (2) :Effect of adsorbent dosage on Acridine dye removal with initial concentration 10mg/L and temperature=25^{o}C.

Adsorbent dosage	**ZnO/GO**	
	C_e	Removal%
0.01	0.30	21.05
0.015	0.29	24.21
0.1	0.28	26.84
0.15	0.25	35.26
0.2	0.20	47.37

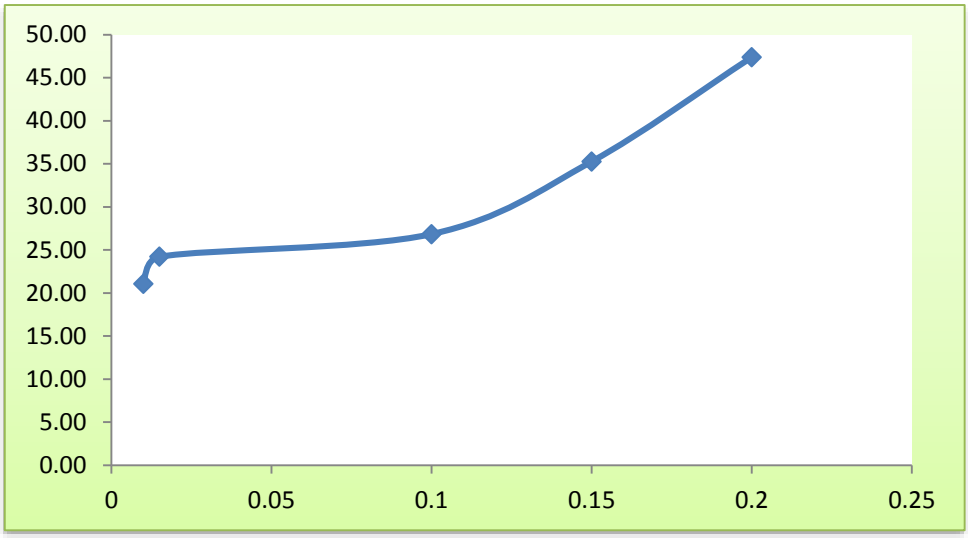

Figure (5): Adsorbent dose versus percentage removal of Acridin orange dye by ZnO/GO nanocomposite.

Effect of initial concentration

Adsorption of dye onto nanocomposite depends on initial adsorbate concentration. To investigate the effect of initial dye concentration on dye adsorption onto nanoparticle, batch type experiments were done at ambient temperature (25 ± 0.5 °C). The initial concentration of dye solution was varied from 10 mg/L to 40 mg/L with optimum adsorbent dose (0.2g).

The effects obtained is presented in graphical form as percentage removal versus initial dye concentration fig 6, which clearly show the effect of initial concentration of solution on with nanocomposite.

It is apparent from the graphs that the percentage removal of percentage removal of Acridin dye decreased from **47.36 to 25.94%** (initial dye concentration of 10mg/L to 40mg/L), the results show that there is a discount in dye adsorption, owing to the lack of available active sites required for the high initial concentration of dye[17].

The higher approval of dye at low concentration may be accredited to the obtainability of more active sites on the surface of the adsorbent for lesser number of adsorbate species. It is observed form the figures that there wasn't any appreciable decrease in the removal of dye with increase in initial dye concentration [18].

Table (3): Effect initial concentration to Acridin dye ZnO/GO and nanocomposite

C_o mg/L	ZnO/GO	
	C_e	Removal%
10	0.20	47.37
20	0.45	41.16
30	0.78	31.70
40	1.05	29.79

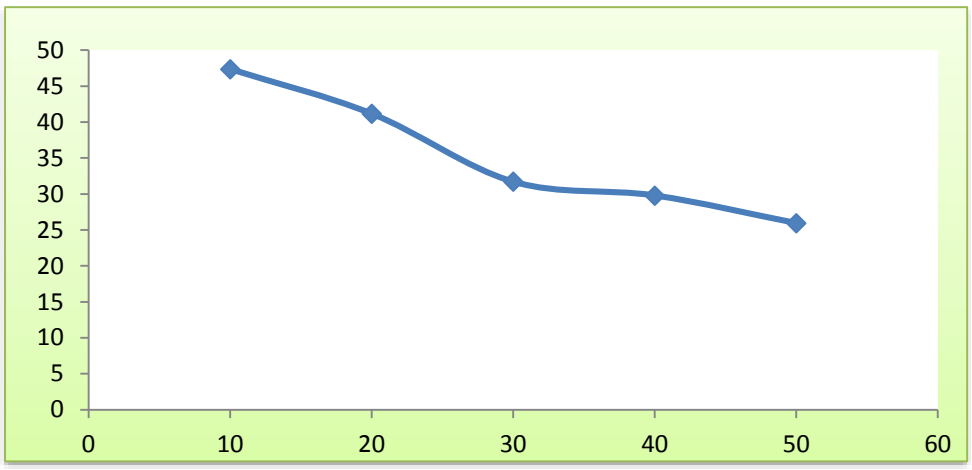

Figure (6):Percentage Removal versus initial Acridin dye concentration by ZnO/GO nanocoposite.

Effect of pH on dye removal

Generally, pH is an important mutable, which controls the adsorption at water- adsorbent interfaces. Therefore the adsorption of dye onto nanocomposite was examined at different pH values ranging from 2 to 12 and pertinent data are presented in fig 7. The percentage removal of dye by ZnO/GO decreased from 45.25407**% to** 12.55992**%** for increase in pH from 2 to 12, with 10 mg/L, It is obvious from figure that there was slight decrease (2% to 10%) in percentage removal with increase in pH of the solution. This may be due to the detail that with increase in pH, OH^- concentration in the solution increases which contests with dye ion. The data suggests in table 4 were that the optimum pH for removal of dye was 2.

Table(4): Effect of pH on Acridine dye removal of ZnO/GO .

pH	**ZnO/GO**	
	C_t	Removal%
2	0.571	45.25407
4	0.613	41.22723
8	0.7	32.88591
10	0.864	17.16203
12	0.912	12.55992

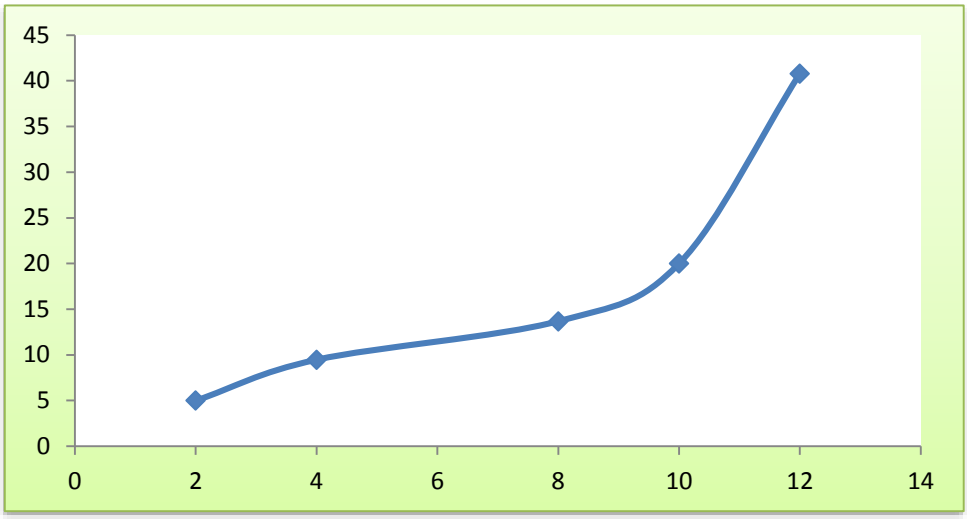

Figure(7):Percentage Removal versus pH on Acridine dye by ZnO/GO

Adsorption kinetics

Lagergren's rate equation (first order**)**

The rate constant of adsorption was determined from the following first-order rate expression known which has been described in introduction. Determination of efficiency of adsorption process requires an understanding of the time requirement of the concentration sharing of the solute in both solution and solid adsorbent or the kinetics of the process and documentation of the rate determining step.

Table(5): Rate constants and maximum adsorption capacity (q_o) obtained from the graph for ZnO/GO nanoparticle

Time	C_t	Q_e	q_t	q_e-q_t	lnq_e-q_t	t/q_t	K_1	First order (R^2)	Second order (R^2)
5	0.334	0.023	0.0046	0.0184	-3.9954	1086.957	4.0101	0.9583	0.8031
10	0.328	0.026	0.0052	0.0208	-3.8728	1923.077			
15	0.318	0.031	0.0062	0.0248	-3.69691	2419.355			
20	0.296	0.042	0.0084	0.0336	-3.39323	2380.952			
25	0.283	0.0485	0.0097	0.0388	-3.24934	2577.32			
30	0.272	0.054	0.0108	0.0432	-3.14191	2777.778			
35	0.263	0.0585	0.0117	0.0468	-3.06187	2991.453			
40	0.252	0.064	0.0128	0.0512	-2.97202	3125			

45	**0.242**	**0.069**	**0.0138**	**0.0552**	**-2.89679**	**3260.87**			
50	**0.228**	**0.076**	**0.0152**	**0.0608**	**-2.80017**	**3289.474**			
55	**0.2**	**0.09**	**0.018**	**0.072**	**-2.63109**	**3055.556**			
60	**0.2**	**0.09**	**0.018**	**0.072**	**-2.63109**	**3333.333**			

Acridin orange dye of Figure (8) are linear showing the validity of the equation and accordingly the first order nature of the adsorption from aqueous solution to ZnO/GO. The correlation coefficient (R^2) has value 0.93 for first order rate equation.

Second order rate equation

It is well apparent from above discussion that the adsorption process followed first order kinetics yet to test whether there was any possibility for the removal process to follow second order kinetics, the data were tested with second order rate equation. The second order rate equation is expressed in introduction [19].

The plots of *t/qt* versus *t* for dye sorption onto nanomaterials at ambient temperature (25 ± 0.5 °C) are presented in Fig.9. Values of k_2 and q_o were calculated from intercept and slope of the plot of t/qt against 't' respectively. The kinetic data for the adsorption of dye onto nanocomposite are summarized in **Tables of (6) .**

The correlation coefficient R^2 has value for second order rate equation was found to be **less** than that of Lagergren's rate equation, which indicates that, the data obtained from the study at different time interval fits the Lagergren's rate equation better that the second order rate equation. Comparing the correlation coefficient of Lagergren equation and second order rate equation, it is evident that the adsorption of dye onto nanomaterial ZnO/GO to Acridine dye follows first order kinetic.

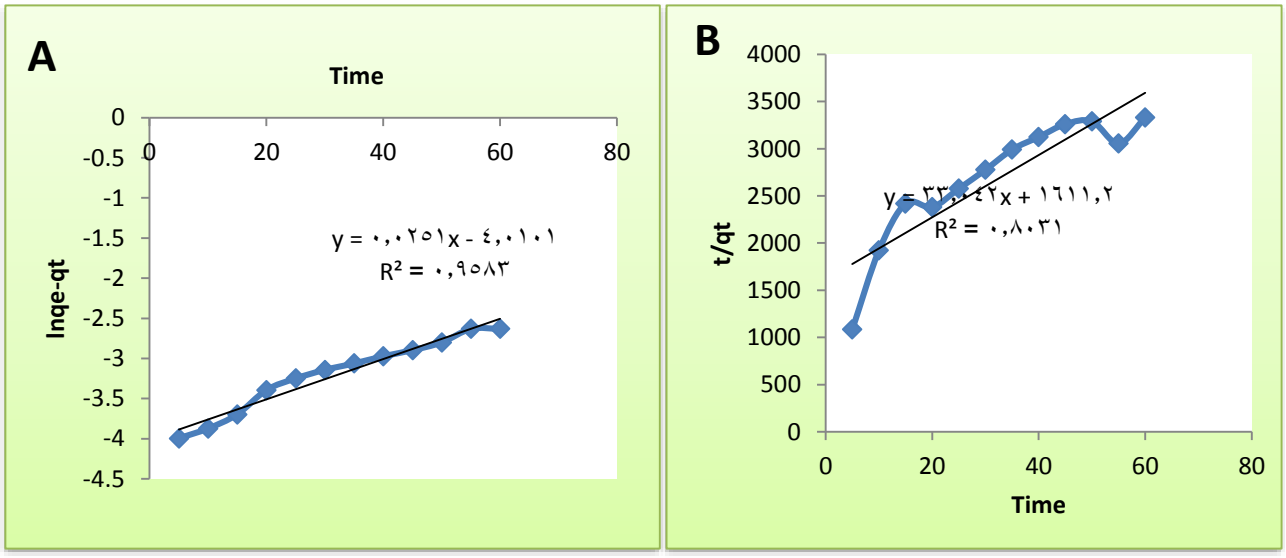

Figure(9):(A):first order equation [time versus ln (q_e - q_t)] and (B) second order equation [time versus t/qt] with initial concentration of 10 mg/L

Conclusions

ZnO/GO nanopartical are widely used for adsorption production, Also the adsorbent preparation does not involve the activation process of the mix hence the preparation is simple and economical. It was concluded from the present study that *ZnO/GO nanopartical* can be used effectively for the removal of dyes from aqueous and industrial effluents. The An optimum to pH 2, In this study the optimum results were obtained for parameters, the best pH is 2, dose is 0.2, the initial concentration is 10 ppm, contact time is 60 minutes and agitation 200rpm was chosen from the experiments conducted. Pseudo first order model best for second order rate equation because of correlation coefficient R^2 value is higher than correlation coefficient R^2 to second order rate equation. In this regard, *ZnO/GO* is a good nanocomposite can be effectively used as a viable and economic adsorbent for removal of Acridine orang dye and other dyes from aqueous and industrial effluents,where we concluded that ZnO / GO nanopartical was a great absorption catalyst

Reference

1. Francis, P., *Laudato si: On care for our common home*. 2015: Our Sunday Visitor.
2. Sankhla, M.S., et al., *Heavy metals contamination in water and their hazardous effect on human health-a review.* Int. J. Curr. Microbiol. App. Sci (2016), 2016. **5**(10): p. 759-766.
3. Hawkes, C., et al., *Smart food policies for obesity prevention.* The Lancet, 2015. **385**(9985): p. 2410-2421.
4. Yagub, M.T., et al., *Dye and its removal from aqueous solution by adsorption: a review.* Advances in colloid and interface science, 2014. **209**: p. 172-184.
5. Chequer, F.D., et al., *Textile dyes: dyeing process and environmental impact.* Eco-friendly textile dyeing and finishing, 2013. **6**: p. 151-176.
6. Pereira, L. and M. Alves, *Dyes—environmental impact and remediation*, in *Environmental protection strategies for sustainable development*. 2012, Springer. p. 111-162.
7. Neon, M.H.K., *Preparation, characterization and application of tio2 nano-composite for the treatment of textile wastewater under solar radiation.* 2017.
8. Halder, D., *Development of clay-Zno composite photocatalyst for effective photodegradation of eosin yellow dye from aqueous solution.* 2019.
9. Han, C., N. Zhang, and Y.-J. Xu, *Structural diversity of graphene materials and their multifarious roles in heterogeneous photocatalysis.* Nano Today, 2016. **11**(3): p. 351-372.
10. Figueiredo, P., et al., *Properties and chemical modifications of lignin: Towards lignin-based nanomaterials for biomedical applications.* Progress in Materials Science, 2018. **93**: p. 233-269.
11. Banerjee, S. and M. Chattopadhyaya, *Adsorption characteristics for the removal of a toxic dye, tartrazine from aqueous solutions by a low cost agricultural by-product.* Arabian Journal of Chemistry, 2017. **10**: p. S1629-S1638.
12. Yuh-Shan, H., *Citation review of Lagergren kinetic rate equation on adsorption reactions.* Scientometrics, 2004. **59**(1): p. 171-177.
13. Basu, S., G. Ghosh, and S. Saha, *Adsorption characteristics of phosphoric acid induced activation of bio-carbon: Equilibrium, kinetics, thermodynamics and batch adsorber design.* Process Safety and Environmental Protection, 2018. **117**: p. 125-142.
14. Rodrigues, A.E. and C.M. Silva, *What's wrong with Lagergreen pseudo first order model for adsorption kinetics?* Chemical Engineering Journal, 2016. **306**: p. 1138-1142.
15. Ghaedi, M., et al., *Removal of malachite green from aqueous solution by zinc oxide nanoparticle loaded on activated carbon: kinetics and isotherm study.* Journal of Industrial and Engineering Chemistry, 2014. **20**(1): p. 17-28.
16. Adeyemo, A.A., I.O. Adeoye, and O.S. Bello, *Adsorption of dyes using different types of clay: a review.* Applied Water Science, 2017. **7**(2): p. 543-568.

17.Tan, K.B., et al., *Adsorption of dyes by nanomaterials: recent developments and adsorption mechanisms.* Separation and Purification Technology, 2015. **150**: p. 229-242.
18.Kannan, N. and M.M. Sundaram, *Kinetics and mechanism of removal of methylene blue by adsorption on various carbons—a comparative study.* Dyes and pigments, 2001. **51**(1): p. 25-40.
19.Liu, Y. and L. Shen, *From Langmuir kinetics to first-and second-order rate equations for adsorption.* Langmuir, 2008. **24**(20): p. 11625-11630.

Estimated the concentration of 238U, 232Th and 40K in flour samples of Iraq markets

Shaymaa Awad Kadhim(1) , Shatha F.Alhous(2),Ahmed shaker Hussein (3),Hayder H. Hussein(4), Azhar S.Alaboodi(5)

[1,4,5]Department of Physics /Faculty of Science/ University of Kufa/Iraq
Department of Physics /Faculty of education for girls / University of Kufa/ Najaf/Iraq[2]
Department of basic science-college of dentistry-university of Babylon –Iraq[3]
*1Email: shaymaa.alshebly@uokufa.edu.iq *2Email: shathaf.alfatlawi@uokufa.edu.iq
*3Email:ahmed.aldulami67@gmail.com *4Email:hayder.alshibana@uokufa.edu.iq
*5Email:azhers.hamza@uokufa.edu.iq

Abstract . Flour is a nutritious type of food that is widely consumed by various age groups in Iraq. This study investigates the presence of long-lived gamma emitters in different type of flour in Iraqi market. Uranium (^{238}U), Thorium (^{232}Th) and Potassium (^{40}K) specific activity in (Bq.kg^{-1}) were estimated in (15) unique kinds of flours that are accessible in Iraqi markets. The gamma spectrometry method with a NaI(Tl) detector has been utilized for radiometric measurements. Likewise right now have determined the internal hazard index. It is found that the specific activity in Flour samples were varied from (13.73±1.89) Bq.kg^{-1} to (2.60±0.30) Bq.kg^{-1} with an average (8.75) Bq.kg^{-1} for ^{238}U, For ^{232}Th From (67.79±0.44) Bq.kg^{-1} to (9.96±0.14) Bq.kg^{-1} with an average (21.88) Bq.kg^{-1} and for ^{40}K from (2680.74 ± 23.60) Bq.kg^{-1} to (283.70±3.41) Bq.kg^{-1} with an average (133.09) Bq.kg^{-1}. Also, it is found that the Outdoor and indoor annual effective absorbed dose equivalent also (Hin) hazard indices was (0.302±0.014) and average annual committed effective dose(0.2205±0.030) mSv.y^{-1} in the flour samples . This study prove that the natural radioactivity and radiation danger records were low also estimated cancer risk has no significant health hazard in Iraqi Flour.

Keywords: Hazard indices, Gamma spectrometry, Flour, Iraq.

1.Introduction

Characteristic radioactivity is brought about by the nearness of Natural occurring radioactive matter (NORM) in the environment. Instances of normal radionuclides incorporate isotopes of Potassium (^{40}K), Uranium (^{238}U and its decay series), and Thorium (^{232}Th and its decay series). In Health Physics, radiation dosimetry is characterized as the estimation of radiation levels that sway on human health[1].The world population is subjected to different types of radiation sources including artificial radiation (15%)and natural radiation (85%) which contains food and drinks (11%). This may give a chance to the contamination of radioactive materials [2]. In fact, NORM can be moved from soil to plants. Thus, each sort of food may have some amount of radioactivity in it[3]. The world population is subjected to different types of radiation sources including artificial radiation, these radionuclides are commonly present in air, soil, and Flour in various sums and levels of movement [4]. Normal radionuclides are found in earthly and oceanic evolved ways of life, with consequent exchange to people through ingestion of nourishment. As such, worldwide endeavors were united cooperatively to apply sufficient strategies in researching radionuclides in food [5], and to set basic rules to secure against elevated levels of inner presentation that might be brought about by food consumption [6].

Since Flour is one of the essential food that is consumed in Iraqis daily lives, the longing to build up a national standard of radioactivity exposure from various kinds of Flour types that available in Iraq markets is very critical, Flour is a powder made from the grinding of wheat used for human consumption. Also, the "Staff of Life", has been an essential commodity to human existence through the centuries and is currently the most widely consumed staple food[7]. Moreover, numerous studied were conducted worldwide to research natural radionuclides in food consumed in various pieces of the world[8, 9]. Another study on vegetables .The annual effective dose due to intake of these radionuclides through

ingestion of vegetable samples was estimated to assess radiological risks, the average annual effective dose was found as 213.27 μ Sv y^{-1}[10] .Radioactivity measurements in staples are very important for checking radiation hazards on human health. where the another study in Iraq found the dose due to consumption of fish by the public has also been determined and it has been below the dose limit recommended by World Health Organization [11, 12]. This paper aims to create radiological baseline data of the hazard radiation in involved foodstuff (Flour samples in Najaf/Iraq). To achieve this aim, the radioactivity levels and radiation hazard indices of consumed Flour types in Najaf, Iraq are calculated and investigated. Since Flour is famous among all ages, the present study centers around limited the natural radioactive in this nourishment

2.Materials and Methods

collection and Preparation (15) samples of the most available kinds of Flour were gathered from the local markets in Iraq to measure natural activity. The types of samples are listed in Table (1) where was the Wight of each sample was 600gm. After collection, each Flour sample was kept in a plastic bag and marked by its name. After collection, these samples were packed in a 1 L polyethylene plastic container of constant volume to arrive at a geometric homogeneity around the Detector, then the respective net weights were measured and recorded with a high sensitive digital weighing balance with a percent of ±0.01%. the plastic container were sealed with adhesive tape, the samples were kept in container for one month to confirm the radioactive equilibrium to take place between the series ^{222}Rn and their short lived progenies [10].

Table 1. The Characteristics of Flour samples available in markets of Iraq

Sq.	**Name of Samples**	**Code**	**Origin**
1	Zero flour	F_1	Turkey
2	Aqeelah	F_2	Iran
3	Ard shiraz star	F_3	Iran
4	Alzamord	F_4	Iran
5	Al Ihasan	F_5	Iraq
6	Flour company	F_6	Iran
7	Al Haidariya	F_7	Iraq

8	Barka zain company	F_8	Iraq
9	Al rahab company	F_9	Iraq
10	Soft	F_{10}	Turkey
11	Kush	F_{11}	Iran
12	Barley flour	F_{12}	Turkey
13	Ameen	F_{13}	Turkey
14	Zer	F_{14}	Turkey

Characteristic radioactivity levels were estimated utilizing a gamma spectrometer which incorporates gamma multichannel analyzer outfitted with NaI(Tl) indicator of crystal dimension(3"*3"). The gamma spectra were analyzed using the ORTEC Maestro-32 information procurement and analysis system. The detector had coaxial closed- facing geometry with the following specifications. The calculated resolution is 7.9% for energy of (661.66 keV) of ^{137}Cs standard source. Relative efficiency at (1.33 MeV) ^{60}Co was 22.2% and at (1.27 MeV) ^{22}Na was 24.4%. The detector was shielded by a cylindrical lead shield in order to achieve the lowest background level . An energy calibration for this detector was performed with a set of standard ^{137}Cs, ^{60}Co,^{54}Mn, and ^{22}Na sources. In this study, the concentration of ^{40}K was determined directly from the peak areas at (1460 keV). The activity concentration of ^{238}U and ^{232}Th were calculated assuming common balance with their decay products. The gamma transition lines of ^{214}Bi (1765 keV) were used to calculate concentration of radioisotope in the ^{238}U-series. The activity concentration of radioisotope in the ^{232}Th-series were determined using gamma transition lines of 208Tl (2614 keV). The checking time for each sample was 5 hours.

Calculation of Activity. Since the counting rate is proportional to the amount of the radioactivity in a sample, $\mathcal{A}_n$is the Activity Concentration of each radionuclide in Bq.kg^{-1} ,which can be determined as a specific activity as the follows [13]:

$$A_n = \frac{(C_n - C_b)}{t\varepsilon_\gamma I_\gamma m_s} \qquad (1)$$

where$\mathcal{A}_n$ is the specific activity of each radionuclide in Bq.kg^{-1}, C_n_the count rate in cps for sample, C_b the count rate in cps for background, ε_γ and I_γ are detection efficiency and emission probability of γ-ray , t is the checking time and m_s is the mass of the sample in Kg .

Where A_{Ra}, A_{Th} and A_K are the specific activity of ^{238}U, ^{232}Th and ^{40}K respectively.

The internal (H_{in}) hazard indices was calculated using Equations (2) [14, 15].

$$H_{in} = \frac{A_{Ra}}{185} + \frac{A_{Th}}{259} + \frac{A_K}{4810} \qquad (2)$$

The internal hazard index has to be less than one as well to provide safe radionuclide levels in all samples .In the event that the determined estimations of files are more prominent than solidarity, radioactivity may make hurt the populace.
The annual effective dose equivalent from outdoor terrestrial gamma radiation is[16]:

D_{eff} =Outdoor dose(nGy h^{-1}) * 0.7(Sv Gy^{-1}) * 8760(h y^{-1}) *0.2 (3)

For indoor exposure, using an occupancy factor of 0.8, the annual effective dose equivalent is:

D_{eff} = indoor dose (nGy h^{-1}) * 0.7 (Sv Gy^{-1}) * 8760 (h y^{-1}) × 0.8 (4)

the average annual committed effective dose, Eave, for ingestion of NORMS in the Flour were calculated using the expression in equation below [17].

$$E_{ave} = C_r . DCF_i . A_i \qquad (5)$$

Where *DCFi* is the dose convection factor for ingestion, for each radionuclide (i.e., 4.5 × 10^{-5} mSv.Bq^{-1}, 2.3 × 10^{-4} mSv.Bq^{-1} and 6.2 × 10^{-6} mSv.Bq^{-1} for ^{238}U, ^{232}Th and ^{40}K respectively for an adult (UNSCEAR 2000), Cr is the consumption rate from intake of NORMS in Flour and Ai is the activity concentration in the Flour sample. Subsequently, based on this data and the non-accessibility of an all-around accepted consumption rate for Flour (90) kg .y^{-1} was assumed for all the Flour eating.

Average annual committed effective dose(AACED) measurements The AACED due to the ingestion of naturally occurring radioactive materials (NORMs) in was estimated according to Equation 9, AACED for an individual is directly proportional to the consumption rate of the components of Flour. By using the same equation, the threshold consumption rate for a Flour was measured as follows [18].

$$C_r = \frac{E_{ave}}{\sum_{i=1}^{3}(DCF_i \times A_i)} \qquad (6)$$

3.Result and Discussion

The specific activity of ^{238}U, ^{232}Th and ^{40}K in various types of Flour samples has been measured as appeared in Table (2) and Figures 1 - 3. The specific activity of ^{238}U was found in the range of (2.60±0.30) Bq.kg^{-1} to (13.73±1.89) Bq.kg^{-1} with an average (8.75±0.71) Bq.kg^{-1}, ^{232}Th from (9.96±0.14) Bq.kg^{-1} to (67.79±0.44) Bq.kg^{-1} with an average (21.87±0.31) Bq.kg^{-1} and ^{40}K from (283.70±3.41) Bq.kg^{-1} to (2680.73±23.60) Bq.kg^{-1} with an average (820.20±10.14) Bq.kg^{-1}.

Table 2. Activity concentration (Bq.kg^{-1}) ^{40}K, ^{232}Th and ^{232}U of Flour of present study.

No.	Sample code	^{40}K	^{232}Th	^{238}U
1	F_1	345.456±3.859	12.439±0.414	9.188±0.805
2	F_2	363.892±3.776	13.578±0.404	10.751±0.970
3	F_3	332.961±3.692	12.373±0.423	13.546±0.781
4	F_4	334.155±3.776	12.976±0.386	11.864±0.734

5	F_5	302.725±3.748	11.648±0.414	5.802±0.686
6	F_6	300.504±3.442	10.603±0.442	9.401±0.757
7	F_7	341.818±3.637	12.561±0.367	11.533±0.781
8	F_8	283.706±3.692	11.507±0.423	9.401±0.686
9	F_9	2680.738±3.415	9.962±0.141	5.494±0.734
10	F_{10}	2174.022±11.661	67.797±0. 442	5.447±1.894
11	F_{11}	949.85±20.546	26.93±0.178	13.735±0.520
12	F_{12}	1071.74±21.656	33.333±0.235	4.736±0.331
13	F_{13}	1256.101±23.600	38.324±0.235	13.735±0.378
14	F_{14}	522.82±20.546	17.232±0.160	4.026±0.355
15	F_{15}	1042.586±21.101	36.911±0.178	2.605±0.307
	Average □S.D	820.205±10.143	21.878±0.318	8.750±0.715
	Average □S.D[19]	133.097	1.9465	6.6025
	Maximum value	2680.738±3.415	67.797±0.442	13.735±0.378
	Minimum value	283.706±3.692	9.962±0.141	2.605±0.307

There is a variety in the specific activity of radionuclides in different Flour samples, in the sample (F_9) which is Iraqi (Al rahab company) has height concentration for(^{40}K and ^{232}Th) while (F_{13}) which is Turkish (Ameen) was height for (^{238}U). The results obtained show that the specific activity of ^{238}U, ^{232}Th and ^{40}K in all Flour samples seemed lower than recommended limit of UNSCEAR (2008) .we noted from our results that all average is higher than values in another publishers [6, 20].

The Outdoor annual effective dose equivalent, Indoor annual effective dose equivalent and the Total annual effective dose equivalent due to ^{238}U, ^{232}Th and ^{40}K in different kinds of Flour samples has been measured as shown in Table (3) and Figures 4 - 6 respectively. Where was in sample (F_{10}) Turkish(soft) was height in all this parameters while was low in sample (F_5) Iraqi (Al Ihasan).

Table 3. Outdoor and indoor annual effective absorbed dose equivalent, Internal radiation hazard and average annual committed effective dose for Flour samples

Sample code	**Outdoor annual effective dose equivalent (mSv.y^{-1})**	**Indoor annual effective dose equivalent (mS . y^{-1})**	**Total annual effective dose equivalent (mSv . y^{-1})**	**Internal radiation hazard, H_{int}**	**AACD (mSv.y^{-1})**
F_1	0.172±0.005	0.033±0.0009	0.025±0.0059	0. 17±0.012	0.2320±0.031
F_2	0.186±0.005	0.036±0.0010	0.222±0.0064	0.186±0.013	0.2710±0.034
F_3	0.18±0.004	0.035±0.0009	0.215±0.0058	0.19±0.011	0.3410±0.030
F_4	0.179±0.004	0.034±0.0008	0.213±0.0055	0.184±0.011	0.2990±0.028

F_5	0.148±0.004	0.028±0.0008	0.176±0.0053	0.139±0.011	0.1460±0.027
F_6	0.153±0.004	0.029±0.0009	0.182±0.0058	0.154±0.011	0.2370±0.030
F_7	0.178±0.004	0.034±0.0008	0.212±0.0055	0.182±0.011	0.2910±0.029
F_8	0.152±0.004	0.029±0.0008	0.181±0.0055	0.154±0.011	0.2370±0.028
F_9	0.792±0.004	0.152±0.0008	0.944±0.0053	0.625±0.010	0.1380±0.028
F_{10}	0.897±0.008	0.173±0.0017	1.07±0.0106	0.743±0.021	0.1370±0.057
F_{11}	0.412±0.007	0.079±0.0015	0.491±0.0093	0.376±0.018	0.3460±0.028
F_{12}	0.448±0.007	0.086±0.0015	0.534±0.0093	0.377±0.019	0.1190±0.025
F_{13}	0.544±0.008	0.105±0.0016	0.649±0.0101	0.483±0.020	0.3460±0.027
F_{14}	0.227±0.007	0.044±0.0013	0.271±0.0086	0.197±0.017	0.1010±0.023
F_{15}	0.449±0.007	0.086±0.0014	0.535±0.0087	0.373±0.017	0.0660±0.023
Average □S.D	0.341±0.006	0.066±0.0011	0.407±0.0072	0.302±0.014	0.2205±0.030
Average □S.D[12]					0.3213 ± 0.1657
Maximum value	0.897±0.008	0.173± 0.0017	1.07±0.0106	0.743±0.021	0.3460±0.028
Minimum value	0.148±0.004	0.028±0.0008	0.176±0.0053	0.139±0.010	0.0660±0.023

The values of all the radiation hazard indices in this study, Internal radiation hazard(H_{int}) , Representative level index and average annual committed effective dose (AACD) are height in sample (F_{10}) Soft (Turkish) except (AACD) in sample(F_{11}) Kush (Irani) While lowest value in sample (F_5) Iraqi (Al Ihasan) except AACD in sample F_{15}(Warameen) Irani ,which was arranged in(table 3) below and in Figures 7-8 respectively .

3.1 Excess lifetime Cancer risk: The risk of cancer due to radiation effects which is called excess lifetime cancer risk (ELCR) can be calculated from the following equation [21]

ELCR =(AACD) $Sv.y^{-1}$ * Rf (Sv^{-1}) (7)

Where, (AACD) the annual committed effective dose of the average duration for adult members of public and risk factor respectively. The value of risk factor (Rf) in the public is 0.05 per Sievert as recommended by ICRP for stochastic effects [22].The average annual committed effective dose for the measured flour in this study, 0.2205mSv, is used to estimate cancer risk for an adult person using the equation (11) above was estimated to be 0.0110 mSv, which gives a risk factor of $5.512*10^{-4}$.The estimated values are significantly less than the ICRP cancer risk of 2.5×10^{-3}based on annual dose limit of 1mSv for general public. Which mean the average of all samples is saving healthy.

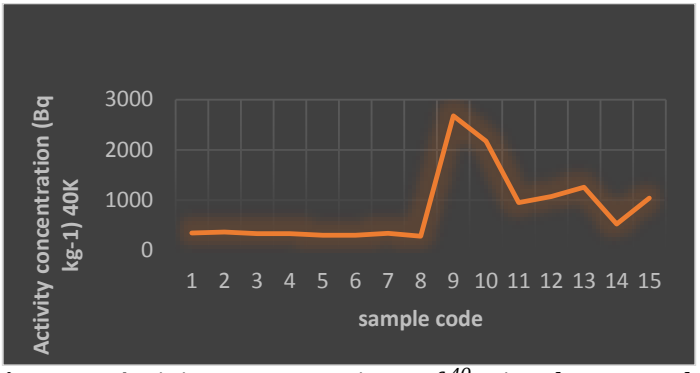

Figure 1. *Activity concentrations of ^{40}K in Flour samples*

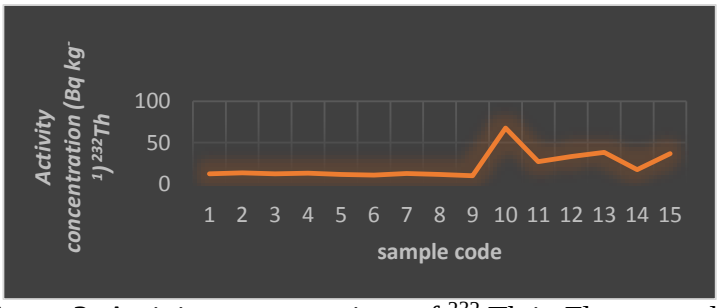

Figure 2. Activity concentrations of ^{232} Th in Flour samples

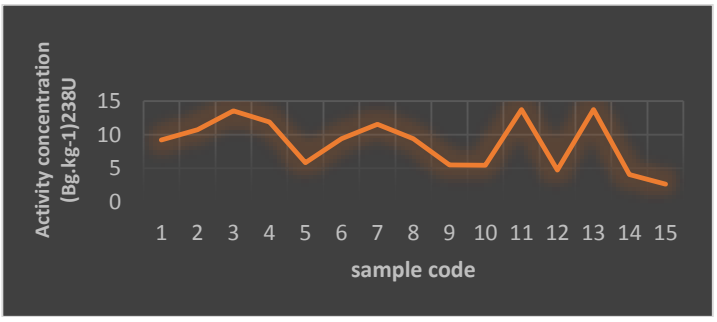

Figure 3. Activity concentrations of ^{238}U in Flour samples

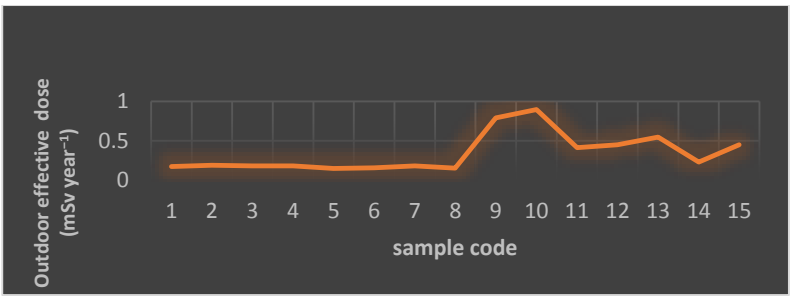

Figure 4. the outdoor annual effective dose (nGy. h^{-1}) in Flour samples

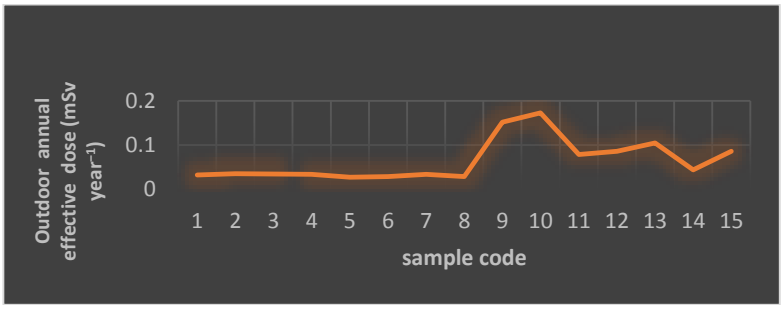

Figure 5. the Indoor annual effective dose (nGy. h^{-1}) in Flour samples

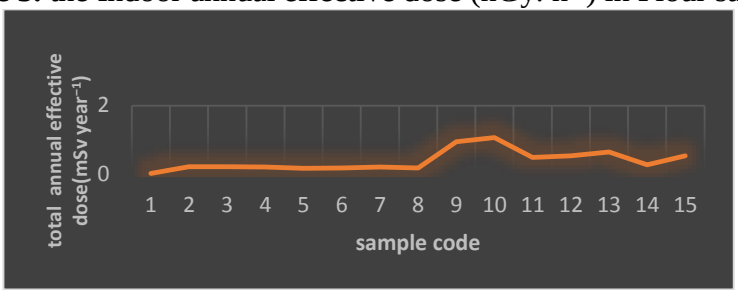

Figure 6. the total annual effective dose (nGy. h^{-1}) in Flour samples

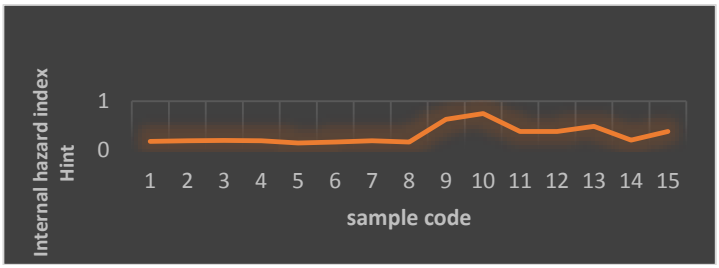

Figure 7. Internal hazard index in Flour samples in Flour samples

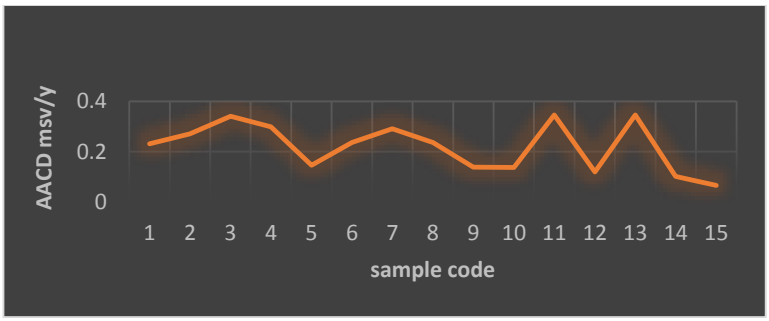

Figure 8. average annual committed effective dose (AACD) in Flour samples

4.Conclusions

The current study is the significant at the national level to study radioactivity of Flour that is available in Iraqi markets. It is found that utilization of Flour as the staple is safe for all ages of individuals in Iraq. Potassium (^{40}K) specific activity in ($Bq.kg^{-1}$) were very high compared with other studies [23] ,especially in sample F_9 which may be because the type of soil or Fertilizers which added for soil containing potassium, this work will help in building up a gauge of radioactivity exposure to the public from ingestion of foodstuff. Also have been found the outdoor and indoor annual effective absorbed dose

equivalent derived from activity Internal radiation hazard and average annual committed effective dose for Flour samples were the results fall within the permissible limits internationally that mean we estimated from this study the cancer risk has no significant health hazard and Iraqi Flour which used in markets are radiologically safe, as per international standards.

Acknowledgements. I would like to knowledge each one of those contributed in declaring this issue ,great gratitude to the staff of the department of physics at Kufa University.

References

[1] Melman, N., *Radiation and health.* 2010: Xlibris Corporation.
[2] Eisenbud, M. and T.F. Gesell, 1997: *Elsevier*.
[3] O'Brien, R. and M. Cooper, *Applied radiation and isotopes*, 1998. **49**(3): p. 227-239.
[4] Al-Hamarneh, I.F. and M.I. Awadallah, *Radiation measurements*, 2009. **44**(1): p. 102-110.
[5] Radiation, U.N.S.C.o.t.E.o.A., *I 1982* report to the general assembly, with annexes. 1982.
[6] Alrefae, T., T. Nageswaran, and T. Al-Shemali, *International Journal of Radiation Research*, 2012. **10**(3/4): p. 117.
[7] Waines, D., Cereals, *bread and society:. Journal of the Economic and Social History of the Orient/Journal de l'histoire economique et sociale de l'Orient*, 1987: p. 255-285.
[8] Guidebook, A., *Measurement of Radionuclides in Food and the Environment*. 1989, International Atomic Energy Agency IAEA, Vienna, Austria.
[9] Anke, M., et al., *Geochemistry*, 2009. **69**: p. 75-90.
[10] Aswood, M.S., M.S. Jaafar, and N. Salih, *Environmental Technology & Innovation*, 2017. **8**: p. 96-102.
[11] Aswood, M.S., A.A. Al-Hamzawi, and A.A. Khadayeir, *SN Applied Sciences*, 2019. **1**(1): p. 21.
[12] Abojassim, A.A., H.H. Al-Gazaly, and S.H. Kadhim,*International Journal of Food Contamination* , 2014. **1**(1): p. 6.
[13] Jibiri, N., I. Farai, and S. Alausa, *Journal of Environmental Radioactivity*, 2007. **94**(1): p. 31-40.
[14] Xinwei, L., , *China. Radiation measurement*s, 2005. **40**(1): p. 94-97.
[15] Alaboodi, A.S., A.M. Hassan, and A.A. Muhmood. in *Journal of Physics: Conference Series*. 2019. IOP *Publishing*.
[16] Ajayi, O., *Radiation protection dosimetry*, 2002. **98**(4): p. 441-444.
[17] Tettey-Larbi, L., et al.,. *SpringerPlus*, 2013. **2**(1): p. 1-9.
[18] Beauvais, Z.S., K.H. Thompson, and K.J. Kearfott, *Health physics*, 2009. **97**(1): p. 50-67.
[19] Abojassim, A.A., H.H. Al-Gazaly, and S.H. Kadhim, *Ukrainian food journal*, 2014(3, Issue 3): p. 333-340.
[20] Alsalihi, A., A.A. Abbas, and R. Abualhail,. *Journal of Basrah Researches (Sciences)*, 2017. **43**(2A): p. 58-69.
[21] Avwiri, G., C. Ononugbo, and I. Nwokeoji, *Comprehensive Journal of Environment and Earth Sciences*, 2014. **3**(1): p. 38-50.
[22] James, A. and A. Birchall, *s. Radiation Protection Dosimetry*, 1995. **60**(4): p. 321-326.
[23] Alshahri, F.,. *Life Science Journal*, 2016. **13**(3): p. 34-42.

A practical study to determine the percentage of radiation in medicinal herbs used in the Iraqi market

Zahra M Hamza[1*] ,Shaymaa A Alshebly[2], Hayder H Hussain[3***]**

1AL- Furat Al- Awssat Technical University 31003, Kufa Technical Institute, Iraq
2,3Department of physics, College of science, University of Kufa, Iraq
* Correspondence E mail: kin.zhr@atu.edu.iq
**Correspondence E mail: shaymaa.alshebly@uokufa.edu.iq
*** Correspondence E mail: hayder.alshibana@uokufa.edu.iq

Abstract. Some commonly used medicinal plants have been chosen to find out the radioactivity concentration and their annual effective dose for 10 samples , Because of that naturally arising radionuclides of 238U, 232Th and 40K. ,Have used Gamma ray spectroscopy was used to find activity concentrations and the results of the analysis indicated that the average activity concentration of 238U, 232Th and 40K in the medicinal plants , where the results was 38.12 ± 1.619 Bq kg-1, 12.95 ± 0.896 Bq kg-1 and 570.70 ± 31.453 Bq kg-1 correspondingly. Chamomile noted ha the greatest concentration of activity to the 238U and 40K Whereas the maximum concentrations of radioactivity for 232Th in Officinalis Borago were noted .The values of the radium corresponding mean (62.715) $Bq.kg^{-1}$.(Outdoor and indoor absorbed dose, Outdoor annual effective dose equivalent, Indoor annual effective dose equivalent and Total annual effective dose equivalent). Where the effective committed annual dose value was less than the world average (0.3 for ingestion of probable radionuclides contained in the UNSCEAR 2000 report. Also Well we found a risk factor was (1.4325*10-5) significantly less than the ICRP cancer risk , all values were below the internationally allowed limits ,the results provide baseline values that may be useful in developing radiation protection rules and regulations in addition to setting ideals and rules for the usage of therapeutic plants or herbal to the competent establishments.

1- Introduction

Agreeing to the International Food Security Authorities Network ,Radioactivity (NORMS) Naturally Occurring Radioactive Materials in air, water, soil, food and persons. [1, 2]. It is assessed that 25% of current doses are resulting from Medicinal herbs, most of which are plants whose fresh parts of plants and excerpts are used in therapeutic crops[3, 4].The increased focus on protective primary health are or basic health caution has made about 70-80% of the world's people depend on mostly on customary drug from plant bases because of this, long-established by the World Health Organization[5, 6] . plant development under certain surroundings from the geochemical fact of opinion and version ,It can provide information in monitoring ecological radioactivity about levels of radioactivity of plants in the environs of importance within the environmental and [7].Recognizable in epidemiologicals revisions for merely dosages above 0.05-0.1 Sv brought at great dosage by Epidemiological programs have not revealed adverse condition belongings in people showing to minor dosages (< 0.1 Sv) supplied in a historical of numerous ages through the concession health of (radiogenic) properties (chiefly tumor) which is charges [8-10].

Some researchers Approximation of Natural Radioactivity of Some Herbal Plants Rummage-sale in Iraq were investigated to limit accepted radiation. The radionuclides were firm by Gross alpha, beta and gamma technique Relational counter + NaI(Tl) indicator type(XLB5) and gamma-ray spectroscopy with (HPGe) techniques [11].This work tries to regulate the exact (activity concentrations) and the yearly operative dosages owed to consumption of NORM due to ^{238}U, ^{232}Th and ^{40}K current in approximately designated plants of therapeutic usually rummage-sale in Iraq to gauge the radiological danger related with the use of these Medicinal herbs. In Iraq, most people use medicinal herbs in many treatments since

ancient times, so we wanted to study the level of radiation in some of these herbs ,Are the samples far from the harmful health?.

2- Materials and methods

2.1. Sample collection The superior of the specimen location was an significant issue in this work, the excellent of a hospital that has the maximum manufacture and use of Medicinal herbs in Iraq. The samples of 10 different Medicinal herbs parts examples were collected where was the weight of the samples(0.310 ,0.380, 0.320,0.460, 0.340, 0.305, 0.440,0.440,0.535 and 0.475) kg respectively (by means of a high complex numerical allowance equilibrium with a percentages of ±0.01%) and The samples were dried to get rid of the humidity affecting the measurements at a(temperature of (42- 44)°C) to evade any moisture adsorption, and to keep the real encumbrance. The models were transferred in categorized polyethylene bags from the Centre to the laboratory, the information about all samples Record in Table 1.

2.2. Sample preparation:

models were formerly punished into fine dust through a stainless steel droplet mortar. The equipped models, in processed method, were filled into evaluated one liter Marinelli plastic mug, hermetically closed, reweighed and kept previous to including [12-14].The flasks were closed to elude any opportunity of out- gabbing of radon and reserved for a dated of 1 month to brand certain the models reached radioactive stability between Ra^{226} and its deterioration foodstuffs in the uranium sequence, and Ra^{228} and its decay foodstuffs in the thorium sequence [15, 16].

Table 1. Physical information of studies samples in this research.

No. S	Sample codes	Commonly name	Binomial name	Medicinal uses	Origin	Parts used
1	H_1	Chamomile	Matricaria chamomilla	used for lumbago, rheumatic problems[17]	Egypt	flower
2	H_2	Rosemary	Marinus oficinalis ros	stimulate memory and brain[18]	Syria	flower
3	H_3	Salvia Officnalis	sage	Purification of the nervous sybark[19]	Syria	leave
4	H_4	Anisumpimpinella	Pimpinella anisum	freshen the breath[20]	India	seed
5	H_5	Mentha	Peppermint	Useful for digestion[21]	Iran	leave
6	H_6	Officinalis Borago	Borage officinalis	rheumatoid arthritis [22]	Iran	flower

7	H_7	*Nigella sativa*	black cumin	Immune sybark stimulator[23]	India	seed
8	H_8	Linum usitatissimum (Linaceae)	Flax	reduced the early phase of carcinogenesis[24]	Sudanain	seed
9	H_9	Trigonella foenum-graecum L	Fenugreek	used for kidney ailments, a vitamin deficiency disease called beriberi[25]	Iraq	seed
10	H_{10}	Cinnamomum zeylanicum J Prel	Cinnamomum zeilanicum Nees	used as a mouth rinse to prevent mouth sores[26]	Iraq	bark

3. Analysis of models

The models were totaled by means of a gamma-ray spectrometry which consist of NaI(Tl) system that involve of a "scintillation gauge" NaI(Tl) of (3"×3") crystal measurement, provided by (Alpha Spectra,Inc.-12I12/3), merged through "a multi-channel analyzer (MCA) (ORTEC –Digi Base) through variety of 4096 channel combined by ADC (Analog to Digital Convertor)" unit, anywhere using the Gamma-ray spectrum examination software, Ortec MAESTRO–32 at exact energies. through interface. Finally, the spectral data was rehabilitated directly to the PC of the laboratory introduced by using (MAESTRO-32) software. The detector is energy calibrated using the distinctive source of known energies like ^{22}Na, ^{60}Co and ^{137}Cs . The activity of specific of ^{40}K was conventional recognized from the top parts at 1460 keV. The ^{238} U and ^{232}Th remained dignified arrogant earthly balance with their decay gathers. To find has concentration values of activity for radioisotope in the ^{238}U-series, gamma transition lines of ^{214}Bi (1765 keV) were working. Similarly, radioisotope activity attentions in the(^{232}Th-series) were recognized by coating gamma transition appearances of (^{208}Tl (2614 keV)). The even comprising period is(5h) period aimed at individually model, to confirm a decent arithmetical meaning.

3.1. Calculations

For respectively separate form, the activity of specific in (Bq/kg) units was intended through means of the comparison (1) [27].

$$\mathcal{A}_n = \frac{(\mathcal{C}_n - \mathcal{C}_b)}{t\varepsilon_\gamma I_\gamma m_s} \quad \text{.....(1)}$$

Where: $\mathcal{A}_n$" is the activity of specific of apiece isotopes in Bq/kg, $\mathcal{C}_n$ the sum level in cps for a model," $\mathcal{C}_b$ "the computation level in cps for background,(ε_γ and I_γ)are discovery efficacy and release opportunity of γ-ray, t is the including period and m_s is the bulk of the model in kg unit.

A public feature was secondhand to parallel its joint radiological properties. This feature is named the Radium corresponding activity ($\mathcal{R}a_{eq}$). As planned by the Society of Trade and industry Support and Expansion , the allowable "Radium equivalent activity" values for harmless practice should remain fewer than 370 Bq/kg. Equation (2) was rummage-sale to explore the "radium equivalent activity" (($\mathcal{R}a_{eq}$). [28].

$$\mathcal{R}a_{eq} = \mathcal{A}_{Ra} + 1.43\mathcal{A}_{Th} + 0.077\mathcal{A}_K \quad \text{.....(2)}$$

Where"($\mathcal{A}_{Ra}$, $\mathcal{A}_{Th}$ and $\mathcal{A}_{K}$)" are the specific activities of ^{226}Ra, ^{232}Th and ^{40}K correspondingly.
"The external ($\mathcal{H}_{ex}$) and internal ($\mathcal{H}_{in}$) risk" guides were planned by means of Equations (3) and (4) [29].

$$"(\mathcal{H}_{ex}) = \frac{\mathcal{A}_{Ra}}{370} + \frac{\mathcal{A}_{Th}}{259} + \frac{\mathcal{A}_{K}}{4810} " \quad \text{.....(3)}$$

$$"\mathcal{H}_{in} = \frac{\mathcal{A}_{Ra}}{185} + \frac{\mathcal{A}_{Th}}{259} + \frac{\mathcal{A}_{K}}{4810} " \quad \text{.....(4)}$$

If the intended values of guides are larger than unity, "Radioactivity may source hurt to the people".
Equation (5) was rummage-sale to compute the outdoor dosage ($\mathcal{D}_{out}$) [30].

$$"\mathcal{D}_{out} = 0.462\mathcal{A}_{Ra} + 0.604\mathcal{A}_{Th} + 0.0417\mathcal{A}_{K}" \quad \text{.....(5)}$$

Whereas the" indoor absorbed dose level" for studies models was designed by means of equation (6) [34].

$$"\mathcal{D}_{in} = 0.92\mathcal{A}_{Ra} + 1.1\mathcal{A}_{Th} + 0.08\mathcal{A}_{K} " \quad \text{.....(6)}$$

The yearly operational dose equivalent from outdoor worldly radiation of gamma is[31]:

" D_{eff} =Outdoor dose(nGy h^{-1}) * 0.7(Sv Gy^{-1}) * 8760(h y^{-1}) *0.2 "..... (7)

For indoor introduction, by means of an tenancy aspect of 0.8, the yearly effective dosage corresponding is:

D_{eff1} = indoor dose (nGy h^{-1}) * 0.7 (Sv Gy^{-1}) * 8760 (h y^{-1}) × 0.8 .....(8)

the average yearly committed effective dose, Eave, for consumption of NORMS in the samples were considered by means of the appearance in equation under [32] .

$$E_{ave} = C_r . DCF_i . A_i \quad \text{.....(9)}$$

Where *DCFi* is the dosage convection impact for ingestion, for separately radionuclide "(4.5×10^{-5} mSv Bq^{-1}, 2.3×10^{-4} mSv Bq^{-1} and 6.2×10^{-6} mSv Bq^{-1} for ^{238}U, ^{232}Th and ^{40}K correspondingly)" for an fully developed [33]. Cr the ingesting rate consumption of NORMS in pharmaceutical plants and A_i is the" activity concentration" in these samples. Usually in Iraq, the regular fraction plant substantial in grams rummage-sale in herbal groundwork or foodstuffs drugs and in eating that nasty about 1 kg for one person(adults) for one year. a ingesting ratio of 1 kg yr^{-1} was expected for wholly the medicinal herbs rummage-sale in this work, Average annual committed effective dosage(AACED) due to the consumption of naturally happening radioactive materials (NORMs) for ^{40}K, ^{238}U and ^{232}Th in these samples .By means of the equal equation, the threshold consumption amount for samples was dignified as follows [34].

$$C_r = \frac{E_{ave}}{\sum_{i=1}^{3}(DCF_i \times A_i)} \quad \text{..... (10)}$$

Where ,E_{ave}= 0.3 mSv/y is the threshold AACED due to the consumption of NORM in these samples.

4. Results and discussions:

We noted from table 2 the $\mathcal{A}_{Ra}$ of ^{238}U in the medicinal herbs varieties from 81.58±1.93 to 8.27±1.23 Bq kg^{-1} with an average value of 38.12±1.61Bq kg^{-1}. The maximum $\mathcal{A}_{K}$ of ^{238}U was noted for Chamomile while the lowermost A_i in (Linaceae) . For the $\mathcal{A}_{Th}$ of ^{232}Th, it wide-ranging from 23.90±1.19 to 3.27±0.98 Bq kg^{-1} with an average value of 12.95±0.89 Bq kg^{-1} in the medicinal herbs. The peak and bottom A_i was noted for Officinalis Borago and Fenugreek correspondingly. ^{40}K noted the main concentration of activity in wholly the medicinal herbs paralleled to the concentration activity (^{238}U and ^{232}Th) detected where was the $\mathcal{A}_{K}$ diverse as of 780.72±11. to 374.36± 6.913 Bq kg^{-1} with an average value of 570.70± 31.453 Bq kg^{-1} for it. Chamomile documented the highest concentration of activity whilst the lowest was record in Cinnamomum zeylanicum. the proportion sandwiched between concentrations of Th/K and Ra/K is practically equivalent in models. the differences in the concentrations of activity could be outstanding toward changes in the "physical site of the plants", the radiochemical procedure of the lands in which these therapeutic plants are developed or cultured since the heights of effectiveness of usual radionuclides are not regularized through the earth and the florae aptitude to engross actual features further than the others. also the in height activity of potassium concentration in these plants might perhaps be owing to the plants competence to engross potassium from the soil additional than the further components [35].

Table 2. The activities of specific of " ^{226}Ra, ^{232}Th and ^{40}K" and their relationships in medicinal plant models

model code	*Activity of Specific (Bq/kg)*			*Ratios*		
	^{226}Ra	*^{232}Th*	*^{40}K*	*Ra/K*	*Th/K*	*Th/Ra*
S1(Chamomile)	81.58±1.93	15.27±1.09	780.72±11.	0.104	0.020	0.187
S2(Rosemary)	59.83±1.79	3.27±0.98	422.97±8.2	0.141	0.008	0.055
S3(Salvia Officnalis)	9.68±1.60	10.17±1.09	549.54±86.	0.018	0.019	1.051
S4(Anisumpimpinell)	40.77±1.54	10.76±0.64	667.96±8.6	0.061	0.016	0.264
S5(Mentha)	48.48±2.34	9.41±1.00	699.59±97.	0.069	0.013	0.194
S6(Officinalis Borago)	16.96±2.05	23.90±1.19	660.25±11.	0.026	0.036	1.409
S7(Nigella sativa)	57.48±1.23	18.00±0.74	511.29±8.4	0.112	0.035	0.313
S8(Linum usitatissimum (Linaceae)	8.27±1.23	10.99±0.85	553.16±68.	0.015	0.020	1.330
S9(Trigonella foenum-graecum L)	38.77±1.17	11.02±0.57	487.13±6.9	0.080	0.023	0.284
S10(Cinnamomum zeylanicum)	19.38±1.32	16.68±0.81	374.36±7.7	0.052	0.045	0.860
mean	38.12±1.61	12.95±0.89	570.70±31.45	0.068	0.023	0.595
max	81.58	23.90	780.72	0.141	0.045	1.409
min	8.27	3.27	374.36	0.015	0.008	0.055
Nigeria [36]	15.6	8.5	67.9	-	-	-
Serbia[37]	2.6	7.4	589.6			
Brisil[12]	-	21.7	976.3			

Table 3. Results of some variables for annual effective dosage in studied samples

Model code	Outdoor absorbed dose (nGy h^{-1})	Indoor absorbed dose (nGy h^{-1})	Outdoor yearly effective dose equivalent (mSv year^{-1})	Indoor yearly effective dose equivalent (mSv year^{-1})	Total yearly effective dose equivalent (mSv year^{-1})
S1	78.518	102.074	0.096295	0.500732	0.597027
S2	45.898	59.668	0.05629	0.292707	0.348997
S3	34.496	44.845	0.042306	0.219989	0.262295
S4	53.255	69.231	0.065311	0.33962	0.404931
S5	57.008	74.110	0.069914	0.363555	0.433469
S6	51.450	66.885	0.063099	0.328113	0.391211

S7	58.447	75.981	0.071679	0.372731	0.44441
S8	34.592	44.970	0.042424	0.220603	0.263027
S9	44.802	58.243	0.054945	0.285715	0.34066
S10	35.413	46.037	0.043431	0.225841	0.269272
mean	49.388	64.204	0.060569	0.314961	0.37553
max	78.518	102.074	0.096295	0.500732	0.597027
min	34.496	44.845	0.042306	0.219989	0.262295

The outcomes for outside, indoor and whole yearly effective dose counterparts are showed in table 3. The regular total (outside plus indoor)yearly actual dose corresponding from terrestrial radioactivity was establish to be 0.3755mSv,of which 0.314mSv derives from interior and 0.060mSv from outside It lies within the globally permitted limits UNSCEAR 2000 Report .

Table 4 . Results of related accounts derived from activity to find AACED in models.

Model code	External radiation hazard, Hext	Internal radiation hazard, Hint	Radium equivalent activity, Raeq (Bq kg^{-1})	Representative level index, Iγr (Bq kg^{-1})	Annual committed effective dose AACED($mSvy^{-1}$)
S1	0.442	0.662	163.540	1.2171	0.010399
S2	0.262	0.424	64.580	0.7135	0.006709
S3	0.180	0.206	24.299	0.5326	0.002819
S4	0.291	0.401	56.235	0.8247	0.006011
S5	0.313	0.444	62.003	0.8836	0.006691
S6	0.275	0.321	51.205	0.7922	0.004779
S7	0.331	0.487	83.300	0.9041	0.007802
S8	0.180	0.202	24.061	0.5338	0.002757
S9	0.249	0.353	54.617	0.6935	0.005471
S10	0.195	0.247	43.307	0.5456	0.003861
mean	0.272	0.375	62.715	0.7641	0.00573
max	0.442	0.662	163.540	1.2171	0.010399
min	0.180	0.202	24.061	0.5326	0.002757

We noted from table 4. The AACED due to the consumption of radionuclides was lesser than the worldwide average (0.3 mSv/y). The AACED due toward the consumption of radionuclides from these samples various from 0.010399 to 0.002757 $mSvy^{-1}$. This shows that there is no radiological health risk

in using these samples determinations. This work may also donate information on native medicinal for these models to formulate guidelines connected to radiological healthcare.
Well we noticed from the table the external hazard index, internal hazard , radium equivalent activity ($(\mathcal{R}a_{eq})$, level index Iγr and Annual committed effective dose . The determined values of these factors were (0.442), (0.662), (163.540) ,(1.2171) and (0.010399) respectively. While the minimum values were (0.180), (0.202), (24.061) , (0.5326) and (0.002757) correspondingly. The considered mean values were (0.272), (0.375), (62.715) ,(0.7641) and (0.00573) respectively. While there is a important rise in the potassium concentration in samples, the designed rates of inside and outside risk guides and their nasty standards were fewer than unity, equally in unkind and ideals of outside engrossed does anywhere completely standards were under the allowable boundary [19].

4.1. Excess lifetime Cancer risk.

The risk of cancer due to radiation effects which is named excess lifetime cancer risk (ELCR) can be intended from the following equation [38]
ELCR = (AACD) $Sv.y^{-1}$ * F (Sv^{-1}) ……(11)

Where, (AACD) the average duration of human life (50 years) and the value of risk factor (F) in the public is 0.05 per Sievert as suggested by ICRP for stochastic belongings [39].
The (AACD)for the measured medical plant in this study, 0.00573mSv, is used to estimate cancer risk for an adult person using the equation (11) above was estimated to be 0.2865 mSv duration for life of 50 years, which gives a risk factor of $1.4325*10^{-5}$.
The estimated values are significantly less than the ICRP cancer risk of 2.5×10^{-3}based on annual dose limit of 1mSv for general public. Which mean the average of all samples is saving healthy.

5. Conclusion

The study estimated the concentrations for activities ^{238}U, ^{232}Th and ^{40}K in different plants that are regularly consumed by population of Iraq. The highest amount of ^{238}U was in Chamomile while for ^{232}Th in Officinalis Borago and for ^{40}K in Chamomile which was low when comparing with UNSCEAR dose levels . The values of (Raeq) are curved to be within the international average allowed maximum value of 370 $Bq.kg^{-1}$.The average yearly effective dose strong-minded in this work due to the consumption of usual radionuclides in therapeutic herb plants is far lower 0.3 mSv/y received per person universal where was AACD in this study (0.00573)mSv for an adult person was estimated to be 0.2865 mSv in life of 50 years also was less than another studies [11]. which gives a risk factor of $1.4325*10^{-5}$. The estimated values are significantly less than cancer risk of 2.5×10^{-3} (UNSCEAR, 2000) based on annual dose so the radiological hazard related with consumption of the accepted radionuclides in these samples is trivial.
Acknowledgements. We, the research team, thank you, each one of those donated in announcing this work. Uncommon gratitude to the staff of laboratory of physics at Kufa University.

References

1. Organization, W.H., *Report of the first global meeting of the International Food Safety Authorities Network (INFOSAN), Abu Dhabi, United Arab Emirates, 14-16 December 2010.* 2011.
2. Kessaratikoon, P. and S. Awaekechi, *Natural radioactivity measurement in soil samples collected from municipal area of Hat Yai district in Songkhla province, Thailand.* KMITL Sci J Section A, 2008. **8**(2): p. 52-58.
3. Gurib-Fakim, A., et al., *Promoting African medicinal plants through an African herbal pharmacopoeia.* African Health Monitor, 2010: p. 64-67.
4. Walther, C. and P. Gruss, *Pax-6, a murine paired box gene, is expressed in the developing CNS.* Development, 1991. **113**(4): p. 1435-1449.
5. Rothman, L.S., et al., *The HITRAN molecular database: editions of 1991 and 1992.* Journal of Quantitative Spectroscopy and Radiative Transfer, 1992. **48**(5-6): p. 469-507.

6. Grassi, D., et al., *Flavonoids, vascular function and cardiovascular protection.* Current pharmaceutical design, 2009. **15**(10): p. 1072-1084.
7. Mukhammedov, S. and K. Tillaeva, *Determination of light elements content by use of recoil protons produced in a nuclear reactor.* 2003.
8. Larroche, C. and L. Mouthon, *Pathogenesis of hemophagocytic syndrome (HPS).* Autoimmunity reviews, 2004. **3**(2): p. 69-75.
9. Fesenko, S., et al., *Comparative radiation impact on biota and man in the area affected by the accident at the Chernobyl nuclear power plant.* Journal of environmental radioactivity, 2005. **80**(1): p. 1-25.
10. Moritz, S., et al., *False memories in schizophrenia.* Neuropsychology, 2004. **18**(2): p. 276.
11. Najam, L.A., N.F. Tafiq, and F.H. Kitah, *Estimation of Natural Radioactivity of Some Medicinal or Herbal Plants Used in Iraq.* Detection, 2015. **3**(01): p. 1.
12. Scheibel, V. and C.R. Appoloni, *Radioactive trace measurements of some exported foods from the South of Brazil.* Journal of Food composition and Analysis, 2007. **20**(7): p. 650-653.
13. Changizi, M., *The vision revolution: How the latest research overturns everything we thought we knew about human vision*. 2010: BenBella Books.
14. Owoeye, J.S. and P. Olatunde Yara, *School facilities and academic achievement of secondary school agricultural science in Ekiti State, Nigeria.* Asian social science, 2011. **7**(7): p. 64-74.
15. Tahir, S., A. Alaamer, and R. Omer, *Study of contents of 226Ra, 232Th and 40K in fertilisers.* Radiation protection dosimetry, 2009. **134**(1): p. 62-65.
16. Kareem, A.A., H.N. Hady, and A.A. Abojassim, *Measurement of natural radioactivity in selected samples of medical plants in Iraq.* International Journal of Physical Sciences, 2016. **11**(14): p. 178-182.
17. Schulz, V., R. Hänsel, and V.E. Tyler, *Medicinal plants, phytomedicines, and phytotherapy*, in *Rational phytotherapy*. 2001, Springer. p. 1-39.
18. Watson, H., et al., *Hypersecretion of luteinizing hormone and ovarian steroids in women with recurrent early miscarriage.* Human Reproduction, 1993. **8**(6): p. 829-833.
19. Tundis, R., et al., *Natural compounds and their derivatives as multifunctional agents for the treatment of alzheimer disease*, in *Discovery and Development of Neuroprotective Agents from Natural Products*. 2018, Elsevier. p. 63-102.
20. Turner, N.J., *Food plants of coastal First Peoples*. 1995: uBC Press.
21. Callcott, L.M., *A scripture herbal*. 1842: Longman, Brown, Green, and Longmans.
22. Escott-Stump, S., *Nutrition and diagnosis-related care*. 2008: Lippincott Williams & Wilkins.
23. Geil, P. and L. Shane-McWhorter, *Dietary supplements in the management of diabetes: potential risks and benefits.* Journal of the American Dietetic Association, 2008. **108**(4): p. S59-S65.
24. Thompson, L.U., et al., *Flaxseed and its lignan and oil components reduce mammary tumor growth at a late stage of carcinogenesis.* 1996.
25. Ebadi, M., *Pharmacodynamic basis of herbal medicine*. 2010: CRC press.
26. Moniruzzaman, M., *Study of Medicinal plants in Nuhashpalli, Bangladesh*. 2015, DAFFODIL INTERNATIONAL UNIVERSITY.
27. Stenström, K.E., et al., *A guide to radiocarbon units and calculations.* Lund University, Department of Physics internal report, 2011: p. 1-17.
28. Faheem, M. and S. Mujahid, *Assessment of radiological hazards due to the natural radioactivity in soil and building material samples collected from six districts of the Punjab province-Pakistan.* Radiation Measurements, 2008. **43**(8): p. 1443-1447.
29. Agbalagba, E. and R. Onoja, *Evaluation of natural radioactivity in soil, sediment and water samples of Niger Delta (Biseni) flood plain lakes, Nigeria.* Journal of environmental radioactivity, 2011. **102**(7): p. 667-671.

30. Altıkulaç, A., Ş. Turhan, and H. Gümüş, *Activity concentration of terrestrial and anthropogenic radionuclides (226 Ra, 222 Rn, 232 Th, 40 K, and 137 Cs) in soil samples.* Environmental Earth Sciences, 2016. **75**(1): p. 41.
31. Karahan, G. and A. Bayulken, *Assessment of gamma dose rates around Istanbul (Turkey).* Journal of environmental radioactivity, 2000. **47**(2): p. 213-221.
32. Njinga, R., S. Jonah, and M. Gomina, *Preliminary investigation of naturally occurring radionuclides in some traditional medicinal plants used in Nigeria.* Journal of Radiation Research and Applied Sciences, 2015. **8**(2): p. 208-215.
33. Psichoudaki, M. and H. Papaefthymiou, *Natural radioactivity measurements in the city of Ptolemais (Northern Greece).* Journal of Environmental Radioactivity, 2008. **99**(7): p. 1011-1017.
34. Chandrashekara, K. and H. Somashekarappa, *Soil to plant transfer factors of radionuclides in Ficus racemosa (L.): A medicinal plant.* Int Res J Biol Sci, 2015. **4**(9): p. 43-7.
35. Bhatti, T. and K. Malik, *Phosphate fertilizers a potential source for Uranium recovery as by product.* National Institute for Biotechnology and Genetic Engineering (NIGBE), Faisalabad, Technical Report No Paec/NIBGE-2, 1994.
36. Olatunde, M., et al., *Natural activity concentration and assessment of radiological dose equivalents in medicinal plants around oil and gas facilities in Ughelli and environs.* Nigeria Environ Nat Resour Res, 2011. **1**(1): p. 201-206.
37. Jevremovic, M., et al., *Radionuclide concentrations in samples of medicinal herbs and effective dose from ingestion of 137Cs and natural radionuclides in herbal tea products from Serbian market.* Isotopes in environmental and health studies, 2011. **47**(1): p. 87-92.
38. Avwiri, G., C. Ononugbo, and I. Nwokeoji, *Radiation Hazard Indices and Excess Lifetime cancer risk in soil, sediment and water around mini-okoro/oginigba creek, Port Harcourt, Rivers State, Nigeria.* Comprehensive Journal of Environment and Earth Sciences, 2014. **3**(1): p. 38-50.
39. James, A. and A. Birchall, *New ICRP lung dosimetry and its risk implications for alpha emitters.* Radiation Protection Dosimetry, 1995. **60**(4): p. 321-326.

Study the Effect of Annealing on the Structural and Optical Properties of Nano SnO_2 Thin Films Prepared by Spray Pyrolysis Technical

Radhiyah M. S.al jarrah* , Noor Ali Jaafer **

*Email: rathyah@yahoo.com, ** noor.ajaafer@gmail.com
University of Kufa/ Faculty of Science/ Department of Physics

Abstract: In this work, the effect of annealing temperature T_a on the structural and optical properties of SnO_2 nanostructure prepared by spray pyrolysis method was investigated. SnO_2 films prepared on glass substrate with thickness 250 nm by dissolved 2.2563 g of $SnCl_2.2H_2O$ in 100 ml of ethanol then added 60 drops from concentrated hydrochloric acid (HCl) . After that the films were annealed at various temperatures (573, 673 and 773 K). X-ray diffraction studies show that the structure of all SnO_2 films is polycrystalline with tetragonal rutile crystalline structure with preferential orientation in the (200) direction.

The optical measurement showed that the nature of the optical transition has been direct with average band gap energies have tendency to decreases from 3.98 eV to 3.73 eV with increasing of T_a. The extent and nature of transmittance and optimized band gap of the material assure to utilize it for photovoltaic applications.

Keywords: Annealing; Band gap; grain size;; Spray pyrolysis; tetragonal; transmittance.

1-Introduction: The thin film physics is one of the most important physics branch that deals with system of very small thickness it's from ten nanometer to a few micrometer [1, 2]. Thin films technology that play important place in the semiconductor application, It gave a clear idea of many of its physical properties [3].

Tin dioxide has been extensively studied for a long time for use as transparent oxide films in optoelectronic devices such as sensor, solar cells, liquid crystal displays (LCD), photo catalysis, lithium ion batteries, wastewater treatment, and large area flat panel displays .The SnO_2 thin films can be doped with a wide variety of transition metal ions to meet the demands of these many practical applications [4-8].

SnO_2 is n-type semiconductor with large exciton binding energy, wide and direct band gap and high carrier mobility [9]. Over time, SnO_2 has proven to be the most commonly used semiconductor oxide gas sensor that can detect a wide range of pollutant gases [10].and it is inexpensive, non-toxic, and can be fabricated via simple processes [11].

SnO2 films have been fabricated using various technologies, including sputtering, chemical vapor deposition CVD [12], spray pyrolysis , atomic layer deposition (ALD) ,pulsed laser deposition (PLD) ,physical vapor deposition (PVD) ,sol-gel, spray pyrolysis [13-15] and Chemical bath deposition (CBD) [12]. In this study tin oxide thin films were prepared by the spray pyrolysis technique, the spray pyrolysis technique is particularly attractive because of its simplicity, fast, inexpensive, vacuumless and suitable for mass production.

The purpose of this work is to finding the best temperature for creation of SnO_2 film and research of their figure of merits characteristics.

Experimental Procedure :

Nanostructure SnO_2 film was fabricated by spraying 0.1 M concentration of tin salt solution on glass substrate at temperature of 450 ^oC, The solution was prepared by solving 2.2563 g of SnCl2.2H2O was dissolved in 100 ml of ethanol then added 60 drope from concentrated hydrochloric acid (HCl) by using drop by drop technique the solution put on magnetic stirrer for 30 minits. The addition of HCl rendered

the solution transparent, microscope glass slides, cleaned with HCL, distilled water solvents, and then put in uletra sonic cleaner for 15 mints .after that put it in ethanol and distilled water solvent and again put in uletrasonic cleaner for 15 mints ,finaly the substrates put in 100 ml of distilled water and eject it then let it dry.The spray rate of the solution was adjusted to be one sprinkling in a minute and the sprinkling time was about 10 seconds. The normalized distance between the spray nozzle and the substrate was 30 cm. SnO_2 films were treated thermally at different temperatures (573,673, and 773) K for two hours in air.
The thickness of the films (t) was determined using the weighing-method as shown in the following equation:

$$t = \frac{\Delta m}{\rho A} \ldots\ldots(1)$$

where Δm represents the mass difference of slide after and before the deposition, A represents the area of the film and ρ is the mass density , the thickness of the films prepared about 250 nm.
The structure of the films was examined by X-Ray Diffraction (XRD) using a Philips X-ray diffractometer system which records the intensity as a function of Bragg's angle. The source of radiation was Cu (kα) with wavelength λ=1.5406 Å, the current was 30 mA and the voltage was 40 kV. The scanning angle 2θ was varied in the range of 20°-60°
Atomic Force Microscope (AFM), (AA3000 Scanning Probe Microscope SPM, tip NSC35/AIBS) shown in photo plate 3.5 from Angstrom Advance Inc. tests were employed to examine the surface morphology.
The transmittance and absorbance of the films was measured using UV-VIS spectrophotometer Shimadzu UV/ Visible recorder spectrometer model 12600 in the spectral range 200-1100 nm.
The intensity of light (I) after crossing thickness of material x in an isotropic medium can be estimated by [16]:

$$I = I_o \exp(-\alpha x) \ldots\ldots\ldots (2)$$

Where I_o is the initial intensity

4. Results and discussion

The results of XRD tests for SnO_2 thin film deposit on glass substrate shown in figure (1), which indicates that, the structure of the films polycrystalline.
It is known that tin dioxide SnO_2 has a tetragonal rutile crystalline structure [17]. The unit cell consists of two metal atoms and four oxygen atoms. Each metal atom is situated amidst six oxygen atoms which approximately form the corners of a regular octahedron. Oxygen atoms are surrounded by three tin atoms which approximate the corners of an equilateral triangle.
The major diffraction peaks of some lattice planes can be indexed to the tetragonal unit cell structure of SnO_2 with lattice constants a = 4.71 Å and c= 3.19 Å, which are consistent with the standard values for bulk SnO_2 (JCPDS-041-1445, card No. 96-900-9083) [17]. There are six apparent peaks with 2θ values of (26.58 º, 33.8º, 37.87º, 51.64º, 61.7 and 65.7) corresponding to SnO_2 crystal planes peaks of (110), (101), (200), (211), (310), and (301) respectively.
The crystallite reveals the nano size and the d space which determined from Scherer's formula equation (3) and Bragg equation equation (4) [18] respectively are listed in table (1).

$$D = \frac{0.9\lambda}{\beta \cos\theta} \ldots\ldots(3)$$

$$n\lambda = 2d \sin\theta \ldots\ldots\ldots(4)$$

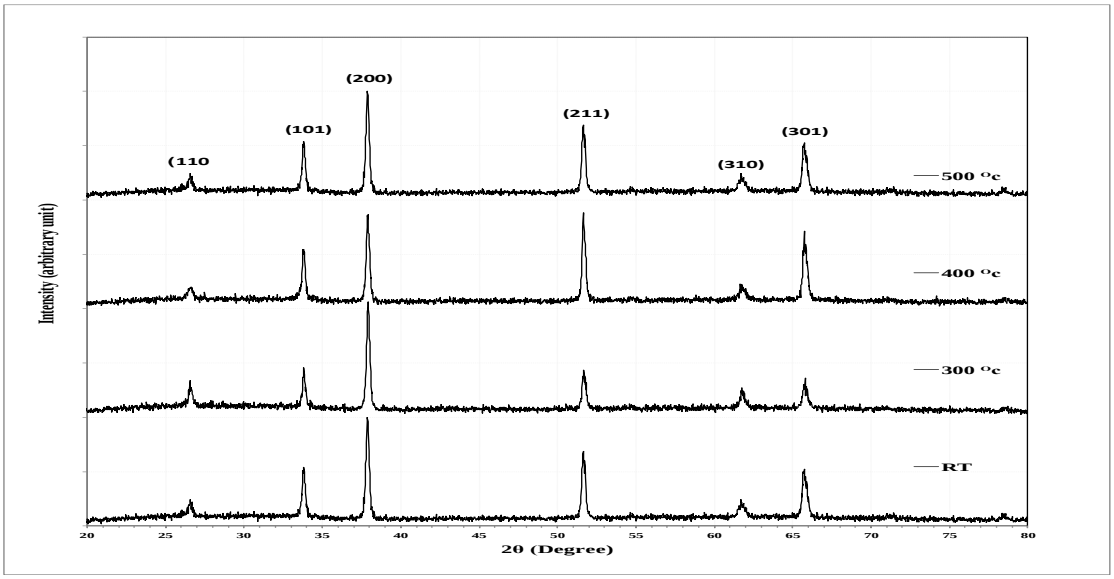

Fig.(1): X-ray diffraction (XRD) pattern of SnO_2 thin film at different annealing temperatures

Table (1) Experimental and stander XRD data for SnO_2 films at different annealing temperatures.

T (^{O}C)	2θ (Deg.)	FWHM (Deg.)	d_{hkl} Exp.(Å)	G.S (nm)	d_{hkl} Std.(Å)	hkl
RT	26.5682	0.2749	3.3523	29.7	3.3498	(110)
	33.8086	0.2342	2.6491	35.5	2.6439	(101)
	37.8717	0.2749	2.3737	30.6	2.3686	(200)
	51.6395	0.2953	1.7686	29.9	1.7642	(211)
	61.7006	0.4481	1.5022	20.7	1.4981	(310)
	65.7026	0.3666	1.4200	25.8	1.4149	(301)
300	26.5479	0.2647	3.3549	30.8	3.3498	(110)
	33.8289	0.2443	2.6476	34.0	2.6439	(101)
	37.9226	0.2749	2.3707	30.6	2.3686	(200)
	51.6904	0.3359	1.7670	26.3	1.7642	(211)
	61.7821	0.2851	1.5004	32.5	1.4981	(310)
	65.7943	0.3768	1.4183	25.1	1.4149	(301)
	26.5886	0.3462	3.3498	23.6	3.3498	(110)

400	33.8086	0.2241	2.6491	37.1	2.6439	(101)
	37.9124	0.2545	2.3713	33.0	2.3686	(200)
	51.6497	0.2749	1.7683	32.1	1.7642	(211)
	61.7312	0.3462	1.5015	26.7	1.4981	(310)
	65.7332	0.3462	1.4194	27.3	1.4149	(301)
500	26.5580	0.2546	3.3536	32.1	3.3498	(110)
	33.8086	0.2545	2.6491	32.6	2.6439	(101)
	37.8717	0.2749	2.3737	30.6	2.3686	(200)
	51.6293	0.2953	1.7689	29.9	1.7642	(211)
	61.7108	0.3768	1.5019	24.6	1.4981	(310)
	65.7332	0.3767	1.4194	25.1	1.4149	(301)

Figure (2) shows surface morphologies of SnO2 nanostructures. It can be seen that films are extremely smooth with RMS surface roughness of less than 3nm. The surface morphology as in figure is shown there are uniform distribution of homogeneous with columnar grains and an increasing in the grain size with annealing. The estimated grain size of the films is in the range of (57.6 – 68.8) nm. The average surface roughness, (RMS) values and the average surface grain size are listed in Table (2).

Table (2): Average crystallite size and roughness for as deposited and annealed SnO_2 thin films from AFM Images.

T_a (K)	G.S (nm)	Root mean square(nm)	Roughness average (nm)	Peak-peak (nm)
R.T	**57.6**	**1.6**	**1.23**	**7.1**
673	**62. 3**	**5. 9**	**4.04**	**21.5**
773	**64. 2**	**9. 5**	**8.15**	**23.7**
873	**68.8**	**3.4**	**3.12**	**12.1**

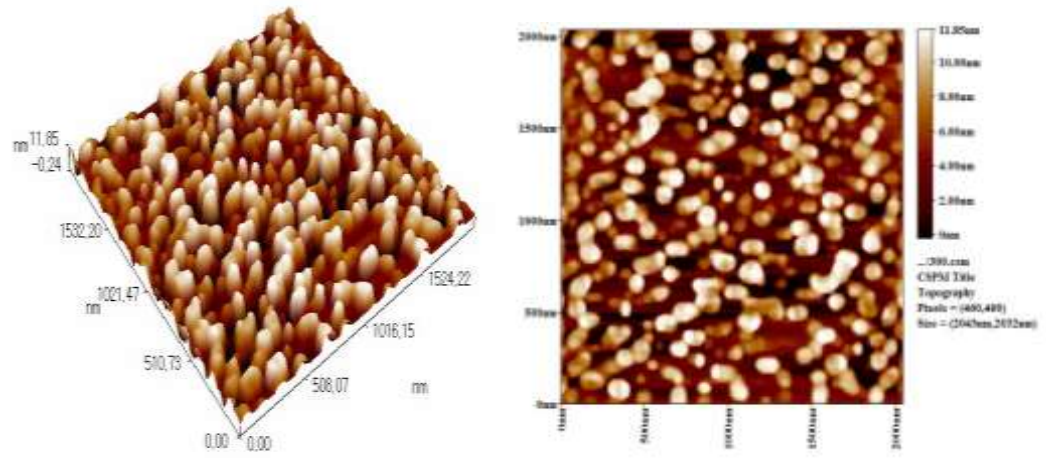
11.85
-0.24
1532.20
1021.47
510.73
0.00
0.00
508.07
1016.15
1524.22
nm

(a)

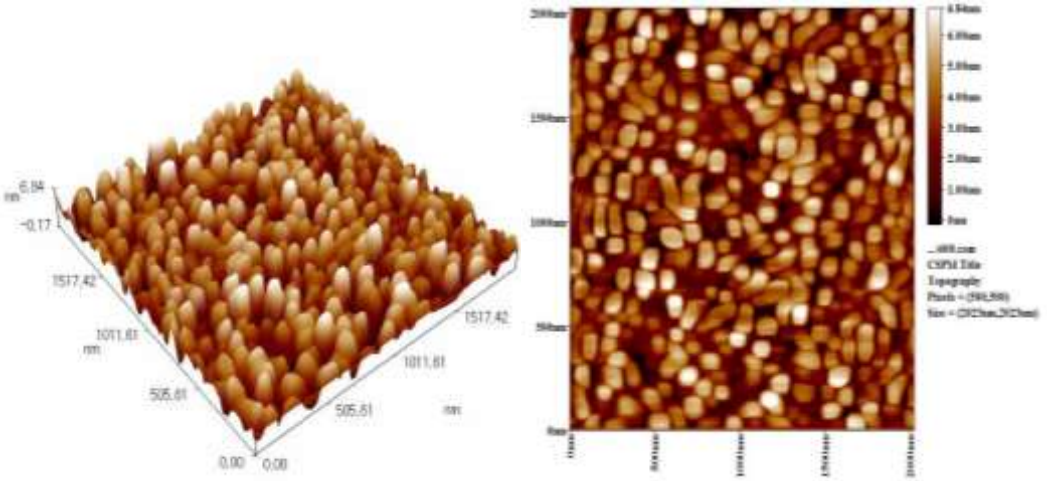
6.84
-0.17
1517.42
1011.61
505.81
0.00
0.00
505.81
1011.61
1517.42
nm

(b)

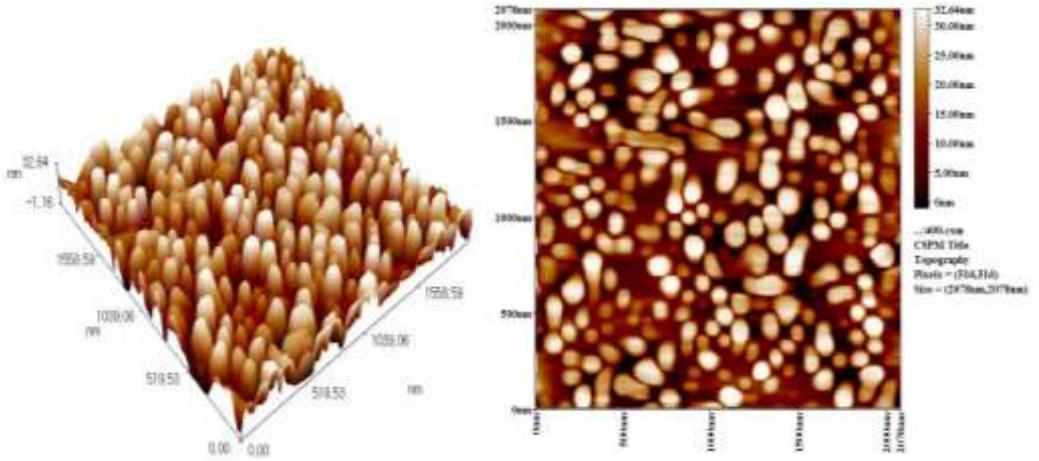
32.64
-1.36
1558.59
1039.06
519.53
0.00
0.00
519.53
1039.06
1558.59
nm

(c)

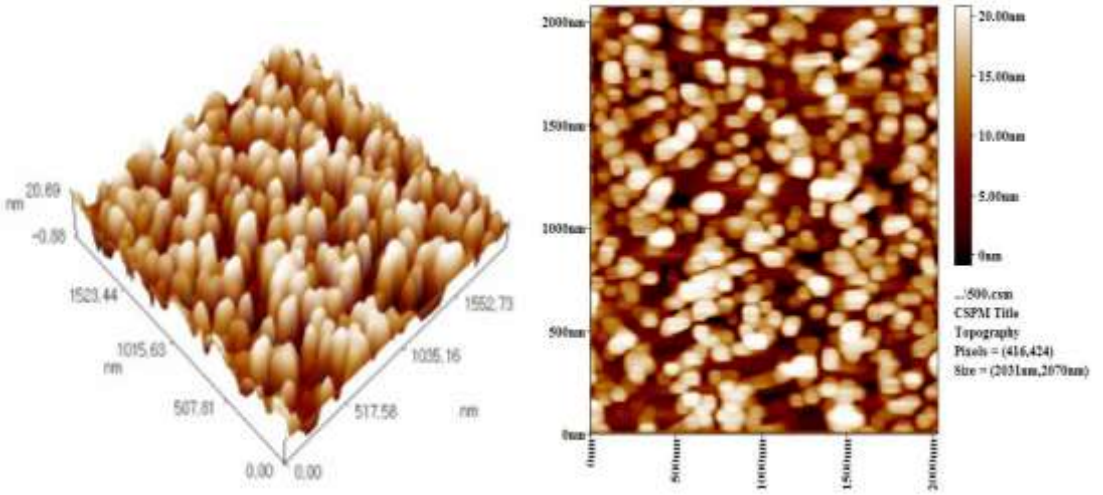

(d)

Fig.(2): AFM images;: at (a:R.T, b: Ta = 573 K ,c: Ta = 673 K, and d: Ta = 773K) of SnO_2 thin films.

The transmittances of SnO2 films with different annealing conditions are shown in figure. (3). From this figure one can be seen clearly that the transmittance of SnO_2 above 85% for all films. Generally the required transmittance of transparent conductive thin film for solar cells and as such these results indicate that SnO2 thin films are a good candidate to be used as a window layer in solar cells.

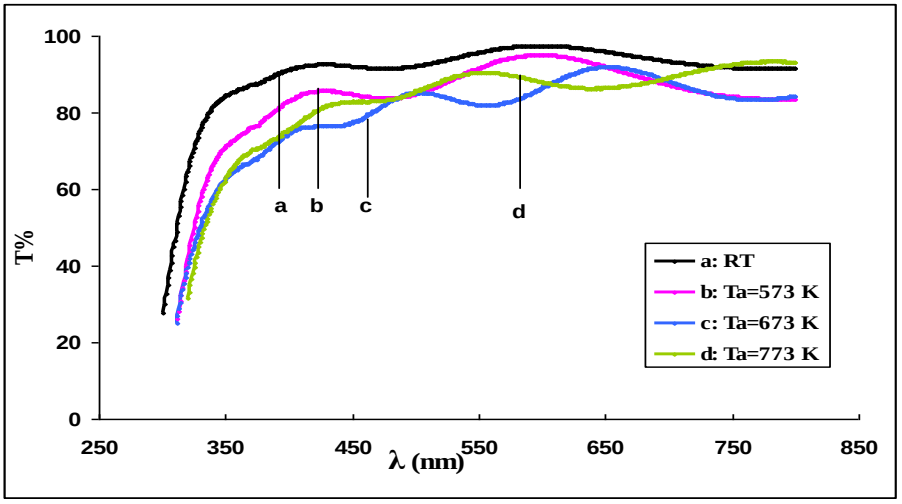

Fig. (3) Transmittance spectrum as a function of λ for SnO_2 film at different annealing temperatures.

Figure (4) shows refractive indices (n) values for SnO_2. The peak of refractive index at ~3.8 eV corresponds to direct band gap transition. The refractive index, in general changes slightly with increasing of annealing temperatures T_a and it is about 2.15 for all sample.

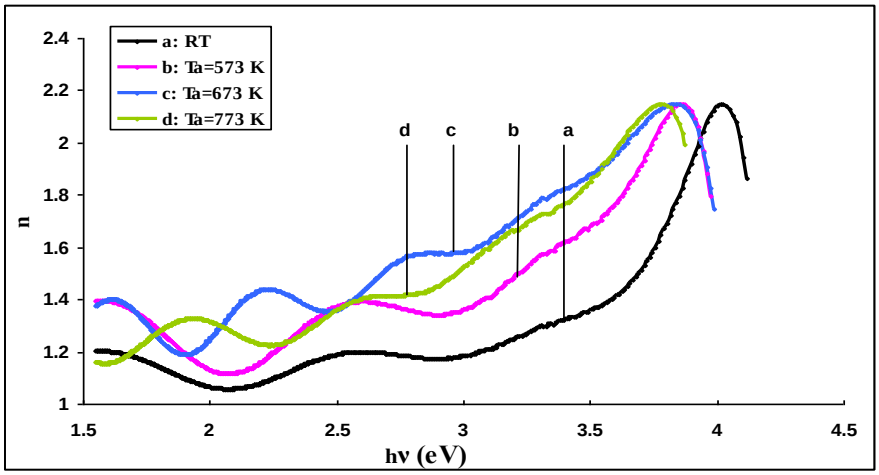

Fig. (4): Variation of n as a function of hυ for SnO_2 films at different annealing temperatures .

The optical energy gaps for both allowed and forbidden direct transition have been calculated using Tauc equation, equation (5): [16]

$$(\alpha h\nu) = B(h\nu - E_g)^r \ldots\ldots(5)$$

Where B is Tauc constant and hυ is the photon energy, α is the absorption coefficient and r =1/2 for allowed direct transition and r =3/2 for forbidden direct transition as in figures (5),(6).The energy gap E_g of the samples was evaluated from the intercept of the linear portion of each curve with the hν. .The obtained values of energy gap for different annealing temperatures are shown in table (3), Band gap lies in the range of(3.98-3.72) eV our results are in good agreement with those reported in literature[19].

The values of optical energy gaps as shown decrease with increasing annealing temperatures this may be attributed to the increase in the localizes levels near the band edges.

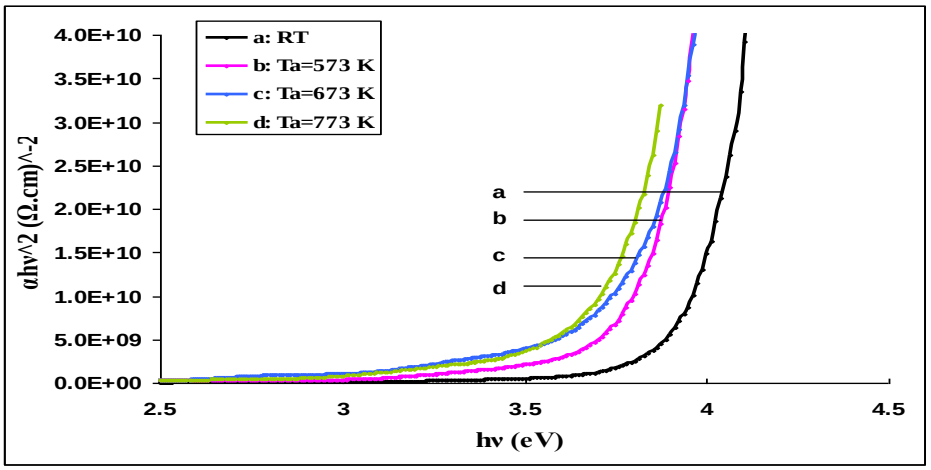

Figure (5). Variation $(\alpha h\upsilon)^2$ versus hυ for allowed direct transition at different annealing temperatures.

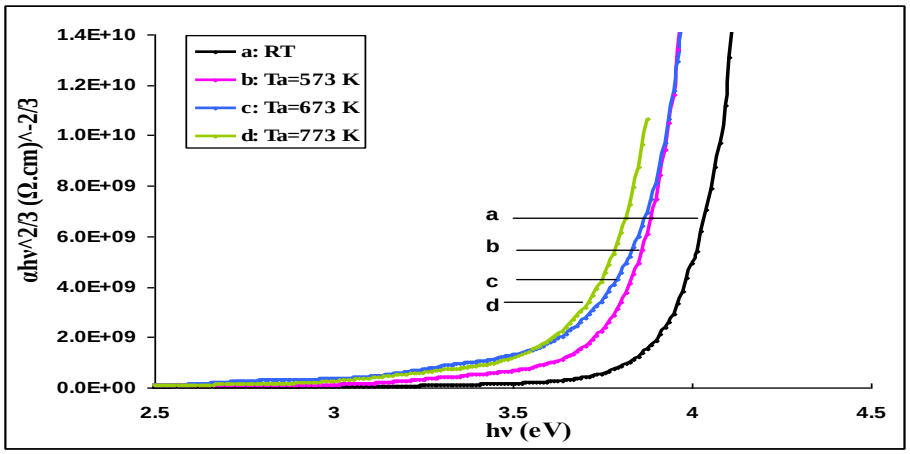

Figure (6). Variation $(\alpha h\upsilon)^{2/3}$ versus hυ for forbidden direct transition at different annealing temperatures.

In polycrystalline semiconductors where there are localized states in their energy gaps, the absorption edge becomes wide. The width of these localized states can be calculated by using Urbach rule [20],

$$\alpha = \alpha_o \exp\left(h\nu / E_u\right) \text{.....(6)}$$

where Eu is Urbach energy which is calculated from the slope of the plot between lnα and hν .as in figure (7). Our results are listed in table (3).

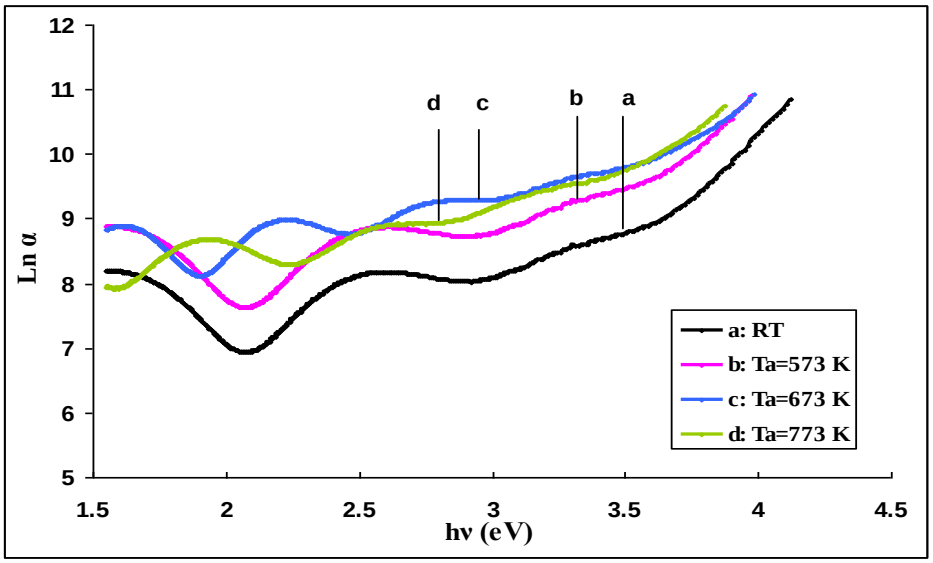

Figure (7). The variation of (ln α) versus hυ for SnO_2 thin films at different annealing temperatures.

Table (2): The values of energy gap for the allowed and forbidden direct transition at different annealing temperatures .

T_a (K)	E_u (Ev)	E_g (Ev)

		Allowed	Forbidden
R.T	1.172	3.98	4
573	0.926	3.86	3.85
673	1.034	3.83	3.83
773	1.103	3.72	3.73

5 Conclusions

There are main conclusions that have obtained from this work.

From X-ray diffraction results can be concluded that the structure of SnO_2 films is polycrystalline with tetragonal structure with preferential orientation in the (101) direction. Annealing process leads to improve in the crystallization.

From the optical properties concluded that the optical transitions in SnO_2 is direct transition and value of optical energy gap decreases with annealing temperature

References

[1] O.S. Heavens ,"Thin Film Physics", John Wily and Sons Inc , New York , (1973) .

[2] R.Ueda and J. B. Millin ," Crystal Growth and Characterization ", Mc Graw-Hill , (1975).

[3] L.Eckortova ,"Physics of Thin Films", (plenum press), (1977) .

[4] J.-K. Choi, I.-S. Hwang, S.-J. Kim, J.-S. Park, S.-S. Park, U. Jeong, Y.C. Kang, J.- H. Lee, Design of selective gas sensors using electrospun Pd-doped SnO2 hollow nanofibers, Sensor. Actuator. B Chem. Volume 150, (2010),p.p 191–199.

[5] S. Das, V. Jayaraman, SnO2: a comprehensive review on structures and gas sensors, Prog. Mater. Sci. Volume 66 (2014), p.p 112–255.

[6] Y. Bouznita,b, A. Hennic,* Characterization of Sb doped SnO_2 films prepared by spray technique and their application to photocurrent generation, Materials Chemistry and Physics Volume 233, 2019, p.p 242-248**.**

[7] K. Inyawilert, A. Wisitsoraat, C. Sriprachaubwong, A. Tuantranont, S. Phanichphant, C. Liewhiran, Rapid ethanol sensor based on electrolytically- exfoliated graphene-loaded flame-made In-doped SnO2 composite film, , Sensors and Actuators B: Chemical, Volume 209, (2015), p.p40–55.

[8] G.O. Testoni, R.A.C. Amoresi, G.M.M.M. Lustosa, J.P.C. Costa, M.V. Nogueira, M. Ruiz, M.A. Zaghete, L.A. Perazolli, Increased photocatalytic activity induced by TiO2/Pt/SnO2heterostructured films, Solid State Sci.Volum 76, (2018), p.p 65–73

[9] A. Tombaka, Y.S. Ocakb,c, F. Bayansald, Cu/SnO2 gas sensor fabricated by ultrasonic spray pyrolysis for effective detection of carbon monoxide ,Applied Surface Science, Volume 493, (2019), p.p 1075-1082 .

[10] HaoyuanXua,b,JianzhongLia,b,,YuFua,b,WenbinLuoa,b,YanwenTiana,b Deactivation mechanismandanti-deactivation modification of SnO2-based catalysts for methane gas sensors, Sensors and Actuators B: Chemical ,Volume 299, (2019) ,P.126439.

[11] S.P. Choudhurya*, S.D. Gunjalb,c, N. Kumarid, K.D. Diwatee, K.C. Mohiteb, A. Bhattacharjeea Facile synthesis of SnO2 thin film by spray pyrolysis technique and investigation of the structural, optical and electrical properties , materialstoday,Volum 3, Issue 6, (2016),P.P 1609-1619.

[12] Donald M. Mattox [Handbook of Physical Vapor Deposition (PVD),Processin], Westwood, New Jersey, U.S.A, P.P:76, (1998).
[12] K. Hu, F. Wang, H. Liu, Y. Li, W. Zeng, Enhanced hydrogen gas sensing properties of Pd-doped SnO2 nanofibres by Ar plasma treatment, Materials Science, Ceramics International ,Volume 09, (2019), P.132.
[13] K. Bunpanga,b, A. Wisitsoraatc,d,e, A. Tuantranontc,e, S. Singkammof, S. Phanichphantc, C. Liewhirana,c,g, Highly selective and sensitive CH_4 gas sensors based on flame-spray-made Cr-doped SnO2 particulate films, Sensors and Actuators B: Chemical, Volume 291, 2019, p.p177-191.
[14] Laifa Sang, Guogang Xu, Zhiwei Chen, Xinzhen Wang, Hongzhi Cui, Gaoyu Zhang, Yajie Dou Synthesis and characterization of Au-loaded SnO_2 mesoporous spheres by spray drying and their gas sensing property, Materials Science in Semiconductor Processing,Volume , (2020), P/ 104710.
[15] Qu Zhoua, Weigen Chenb, Lingna Xua,b, Rajesh Kumarc, Yingang Guia, Zhongyong Zhaoa, Chao Tanga, Shiping Zhua Highly sensitive carbon monoxide (CO) gas sensors based on Ni and Zn doped SnO2 nanomaterials, Materials Science, Volume 44,(2018) 4392-4399.
[16] J.Taus, [Amorphous and Liquid Semiconductor] Plenums Press, New York and London, 271, (1974).
[17] JCPDS-International Centre for Diffraction Data. All rights resaved ,PCPD Fwin Vol.1.30, card no. 36-1451, N 1997.
[18] Radhyah Mahdi Shaker Jarrah, Effect of Substrate Temperature and Zn Additive toCdTe Thin Films on AC Mechanism and Cole-Cole Diagram, International Journal of Science and Research (IJSR), Volume 5 Issue 5, 2016, p.p1557-1563.
[19] A.Mohammed , M.Bagheri , D.Mohagheghi, M. Shokooh , Saremi, "The influence of Al doping on the electrical, optical and structural properties of SnO2 transparent conducting films deposited by the spray pyrolysis technique", J. Phys. D. Appl. Phys., Volume 37, (2004), p.p. (1248-1253).
[20] F. Urbach, P hys. Rev., 92 (1953) 1324.

دراسة تاثير التلدين على الخواص التركيبية والبصرية لأغشية SnO_2 الرقيقة النانوية المحضرة بتقنية الرش الحراري

الخلاصة:

في هدا العمل تم استقصاء تأثير درجة حرارة التلدين على الخواص التركيبية والبصرية لمادة SnO_2 النانوية التركيب المحضرة بطريقة الرش الحراري . حُضرت أغشية SnO_2 على ركائز من الزجاج بسمك 250 نانوميتر ودلك بادابة 2.2563 غرام من مادة $SnCl_2.2H_2O$ في 100 مل من كحول الايثانول بعدها تم إضافة 60 قطرة من حامض الهيدروكلويك (HCl) .بعدها تم تلدين الأغشية لمختلف الدرجات الحرارية .(573, 673 and 773 K).

دراسة حيود الأشعة السينية بينت بان تركيب جميع أغشية SnO_2 متعدد البلورات >ات تركيب بلوري نوع رباعي الإضلاع يتمحور بالاتجاه (101) .

بينت قياسات الخواص البصرية بان طبيعة الانتقالات البصرية مباشرة مع معدل قيم فجوة الطاقة تميل للنقصان من 3.98 إلكترون فولت إلى 3.73 إلكترون فولت مع زيادة درجة حرارة التلدين.

حجم البلورات التي حصلنا عليها وطبيعة الانتقالات وقيم فجوة الطاقة للمادة قيم مناسبة لاستخدام المادة في التطبيقات الفوتوفولطائية

Measurement of Hearing Ability of Persons of Different Age Groups

Bashar Taha Jawad Al-Hamzawi1, KHELFA FADEL SHEDHAN MUSELMAWE2, Mohammed Yahya Hadi3, Mohammed Abdul kadhim Hadi Al_ Sadi4, Ali Hussein F Alnasraui5.

1,2Directorate General of Education in Babylon Governorate
3,5College of Biotechnology, Al- Qasim Green University, Iraq.
4Collage of Environmental sciences, Al- Qasim Green University
5Ali.hussein@biotech.uoqasim.edu.iq . 5alialnasraui@gmail.com

Abstract: The human ear is most sensitive. Hearing problems increases with age as well as sound pollution. In today's life, due to noise pollution or some reasons, per year, many people undergo from the problem of tentative hearing loss. In this experiment, 16 patients of different ages were taken, ranging from 20 years to 55 years of both sexes and we studied hearing sensitivity and it was compared between the right and left ears of each patient, as well as the comparability of hearing for different ages taken in this research.

Keyword: Audiometer, Rinne's test , Triveni , Weber's test , Tympanometry Test

1. Introduction:

In this paper I have discussed the audibility of persons of different age groups through using "Triveni Tam-25 Audiometer". It is computerized portable device. This is an acoustic instrument for measuring hearing ability in terms of loudness and pitch of sounds. Loss of hearing occurs due to disorders in ear. It sometimes can put a person in a state of incomprehension of the speaker and thus be construed as a lack of cleverness. Loss of hearing can be unfounded for signs of an inability to operate well in the workplace [1]. Our college conducted free health check-up for senior citizens of our nearby area. Around 40 persons have been examined through this free health check-up.

2. Sound

Sound signifies the sensation received by the ear. It is also referred to as physical cause which stimulates the auditory nerves to produce the sensation of hearing. Sound is produced by the vibrations of material bodies. These vibrations are transmitted in the surrounding medium & it carried by the medium to the ear . The eardrum is thrown into similar vibrations & produces sensation of sound. Sound energy is mechanical energy of the vibrations medium developed from the mechanical energy of the vibrating source. The vibrations lie within a certain limit to make sound audible. It is known as "limits of audibility". The lower being about 20 vibrations per second (20Hz) & upper limit being about 20,000 vibrations per second (20kHZ) [2]. The audible Sound is known as sonic sound and waves carrying this sound are called sonic waves .Sound required material medium for propagation which may be solid, liquid or gas.

3. Amplitude

The average pressure (*P0*) at sea level without sound is disturbing the air is 1atm, this value equals to 760 mmHg or(1 X 106 dyne/cm^2), superimposed Sound pressure waves on average pressure. Since sound waves are oscillatory , the immediate absolute pressure (P) periodically differs above and below the average pressure. The sound pressure amplitude p is equal to the difference between the average and absolute pressures the sound pressure amplitude is generally expressed as dynes per square centimetre. The threshold of human hearing for a 1000-Hz pure tone is 2 x 10^{-4} dyne/cm^2 [3].

4. Measuring Hearing Ability Methods

Part of an ear examination is a hearing test that judges a person's ability to hear by measuring the ability of sound to reach the brain. we hear sounds as vibrations of air, fluid, and solid materials about ours. The vibrations produce sound waves, which vibrate at a certain speed (frequency) and have certain amplitude (height from origin point) [4]. Hearing happens when these sound waves travel through the ear and are turned into nerve impulses. These nerve impulses are sent to the brain, which "hears" them. Basically, there are four methods which measure the hearing loss and detect the problem in ear .

- Test method of Rinne
- Test method of Weber
- Test method of Tympanometry
- Audiometry test method

4.1. Rinne test method

Foundation of the vibrating tuning fork is set on mastoid procedure, until the subject cannot feel the vibration and can't hear the sound. At the point when the subject doesn't hear the sound any more, the tuning fork is held in air before the ear of same side.

Typical individual hears vibration in air significantly after the bone conduction stops in light of the fact that, in ordinary condition air conduction through ossicles is superior to bone conduction. In any case, in conduction deafness, the vibrations in air are not heard after discontinuance of bone conduction. In this way in conduction deafness, the bone conduction is better than air conduction. In nerve deafness, both air conduction and bone conduction are reduced or lost [5].

4.2. Test method of Weber

The standard of the vibrating tuning tine is positioned over a vertex about the cranium and the brow middle. Hear the sound on a normal character equally over each side [6]. In unilateral conductance deafness (one ear is deaf), the sound is heard louder into the diseased ear. In unaffected ear, even is an overlaying impact of environmental noise. So the sound through skeleton transportation is no longer heard as truly so about the affected side. On the affected side, the noise is louder fit in imitation of the penury regarding the covering impact on environmental noises.

4.3. Tympanometry Test

Tympanometry testing is used to assess the condition of the ear drum and middle ear. It is the measure of energy transmissions through the middle ear. The test should not be used to access the sensitivity of hearing and the results of this test should always be viewed in conjunction with pure tone audiometry [1]. The tympanometry test detects the problems such as fluid/wax build-up perforated eardrum; ossicles bone damage, or tumors in the middle ear this test differs from Audiometric Test **.**

Tympanometry is an objective test of middle-ear function. It is performed by inserting a Tympanometry into the ear canal. Tympanometry provides information regarding the nature of the hearing loss, particularly the difference between a sensor neural and a conductive hearing loss. During this test, a soft Plugin placed on a person’s ear. This plug changes pressure to make loud noise and tracks, a person’s responses to the sound and various pressures movement of the eardrum is measured as well as the reflexes of the tiny muscles attached to the ossicles. Tympanometry is a measurement of admittance in the ear canal as the air pressure within the canal is varied. These measurements provide useful information regarding the middle ear and Eustachian tube function, which are of great interest when investigating conductive hearing disorders **.**

The graphic displays of such measurements are called Tympanograms and are obtained using a probe inserted in the ear canal. Tympanograms can be very useful for some applications but vary with individual ear canal characteristics, such as shape and volume [2]. The tympanometry looks likely an echoscope. However, it delivers sound waves, while a vacuum creates both positive and negative pressures within the ear canal. The returned energy creates a waveform that a physician can use to evaluate for disorders of the middle ear[4]. This waveform is called a Tympanograms. Possible disorders of the middle ear that can be evaluated by tympanometry include:

- Acute otitis media
- Tympanosclerosis
- Tumor in the middle ear
- Tympanic membrane scarring
- perforated tympanic membrane
- otosclerosis
- cholesteatoma

Figure1. Tympanometry

4.4. Audiometry test

An Audiometry evaluation is painless, non-invasive hearing test that measures person's ability to hear different sounds, pitches or frequencies. Audiometry test possible detect whether you have sensory neural hearing loss occurs due to damage to the nerve or cochlea, or conductive hearing loss occurs due to damage to the ear drum or tiny ossicles bones. Audiometry tests to be done with the help of audiometers [1].

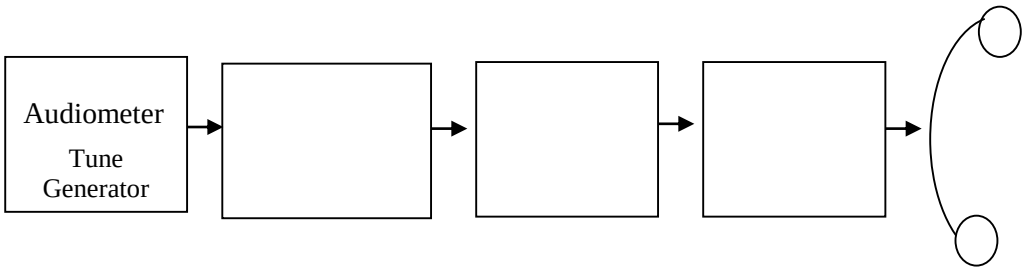

Figure2. Block diagram of Basic audiometer

Audiometer means audio + matron (to measure).An audiometer is a special instrument that is used to measure the acuity of hearing or hearing level. Bekesy`s automatic audiometer with which the client makes his own audiogram by pushing and releasing a button to indicate whether or not he hears pure tones at changing intensity levels [5]. An automatic audiometer is instrument which utilizes client control principle to test hearing, an operator being needed only to start the machine.

5. TRIVENI

An audiometer that was built for field or clinical use by field based and clinical based Audiologists from around the world who has shared their ideas on the perfect low-cost audiometer.

Figure3. TRIVENI TAM-25

5.1. New in the TAM 25;

- Narrow & Speech band masking now available along with wide band masking. A separate toggle switch for left and right channels.
- A separate toggle switch for masking select.
- The TAM-25 is able to accept both 10 and 8 ohms headphones to accommodate the standard TDH 39, 49, 50 and DR 49, and HD01 (that maybe included as standard).
- Quicker calibration using the protocol found at the end of this manual. Additionally calibration for masking is also available.
- The instrument's distortion is under 3%.
- The revised P.C software has 2 way communications allowing the audiometer to be operated by both the P.C. and the TAM-25 keys.
- The P.C software has a new installer which should allow seamless installation on all windows operating platforms [7].

5.2. 5Packing list

- TAM- 25 Audiometers.
- S.M.P.S Power supply with battery backup (Optional).
- HD-01 Headphones (Optional).
- Radio Ear B71 Bone conductor.
- 9 pin serial cable for computer connection.
- External microphone with lapel clip.
- CD containing TAM - Control software.
- Patient Response Switch
- Operating Manual.

5.3. Speech-Tone section

- Oscillator: Analog with digital control.
- Pure Tone Attenuator: in Steps of 5dB.
- Attenuator Range: -20dB to 120dB.
- Attenuator Linearity: Maximum Error at Any One.
- Attenuator Setting is: ±1B.
- Tone Interruption: Less than 100ms for rise & Decay of Tone.
- Frequency Range:
- For Air Conduction: 250/s, 500/s, 750/s, 1K/s, 1.5K/s, 2K/s, 3K/s, 4K/s, 6K/s, 8K/s
- For Bone Conduction: 250/s, 750/s, 500/s, 1K/s, 1.5K/s, 2K/s, 3K/s, 4K/s, 6K/s
- Frequency Accuracy: within 3%.
- Hearing Level Accuracy: within 2dB.
- Maximum dB settings: shown in table1

Table1. Maximum dB settings

For Air Conduction		For Bone Conduction	
Frequency kHz	Intensity (dB)	Frequency kHz	Intensity (dB)
0.25	90	0.25	50
0.50	120	0.50	70
0.75	120	0.75	70
1.0	12	1.0	70
1.5	120	1.5	70
2.0	120	2.0	70
3.0	120	3.0	70
4.0	120	4.0	70
6.0	100	6.0	70
8.0	100	8.0	70
Speech	100	Speech	70

5.4. Triveni TAM-25 audiometer software features

- Using the Traven Audiometer software the audiometer can be turned into a complete P.C based audiometer.
- Patient records can be easily maintained on P.C thus eliminating paper work.
- Old records can be reviewed and updated later.
- The intuitive user interface allows you to work much faster and efficiently.

l

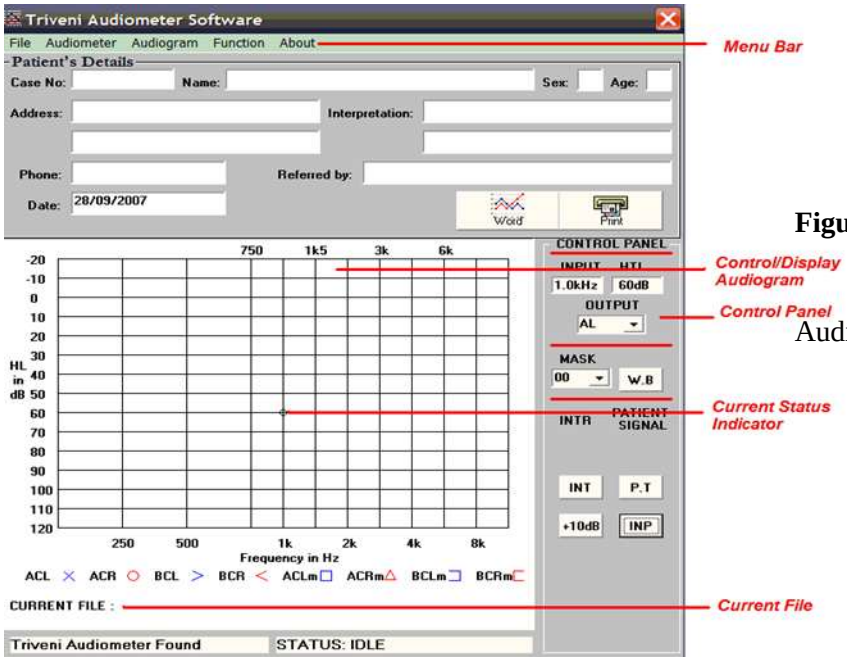

Figure4. TRIVENI TAM-25 Audiometer software features

6. Results

In this experiment has taken 16 Patients with different ages and we got on the results which show in the following tables

Table2. Observation data of Patient-1- his age 55 years & Sex: male

frequency (Hz)		250	500	750	1K	1.5K	2K	3K	4K	6K	8K
Intensity	RE	30	20	15	15	30	25	15	25	35	40
	LE	20	25	15	15	20	30	35	45	60	50

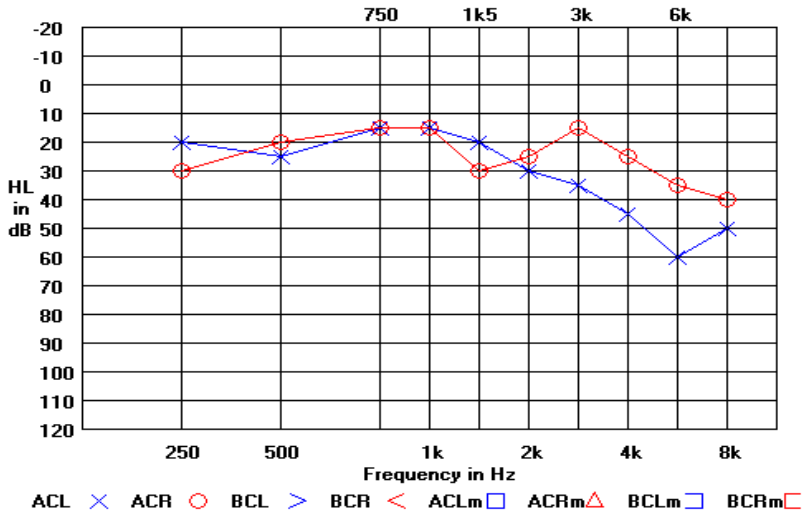

Figure5. A graph of table2 show left ear is less sensitive than Right ear than Right ear within the range 2K to 8K

Table3. Observation data of Patient-2- his age 38 years & Sex: male

frequency (Hz)		250	500	750	1K	1.5K	2K	3K	4K	6K	8K
Intensity	RE	35	35	35	35	35	30	25	20	30	30
	LE	35	35	30	30	40	25	15	20	55	55

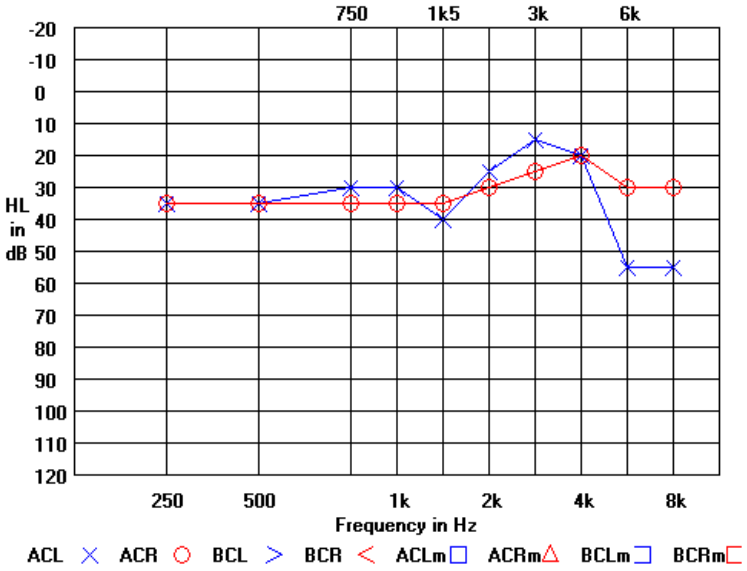

Figure6. A graph of table3 show left ear is less sensitive than right ear

Table4. Observation data of Patient-3- his age 20 years & Sex: male

frequency (Hz)		250	500	750	1K	1.5K	2K	3K	4K	6K	8K
Intensity	RE	20	30	15	20	25	15	15	5	15	15
	LE	25	30	25	20	20	15	15	10	10	20

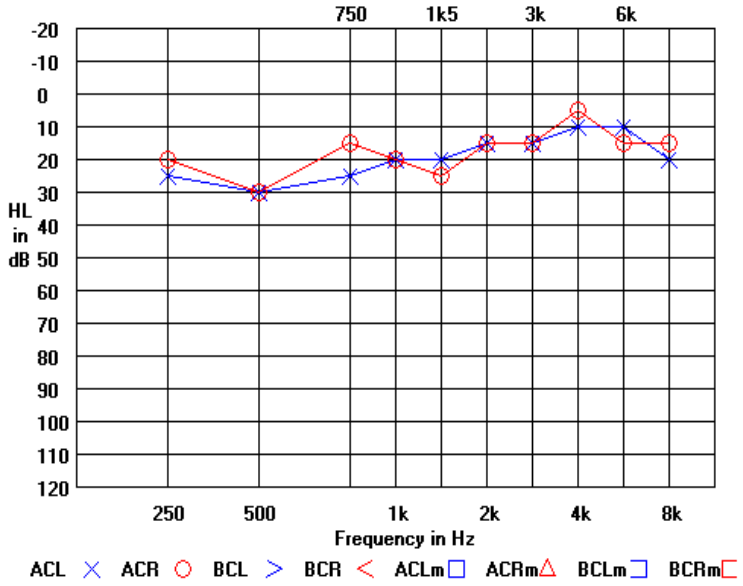

Figure7. A graph of table4 show both ears are equally sensitive

Table5. Observation data of Patient-4- his age 20 years & Sex: male

frequency (Hz)		250	500	750	1K	1.5K	2K	3K	4K	6K	8K
Intensity	RE	40	40	20	30	30	25	20	20	25	15
	LE	25	30	30	35	30	25	15	30	25	20

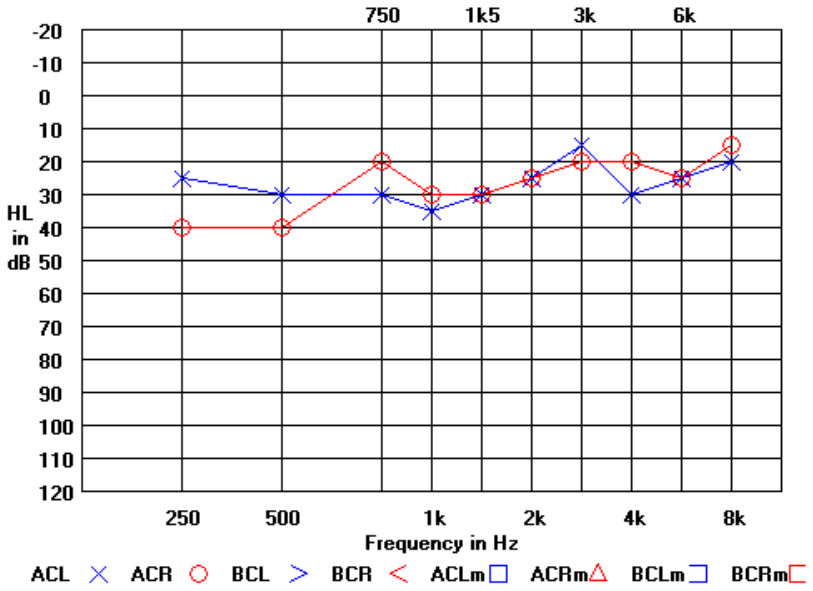

Figure 8. A graph of table5 show both ears are equally sensitive

Table6. Observation data of Patient-5- his age 20 years & Sex: female

frequency (Hz)		250	500	750	1K	1.5K	2K	3K	4K	6K	8K
Intensity	RE	30	30	25	30	35	20	20	25	15	15
	LE	30	30	35	30	25	20	15	15	15	25

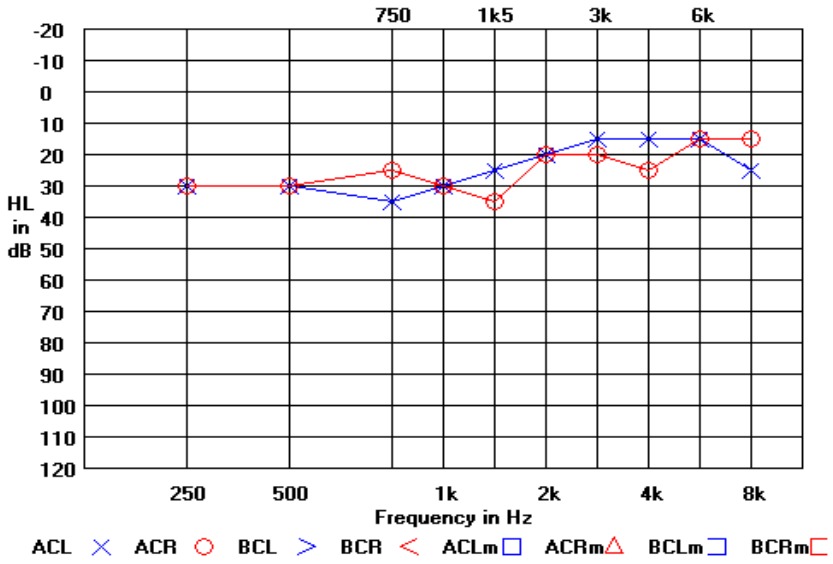

Figure 9. A graph of table6 show both ears are equally sensitive

Table7. Observation data of Patient-6- his age 32 years & Sex: female

frequency (Hz)		250	500	750	1K	1.5K	2K	3K	4K	6K	8K
Intensity	RE	45	40	30	30	25	5	10	20	20	5
	LE	10	30	-10	-10	-10	-20	-20	-5	-5	-15

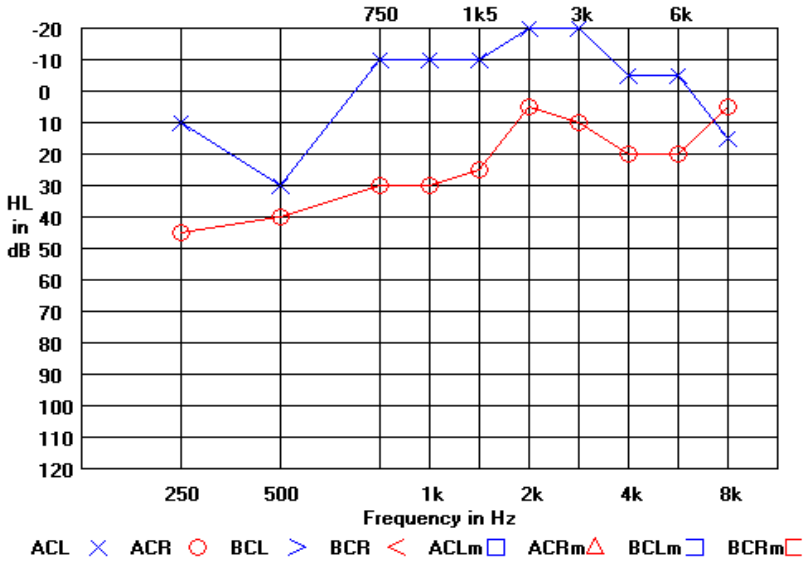

Figure10. A graph of table7 show right ear is less sensitive than Left ear

Table8. Observation data of Patient-7- his age 39 years & Sex: male

frequency (Hz)		250	500	750	1K	1.5K	2K	3K	4K	6K	8K
Intensity	RE	35	30	25	25	35	35	30	35	45	35
	LE	35	30	20	25	20	20	15	20	20	15

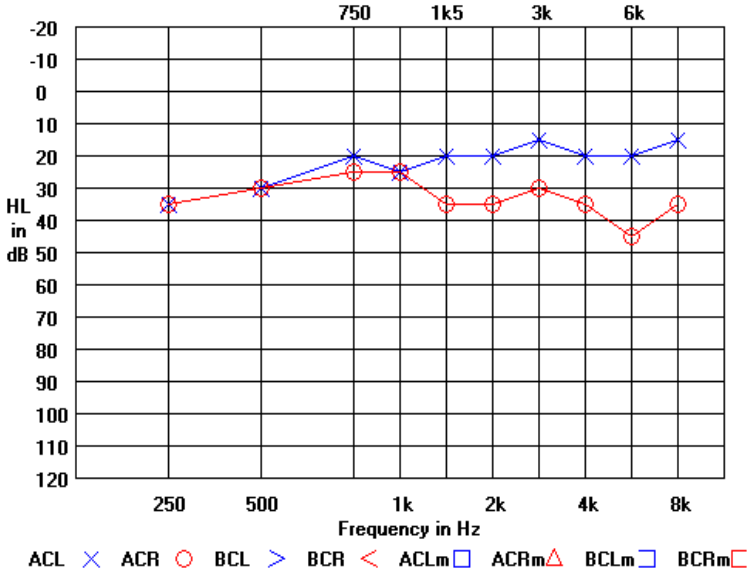

Figure11. A graph of table8 show right ear is less sensitive than Left ear within the range

Table9. Observation data of Patient-8- his age 40 years & Sex: female

frequency (Hz)		250	500	750	1K	1.5K	2K	3K	4K	6K	8K
Intensity	RE	25	20	15	30	30	25	20	30	35	35
	LE	35	20	30	35	40	30	25	30	20	20

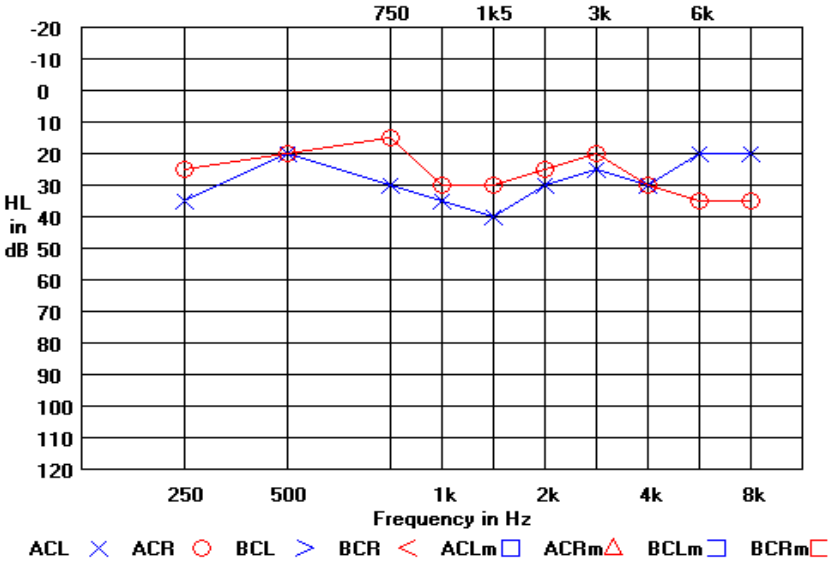

Figure12. A graph of table9 show left ear is less sensitive than Right ear within range

Table10. Observation data of Patient-9- his age 21 years & Sex: male

frequency (Hz)		250	500	750	1K	1.5K	2K	3K	4K	6K	8K
Intensity	RE	20	15	20	15	25	15	25	20	10	-5
	LE	25	-10	15	15	15	10	15	15	15	0

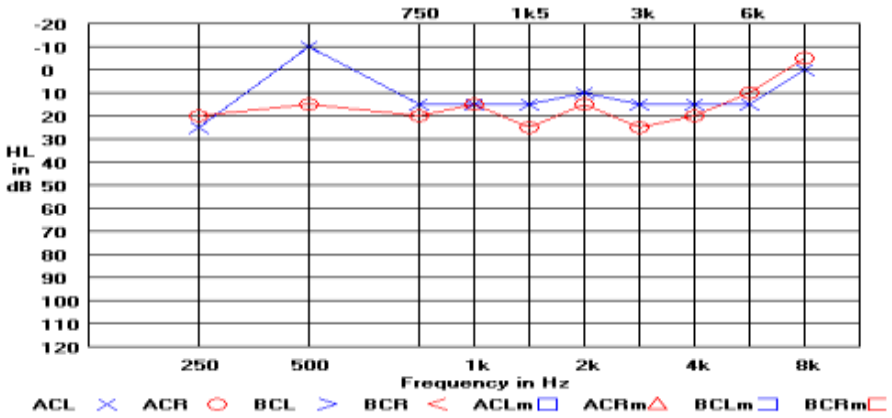

Figure13. A graph of table10 show right ear is less sensitive than Left ear within the range 1.5K to 4K.

Table11. Observation data of Patient-10- his age 48 years & Sex: female

frequency (Hz)		250	500	750	1K	1.5K	2K	3K	4K	6K	8K
Intensity	RE	40	30	35	20	35	25	25	20	50	30
	LE	40	35	40	30	20	20	25	25	70	60

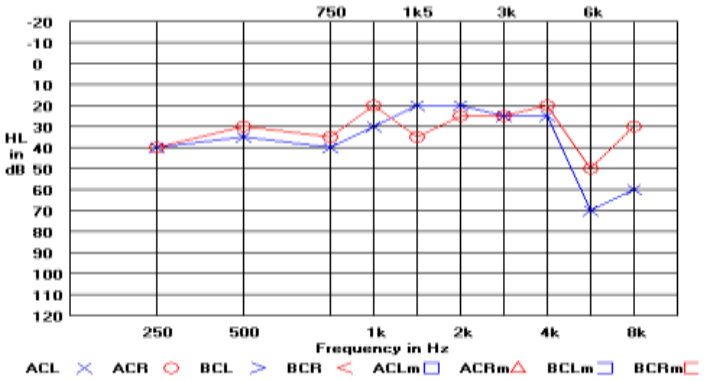

Figure14. A graph of table11 show left ear is less sensitive than Right ear within range 4K to 8K.

Table12. Observation data of Patient-11- his age 31 years & Sex: female

frequency (Hz)		250	500	750	1K	1.5K	2K	3K	4K	6K	8K
Intensity	RE	20	25	20	25	35	30	35	25	50	35
	LE	35	35	25	25	35	30	35	30	40	45

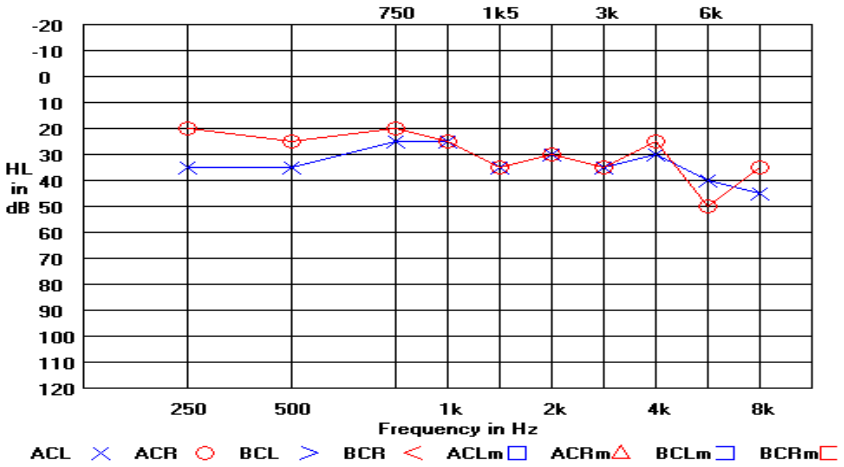

Figure15. A graph of table12 show right ear is sensitive than left ear within range 250Hz to750Hz.

Table13. Observation data of Patient-12- his age 47 years & Sex: female

frequency (Hz)		250	500	750	1K	1.5K	2K	3K	4K	6K	8K
Intensity	RE	35	30	30	35	40	30	20	30	30	15
	LE	40	40	35	35	40	35	30	20	30	20

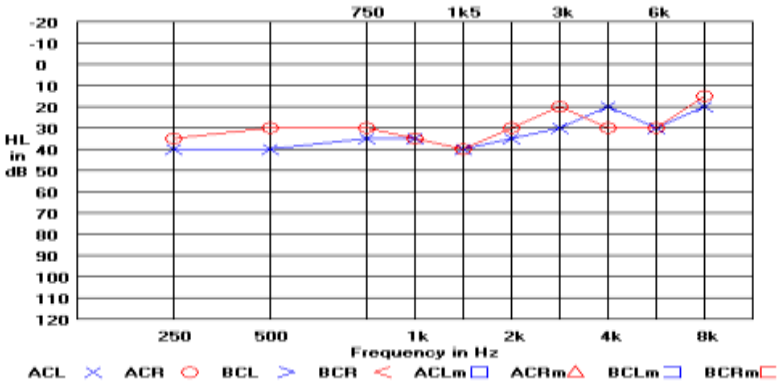

Figure16. A graph of table13 show right ear is more sensitive than left ear within

Table14. Observation data of Patient-13- his age 21 years & Sex: female

frequency (Hz)		250	500	750	1K	1.5K	2K	3K	4K	6K	8K
Intensity	RE	25	25	30	15	15	10	10	5	20	10
	LE	15	30	30	25	30	15	5	10	15	15

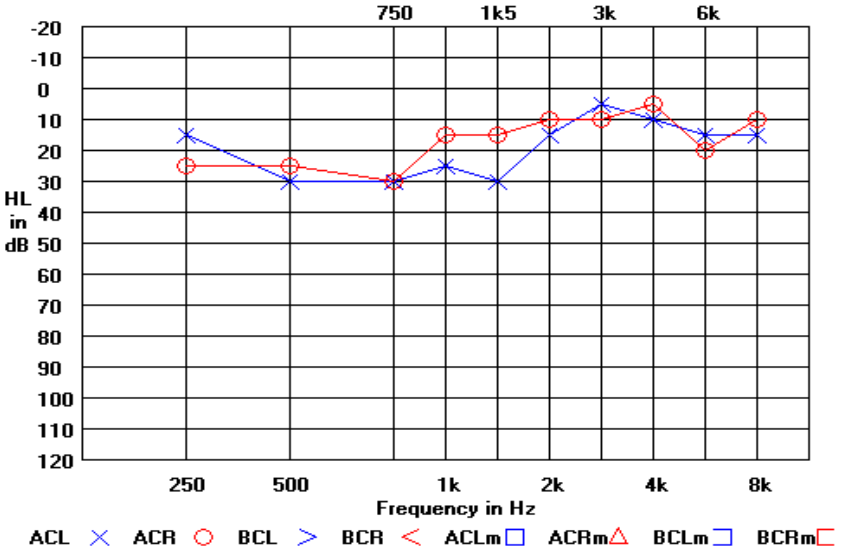

Figure17. A graph of table14 show both ears are equally sensitive.

Table15. Observation data of Patient-14- his age 23 years & Sex: male

frequency (Hz)		250	500	750	1K	1.5K	2K	3K	4K	6K	8K
Intensity	RE	35	35	25	25	30	15	15	0	15	5
	LE	35	30	25	25	25	15	20	0	15	5

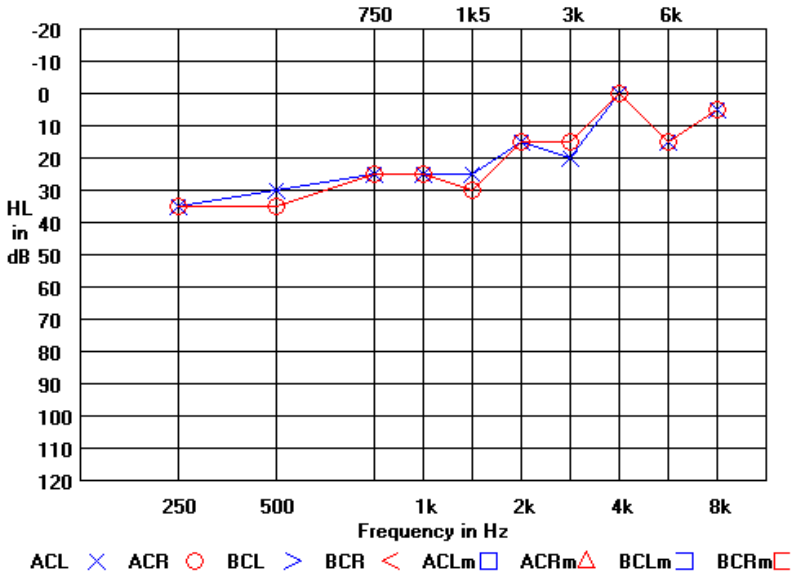

Figure18. A graph of table15 show both ears are equally sensitive within the range 750Hz to 1K & 4K to 8K.

Table16. Observation data of Patient-15- his age 36 years & Sex: female

frequency (Hz)		250	500	750	1K	1.5K	2K	3K	4K	6K	8K
Intensity	RE	25	25	30	25	30	20	15	20	25	25
	LE	35	30	30	30	35	20	15	20	25	20

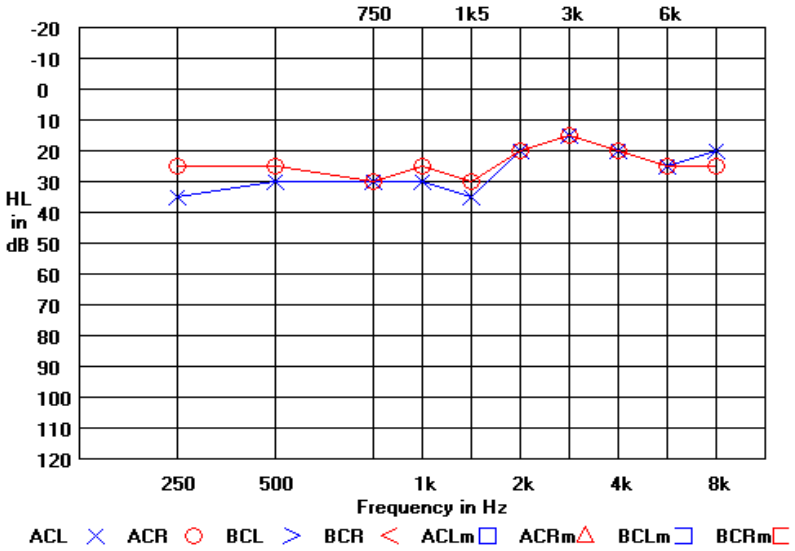

Figure19. A graph of table16 show both ears are equally sensitive within the range 2K to 6K.

Table17. Observation data of Patient-16- his age 25 years & Sex: female

frequency (Hz)		250	500	750	1K	1.5K	2K	3K	4K	6K	8K
Intensity	RE	20	25	15	25	25	15	15	15	30	25
	LE	25	15	15	15	10	15	15	15	15	20

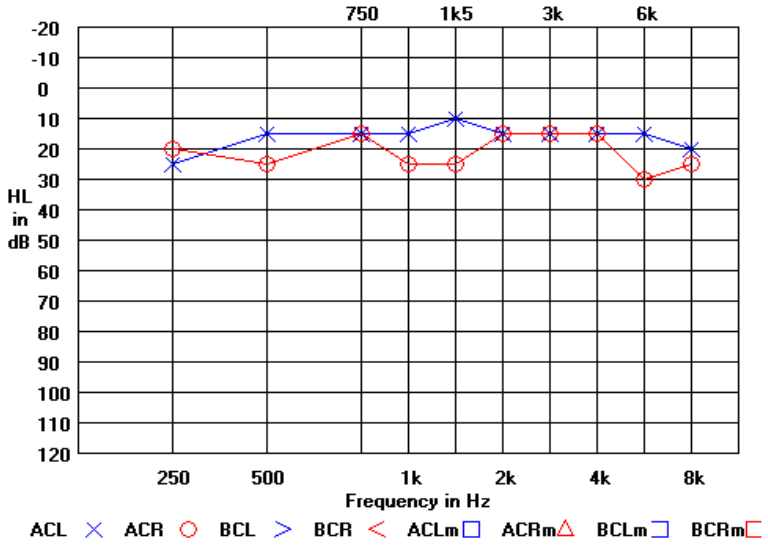

Figure20. A graph of table17 show Left ear is sensitive than right ear within the range 1K to 1.5K & 6K to 8K.

Table18. Statistical results

Sr. No.	Description	Result	
		Right ear	Left ear
1	Total no. of patients checked	16	16
2	Normal patients	4.54%	13.63%
3	Patients having Minimal loss	54.54%	45.45%
4	Patients having Miid loss	40.92%	38.63%
5	Patients having Moderate loss	—	2.29%
6	Patients having Moderately severe loss	—	—
7	Patients having severe loss	—	—
8	Patients having profound loss	—	—

7. Conclusions

I have measured hearing ability of 16 persons of different age groups it is observed that, Threshold of hearing changes from person to person. and it depends upon one`s sensitivity of ear. Because of this sensitivity of ear to respond at various frequencies is different for different person.

From the above data, it is also observed that left ear is less sensitive than right ear. Most of the patients have hearing loss at high frequencies i.e. sensitivity of ear to respond to higher frequency is minimum as compared to respond to low frequency.

From this observation I conclude that, sensitivity of ear to respond to high frequency decreases with increasing age of the person. Because of this, they are unable to hear conversational speech especially if there is background noise such as television or radio. Among them, 2.29% patients have Moderate loss. Therefore under the guidance we advised them to consult their results to ENT specialist.

8. reference

[1]Wojtczak, Magdalena, Jordan A. Beim, and Andrew J. Oxenham. "Weak middle-ear-muscle reflex in humans with noise-induced tinnitus and normal hearing may reflect cochlear synaptopathy." ENeuro 4.6 (2017).

[2]Mohd Nawi, Nazri, et al. "Hybrid Bat-BP: a new intelligent tool for diagnosing noise-induced hearing loss (NIHL) in Malaysian industrial workers." Applied Mechanics and Materials. Vol. 465. Trans Tech Publications Ltd, 2014.

[3]Alnasraui, A. H. F. (2018). Development of SOI Based Microdosimeter for Tackling Tissue Equivalence by BNCT and Fast Neutron and Proton Therapy. Journal of Pharmaceutical Sciences and Research, 10(3), 442-449.

[4]Gu, Jianwen Wendy, et al. "Tinnitus, diminished sound-level tolerance, and elevated auditory activity in humans with clinically normal hearing sensitivity." Journal of neurophysiology 104.6 (2010): 3361-3370.

[5]Faraj, A. H., Hadi, M. Y., & TAldalawi, A. A. (2019, September). Study Effective Atomic Numbers and Attenuation Cross-Section of Caprylic Acid by Using Gamma Ray Sources. In Journal of Physics: Conference Series (Vol. 1294, No. 2, p. 022023). IOP Publishing.

[6]Alnasraui, A. H., & Turki, A. A. (2018). Calculation of Heart Rate Variation Owing to the Effect of Electromagnetic Fields Waves (EMF). Journal of Kufa-physics, 10(2), 48-53.

[7]Al-Nasraui, A. H. F. (2018). Effect of Stress and Radiation of Mobile Phones on Heart and its Capabilities. Journal of Kufa-physics, 10(2), 16-25.

Preparation and characterization of (WO3:Co3O4) nano catalyst for fuel cell application

Haleemah J. Mohammed

Ministry of Science and Technology, Baghdad, Iraq
alhamdaniya2003@yahoo.com.

Abstract: This research focused on preparing the (WO_3: Co_3O_4) nano catalyst by an electrochemical deposition technique, the electrochemical deposition cell consists of (WO_3: Co_3O_4) electrode as an anode, mesh stainless steel electrode as a cathode and an aqueous solution as an electrolyte. (WO_3: Co_3O_4) were grown on mesh stainless steel electrode, and XRD was used for characterization of nano catalyst, the topography properties were studied by atomic force microscopy (AFM), study the characterization of the electrochemical parameters. For this cell in terms of the impact of hydrogen volume on current, voltage, As well as the study of the effective results of the different concentration electrolyte arrangements extending from 0.14 M to 0.28 M KOH.

1 Introduction

The distinctive and desirable properties make the nanoparticles of metal oxide, and thin films an attractive candidate for materials science and their applications such as photocatalysts, photoelectrochemical, and fuel cells [1], Photocatalysis refers to oxidation and reduction reactions on semiconductor surfaces by valence band holes, and conduction band electrons, Many metal oxides (SnO_2, $Co3O_4$., ZnO, MoO_3, ZrO_2, α-Fe_2O_3, WO_3) [2,3]. One of the few stable oxides is Co_3O_4. Interest in as an effective photocatalyst has increased due to its important electronics. Chemical and magnetic properties. It is a p-type semiconductor [4,5],nanosheet Co_3O_4 has gained special attention over the past decades making, it the anode electrode possible for the reaction of oxygen development in alkaline solutions[6], as for nano WO_3, it was found to have great potential in energy transfer applications, so it attracted the attention of researchers. Also, due to the promising physical and chemical properties , as well as excellent electrical and optical properties [7]. Nanocomposite Co_3O_4: WO_3 is characterized by high performance photocatalytic [8]. Not only has been surface surfaces that the nanoparticles possess, the nanostructures of the metal oxide catalyst, they produce nanoparticles of custom shape and size, and are also important in determining the surface geometry, exposure to faces, and the electronic structure of composite catalysts [9]. Furthermore, morphology has been found to have important effects on the catalytic properties of crystalline nanoparticles [10], the nano catalytic materials act as surface atoms or low-coordinate edges as active sites to stimulate and divide the water. This is effective for providing hydrogen and oxygen to fuel cells, and it involves two The electrochemical reactions of the hydrogen (HER) and oxygen reaction (OER) [11.12]. Aim: To study the relation between for electrochemical factors during the preparation of nano catalyst for fuel cell application

2 Experimental

2.1. *Preparation of nano catalyst (WO_3:CO_3O_4).*

Nano WO_3 was mixed with Co_3O_4 and ethanol 2: 2: 2, respectively, and these materials were mixed by Sonicators Qsonica.LLC. Because of the properties these materials possess, they cannot be mixed with any other mixer. Next, the mixture was placed in a 4 x 5 cm 2 mold. The mixture was left 4 hours and then placed in a drying oven at 200 ° C for two hours. As shown in Figure 1.

2.2. *Preparation of Nano electrodes*

The desired electrode after attaching it to the negative electrode, the other electrode nano (WO_3: Co_3O_4) connected to the positive electrode of the power supply (5.1V and 0.60A). the coating solution was added an aqueous solution, its black coating layer of nano (WO_3: Co_3O_4) atoms were produced. After the coating was completed, it has been cleaned with deionized water and dried. As shown in Figure 2

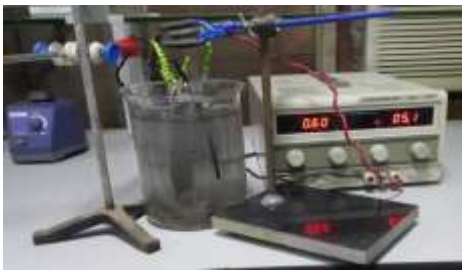

2.3. *Preparation of hydrogen gas unit*

The electrolysis cell consists of two cylinders, the first cylinder in which the cell HHO (The chemical name is her oxyhydrogen), is placed. As shown in Figure 3a. These electrodes were electrodes made of stainless steel, these electrodes were immersed in an electrolyte solution (KOH).and for the other cylinder, water is placed. As shown in Figure 3b

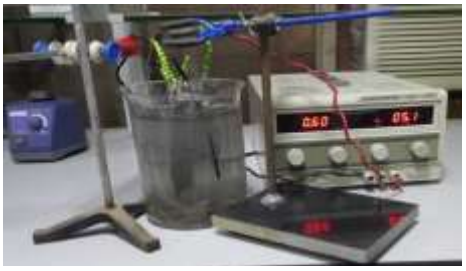

2.4. *Design of fuel cell*

The nanocatalyst (WO_3:Co_3O_4) to electrodes were used. Made for this purpose, with an area (4.5x4) cm^2 and thickness 0.1 cm. Three holes for entering the first and second hydrogen to introduce oxygen and the third to release water vapor .As shown in Figure 4

3.Results and discussion

3.1. ***XRD*** *Measurement*

The XRD patterns of (WO_3:Co_3O_4) nano catalysts are prepared , there is an obvious sharp WO3 (002) plane at 2θ=19.66°. showed a series of diffraction peaks at 2θ of , 44.40° , 54.14° , and 61.87° The XRD patterns for the characteristic reflections for Co_3O_4 showed a series of diffraction peaks at 2θ of 20.06°, 29.404° and 37.84°, are often assigned to (111), (220) and (311) planes was present in a polycrystalline form. Indicating that the Co_3O_4 particles are covered on the surface of the WO3 particles with greater space As shown in Figure 5.

Figure 5.X-ray diffraction analysis of

- 3.2. AFM Measurement

The surface morphology of the nano catalyst (WO_3:Co_3O_4) has been verified using AFM analysis that is fully focused on the nano scale characterization. Surface morphology of the catalytic layers revealed the presence of a sponge-like structure when the current density increases, where nano crystalline can be seen and distributed throughout the entire surface, as well as Analysis of the morphology of the catalyst Porous under varying current density conditions. The network was obtained very highly spaced, randomly oriented and highly correlated of pores. However, the increase in the current density of small pores

requires showing forms, leading to an increased catalyst porosity. As shown in Figures 6a,b ,the better results for morphology and roughness of the nano catalyst (WO_3:Co_3O_4) , becouse the reason is in a perfect crystal structure, This result was supported by XRD measurements, which exhibited a smaller grain size. It was found that the average grain size was 50 nm

Figure 6a, Surface morphology of nanocatalyst WO_3:Co_3O_4,

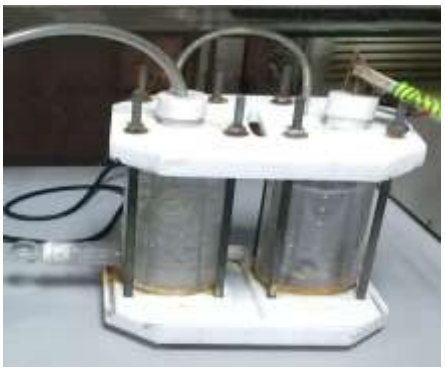

Figure 6b, granularity normal distribution .of nano catalyst

3.3 . *The Effect of the Electrochemical Parameters to the Volume of Hydrogen Gas*:

It has been studied the size of hydrogen. It is clear that when the variation of the volume with increasing time for constant voltage (6.2) V, as shown in table 1, and Figure 7, addition, the increase in the concentration of electrolyte solution leads to an increase in the number of energy carriers, which in turn increases the hydrogen production, as shown in table 2, and figure 8,which correspond to the data for these papers [13].

Table 1. Show the relationship between the volume of gas with current

Time (min)	Voltage (V)	Current (A)	Volume of H (ml)
10	6.2	0.5	0.6
15	6.2	1.3	1.7
20	6.2	1.9	2.8
25	6.2	2.2	4.8
30	6.2	2.5	7.3
35	6.2	3.0	10.4
40	6.2	3.4	13.9

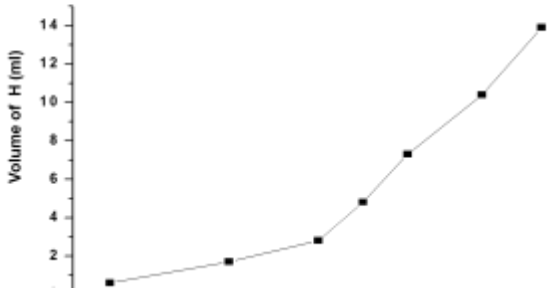

Figure 7.The relationship between Volume of hydrogen and Current

Table 2. Shows the concentration Potassium hydroxide with Voltage and Volume of hydrogen

Concentration KOH (M)	Voltage (V)	Time (min)	Volume of H (ml)
0.14	2.5	10	3
0.18	3.4	15	4.6
0.22	4.6	20	8.2
0.25	5.3	25	10.6
0.28	6.2	30	12.8

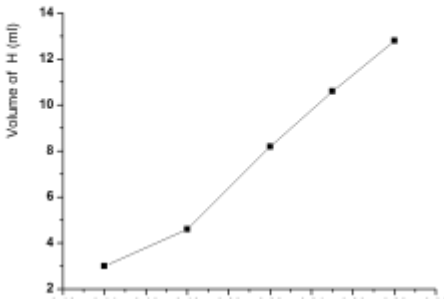

Figure 8.The volume of hydrogen function for concentration potassium hydroxide

Hydrogen gas, As described above, has been pumped into the cell via the anode of the catalyst (WO_3:Co_3O_4) . The resulting electrons have transferred to the anode, which is separated from the cathode by a nano catalyst (WO_3:Co_3O_4) . Then the electrons are transferred from the anode through the outer circuit to the cathode. This transfer occurs due to the difference between the anode and cathode electrodes. Oxygen reduction in the cathode occurs using the transported electrons, protons and molecular oxygen [14] , To obtain a voltage of 1.56 volts by the fuel cell, As shown in Figure 9.

Figure 9. The electrolysis cell and fuel cell

4 Conclusions

The results showed an improved X-ray diffraction pattern. All the materials involved in the manufacture of the cell electrolysis are simple primary materials and cheaply available in the local market. fuel cell developed so that (WO_3:Co_3O_4) used as a catalyst and a coating material to the cell to accelerate the process of interaction as well as increase the surface area to the electrodes. This study found that the increase in the current increases the current. volume of hydrogen.

NOT : The preparation of nano CO_3O_4 , as well as nano WO_3 , have not been presented because they have been published in a previous paper**.**

References

[1] P-J. A. Rodriguez, M. Fernandez-Garcia. 2007.*Wiley Interscience*, New York. pp. 79–119.

[2] Carp O, Huisman CL, Reller A. 2004. *Progress in Solid State Chem*istry;32:33-177.

[3] Kabra K, Chaudhary R, Sawhney RL.2004. *A Review. Industrial & engineering chemistry research*.43:7683.

[4] Di Zu, Haiyang Wang, Sen Lin, Gang Ou, Hehe Wei, Shuqing Sun & Hui Wu ,2019. *Nano Research* volume 12, pages 2150–2163.

[5] Li, Y.; Tan, B.; Wu, Y. 2008. *Nano Lett*. 8, 265−270.

[6] Zhang, W., Sherrell, P., Minett, A.I., Razal, J.M., Chen, J. 2010. *Energy Environ. Sci. 3, 1286–1293.*

[7] Huang K, Zhang Q, Yang F and He D .2010 . *Nano Res*. 3 281–7.

[8] Makhlouf, S. A. 2002. *J. Magn. Magn. Mater*..246, 184−190.

[9] Y. Xia, Y. Xiong, B. Lim, S.E. Skrabalak. 2009.Angew. *Chem. Int. Ed*. 48 .60-103.

[10] L. Hu, Q. Peng, Y. Li, Selective .2008. *JACS*, 130 . 16136-16137.

[11] A. K. Geim, K. S. Novoselov. 2007. *Nat. Mater. 6*, 183.

[12] T. F. Jaramillo, K. P. Jorgensen, J. Bonde, J. H. Nielsen, S. Horch, I. Chorkendorff. 2007.*Science, 317*, 100.

[13]] Wendt, H., & Plzak, V. 1991. *Kerntechnik, 56*(1), 22–28.

[14] Sara Faulkner.2017 .*The University of Queensland* . 2 June.

Utilizing k-means clustering to extract bone tumor in CT scan and MRI images

Widad Dhahir Kadhim1, and Rabab Saadoon Abdoon2

1University of Babylon, College of Science, Department of Physics, Iraq
2University of Babylon, College of science, Department of Physics, Iraq
* widaddhahir9@gmail.com

Abstract. Segmentation is one of the most significant parts of medical image processing. In image segmentation, the digital image is part of multiple sets of pixels. Magnetic Resonance Imaging, MRI and CT scanning is very important imaging techniques to explore the inner physiological constructions of the body noninvasively. A bone tumor is one of more life-threatening diseases, so exact detaching of the tumor regions is a pressing need. In this work, the K-means algorithm is employed on six MRI and CT scan images with different numbers of clusters. As well as many morphological operations like opening and dilation were applied after extract the fine tumor areas effectively. The results and the calculated surface areas of the separated tumor regions were compared to the radiologist delineation and the percent relative differences were found ranged from (0.63-1.75) % for MRI images and (0.34-1.51) % for CT scan images. This result indicates the high-quality performance of the adopted segmentation clustering-based method.

Keywords: K-means, Segmentation, MRI, CT scan, Bone tumor.

1. Introduction

The grown-up human skeleton features a sum of 213 bones, [1]. The bones of the skeleton is characterized by save support for the rest of the body, allow locomotion, by movement imparting levers for the muscles, protection inner organs and structures, make acid-base balance and maintenance the mineral homeostasis, work a store of growth factors and cytokines, and supply the environment for hematopoiesis inside the marrow place area[2]. The bone tumor is masses of tissue that are shaped inside the bone cells [3]. Discovered two kinds of bone tumors, Benign (Noncancerous) and Malignant (Cancerous) [4]. Becomes the benign tumor very large and press on nearby tissues, they don't normally reoccur, when removed by a medical procedure. Includes the malignant tumor a bigger nucleus that looks different from an ordinary cell's nucleus after they are removed can reoccur [5, 6]. Bone tumors influence which bone in the body and evolve in which part of the bone. the growth bone tumor make benign tumor becomes weaken bone and smash healthy tissue [3]. CT has transformed a lot of medical imaging by giving three-dimensional views of the member or body

region of interest [7]. In Computed tomography (CT), to detection diverse diseases and conditions utilizes sophisticated x-ray technology. CT scanning is quick, painless, noninvasive and precise. In emergency cases, it can uncover quickly enough. Diagnose issues such as cancer, cardiovascular sickness, infectious disease, appendicitis, trauma, and musculoskeletal disorders [8]. MRI is an imaging way that activates a powerful magnetic field and radiofrequency waves to discern organs, flaccid tissues, and bones. There is no being exposed to ionizing radiation as in usual x-rays and computed tomography (CT). To get a variety of disorders, such as strokes, tumors, spinal cord injuries, multiple sclerosis, and eye or internal ear problems use MRI. As well as, MRI has the major feature is not exposing patients to radiation. In the differential prognosis of benign bone pests such as simple or aneurysmal bone cysts magnetic resonance imaging (MRI) may be very helpful [9]. In this work, the implementation of one segmentation method to detect and extract bone tumor regions in CT scan and MRI images of different orientations and methods: clustering K-means.

2. K-Means

K-Means is from the many of the difficult clustering methods, used clustering algorithm to partition data into a determined number of clusters. k- Means classify the pixels into clusters being based on their intensity values. Every cluster is usually characterized by constant intensity. k- means clustering is often fitting for medical image segmentation for the reason that a variety of clusters (k) is typically regarded for photos of precise areas of human anatomy. in biomedical programs, the spatially various depth change of a biomedical structure is typically caused by inhomogeneity inside the method of image acquisition, including the inhomogeneous distribution of the comparison agent in CT imaging or inhomogeneous distribution of the magnetic discipline gradient in MRI imaging. a preliminary segmentation is obtained through the simple k-mean algorithm, the ordinary probability function is maximized on a point-point foundation, with the mean and the variance of every cluster is up to date after every iteration[10]. When the changes in the cluster seeds from one level to the next are close to zero or smaller than a pre-specified value algorithm stops. Each object is assigned to just one cluster [11]. K-means means algorithm aims to reduce the target function that represents the function of squared error which obtained by [12].

$$J(V)= \sum_{i=1}^{c} \sum_{j=1}^{c_i} (\|x_i - v_i\|)^2 \quad .....(1)$$

Where: ‘c’ is the number of cluster centers while ‘ci’ is the number of data points in the ith cluster and ‘||xi - vj||’ is the Euclidean distance among xi and Vj. Many researcher were adopted this algorithm to extract abnormal regions in the medical images for difference body organs like [13-21].

3. Morphological Operations

Morphological operators are used in image processing due to their robust performance in preserving the shape of a signal ,while suppressing the noise [22]. The basic idea in mathematical morphology is to convolve an image with a given mask (known as the structuring element) [23].

There are two basic morphological operators: erosion and dilation, opening and closing are two derived operations in terms of erosion and dilation. Here a brief introduction to the morphological operations [24]:

The primitive operations of mathematical morphology, dilation, and erosion, are based on set theory. A binary image is considered as a set of points (white region) containing in some universal set (background, or black region). The morphological structuring element is a second set of points required for the transformation. The shape of this structuring element defines the results produced by the morphological filter.

1- Opening: The opening consists of an erosion followed by dilation and can be viewed as the union of all points in B everywhere that B is contained in X.

The opening is denoted in terms of the primitive operations of dilation and erosion as simply [25]:

$X^{op}=(X\ominus B)\oplus B$ ……..(2)

2- Dilation: Considers the dilation of a binary image by a simple hexagonal structuring element B. This dilation can be expressed as the locus of centres x of the structuring element B_x where the intersection of the image X and B_x is nonempty. This is often referred to as B_x hitting X and, therefore, the name "hit " is often applied to this operation. It may be expressed as [26]:

$X\oplus B=\{x: B\_X\cap X\neq\emptyset\}$ ……..(3)

4. Experiments and methodologies

The method was executed by using the Mat lab program; the proposed procedure to achieve the extraction of the tumour regions is summarized in Figure (1).

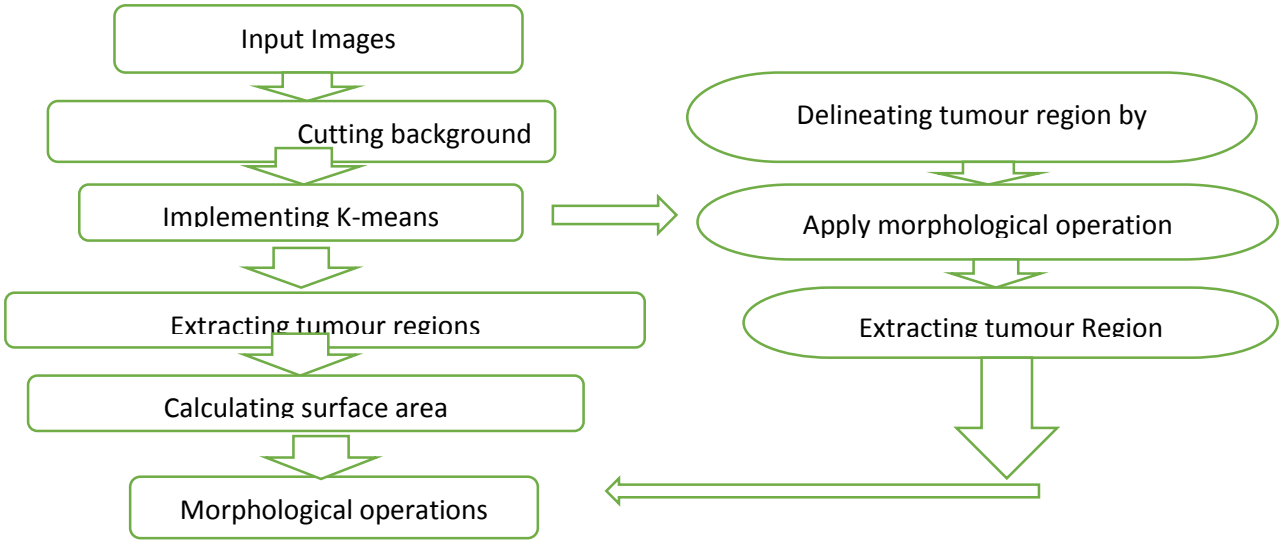

Figure 1. The blueprint of the proposed work.

5. **Input Dataset** The experimental images are three bone MRI image and three bone CT scan images with for the sizes of (244 x 443), (142 x174), (225 x 225), (261 x 342), (288 x 267), (291 x 273). The adopted images were acquired from different resources: Hila teaching hospital and websites. Figure 2 presents the experimental images.

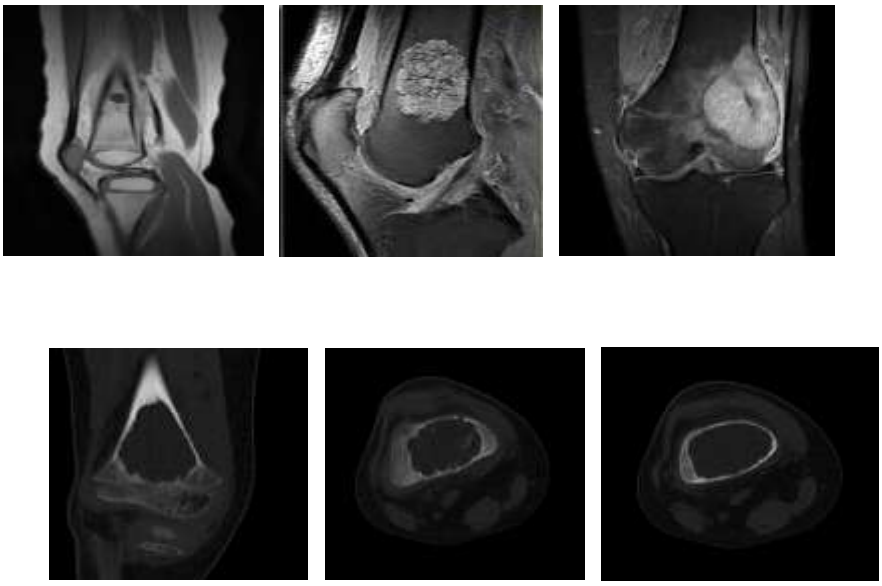

Figure 2. Input bone images: MRI in first row and CT scan in the second row.

6. Results and discussion in this study

The results of implementing the proposed work are as follows:

6.1 K-Means Algorithm

K-Means clustering algorithm was implemented with different number of clusters for the six input images, It is found that the proper number of clusters were (3, 5, 6, 6, 3 and 5) for the images (bon1, bon 2, bon 3, bon 4, bon 5 and bon 6) respectively. Figure (3) represent the results of implementing this method.

(a) 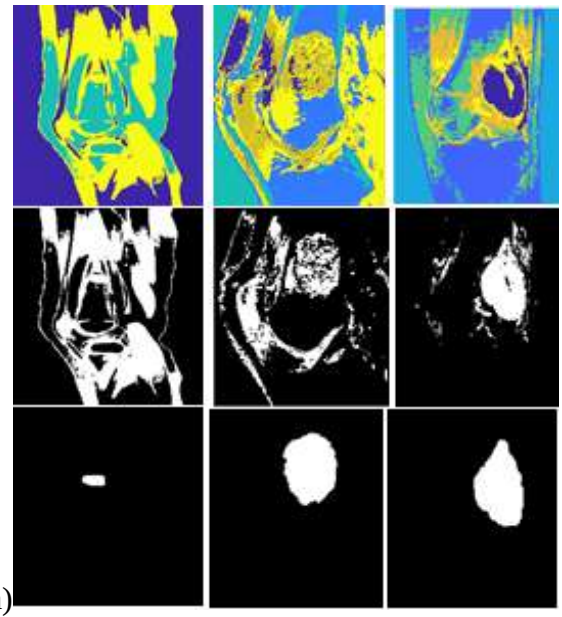 (b) 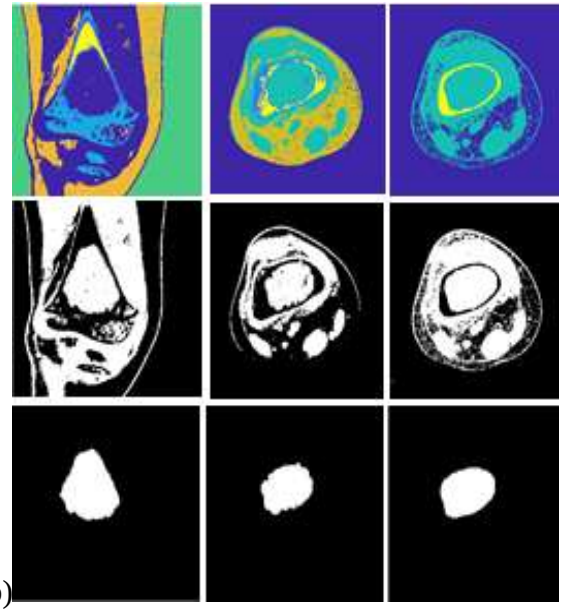

Figure 3. Results of implementing K-means algorithm: (a) for MRI and (b) for CT scan.

Figure (3), the first row represents the segmented image, the second row represents the image of the abnormalities cluster and the third row represents the extracted abnormal regions.

6.2 Radiologists Delineation

By viewing the results images the manual delineation to extract the abnormal regions is show in the figure (4).

(a) 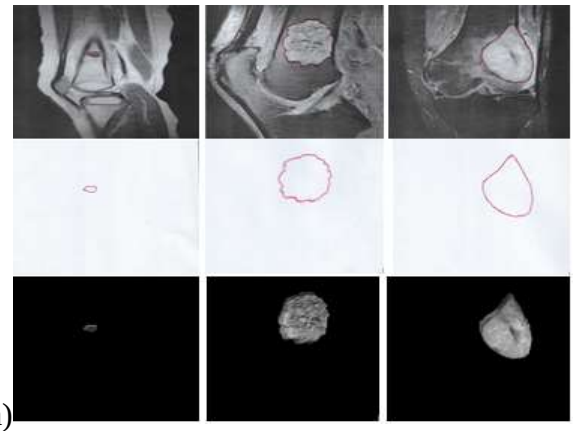 (b) 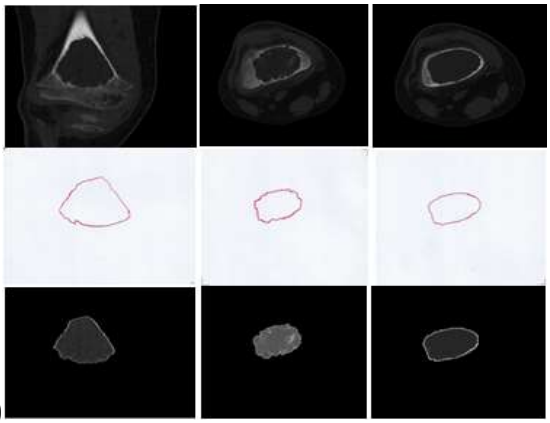

Figure 4. Radiologist delineation of the abnormal region of bone: (a) MRI images, (b) CT scan images.

Figure 4. The first row represents the original image, the second row represents the manual delineation regions images and the third row represents the extracted abnormal regions in grey.

Schedule (1): The calculated surface area of the extracted tumor regions utilizing the K-Means algorithm and radiologist delineation as well as the percent relative differences%

Image	Modality	Extracted Surface Area K-Means (pixel)	Surface Area Radiologist (pixel)	Percent Relative difference%
Image1	MRI	407	400	1.75
Image2	MRI	2061	2048	0.634765625
Image3	MRI	4342	4372	0.6861848124
Image4	CT Scan	6780	6757	0.340387746
Image5	CT Scan	7132	7242	1.5189174261
Image6	CT Scan	4845	4901	1.1426239543

6.3 Comparison

By comparison the results of tumour region in grey that obtained from the manual delineation the abnormal region and the tumour region in grey that obtained from the applying the K-Means algorithm.

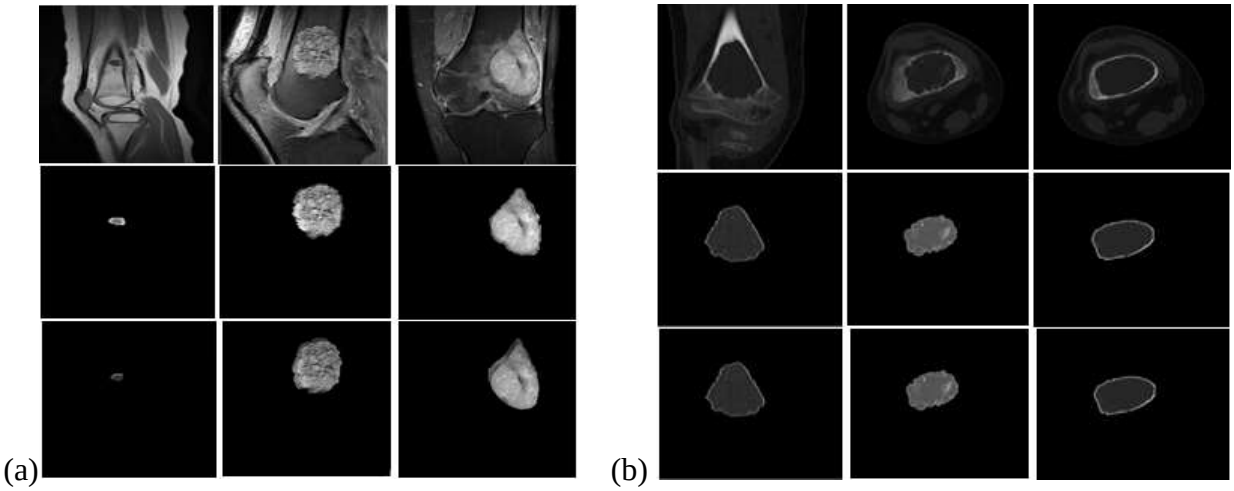

Figure 5. Represent the comparison between the original images in the first row, the second row extracted abnormal regions in grey by K-Means algorithm and the third row represent the extracted abnormal regions in grey by manual delineation.

Conclusion

In this work, clustering based segmentation method K-Means, was implemented to extract the bone tumour in MRI and CT scan images with different number of clusters. From the result. It was cleared that the proper number of clusters were (3, 5, 6, 6, 5, 3) for MRI and CT images respectively. As well as the results insure the high quality performance of the adopted segmentation method since the present relative differences with the radiologist delineation were ranged from (0.63 to 1.75) % for MRI images and for CT scan images were ranged from (0.34 to 1.51) %.

Acknowledgments

Authors wish to express their thanks to Dr. Sabah Jassim Mohammed who works in AL-Askndryh general hospital for his efforts in the delineation of the tumor regions in the adopted MRI and CT scan images.

References

[1]Balthazart J, Baillien M, Cornil CA, Ball GF. Preoptic aromatase modulates male sexual behavior: slow and fast mechanisms of action. Physiology & behavior. 2004 Nov 15;83(2):247-70.

[2] Taichman RS. Blood and bone: two tissues whose fates are intertwined to create the hematopoietic stem-cell niche. Blood. 2005 Apr 1;105(7):2631-9.
[3] Mistry K, Dargad S, Saluja A. Rough Fuzzy Technique for Giant Cell Tumor Detection. InInternational Conference on Communication, Networks and Computing 2018 Mar 22 (pp. 340-350). Springer, Singapore.
[4] Abdel-Maksoud E, Elmogy M, Al-Awadi R. Brain tumor segmentation based on a hybrid clustering technique. Egyptian Informatics Journal. 2015 Mar 1;16(1):71-81.
[5] Mistry KD, Talati BJ. Integrated approach for bone tumor detection from mri scan imagery. In2016 International Conference on Signal and Information Processing (IConSIP) 2016 Oct 6 (pp. 1-5). IEEE.
[6] Machado D, Giraldi G, Novotny A, Marques R, Conci A. Topological derivative applied to automatic segmentation of frontal breast thermograms. InWorkshop de Visao Computacional, Rio de Janeiro 2013 (Vol. 350).
[7] Brenner DJ, Hall EJ. Computed tomography—an increasing source of radiation exposure. New England Journal of Medicine. 2007 Nov 29;357(22):2277-84.
[8] Woertler K. Benign bone tumors and tumor-like lesions: value of cross-sectional imaging. European radiology. 2003 Aug 1;13(8):1820-35.
[9] Nelson CA. Incidental findings in magnetic resonance imaging (MRI) brain research. The Journal of Law, Medicine & Ethics. 2008 Jun;36(2):315-9.
[10] Chen CW, Luo J, Parker KJ. Image segmentation via adaptive K-mean clustering and knowledge-based morphological operations with biomedical applications. IEEE transactions on image processing. 1998 Dec;7(12):1673-83.
[11] Mingoti SA, Lima JO. Comparing SOM neural network with Fuzzy c-means, K-means and traditional hierarchical clustering algorithms. European journal of operational research. 2006 Nov 1;174(3):1742-59.
[12] Pal NR, Pal K, Keller JM, Bezdek JC. A possibilistic fuzzy c-means clustering algorithm. IEEE transactions on fuzzy systems. 2005 Aug 8;13(4):517-30.
[13] Mignotte M. Segmentation by fusion of histogram-based $ k $-means clusters in different color spaces. IEEE Transactions on image processing. 2008 Mar 31;17(5):780-7.
[14] Avula M, Lakkakula NP, Raja MP. Bone cancer detection from mri scan imagery using mean pixel intensity. In2014 8th Asia Modelling Symposium 2014 Sep 23 (pp. 141-146). IEEE.
[15] Abdoon RS, Abood L, Ali S. Adaptive Techniques for Brain Tumor Detection in MRI. LAP LAMBERT Academic Publishing; 2015.
[16] Sinthia P, Sujatha K. A novel approach to detect bone cancer using k-means clustering algorithm and edge detection method. Asian Research Publishing Network, ARPN Journal of Engineering and Applied Sciences. 2016 Jul;11(13):8002-7.
[17] Abdoon RS, Khudair OS. Implementing Segmentation Techniques to Isolate Brain Tumors in CT Scan and MRI Images for Different Orientations and Modalities. Journal of Advanced Microscopy Research. 2017 Sep 1;12(2):116-29.

[18] Ng HP, Ong SH, Foong KW, Goh PS, Nowinski WL. Medical image segmentation using k-means clustering and improved watershed algorithm. In2006 IEEE southwest symposium on image analysis and interpretation 2006 Mar 26 (pp. 61-65). IEEE.
[19] Juang LH, Wu MN. MRI brain lesion image detection based on color-converted K-means clustering segmentation. Measurement. 2010 Aug 1;43(7):941-9.
[20] Malathi R, AR DN. Brain tumor detection and identification using K-Means clustering technique. InProceedings of the UGC Sponsored National Conference on Advanced Networking and Applications 2015 Mar 27.
[21] Dhanachandra N, Manglem K, Chanu YJ. Image segmentation using K-means clustering algorithm and subtractive clustering algorithm. Procedia Computer Science. 2015 Jan 1;54:764-71.
[22] Kapur T, Grimson WE, Wells III WM, Kikinis R. Segmentation of brain tissue from magnetic resonance images. Medical image analysis. 1996 Jun 1;1(2):109-27.
[23] Bezdek JC, Hall LO, Clarke L. Review of MR image segmentation techniques using pattern recognition. Medical physics. 1993 Jul;20(4):1033-48.
[24] Klingler JW, Vaughan CL, Fraker TD, Andrews LT. Segmentation of echocardiographic images using mathematical morphology. IEEE Transactions on Biomedical Engineering. 1988 Nov;35(11):925-34.
[25] Maragos P, Schafer R. Morphological filters--Part I: Their set-theoretic analysis and relations to linear shift-invariant filters. IEEE Transactions on Acoustics, Speech, and Signal Processing. 1987 Aug;35(8):1153-69.
[26] Johnson C, Johnson RC. Cognizers: Neural networks and machines that think.
.

Investigate the Structural and Optical Properties of Nickel Phthalocyanine (NiPc)Thin Films Prepared by Chemical Spray Pyrolysis Method .

Sura N Tarrad[1] , Saleem A Hussain[2] , Falah H Al-asady[3]
suranoaman@gmail.com ,Saleem.hussain@qu.edu.iq ,

Drfh24@yahoo.com
1Department of Physics ,College of Science , University of Thi-Qar , Thi-Qar,Iraq.
2Department of Physics , College of Education ,University of Al-Qadisiyah, ..Diwaniyah ,Iraq
3Department of Physics ,College of Science , University of Thi-Qar , Thi-Qar,Iraq

Abstract. The technique of the chemical spray pyrolysis has been employed to deposit Nickel Phthalocyanine (NiPc) on different substrate types at temperatures 150 ^{o}C to investigate their structural, Scanning Electron Micrographs, X-ray diffractograms and optical properties. The results of X-ray diffraction show that structure of the powder is polycrystalline with monoclinic structure, and the results of XRD for a thin film of NiPc shows polycrystalline with a fairly weak degree of crystallization, SEM revealed that the surface of the film is usually homogeneous, the roughness of NiPc films was evaluated by AFM technique and the results showed that the grain size increases with increasing of concentration. The optical measurement using UV-Visible Spectra showed that the NiPc thin films have an optical constant like the absorption coefficient and have a direct energy gap for all samples.
Key words: Organic semiconductor , Nickel Phthalocyanines , structural and optical properties.

1. Introduction

In 1907, Phthalocyanines was discovered and used as a product in preparation of benzene derivations (ortho disubstituted), it characterized by electron delocalization and high planarity [1]. Nickel Phthalocyanine is semiconductor organic compounds used as an optoelectronic device as thin films. Modules of the thin-film are cheap compounds that have low energy, low costs, and low capital costs. Thin-film technologies are being developed as a means to substantially reduce the cost of electronic systems. The thin films have a future due to there is no energy-needed hardware parts in it. The technology of the memory depended on thin-film electronics for manufacturer PC, servers, mobile phones and digital cameras [2]. In this research, thin-film Nickel Phthalocyanine (NiPc) was deposited using the CSP technique, structural and optical properties were studied.

2. Experimental Work

The Nickel phthalocyanine provided from (Aldrich Chemical-USA) dissolved in ethanol to form a solution at (10:1) concentration. Using of the chemical spray pyrolysis for the accumulation of NiPc thin film at several types such as micro-glass, silicon, and glass at the temperature (150) C and two bar as pressure and the period was twelve seconds, and the distance was (30) centimetre. The glass has (75x25x1.35) mm as dimensions while the micro-glass have (20x20x1) mm as dimensions to the preparation of the film by the chemical spray pyrolysis techniques. Results of the X-ray diffraction are confirmed for thin films coated by radiation of Cu Kα of at wavelength 1.54059Å.

the previously prepared aqueous solutions are atomized by a special nozzle glass sprayer at heated which are fixed on thermostatic controlled hot plate heater. An air gas is used as a carrier gas and the spray is atomized via an air compressor. The substrate temperature was maintained to be 150±10 oC during spraying to deposition of the thin films at different levels, the distance between the substrate and spray nozzle was kept at 30 ±1 cm

3.Result &Discussion :

3.1 XRD measurements:

Phthalocyanines have two forms of crystal phases (α and β). The α-phase is getting from thin film or polycrystalline powder at (25) C. the β-phase is getting at thigh temperature [3]. Size of the crystal calculated by [4].

$$D = \frac{k\lambda}{\beta \cos\theta} \qquad (1)$$

D = crystal size average
k = relates and constant to the dimensionless shape factor
θ = the Bragg angle based on the peak
β = at the half of the maximum intensity (line broadening)

Value of the shape factor was (0.9), however, it different depended on crystallite. Powder and structures of the NiPc films are examined by the XRD system. The voltage was (30) kV, Cu (K_α) is the source of radiation, the current was (20) mA and the wavelength was 1.5405 Å. The range of the scanning angle was (10–80).

The interplaner distance d (hkl) for different planes was determined by using Bragg's law, grain size calculated from Scherrer equation eq. (1). The results compared with standard values for NiPc Powder. Figure (1) shows the results of X-ray diffraction of NiPc powder, the figure showed that the material is polycrystalline. Figure (2) and show NiPc thin films are made by deposition on the glass, Figure (3) show NiPc thin films prepared and deposited on micro and silicon substrate in figure (4). The results showed that the prepared and deposited thin films on glass and micro-glass substrates have a crystalline structure closer

to amorphous, or it is possible to say that the films have low crystallization for three conurbations, while the prepared film on the Silicon wafer substrate has a polycrystalline structure. The relation of substrate types and average crystal size is shown in Table (1).

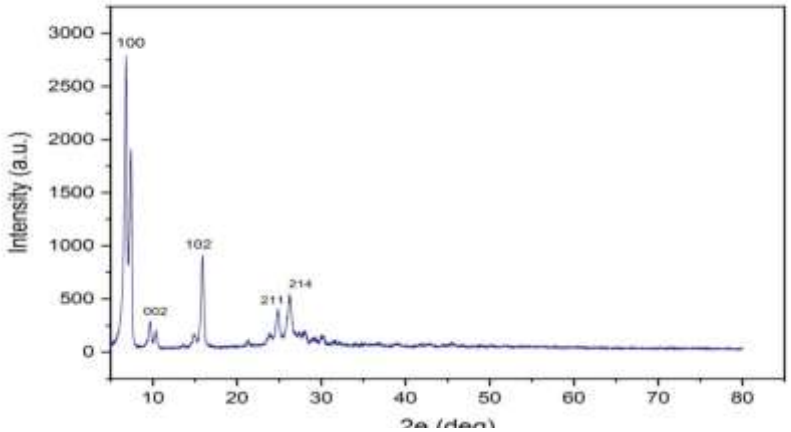

Figure1. XRD for NiPc powder

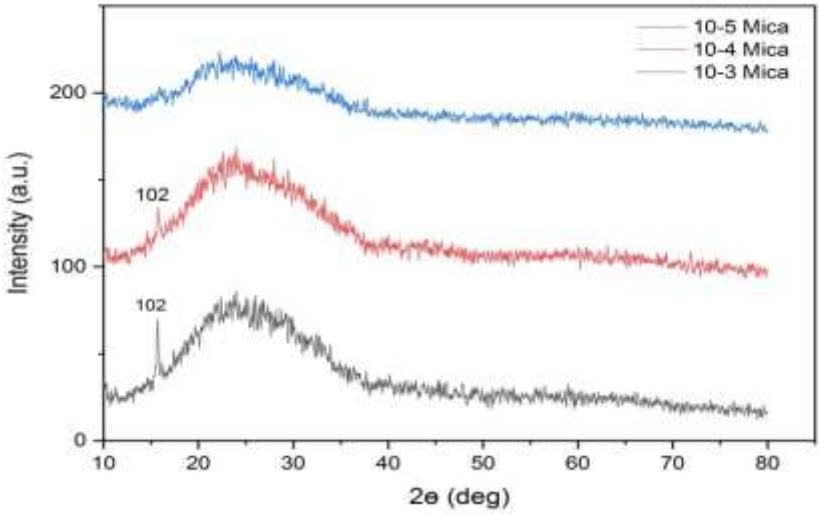

Figure 2. show X-ray diffraction for NiPc thin films prepared and deposited on Mica glass **.**

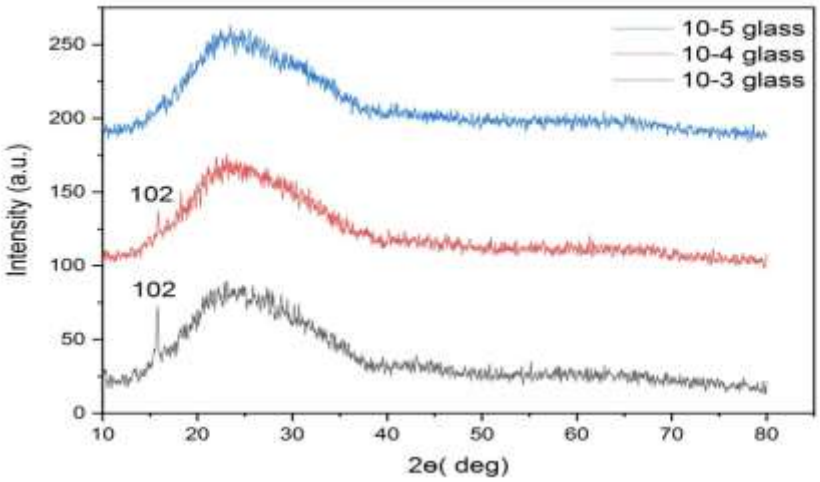

Figure 3. show X-ray diffraction for NiPc thin films prepared and deposited on glass**.**

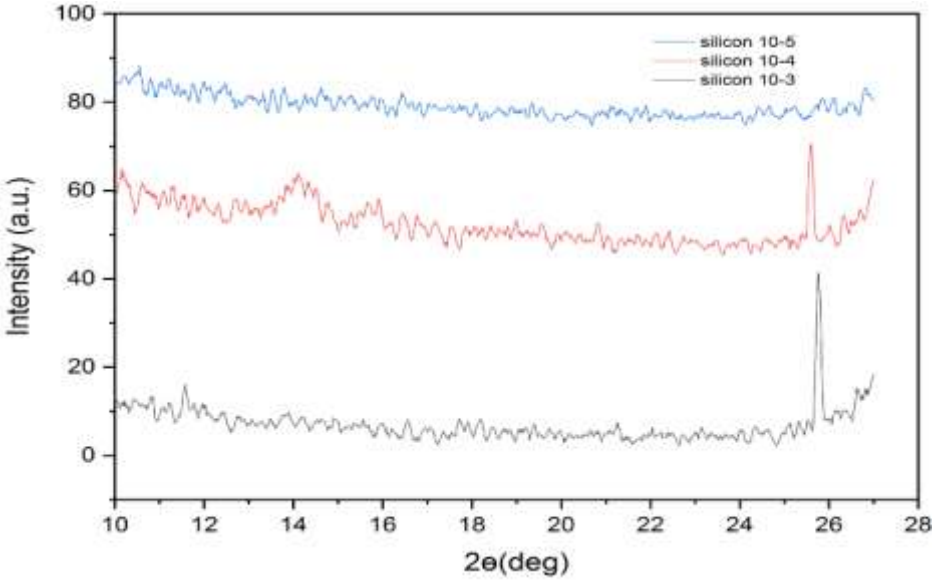

Figure 4. show X-ray diffraction for NiPc thin films prepared and deposited on silicon**.**

Table 1. Represents the results of X-ray diffraction of thin films NiPc .

Compound	substrate	2Ɵ (deg)	(hkl)	d(A^o) (Observed)	d(A^o) Standard	FWHM (deg)	Grain size (nm)
NiPc 10^{-3}M	Micro	15.673	102	5.6495	5.5700	0.6300	14. 69
	Glass	15.857	102	5.5842	5.5700	0.5300	15.53
	Silicon	25.803	211	3.4499	5.5700	0.0920	90.91
NiPc 10^{-4}M	Micro	15.832	102	5.5929	5.5700	0.4000	20.77
	Glass	15.902	102	5.5685	5.5700	0.5000	16.46
	Silicon	25.638	211	3.4717	5.5700	0.06250	133.78
NiPc 10^{-5}M	Micro	Amorphous					
	Glass	Amorphous					
	Silicon	Amorphous					

3.2 UV-visible measurements:

The UV-Vis spectrum finds the Nickel Phthalocyanine emerge from the orbits of the molecules on central elements ions [5]. The optical absorption spectrum is very necessary for solar cells fabrication with different thickness of Nickel Phthalocyanine as Figure (4).

Q-band and Soret bands are shown in electronic transitions in the UV-Vis. The Q-band was showed (540-700) nanometres due to $\pi-\pi*$ transition from highest orbital (occupied) to the lowest orbital (unoccupied) of the phthalocyanine. The peak (601) nanometres of $\pi - \pi*$ transition of phthalocyanine where the shoulder peak with low absorption was (670) nanometres increase for monomer part for the second $\pi - \pi*$ transition [6]and[2].

The absorption spectrum depends largely on the amount of energy of the levels, which in turn are related to the crystalline and chemical composition of the substance absorption was measured as a function of wavelengths (300-1100) nm. It is noted that absorption increases when concentration increases[7]was found that there was consistent with the international card and published research and it was at a rate of value equal to (a_o = 3.792 Å, co = 16.34 Å). The absorption spectrum was measured depending on the wavelength. By the study of the absorbance spectrum, we can find many optical constants. The measurements were made at the wavelength range (300-1100) nm for all (CuS) thin film. The results of the UV-VIS measurements are shown in figure (4) which represents the change of the absorbance spectrum of the wavelength. The figure showed that the absorbance would increase with an increase in the number of pulses and this leads to an increase in thickness. In another means, the incident photon can stimulate the electron and transfer to the conduction come from the valence because the photon energy is more than the semiconductor energy gap, therefore, the absorbance increases with increasing wavelength and that similar to the previous studies [8]and [9]**.**

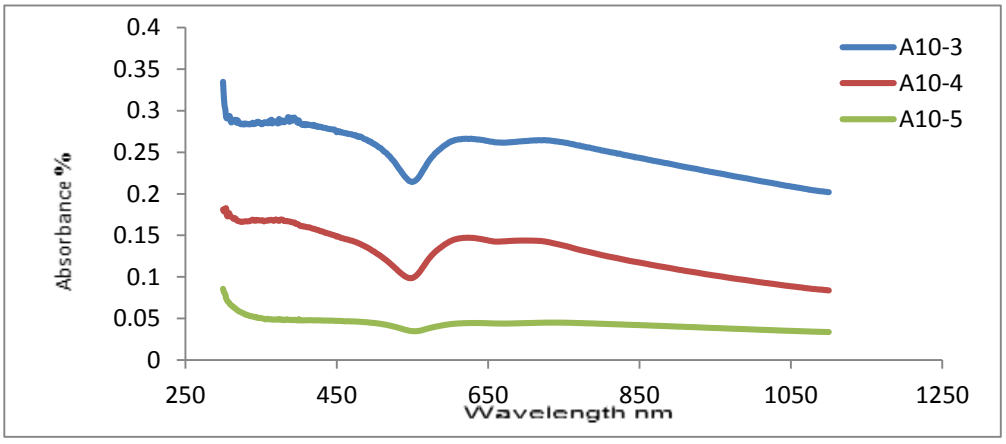

Figure 5. shows The absorption spectrum for (NiPc)

Dependence of wavelength absorption coefficient of thin films deposited at different concentrations. Absorption coefficient was calculated using equation : [23]

$$\alpha = 2.303 \frac{A}{t} \qquad (2)$$

A = average of the absorbance
t = thickness of the thin [10]

The variations in absorption coefficient with wavelengths variations at different molar concentration are shown in figure (6), we can see that the high value of absorption coefficient (up to 104 cm^{-1}) that represent high chance to direct transition due to traps inside energy gap, and these traps decreasing with increasing of concentrations [11]

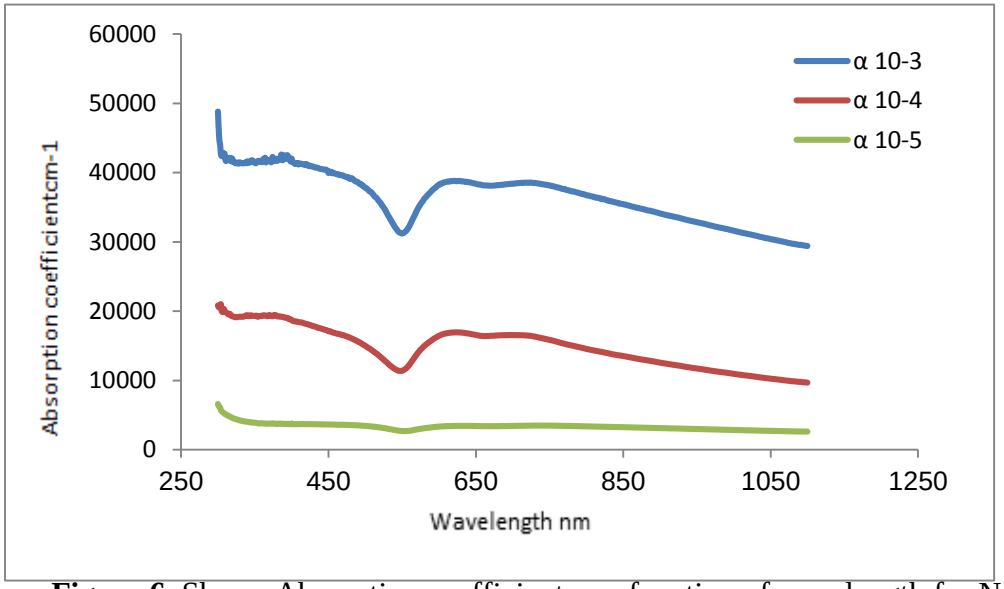

Figure 6. Shows Absorption coefficient as a function of wavelength for NiPc .

Value of the optical energy gap of NiPc thin films determine by Tauc equation for determining the optical energy gap by the plotting the relations of $(\alpha hv)^2$ versus photon energy and establishment of the optimum linear as followed formula $[(\alpha hv)^2 = 0]$ as Figure (7). The optical energy gap become high with increasing concentration as Table (2) due to decreasing of the defect states near the bands[8]and[9].

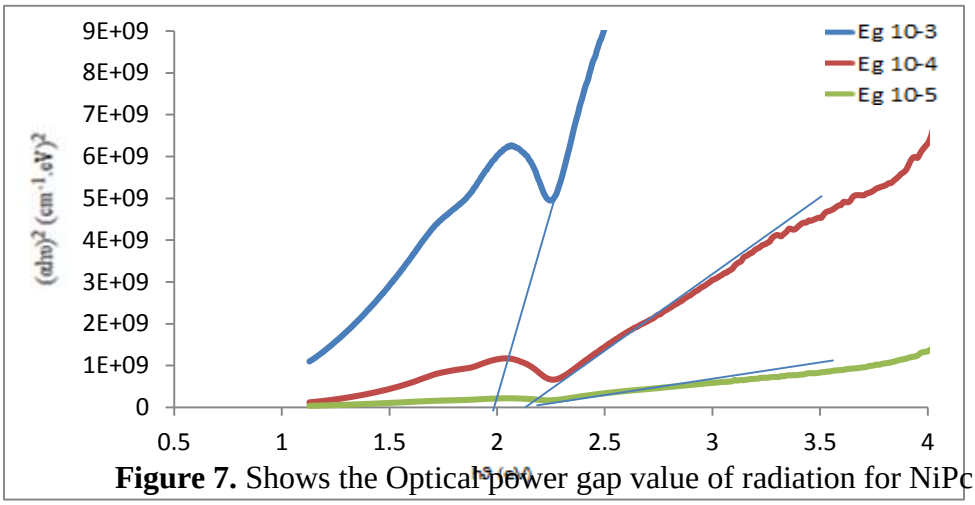

Figure 7. Shows the Optical power gap value of radiation for NiPc thin films .

Table 2. The value of the optical energy gap for different molar concentration

Sample		E_g (eV)
NiPc 10^{-3}M	eV	2
NiPc 10^{-4}M	eV	2.2
NiPc 10^{-5}M	eV	2.4

3.3 Scan Electronic Microscope(Surface Morphology)

Analysis of SEM is active sufficient tool that applied for focusing electrons beam for formed high resolution, complex images of the surface of the sample. This subject is very interest in the evaluation of

SEM. The results of NiPc thin films show that the crystallized metal, precipitated on glass substrates was consistent and XRD patterns produce the results. Analysis of crystal morphology from Figure (8) illustrates this. It forms a penile-like morphology of varying lengths that increases with increasing concentration. The penile shape and elongated is due to the interaction of the molecules leading to produce stacked layers of the Pc [12].

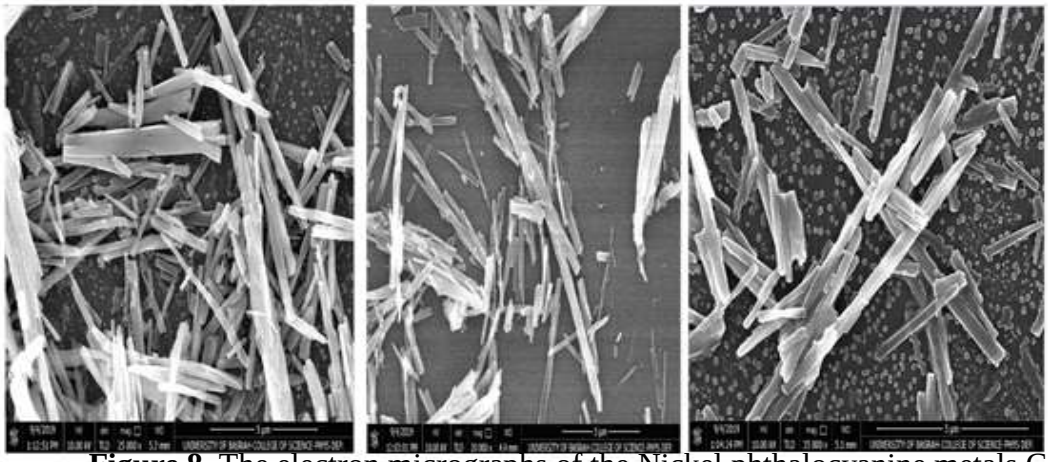

Figure 8. The electron micrographs of the Nickel phthalocyanine metals Concentrations a. 10^{-3}M , b. 10^{-4}M ,c. 10^{-5}M.

3.4 Atomic Force microscope (AFM)

To study the topography of film surfaces and the effect of changing the proportions of materials involved in film composition. The surface morphology of NiPc thin films was determined by Atomic Force Microscope, average roughness was tabulated in Table (3) which shows the roughness increase with Concentrations increase.

Table 3. shows surface roughness and thin film (RMS) values

Compound	*Roughness Average (nm)*	*Root Mean Square (nm)*
NiPc:10^{-3}M	2.1	2.4
NiPc:10^{-4}M	2.78	3.34
NiPc:10^{-5}M	3.49	4.2

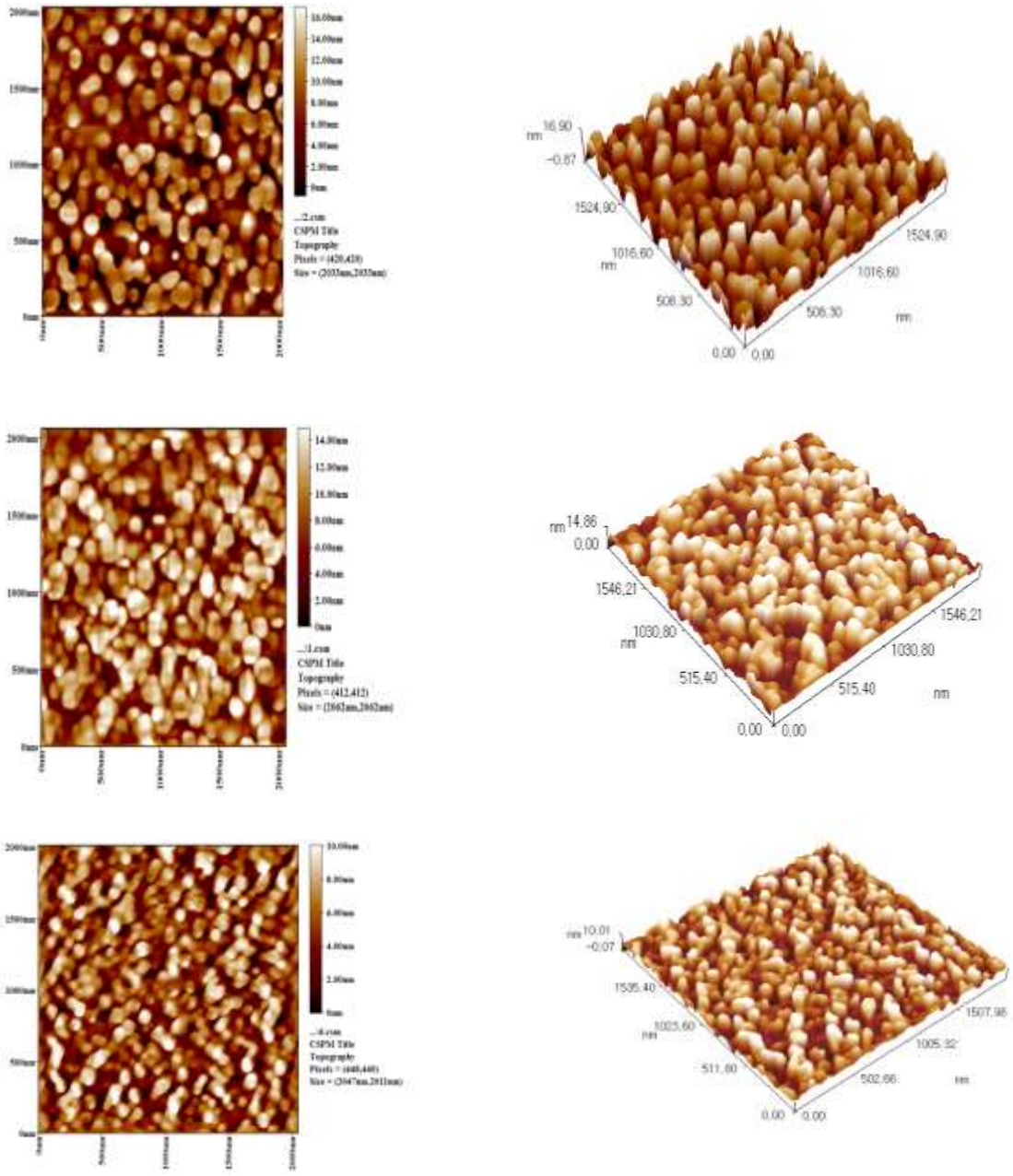

Figure 9. AFM images of NiPc thin films with different Concentrations.

4. Conclusions.

The properties of the prepared material depend on the substrates, where the synthetics have a more amorphous composition on the glass substrates ,micro glass and a polycrystalline composition on the silicon substrates. It was also found that the material with properties depends largely on the molar concentration of the prepared material. The energy gap changes markedly as concentration changes **.**

References

[1] K. M. Kadish, R. Guilard, and K. M. Smith, The Porphyrin Handbook: Phthalocyanines: Synthesis, vol. 15. 2012.

[2] A. B. P. Lever, "The Phthalocyanines," Adv. Inorg. Chem. Radiochem., vol. 7, no. C, pp. 27–114, 1965.

[3] of Thin Films Physics. .

[4] Charles_Kittel,_Introduction_to_Solid_State_Physical.2005 .

[5] T. Oppenlnder, Photochemical Purification of Water and Air. 2007.

[6] W. Chidawanyika, "PHOTOPHYSICOCHEMICAL STUDIES OF d 10 METALLOPHTHALOCYANINES AND THEIR INTERACTION WITH NANOPARTICLES," Philosophy, no. January, 2010.

[7] J. P. Zhong et al., "Highly active Pt nanoparticles on nickel phthalocyanine functionalized graphene nanosheets for methanol electrooxidation," Electrochim. Acta, vol. 113, pp. 653–660, 2013.

[8] M. S. Fakir, Z. Ahmad, and K. Sulaiman, "Modification of optical band gap and surface morphology of NiTsPc thin films," Chinese Phys. Lett., vol. 29, no. 12, pp. 1–5, 2012.

[9] N. K. Abbas, A. F. Abdulameer, and A. H. Kadhum, "The structure and optical properties of organic semiconductor bulk hetrojunction blend (NiPcTs / Alq 3) thin films," vol. 15, no. 33, pp. 40–48, 2017.

[10] C. Wenzel, K. Wetzig, J. Thomas, M. Hecker, and W. Brückner, Thin Film Preparation and Characterization Technique. 2005.

[11] F. Ghani, J. Kristen, and H. Riegler, "Solubility properties of unsubstituted metal phthalocyanines in different types of solvents," J. Chem. Eng. Data, vol. 57, no. 2, pp. 439–449, 2012.

[12] Z. Cheng, N. Cui, S. Jiang, H. Zhang, L. Zhu, and D. Xia, "Microwave-Promoted Synthesis of Sulfonated Metallophthalocyanines and Aggregation in Different Solvents," Adv. Mater. Sci. Eng., vol. 2015, pp. 1–7, 2015.

Study the Structural and Optical Properties Pure Copper Sulfide (CuS) Films Prepared by Pulsed Laser Deposition (PLD)

Meriam K Chloob1, Saleem A Hussain1

mmkk909084@gmail.com , Saleem.hussain@qu.edu.iq
1Department of Physics , College of Education ,University of Al-Qadisiyah, Diwaniyah ,Iraq

Abstract. In this research, thin film copper sulfide (CuS) were prepared by the pulse laser deposition (PLD) on glass substrate with different thicknesses .The structural and optical properties of copper sulfide thin films were studied and the results of X-ray diffraction (XRD) were analysis. It was found that CuS films have a polycrystalline structure with hexagonal system. The optical properties of the CuS films were studied by measuring and calculating Transmittance and absorbance spectrum respectively within the wavelength range (300-1100) nm. The results of the absorbance spectrum showed that absorbance of the films increase with an increase in the number of pulses (increasing thickness) and that the type of the electronic transition are allowed direct type. The energy gap values between (2.2-2.9) eV, and the it decrease with an increasing of thickness.

Key words: copper sulfide , thin films , pulsed laser deposition

1.Introduction

The copper sulfide belongs to an important class of semiconducting compounds called Chalcogenides. It is formed by the interaction of one of the transition metals with one of the sixth group elements in the periodic table such as sulfur or selenium, and these compounds have received great attention because of their great diversity in its various characteristics and the high ability to control on these characteristics [1]. As with most Chalcogenide compounds, CuxS have many phases, depending on the copper-sulfur ratio in the compound , CuxS at room temperature has five known stable phases , Chalcocite phase (Cu2S), Djurleite phase, Digenite phase, Anillite phase, and Covellite phase [2].In nature, it is found as a metal form and Calcite (Cu2S) and Cusylite (CuS) are the most common. The calcite is crystallized as an orthopedic (Orthorhombic) form with a density of 5.5-5.8 (g/cm3), and it has a light grey color on the newly cut surface, but it rusts to black after exposure to the atmosphere. It is found in secondary deposits that originate in areas rich in sulfide deposits. This mineral is used as an important source for the copper. While, the Covelite (CuS) crystallized in a hexagonal form as masses or thin layers, or grains speeded scattered on the copper minerals with a density of (4.6-4.76) g/cm^3. It has a metallic luster and a blue-violet color. The Covilite is one of the uncommon minerals, and is found in similar areas of the Calcite mineral and is not a major source of copper [3].

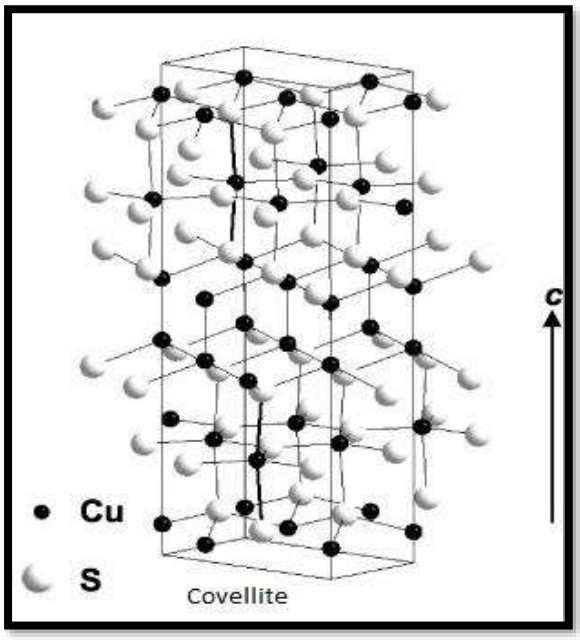

Figure1. The crystal structure of the CuS phase [1]

2.Experimental Work .

The pulsed laser deposition system consists of several parts arranged where they are used in preparing thin films deposited on different bases as Figure (1) that showed the pulsed laser deposition system is as follows (laser device, deposition chamber, rotary vacuum pump, vacuum pressure gauge, holder Target, digital thermometer). The laser device is the ND-YAG laser with the following specifications (Huafei Tongda Technology- DIAMOND-288 pattern EPLS).The laser energy (100-2000)mJ, the frequency (1-6)Hz., the wavelength(λ) (532 ,1064)nm ,the pulse duration 10 ns cooling method: The presence of an inner girdle that replaces hot water with cold water[4].The thin-film deposition of the CuS according to the value of (x) that was performed inside the vacuum pump chamber in the laser system (Nd-YAG pulse laser) under vacuum pump .The process of precipitation thin film (10-3 mbar) included as in the following steps:

- The interaction of the pulsed beam laser beam with the target (disc)
- The formation and expansion of the plasma inside the deposition chamber towards the glass slide that is caused by lasers.

- Thin film precipitation on the glass slide at temperature at (275◦C) at a vacuum pump pressure of (10-3) mbar, the laser energy was (600) mj, the frequency (6Hz) where the incident laser beam is made at an angle (45˚) with the target surface and the slide is fixed (10 cm) from the target.

The thickness of the thin films was measured using the Michelson method of optical interference, and this method is based on the interference of the rays reflected from the surface of the thin layer and the substrate on which the deposition was placed, the He-Ne laser was used with a wavelength (632.8 nm) and at a angle of incidence of 45º.

Figure2. Pulsed Laser Deposition System (PLD).

3.Result &Discussion :

The X-ray diffraction results for the copper sulfide films prepared by the pulsed laser precipitation method showed that the films were of a polycrystalline structure and that the lattices of this structure have a hexagonal system and that the preferred direction of growth was toward (100). Figure (3) shows the diffraction of X-rays of the prepared films, and it is clear that the positions of the peaks corresponding to the reflections at the following angles; for the prepared film with a number of pulses equal to 50 pulses at the angle (2Θ= 27.2871º) and the prepared film with a number of pulses equal to 100 pulses, the reflections corresponding the angles (2Θ=16.1320˚,20.7806˚, 24.7116˚, 27.2847˚, 33.1087˚) , while for the film prepared with a number of pulses equal to 150 pulses, the reflections corresponding the angles (2Θ= 16.0940˚, 20.3219˚, 24.0728˚, 27.2538 ˚, 33.6642o). Comparing the results shown in Figure 3 and listed in Table (1) with the ICDD numbered (06-0464) it was found that the results are almost somewhat identical with the observation that the peaks appearing on the prepared membranes are clearly demonstrated by increasing the number of pulses that mean increasing The thickness of the prepared films, which indicates that the degree of crystallization

of the prepared films increases with the increase in the thickness of the films. This result is consistent with the published research[5].

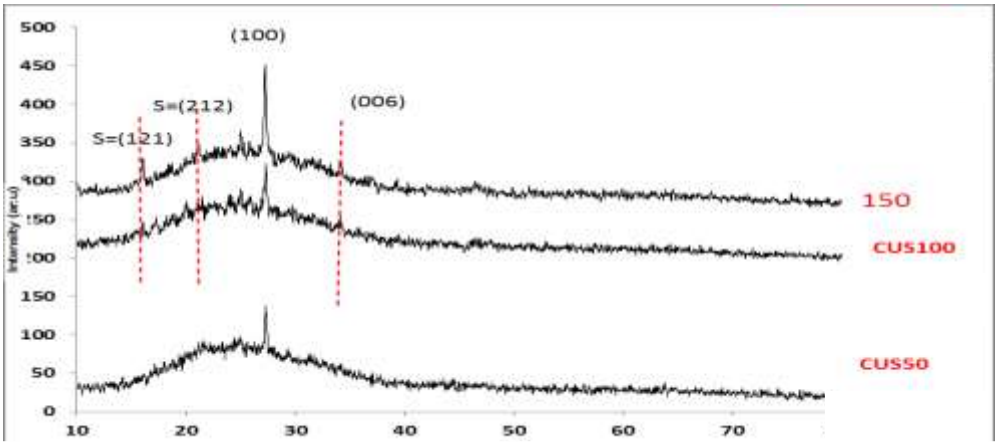

Figure 3. X-ray diffraction spectrum for pure CuS films.

Table 1. Results of XRD of CuS Thin Films Prepared by PLD.

Sample	2θ (Deg.)	d_{hkl} Exp.(Å)	d_{hkl} Std.(Å)	FWHM (Deg.)	C.S(nm)	hkl	Phase	card No.
CuS 50 Pulse	27.2871	3.2656	3.2850	0.2400	34.0506	(100)	Hexagonal	**00-006-0464**
CuS 100 Pulse	16.1320	5.4898	5.3400	0.2000	40.1052	(121)	Orthorhobic	**00-042-1278**
	20.7806	4.2710	4.5290	0.1200	67.2837	(212)	Orthorhombic	**00-042-1278**
	24.7116	3.5998	3.6600	0.0400	25.0150	(125)	Orthorhombic	**00-042-1278**
	27.2847	3.2659	3.2850	0.3250	25.1449	(100)	Hexgonal	**00-006-0464**
	33.1087	2.6265	2.7240	0.3800	21.8022	(006)	Hexagonal	**00-006-0464**

	16.0940	5.5027	5.3400	0.2840	28.2418	(121)	Orthorhombic	**00-042-1278**
	20.3219	4.3664	4.5290	0.0800	100.8524	(212)	Orthorhombic	**00-042-1278**
CuS 150 Pulse	24.0728	3.6939	3.6600	0.1600	49.6674	(125)	Orthorhombic	**00-042-1278**
	27.2538	3.2695	3.2850	0.2667	30.6395	(100)	Hexagonal	**00-006-0464**
	33.6642	2.6601	2.7240	0.0300	276.5627	(006)	Hexagonal	**00-006-0464**

It was found from the calculated values that the average grain size of the crystals decreases with the increase in the thickness of the prepared thin films, and this result was in agreement with Research No. [7] and did not agree with Research No. [6]. Lattice constants (ao) and (co) were also calculated for all thin films prepared using the relationship of the hexagonal system ($\frac{1}{d_{hkl}{}^2} = \frac{4}{3}\left(\frac{h^2+hk+k^2}{a2}\right) + \frac{l^2}{c^2}$) and it was found that there was consistent with the international card and published research and it was at a rate of value equal to (a_o = 3.792 Å, co = 16.34 Å). The absorption spectrum was measured depending on the wavelength. by the study of the absorbance spectrum, we can find many optical constants. The measurements were made at the wavelength range (300-1100) nm for all (CuS) thin film. The results of the UV-VIS measurements are shown in the figure (4) which represents the change of the absorbance spectrum as a function of the wavelength. The figure showed that the absorbance would increase with an increase in the number of pulses and this leads to the increase in thickness. In another mean, the incident photon can stimulate the electron and transfer from the valence band to the conduction band because the energy of the incident photon is greater than the energy gap of the semiconductor, therefore, the absorbance increases with increasing wavelength and that similar to the previous studies [8] [9**].**

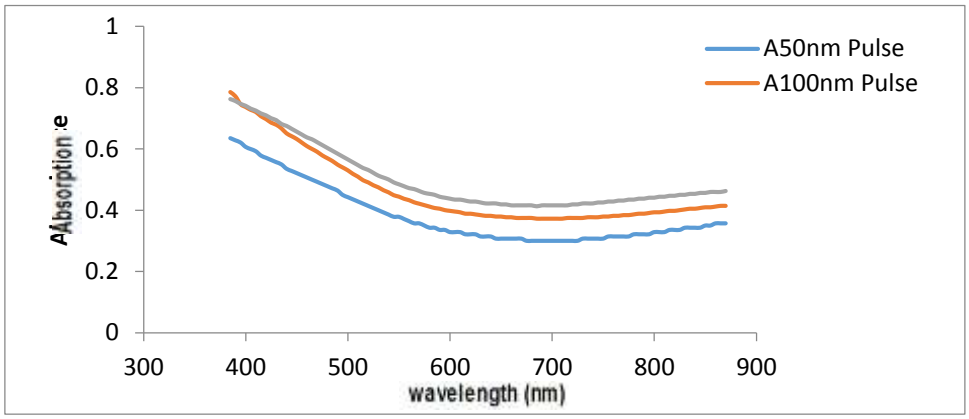

Figure 4. shows the change of absorption with increasing wavelength.

The transmition measurement was performed within the wavelength range (300-1100) nm of all (CuS) thin film. The results of the UV-VIS measurements showed that the transmition spectrum exhibits a completely different behavior of the absorbance spectrum as shown in Figure (5). The transmition of the thin film decreased with increasing the wavelength; In addition, these results showed that the CuS thin film possess a high transmition in the visible and infrared rays spectrum range area at the value (500-760) nm. This region is called the basic absorption edge, and this edge of absorption forms a curve, that confirms that the material is polycrystalline. The absorption and transmition are affected by several factors such as the type of material, thickness, wavelength radiation, surface nature and the crystal structure. The variation in the transmition of thin film (CuS) depends on the method and conditions for preparing the thin films and that agreement with [10].

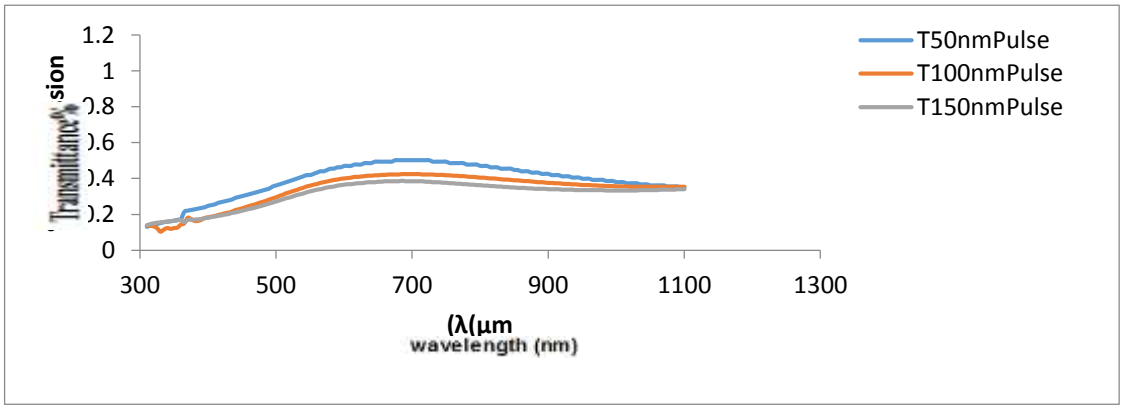

Figure 5. Shows change of the transmition spectrum with an increasing number of pulses .

The calculation of the energy gap is of great importance. By its value, we can determine the electro-optical application that appropriates for the use of the prepared thin film in it such as photodiodes, solar cells, detectors, etc. The value of the optical energy gap for direct transmission is calculated by drawing a relationship between $(\alpha h\upsilon)^2$ with the incident photon energy ($h\upsilon$) as in the figure(6). The intersection point gives a value of the energy gap to the direct possible transitions of the thin film. The figure (6) shows that the energy gap for the prepared thin films are decreasing from (2.9 eV - 2.2 eV) with increasing of the films thickness from (50 nm – 150 nm)

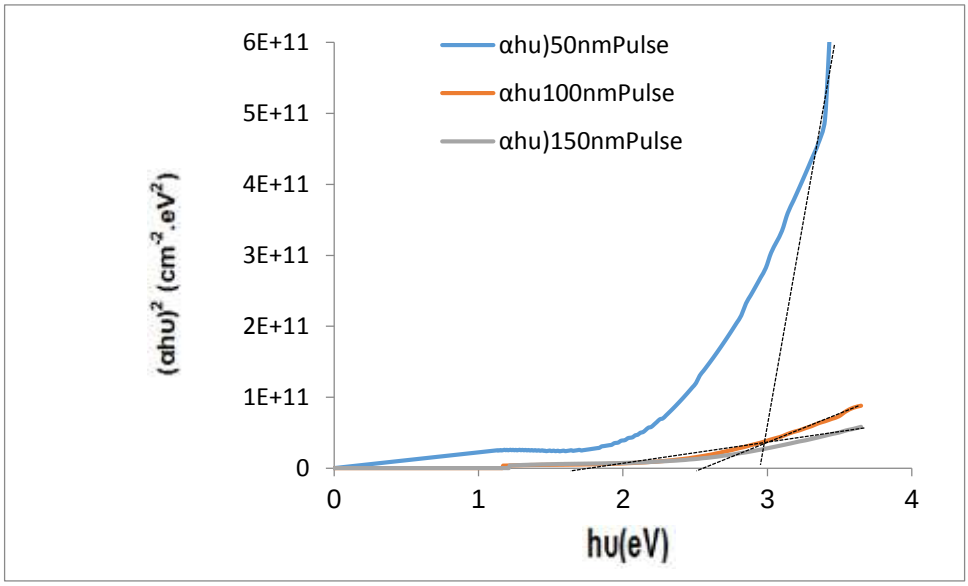

Figure 6. Shows the energy gap differences according to the wavelength.

4. Conclusions.

The copper sulfide (CuS) films deposited on glass bases prepared by the method of evaporation by a pulsed laser and with different PULSES where the results of X-ray diffraction showed that the films have a various crystalline structure of the hexagonal type. It was clear from the results of the optical measurements that the nature of the electronic films was direct transitions of the allowed type, and the value of the optical energy gap decreased with the increase of the number of pulses. That is decreases with increasing thickness, and the value of the energy gap was within the range (2.2ev-2.9ev) .

References

[1] Mustafa Amer Hassan, “The effect of annealing processes on some physical properties of the Cu2S film prepared by thermal decomposition method”, Master Thesis, University of Technology, Department of Applied Sciences (2006).

[2] M. T. S. Nair and P. K. Nair, "Chemical Bath Deposition of CuS Thin Films and their Prospective Large Area Applications", Semicond. Sci. Technol., Vol. 4, pp. (191-199), (1989).

[3] Dr. Mohamed Ezz El-Din, "Mineralogy", Cairo The Anglo-Egyptian Library, (1994).

[4] R.F.Bunshah " Hand Book of Deposition technologies for films and Coatings" Book ,2th ,(1994),William Andrew publishing 13Eston Avenue ,Norwich,NY13815.

[5] W. Daranfed, M. S. Aido, A. Hafdallah and H. Lekiket, "Substrate Temperature Influence on ZnS Thin Films Prepared by Ultrasonic Spray", Thin Solid Films, Vol. 518, pp. (1082-1084), (2009).

[6]M. Caglar, S. Ilcan and Y. Caglar, "Influence of Substrate Temperature on Structural and Electrical Properties of ZnO Films", J. Sci, Vol.7 No.2, pp. (153-159), (2006).

[7]A. Wei, J. Liu, M. Zhuan and Y. Zhao, "Preparation and Characterization of ZnS thin films prepared by chemical bath deposition", Mater. Sci. Semicond. Proc, Vol. 16, pp. (1478-1484), (2013).

[8] M. Adeliford, H. Eshghi and M. B. Mohagheghi, "Synthesis and Characterization of Nanostructure CuS-ZnS Binary Compound Thin Films Prepared by Spray Pyrolysis", Opt. Commun., Vol. 285, pp. (4400-4404), (2012).

[9] W. Daranfed, M. S. Aido, A. Hafdallah and H. Lekiket, "Substrate Temperature Influence on ZnS Thin Films Prepared by Ultrasonic Spray", Thin Solid Films, Vol. 518, pp. (1082-1084), (2009).

[10] T. K. Pathak, V. Kumar, L. P. purhit, H. C. Swart and R.E. Kroon, "Substrate dependent Structural, Optical and Electrical Properties of ZnS Thin Films Grown by Rf Sputtering", Physica E, Vol. 84, pp. (350-356), (2016).

Next Generation of High-Speed Optical Communications Networks Using OFDM Technology

Atta Takhum Jaber[1], Soudad S. Ahmed[2], and Shehab Ahmed Kadhim[3]

[1´2]Department of Physics, College of Science, University of Baghdad, Baghdad, Iraq.
[3] Ministry of Science & Technology.
toatt.711@gmail.com

Abstract. The usage of data transmission through Optical Fiber is highly preferred in every area where transferring of data is needed from one end to another. Moreover, nowadays the infrastructure of telecommunications is in good shape and size to handle data transmission through its optical fibers which have low attenuation and higher bandwidth. The seeking of data rate higher than 100Gbit/second and above has been increased to build it in urban and rural areas, and for long and short hauls. Consequently, the current goal is to propel this transmission system into the next appropriated level to avoid any decline of the optical infrastructure than its current capacity. To fulfill increased demand for bandwidth in Broadband services one of the most trusted technology is the Orthogonal Frequency Division Multiplexing (OFDM). The Orthogonal Frequency Division Multiplexing has been placed on-demand in optical communication, it is used in Long haul transmission Format in Direct and Coherent detection. OFDM has many features and abilities can boost the optical fiber performance by eliminating several limits of conventional Optical Fiber communication. OFDMA has polarization mode dispersion (PMD) and chromatic dispersion (CD) which are considered a big addition to the current systems. In addition to that, the easy correlation of the coherent optical OFDM with Wavelength Division Multiplexing (WDM) systems can further advantages in the transmission system such as super bandwidth, high spectral efficiency, and extra data rates. Furthermore, the WDM systems can improve data rate and capacity by using multiple wavelengths over a single fiber. This work aims to bring implementation and to perform a deep-dive study of higher data rates using Direct and Coherent Optical OFDM for long path transmissions. This research starts with a unique user and then extends to the add the OFDM - WDM system to get a data rate of 100 Gbps. Regarding the software portion, the Optisystem simulation tool was used for the design and implementation of the system. Moreover, the modulation type used is QAM for the OFDM signal, and I/Q modulation is deployed, while Coherent and Direct detection is used at the receiving portion. Q Factor, the bit error rate and eye diagram were discussed to study the System's Performance and Quality. This work found CD-OOFDM is the best system for next generation of optical. The work

compared WDM CD-OOFDM with SMF-DCF to DD and CD-OOFDM. In addition to that, it compared WDM CD-OOFDM with SMF-DCF to CD-OODFM with SMF. Therefore, the results showed that WDM CD-OOFDM with SMF-DCF achieved 25 Gbps for four channels of the WDM system at 120km channel, where the carrier frequencies were from 193.05THz to 193.2THz.

Keywords: DD-OOFDM, CD-OOFDM), Integration of CD-OOFDM with WDM for long haul high data rate transmission.

Introduction.

Optical and other digital communication systems play a large role in modern communications. They lead to include the sent signals as data on optical carriers or other digital communication systems. The forms used to include data in an optical communication system are similar to the types used in radio-frequency communication systems (RFS) with phase, amplitude, and data frequencies transmitted by the optical carrier [1].

OFDM is an encouraging technology that can help meet growing demand and benefit from bandwidth in Broadband services.

OFDM technology has gained a great role in optical communication systems, especially after proposing DD-OFDM and coherent detection-OFDM techniques OOFDM, was developed to satisfy the fast-growing need for higher bandwidths in broadband services. OFDM increased the average concentration in the visual correspondence network, particularly after it was set as a nice long communication segment in consistent and direct discovery. In addition, OFDM can overcome many visual limitations of optical fibers, for example, chromatic_dispersion (CD) and polarization_mode_dispersion (PMD). [2].

In addition, it is possible to combine OFDM systems with WDM systems, which can provide communication system with high band width, high spectral efficiency, and large data rate.

WDM systems have the ability to improve capacity and data-rate by posting many wave-lengths through single fiber.

The increasing demand for voice, messages, and video transmission services has led to manipulate high bandwidth and data rate [3,4].

Recently, there is a great effort in the field of research and development in various research centers to meet the increasing demand in transport networks, especially in 100 Gbps Ethernet and beyond. To increase the data rate, this frequency band must be expanded to enhance spectral efficiency.

Direct Detection -OOFDM

Below is an illustration of the Direct Detection (DD) -OFDM system as shown in Figure (1), which begins with a DD-OOFDM transmitter. The data is transmitted to the optical fiber, which in turn carries the data to the DDOFDM receiver. Figure (1) shows the system is used for transferring one bit stream over one communication channel using one sequence of DDOFDM symbols.

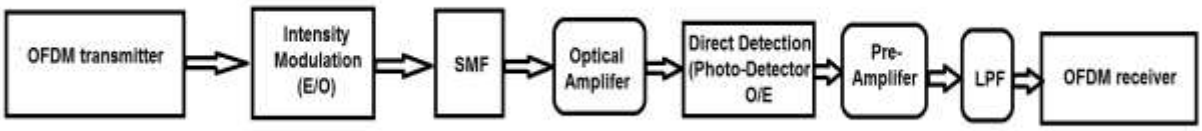

Fig. (1) DDOFDM Sequenced Diagram

The electric sign of OFDM is produced by the OFDM transmitter, where it is transferred from the electric field to the optical domain using the electric / optical converter (E / O), which also adjusts the intensity.

The optical-fiber can be used to send the resulting of optical-sign. The loss of fiber is compensated for by using an optical amplifier. On the other side of the system, specifically at the receiver, the sign is returned from the optical field to the electrode by means of an adapter that converts the signal from optic to electric (O per E); (photodiode).

The equation below represents the electrical signal received:

$$A_e(t) = |A_0(t)|^2 h_e(t) + w(t) \qquad 1.1$$

As; $A_e(t)$is the electrical signal in the receiver; the optical OFDM sign, $h_e(t)$ is the response of impulse; (impulse) of the electric field while the w (t) clarified the noise of the method.

After the conversion process, a decrease in the signal happens. Thus, the signal requires to be amplified again as it flits through a Low Pass Filter (L.P.F.). Then, will be sent to the receiver of OFDM. In order to obtain the initial sign [5].

Coherent-Detection an Optical a OFDM a(CD-OOFDM)

The CD-OOFDM system is illustrated in Figure (2). It is noted that the CD-OOFDM system is comparable to the DD-OOFDM system and the difference between them is in the actual per imaginary (I per Q modulator) as well as the local-oscillator(L.O.).

A local optical oscillator is can be used with an optical-coherent system to create optic signs at certain wave lengths. With reference to the local-oscillator frequency, optical coherent-detection is split into two types:

homodyne detector as well as heterodyne detector [6]. The block diagram of a basic CD-OOFDM transmitter is shown in Figure (2).

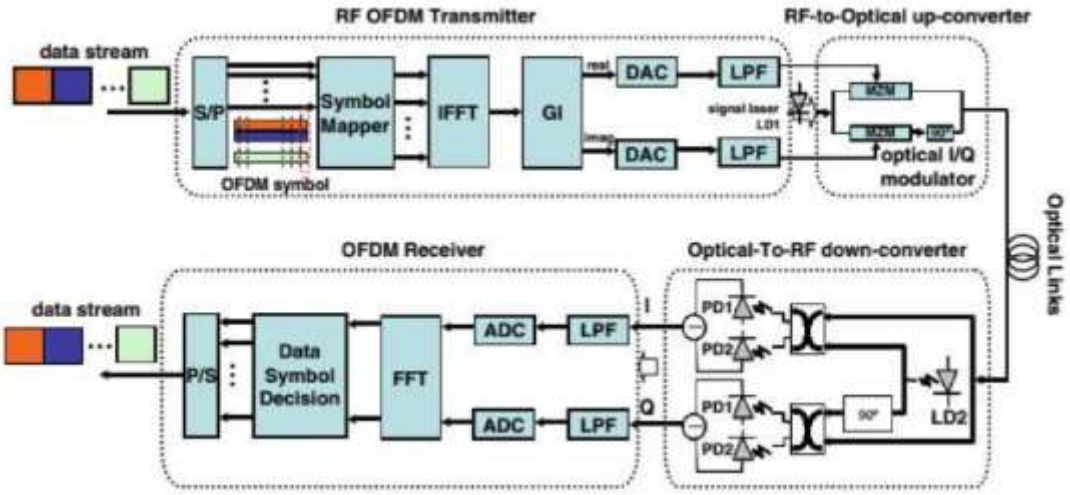

Fig. (2) CDO-OFDM Block Diagram

Heterodyne-detection

When the L.O. does not adapt the arriving sign within the photodiode as well as whenever the two signs are combined, a new frequency is created; the Intermediate-frequency (IF.), which represents the variation between the two-frequencies. This method reduces the noise caused by the heat and the test noise, that leads to the improvement of the Signal to noise ratio (S.N.R.) execution. Anywise, the source frequency tends to deviate with the passage of time. Hence, IF must be monitored continuously. The local oscillator should also be changed in order to maintain the stability of the IF [7].

Homodyne detection

The L.O. frequency is identical to the received sign. Among the other components is the (modulator of I per/ Q). The (I per Q) ingredients of the digital sign are transformed into an analog sign by the (D/A) converters on the transmitter. The switching unit (I per Q) composes of two MZM units raising the converts the complex OFDM. to the optical field [7,8]. The modulated sign can be formed as follows;

$$\boldsymbol{E(t) = x(t)\, exp^{j\,(W_{LD1}t + \emptyset_{LD1})}} \qquad \textbf{1.2}$$

$\boldsymbol{x(t)}$ is the transmitted electrical sign, $\boldsymbol{\emptyset_{LD1}}$ and $\boldsymbol{W_{LD1}}$ are the phase and angular frequencies of the laserdiode respectively. The sign at the recipient is as follows;

$$E_r(t) = E(t) \otimes h(t) + w(t) \qquad 1.3$$

$h(t)$ represents the signal carrier response whereas the w(t) denotes the noise of the channel. The arriving sign is discovered by a couple of coherent detectors and optical (90˚) hybrid to execute (I per Q) performance. The conversion is from optic to electric.

Any detection device composed of two couplers and photodiode -type 4-digit optical outlets; The Four 90˚ Optical Hybrid Parts. It is given as follows;

$$\boldsymbol{E_1 = \frac{1}{\sqrt{2}}[\, E_s + E_{LD2}\,]}$$

$$\boldsymbol{E_2 = \frac{1}{\sqrt{2}}[\, E_s + E_{LD2}\,]} \qquad \boldsymbol{1.4}$$

$$\boldsymbol{E_3 = \frac{1}{\sqrt{2}}[\, E_s + E_{LD2}\,]}$$

$$\boldsymbol{E_4 = \frac{1}{\sqrt{2}}[\, E_s + E_{LD2}\,]}$$

Represents the signals , $\boldsymbol{E_s}$ is the incoming signal and $\boldsymbol{E_{LD2}}$ the signals of the local oscillator. On the other hand, the signal is restored The in-phase using two phase detection (PD1 and PD2) through which Photo-Current can be given in the following form;

$$\boldsymbol{I_1 = |E_1|^2 = \frac{1}{2}\{\, |E_s|^2 + |E_{LD2}|^2 + 2Re\{E_2 E_{LD2}\}\,\}}$$

$$\boldsymbol{I_2 = |E_2|^2 = \frac{1}{2}\{\, |E_s|^2 + |E_{LD2}|^2 + 2Re\{E_2 E_{LD2}\}\,\}}$$

$$\boldsymbol{|E_s|^2 = |E_r|^2 + |n_0|^2 + 2Re\{E_r n_0\}} \qquad \boldsymbol{1.5}$$

$$\boldsymbol{|E_{LD2}|^2 = |l_{LD2}(I + l_{rin}(t))}$$

$\boldsymbol{l_{LD2}}$ and $\boldsymbol{l_{rin}(t)}$ represent the relative intensity noise and average power of the laser-diode. Due to the stable detection, the in-phase ingredient of photo current will be as follows;

$$I_l = 2\mathrm{R}\ \mathrm{e}\ E_s\ E_{LD} \qquad 1.6$$

In the same way, the quadrature components can be derived from other photo detection devices as follows;

$$I_Q = 2\ \mathrm{I}\ \mathrm{m}\ E_s\ E_{LD} \qquad 1.7$$

From the equations (1.6) and (1.7) the complex photo-current

$$\tilde{\mathrm{I}}(t) = I_l\ (\mathrm{t}) + jI_Q\ (t) = 2\ E_s\ E_{LD} \qquad 1.8$$

After finalizing optical detecting, the sign is sent to the OFDM receiver to elicit the original sign [9].

Integration of CO-OFDM with WDM for long-haul-high-data-rate transmission

WDM is a significant factor. It is able to give more facilities and flexibles in system design and streamline network. WDM collects some of optical carrier signs in a SMF utilizing variation wave lengths or different laser light in optic OFDM. Using WDM assists to boost system capacity and provide a huge rise in the average of information transmitted through a single-fiber. When using different wave-lengths, each wave-length constitutes a discrete channel. WDM splits the optic spectrum into least channels, that are in turn used to send and collect information at the same time. Fig. (3) Constellation Diagram of 4QAM. Figure (3) addresses the four quadrants of the I/Q constellation diagram, as mentioned.

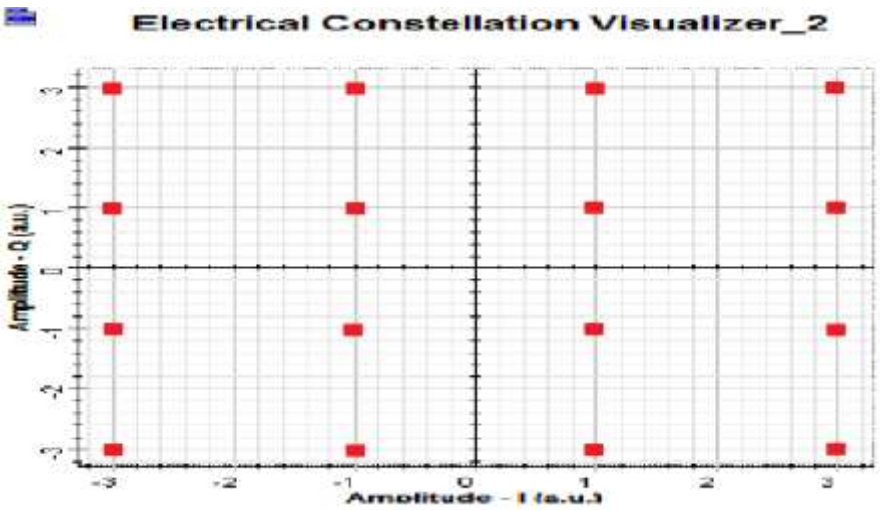

Fig. (3) Constellation Diagram

Designing the WDM CD-OOFDM System with SMF-DCF The CD-OOFDM Transmitter with a 120 KM length is shown in figure (4). The CD-OOFDM Transmitter is designed with P.R.B.S. Generator to create a bit series as it has been designed using 4QAM en-coder. The 4QAM sign is linked to include OFDM Modulator with the use of 512-Sub-carrier and 1024-FFT-Points. The resulting signal is sent from the OFDM to the optical (I per Q) Modulator, that composed of two Mach Zehnder modulators (MZM). The Optic Modulator modifies the sign from the electrical sign to visual sign. So as to acquire 100Gbs, there are four units of OFDM signals. The exception is the visual transmitter laser which is a wavelength that begins from 193.05THz to 193.2THz within a distance of 50GHz. The WDM composed of four channels to uphold the four bands of the Channel. Each signal of OFDM signals contains 25Gbps Bits-Rate that provides a total data-rate of 100.Gbps. Figure (4) shows the concept of RoF system Block-Diagram of WDM and CDOFDM System with SMF. -DCF of 120km.

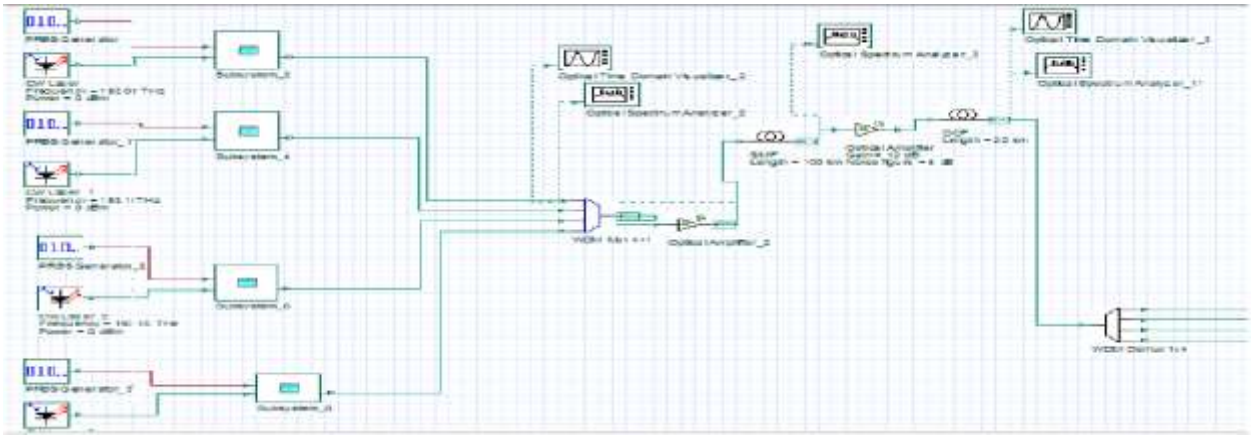

Fig. (4) Block-Diagram of WDM. CDOFDM. System with SMF. -DCF. of 120km

The output signs from the transmitter launch WDM De-multiplexing. The four different wavelengths are integrated into a single signal sent across the visual fiber. The resulting signal is sent from the WDM via the SMF-SMF system.

The Attenuation of SMF is 0.2dB / km. Whereas, The attenuation of DCF is 0.4dB / km. The Dispersion of SMF is 16(dB / km. nm) for 100km. The dispersion of SMF is 1600ps /nm. As a result, dispersion of SMF has to be compensated for 100km where long DCF is required with 20km length with dispersion -80 ps / (km. nm), which produces -1600ps / nm, which is negative. An optical amplifier is used with a power of 20dB to amplify the signal and compensate for what it has lost. The parameters to SMF and DCF are shown in table (1).

The optical signals received from the optical connection are detached into four-wave-lengths by WDM demultiplexer. Any wavelength is discover by its receiver. Four receivers are made to sustain the similar parameter unless the center-frequency of the receiver as well as the LO that has a frequency corresponding to the laserwave length of the transmitter. In addition to that any receiver is consisting of two balanced (C-detectors) devices with L.O. to make optic I per Q conversion to electrical and omit any noise. Moreover, each of these detectors composed of two couplers and two PIN photodetectors. Any of these PINS contains a dark current of 10nA. After detecting the sign, it is sent to OFDM-de modulator which in turn contains comparable parameters.

Table (1) SMF and DCF Parameters

Fiber type	Length	Attenuation	Dispersion	Slope	Effective Area	Nonlinear refractive index n_2
SMF	100km	0.2dB/km	16ps/km.nm	0.08ps/(nm².k)	80μm²	$2.6x10^{-20}$
DCF	20km	0.4dB/km	-80ps/nm.km	-0.45ps//(nm².k)	30 μm²	$2.6x10^{-20}$

Simulation and Result

The radio frequency spectrum (RF) of the I / Q component of CD-OOFDM WDM is located on the side of the transmitter as shown in Figure (5).

The RF-power is measured at approximately 40dB. The RF of the (I / Q) component of the CD-OOFDM WDM method is located on the side of the sender device as shown in Figure (6).

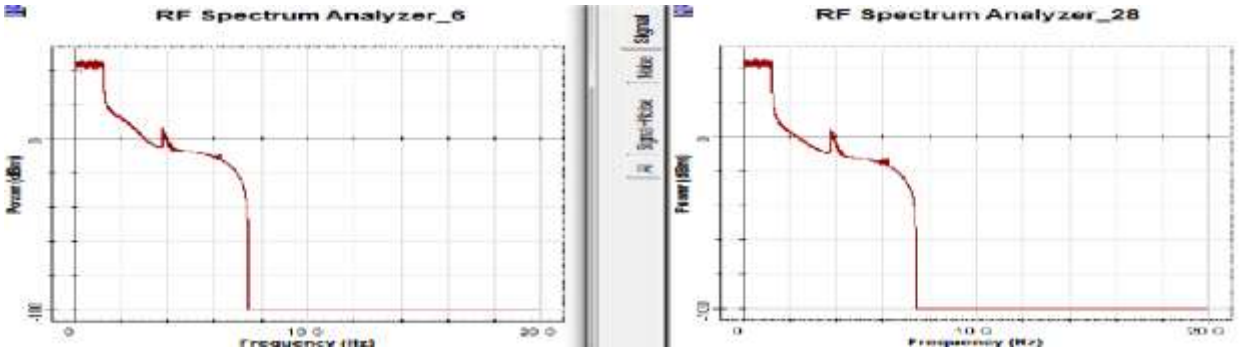

Fig. (5) RF-OFDM. Spectrum (I per Q) ingredient at the CDOFDM path

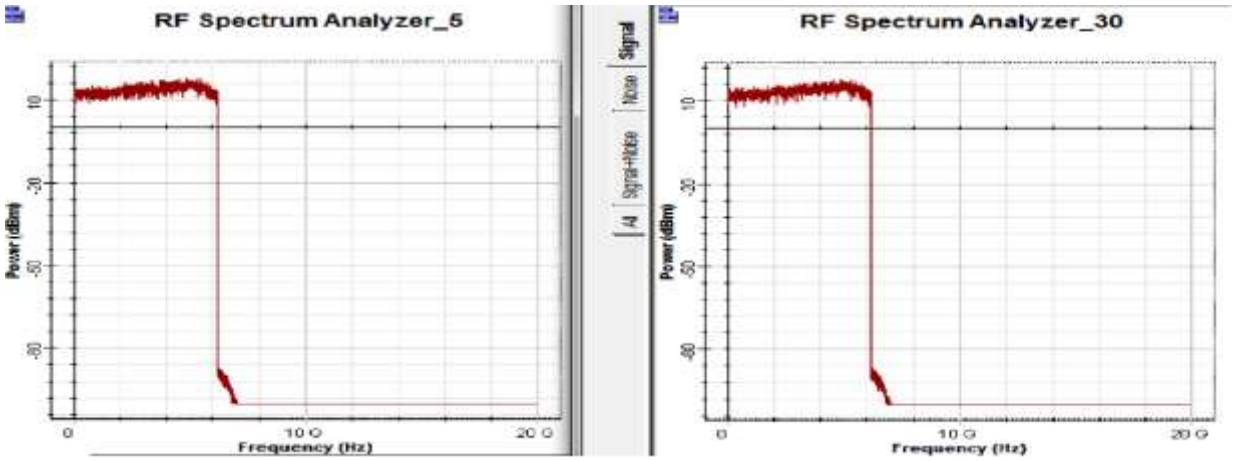

Fig. (6) RF-OFDM. Spectrum (I per Q) Component at the CDOFDM Receiver

It is noted that there is a decrease of the RF power to 20 dB when it is compared to the figure (7); Figure (8) shows the four OFDM spectra following the WDM system. The four WDM paths begin with 193.05THz and up to 193.2THz. The channel spacing is 50GHz.

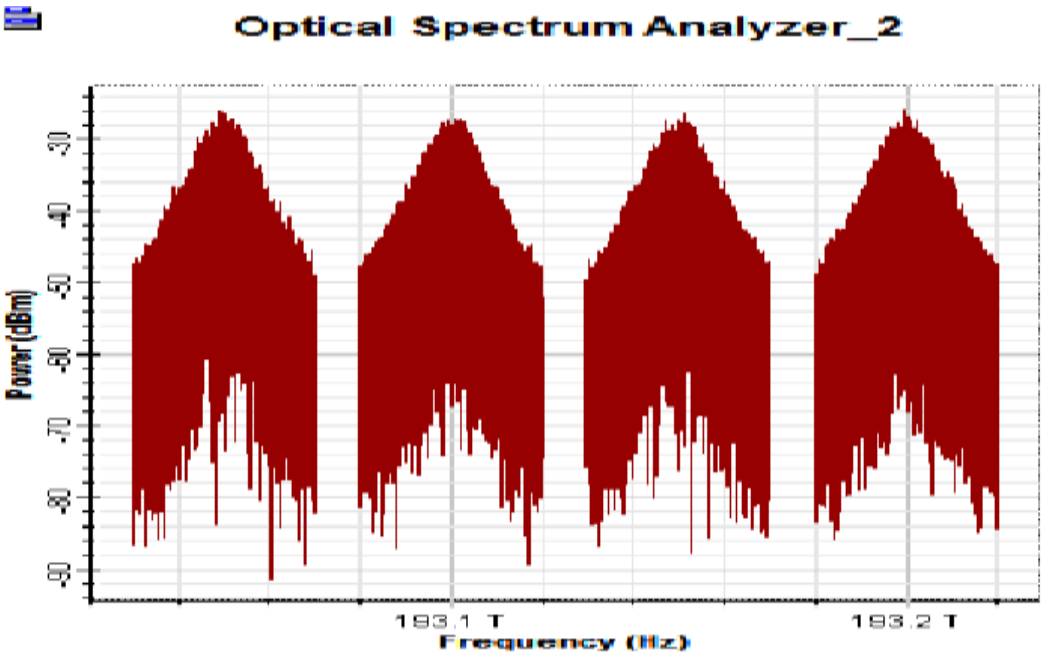

Fig. (7) 4OFDM Sign after the WDM Channels

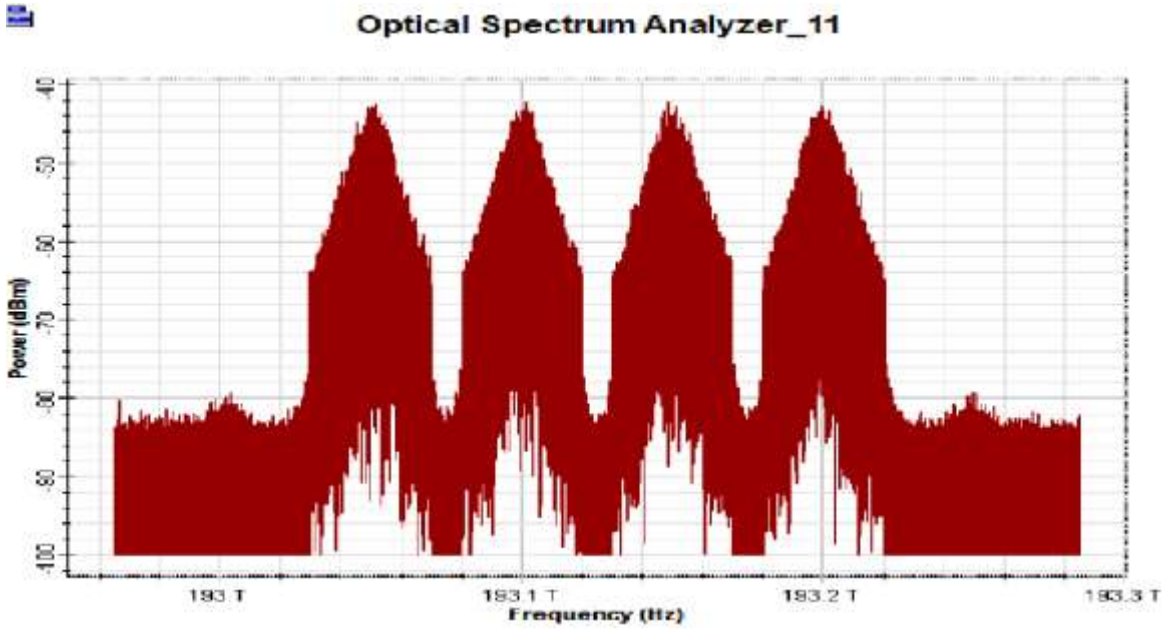

Fig. (8) 4OFDM Sign after SMF Optical-Link of 120(km)

Figure (9) shows the constellation-diagram of the 4QAM in the receiver after the SMF-DCF optical connection. In this diagram, the blue dots signify the sign. The green dots signify the noise. The sign is retrieved when the CD is removed from the SMF.

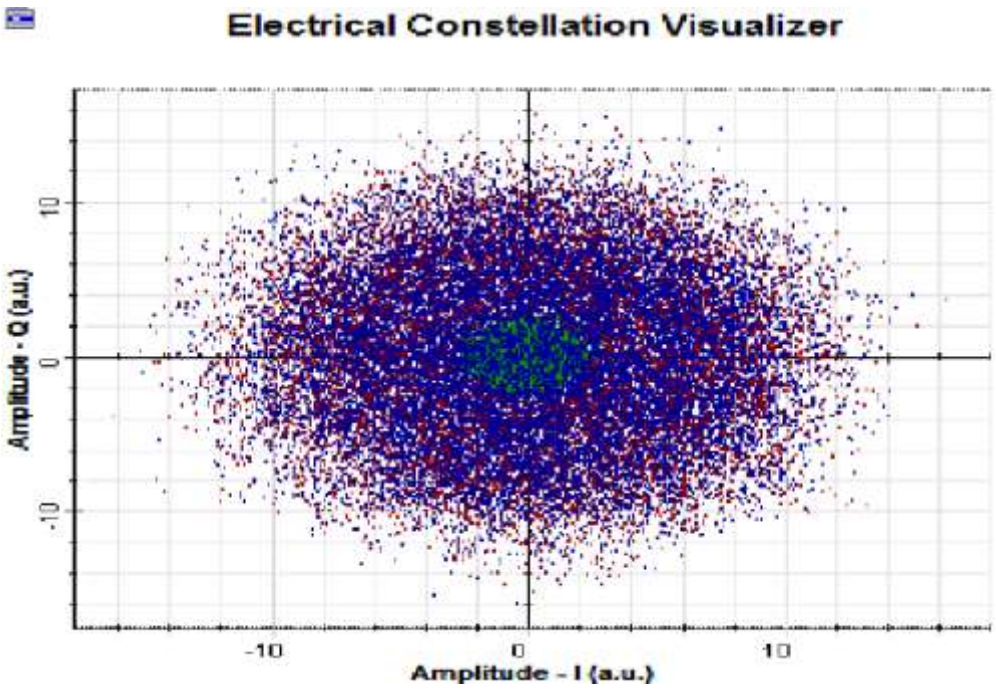

Fig. (9) The Constellation of 100 Gbps WDM CDOFDM System beyond 120 km

When design the completed, the Q-factor, bit-error-rate (BER), as well as eye-diagram are chosen in order to select and explore the system to identify the type of signal, shapes, and parameters are shown in figures (10), (11) and (12), respectively.

Fig. (10) BER for 120 km of Transmission Length of SMF-DCF Optical connection

Fig. (11) Q. Factor

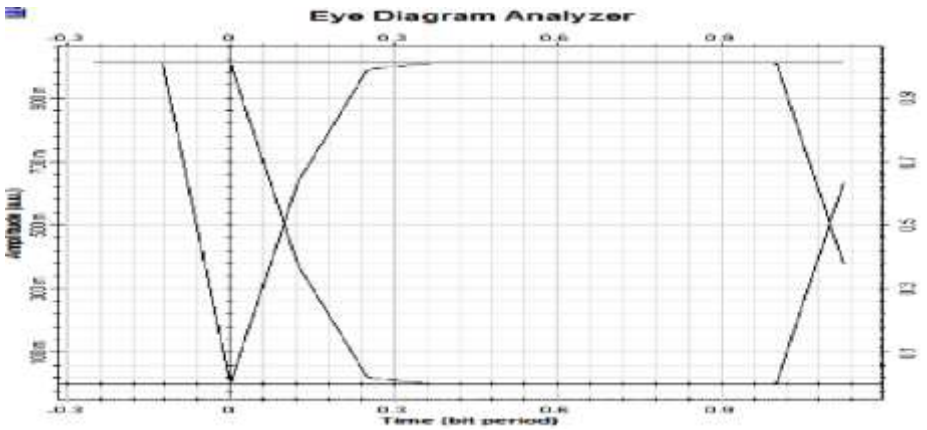

Fig. (12) Eye Diagram for 120km of a Transmission Length of SMF-DCF Optical Link

Table (2) awards the sign information at the receiver for 100 Gbps WDM CD-OOFDM system.

Tab. (2) sign information at the receiver for 100 Gbps. Sign details at the receiver

Max.Q-Factor.	**5.05e+049**
Min. B.E.R.	**0**
Eye-Height	**1.01**
Thre.shold	**3.330191e-010**

Conclusion

Data Rate has become a telecommunication crisis, not just in conventional systems but all over telecommunication systems such as 5G which is the fifth generation of wireless communications technologies supporting cellular data networks. Our work found a system design can fit in the front haul for the 5G systems easily. This work achieved high speed using a DD-OOFDM system which is found having the most simple to send and receive data; it is less expensive than the CD-OOFDM system and it has more protections against noise. However, it can be stated that CD-OOFDM is the next generation of optical media technology instead of DD-OOFDM as it combines all the advantages of coherent optical and OFDM systems. Besides, many restrictions that show in SMF systems including CD and PMD have been overcome. Also, combining OFDM technology with WDM technology and designing and building a system for them provides high bandwidth transmission and large data rate in addition to high spectral efficiency without growing cost or make the system more complicated.

To increase the demand in Bandwidth and data rate, it is suggested that the WDM and OFDM systems be combined. There are there effective systems have been compared. Sustainability of these systems is a key factor, so that next generation networks can adopt the best one.

In the present study, three diverse systems are designed for diverse rates utilizing DD and CD-OOFDM. The first design is based on DD-OFDM. In this system, (7.5 GHz frequency carrier) is used. The data rate is 10 Gbps. The modulator is 16-QAM, 256 subcarriers, and 512 FFT points. In addition to that, the various transmission links are checked. Moreover, as the length of the transmitter channel increases, the Q factor coefficient decreases with an increase in the worth of BER. The better worth of BER is at zero.

The second one is based on CD-OODFM with SMF. The data rate is 40 Gbps with the embedded type 16-QAM modulation, 512 subcarriers, and 1024FFT-points. The length of the transmission connection is 150(km). After designing Simulations of this system, the best value for BER is zero.

The third and last design based on WDM CD-OOFDM with SMF-DCF. It is 120km long. The four channels of the WDM system of 25 Gbps with a built-in 4QAM transmitted the signal, as the carrier frequencies from 193.05THz to 193.2THz were channeled carrier with a 50GHz channel wideness, 512-sub-carrier and 1024FFT-points. The system is made and simulated to obtain a worth for B.E.R. that is zero.

In the DD-OOFDM system, the photodiode is utilized to convert the signal from optical to electrical. Whereas, in CD-OOFDM detection, two similar couples of stable coherent-detectors with L.O. are utilized to convert the (I per Q) the signal from optical to electrical.

References:

[1] Chen X. 2015. Design and Optimization of Optical Fiber Based PSK Demodulators for High-Bit-Rate Optical Networks. PhD Dissertation, University of Polytechnic of Madrid. Spain.

[2] Mansor N. 2014. Coherent OFDM for Optical Communication systems. The Islamic University – Gaza.

[3] Akinwumi A. and Elizabeth A 2018 Design and simulation of 1.28 Tbps dense wavelength division multiplex system suitable for long haul backbone, arXiv:1810. 00618v1.P7

[4] Kaushik A, Gautam A.K. 2019. Next Generation Optical Fiber Research for The Ultra High Speed. S.D. College of Engineering & Technology, Muzaffarnagar. ISSN:2455-2631.P3

[5] Pan J. 2010, a Nonlinear Electrical compensation for the Coherent Optical OFDM System, Ms. Thesis, Miami University. Journal of Light wave Technology Vol. 29, Issue 2, pp. 215-221

[6] Giacoumidis E. 2011 Adaptive optical OFDM for local and access networks PhD Thesis, Bangor University, a2011.

[7] Wasiu P. 2009. Subcarrier intensity modulated free-space optical communication systems, PhD Thesis, North Umbria University, Newcastle. Journal of Lightwave Technology Vol. 27, Issue 8, pp. 967-973.

[8] Wei Li, Zengming Meng, Xudong Yu, Jing Zhang 2015 Experimental study of balanced optical homodyne and heterodyne detection by controlling sideband modulation, arXiv:1508.04974v1. P2

[9] Anzuola E. 2012 Digital coherent transceiver for optical communications from Design to Implementation, Master Thesis. MERIT, Polittecnica Catalunya University. P 27-29.

Thermal analysis for stability the nanocrystals ZnSe(diamantane)

H A T Al-Ogaili 1* and R. A. Al-Wardy2

1Department of Physics, College of Science, Wasit University, Kut –Iraq.
2Department of clinical laboratory science/college of pharmacy/Mustansiriyah university, Baghdad -Iraq.
e-mail: hananabd81@gmail.com

Abstract.The chalcogenide structures are studied at nano scale theoretically, Znic Selenium is one of these structures studied theoretically by DFT, once as a diamantane(Zn_7Se_7 as cubic in solid state) or again diamondoids ($Zn_7S_7H_{14}$),where similarity in formula but different from wurtziod(Zn_7Se_7) in stoichiometry at nano-limited , the molecules ZnSe diamantane are formed from change size. However both of the spectra and electronic properties of molecules ZnSe diamantane are calculated. In this work, used RB3LYP/3-611 G(p,d) as a base set, it can note that the blue shift of the Raman spectra, the energy gap 2.767 eV for ZnSe diamantane approach to the experimental values , the longitudinal optical of same structure is 208 cm^{-1}, also maximum force and displacement of atoms are investigated .In this research, bond length is 2.46 Å, also investigated the effects on the surfaces of molecules.
Key words: diamantane ZnSe, DFT, Chalcogenide, GFE, ZnSe, II-VI, stability

1-Introduction:

The Nanostructures features in II-VI group at the periodic table became more interesting in nanotechnology field dependent on important of their applications and the modern progress in optoelectronic devices, one of these structures of semiconductors are monochalcogenide Zn that connect with other element X such as (S, Se, O and Te) to form compounds ZnS , ZnSe ,ZnO, and so on [1-3].

Most of these compounds more important in technological development where utilized in several applications recently [3] such as high densities in optical memories, devices of the laser or photo detectors, also solar cells etc. currently, most of the researches in the fields of optoelectronics and electronics shown that investigations of electronics and structural features for these appliances have considerable in their development that appear in the new nanotechnologies.

Newly, many researchers studied the properties of compounds above such as electronic or structural by many methods theoretical and employed theoretical calculations in Ab – initio route also used empirical [1-2] some researchers such as Walter and et .al studied the electronics and band structure characteristics of Zn(Te ,Se) by empirical pseudopotential [4], and other Huang and et al [5] that employed LCAO route to

computed density of state and band structures of ZnX compounds and group of Karazhanov [2] computed characteristics of the electronic structure by density functional theory (DFT) of ZnX .

Thermal analysis of The Gibbs free energy (GFE) that contain four parameters either be the electronic, or translational, or vibrational and also the rotational, these parameters considered as the freedom degrees of any molecule that impact on the total energy of molecules [6].

There are three cases of GFE: if the GFE case less than 0 (spontaneous reactions or named exergonic) or the GFE case greater than zero (unspontaneous reactions or named endergonic) and finally there is reaction in the equilibrium case if GFE = 0

To optimize some characteristics of electronics and geometrical or Raman spectrum of ZnSe diamantane(Zn_7Se_7) as Zinc Blende (cubic) via theoretical calculations that utilized DFT in Gaussian program(09), this simulation required some approximations such as Generalized Gradient Approximation (GGA) which existing in DFT that is included in Ab – initio calculations.

2- Theory:

Theoretically, To study features of ZnSe(Zn_7Se_7) diamantane that similar to cubic structures in bulk but deferent in number molecules that form the compound where this structures forms at nano-scale and have dangling bonds in end the terminals to ability it to connect with other atoms like H or N … in this study , there are two bonds can connect with the suggested atoms.

DFT applied in this simulation to important it and it has high accuracy to obtain on best results and comparison with the experimental results, and named diamantane comes from diamond carbon and has same shape of it, also diamondoids ($Zn_7Se_7H_{20}$) named of molecules that connect with hydrogen. Also Se and Zn considers as heavy atoms that delay during the work in program Gussian09 may be needed many months to complete it, therefore , in this calculations that focused on diamantane only ,and neglected the rest like (tetra $Zn_7Se_7H_{28}$, hexa $Zn_7Se_7H_{30}$, octa $Zn_7Se_7H_{42}$ …ect. that prefix accompany with the diamantane ZnSe with adding H-atom.

In this study used 6-311 G and RB3LYP to represent the molecules in Gauss view 06 and the results of spectrum and all calculations, the previous results used wurtziod of ZnSe as nanotube [7], now in this paper completes the result of diamantane Zn_7Se_7 (bare) and diamondoids $Zn_7Se_7H_{20}$ or take partial diamondoids $Zn_7Se_7H_{14}$ similarity in the formula but there different in the structures geometrical with wurtziod (Zn_7Se_7) that studied previously as shown in figure 1. , this molecule formed by various the size molecules. Also used using Gibbs function to know the stability at nano-scale for these structure from thermodynamics calculations.

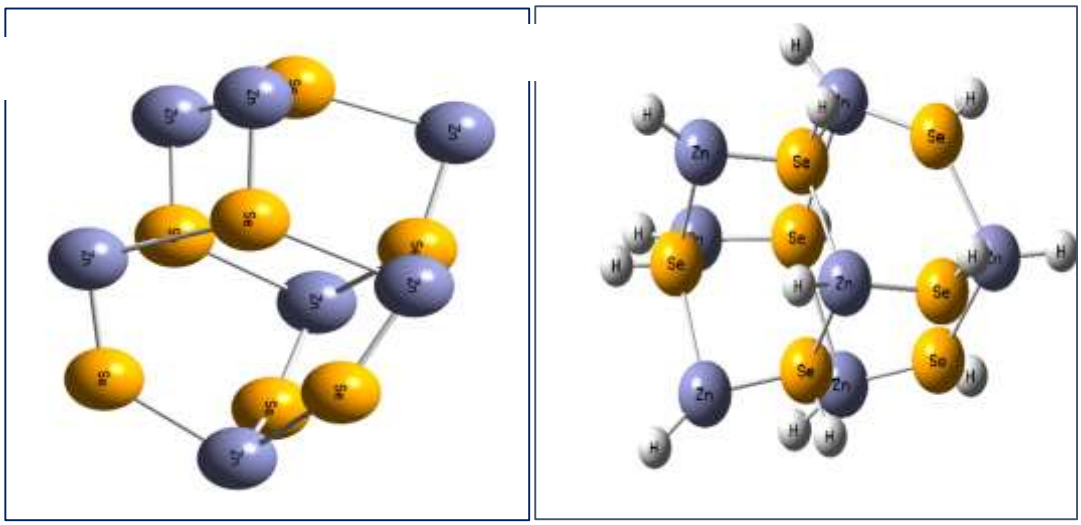

Figure 1. Shows the geometrical structures of ZnSe (a- diamantane, b- diamondoids).

3-Results

Electronic features of ZnSe diamantane like energy band also the bond length can be noted in two figure 2 and figure 3, found that Eg of this molecules are 2.76 eV approximated to experimental values [8], the band gaps calculated from (HOMO and LUMO) levels that give information about the occupied and unoccupied molecules levels of of ZnSe diamantane, increasing the dangling bonds at surfaces of molecules due to increase energy gaps spontaneously by the adding levels to forbidden gaps [9-10].also all the calculations achieved at temperature 298 ^{0}K and pressure 1atom for molecules at point group C1.

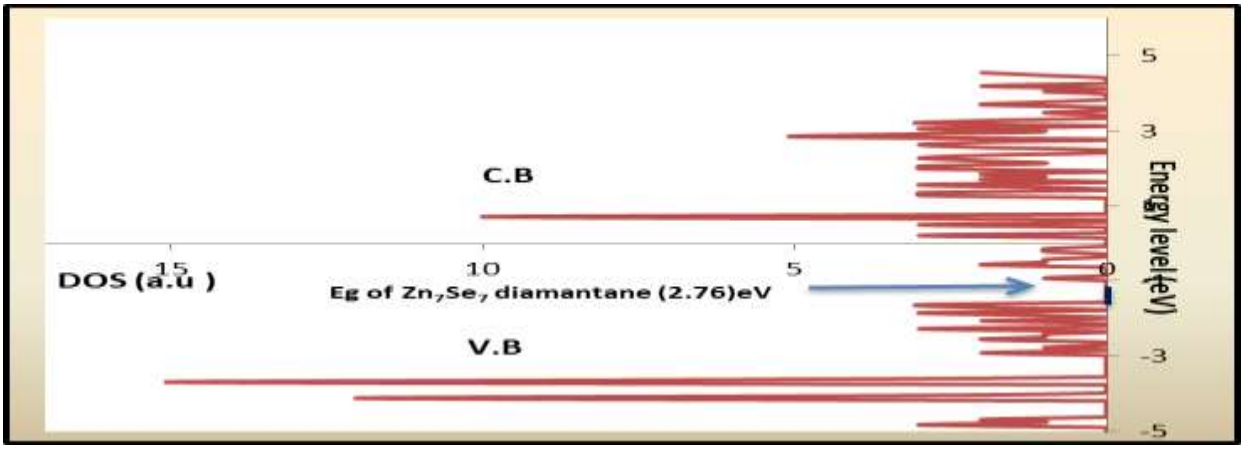

Figure 2. Change the energy levels (HOMO –LUMO) of ZnSe diamantane.

[Grab your reader's attention with a great quote from the document or use this space to emphasize a key point. To place this text box anywhere on the page, just drag it.]

Also bond length of ZnSe molecules as diamantane is 2.46 close to experimental value, where note that board of bond is sharp in this case diamantane of Zn_7Se_7 .

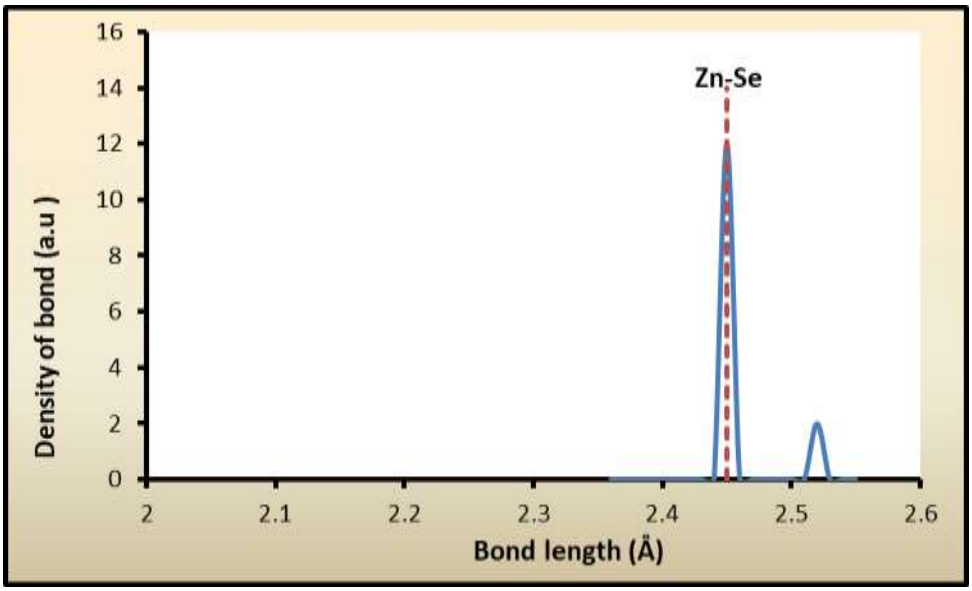

Figure 3. Bond density of ZnSe diamantane.

The vibrational properties are studied when imaginary frequency(cm^{-1}) equal zero; Phonons spectra of ZnSe diamantane that illustrated in figure 1 which come from Raman spectra to study characterizations of ZnSe diamantane, to study longitudinal optical LO for this molecules and comparative with the experimental findings, noted that low intensity for all peaks in Raman reach upper summit of ZnSe to 2.4 a.u. , while the other summits be lower , the value of LO of ZnSe is 208 cm^{-1} less than the experimental.

Raman scattering give more information about the oscillation and dynamics of lattice for any material, also study IR spectra as shows in figure 5. notice that there high intensities of spectra molecules of ZnSe diamantane reach above 700 a.u.

Practically, at the nano-scale found that the findings of Raman shifts ZnSe have values for 2TA(transverse acoustic) and TO (transverse optical)are 120.9cm^{-1} and 204.2 cm^{-1} while 1LO 239.4 cm^{-}

[1][11],respectively. Theoretically, phonon mode of LO of ZnSe diamantane is 208 cm^{-1} less than the practical value.

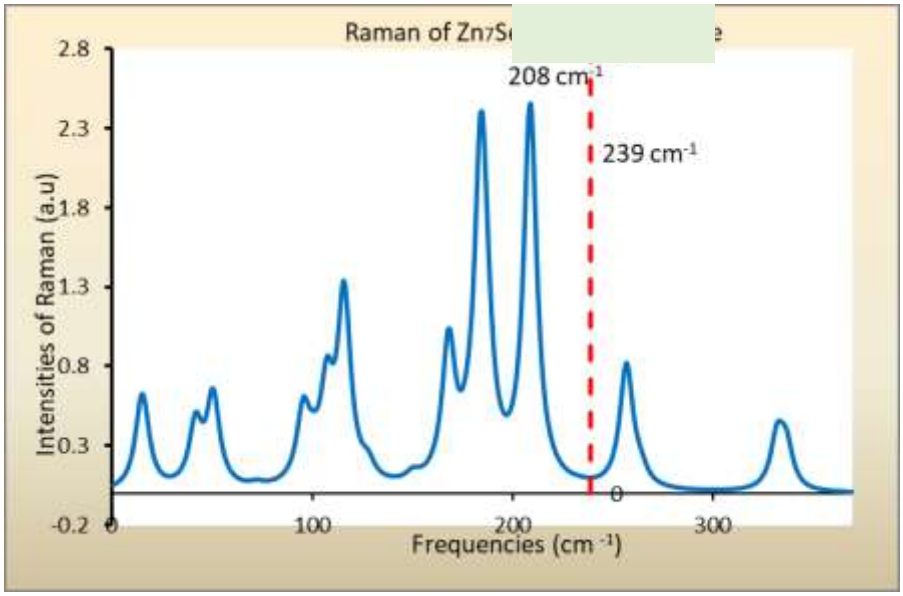

Figure 5. illustrates Raman shift of ZnSe diamantane (bare) .

The positions of phonon modes located at center for Brillouin zone i.e. the clusters have high symmetry at center, also the GGA approximations consider high accuracy used in this calculations instead of LDA approximations where the spin electrons be neglected [7].The spin of ZnSe molecules singlet and multiplicity =0, also maximum force converged to 0.000053 while maximum displacement not converged 0.027160.

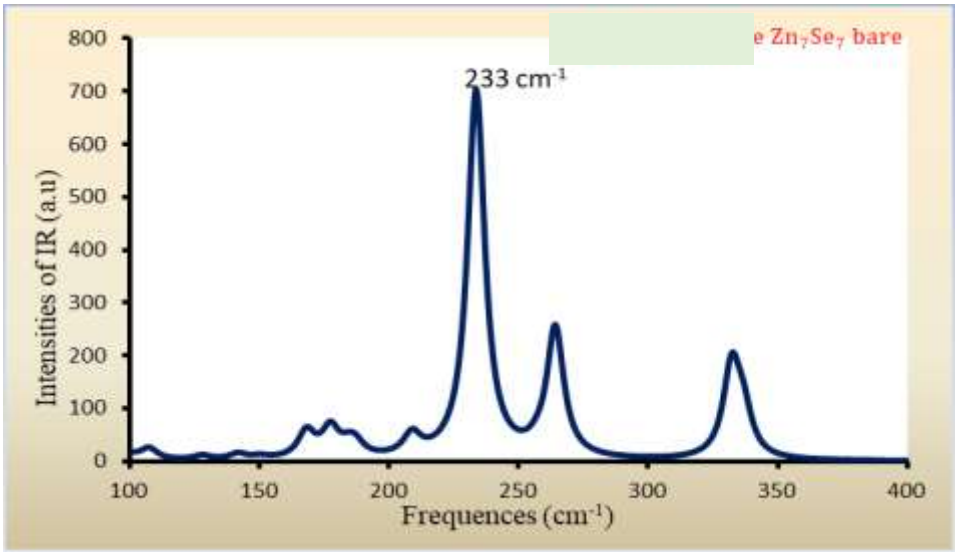

: shows IR spectra of ZnSe diamantane(bare). **Figure** 4

Gibbs function used in the thermal analysis to know or decide any the structures of ZnSe (diamantane or wurtziod) have stability, after know the absolute values of this function where find in the thermodynamics features of molecules during the computations in program Gaussian 09.

Theoretically, Zn_7Se_7 diamantane is less stable than wurtziod(Zn_7Se_7) due to the later has GFE is 1.27 eV spontaneous and (the most negative) , inverse the GFE value of wurtziod about 1.004eV be positive and unspontaneous , the substances be stable due to quantum confinement of molecules at nano-limited [9].

4-Conclusion:

The virtual lab used to representation the material theoretically by matrixes system of position the atoms of Zn, Se to obtain on results focused on the geometrical structures of ZnSe diamantane, approaching to the practical values, where Gaussian 09 used for this purpose, therefore, it can study all characterizations of ZnSe diamantane with many methods in theory, DFT considers better than other the ways of theory due to it computed all electrons in structures, also the cage of ZnSe diamantane obtain from size variation of the nano-crystals. The findings have been extracted some properties electronics or spectroscopes for this cage of ZnSe diamandiods or diamantane, also concluded that the stability of the molecules of ZnSe diamantane less stable than wurtziod nano-sturctues from the Gibbs function.

References

[1] Bredin J L 1994 *J.Phys. Today* **47** 5

[2] Karazhanov S Zh, Ravindran P , Kjekshus A , Fjellvag H and Svensson, B G 2007 *Phys. Rev. B* **75** Article ID: 155104

[3] Hanan A T A *et al* 2018 *IOP Conf. Series* **454** 01214

[4] Walter J P, Cohen M L, Petroff Y and Balkanski, M 1970 *Phys. Rev. B* **1** 2661.

[5] Huang M Z and Ching WY 1993 *Phys.Rev. B* **47** 9446

[6] Mudar A A and Hasan M A 2018 *Surf. Rev. and Letters* **25** 1850008

[7] H. A. T. Alogaili, M. A. Mohammed *2019 Chalco. Lett.* **16** 507

[8] Su Q, Li L J , Li S Y , Zhao H P 2013 *Mater. Lett*. **92** 338

[9] Hussain M T, Thjeel H A 2018 *Chalco. Lett.* **15** 523

[10] Kim H K, Huh S H, Park J W, Jeong J W, Lee G H 2002 *Chem. Phys. Lett*. **354** 165.

[11] Lu G, An H ,Chen Y , Huang J , Zhang H , Xiang B , Zhao Q, Yu D, Du W 2005 *Cryst. Groth.* **274** 530.

Electrical Characterization of Thin Films (TiO2: ZnO)1-x (GO)x / FTO Heterojunction Prepared by Spray Pyrolysis Technique.

M J Alsultani[1] , H H Abed[2] , R A Ghazi[3] and M A Mohammed[4]

[1] Department of environmental health, Al Qasim Green University, Iraq.
[2] Physics Department, University of Babylon, Iraq.
[3] Department of Medical Physics, AL- Mustaqbal University College, Iraq.
3 Department of Soil Science & Water Resources, University of Al-Qadisiyah, Iraq
4

Abstract. Thin films from $(TiO_2: ZnO)_{1-x}(GO)_x$ (x=0.2, 0.4, 0.6, 0.8) ml have been prepared by spray pyrolysis technique through depositing on FTO coated glass substrates. Electrical characteristic was investigated by current-voltage (I–V) , capacitance-voltage (C–V) measurements. The (I-V) measurement showed that heterojunction from symmetric type (isotope), Ideality factor (β) value increased from1.63 to 2.48 where (β) > 1 the recombination current was dominates, rectification ratios increased from 30.62 to 77.43 because of reduction in the depletion layer from 127nm to 56.4nm which investigated by (C-V) measurements, as well as the built-in voltage (V_{bi}) and the barrier height $Ø_B$ decreased from 1.42 V to 0.65 V and 1.62 to 0.79eV respectively. The increase in graphene oxide ratio lead to increase in the majority carriers in turn leads to reduction in Fermi levels . Such tests showed that the electrical properties of the prepared thin films improved and indicated that GO acts as a semiconductor and can be used for flexible and transparent optical-electronic devices.

1. Introduction

Semiconductor photocatalysis has much interest in last decade due to its potential uses to reduce conservational difficulties [1, 2]. TiO_2 is a many-sided material, a very good photocatalyst for environmental pollutant inspection, non-toxicity, comparatively low cost, and brilliant chemical stability [3, 4]. The wide bandgap and long life of holes and electrons gave the TiO_2 excellent photocatalytic characteristic, electrons - holes pairs generated by the TiO_2 photocatalyst causing series of reactions them ultimately mineralize the pollutants [5, 6].

Zinc oxide (ZnO) is one of the metal oxide semiconductors that have drawn great attention due to its noticeable combination of physical properties. ZnO has wide bandgap 3.370 eV at 300K, high exciton binding energy 60 mV [7], n-type semiconductor has wurtzite structure and varied growth morphology, all of these properties makes ZnO as a majority material in the broad-band semiconductors and nanotechnology fields[8]. Also, ZnO exhibited unique electrical properties which makes it useful for different applications such as in ultraviolet emitting diodes (LEDs) [9], photovoltaic devices [10], optical waveguides [11], gas sensors, etc. [12].

GO is another admirable entry in a field of photocatalysis, which support a duo in achieving effective of degradation as it scatters and transmits shuttles electron. Therefore it can greatly reduce the problem of recombination [13]. Two-dimensional nanosheet carbonaceous has much caution lately due to its impressive properties like amazing electrical [14], mechanical and thermal properties [15, 16], superior mechanical strength, large specific surface area, and excellent charge mobility [17, 18]. Graphene incorporation into TiO_2 has been extensively studied to improve the photocatalytic activity of TiO_2 [19, 20]. TiO_2-graphene nanocomposite also demonstrated a good performance in solar cells because of the ability of graphene to enhance charge collection and reduced recombination [21]. The chemical, physical, and photochemical properties of the formed TiO_2 / ZnO compounds depend on the prepared methods. To improve the photodegradation efficiency of the TiO_2 catalyst, TiO_2/ZnO coupled semiconductors were prepared by various methods such as solid-state reaction method [22], thermal evaporation [23], and a hydrothermal reaction [24].The spray pyrolysis technique has a relatively low cost, applicable to large-scale areas, and easy to manipulate [25]. Moreover, this technique can be used for deposition on tubing walls [26]. The present work describes the effect of adding graphene oxide in different ratios on the optical, (I-V) and (C-V) electrical properties of $(TiO_2: ZnO)_{1-x}(GO)_x$ thin films deposited on FTO glass.

2. Experimental

Procedures consist of mixing two compounds TiO_2 and ZnO in the same ratios with graphene according to relation $(TiO_2: ZnO)_{1-x}(GO)x$, TiO_2: ZnO. Solution has been prepared by dissolving 0.40 mg of TiO_2 and ZnO nanopowders separately in 10 ml of distilled water on room temperature; a magnetic stirrer was integrated for 30 minutes to facilitate the complete dissolution. The modified Hummer method wasTemperature was adjusted to constant at 95 ^{0}C for 60 min although water was added constantly. Further addition from deionized water was added so that the volume of the suspension was 200 mL, after 5 min the 7.50 mL of H_2O_2 was added. The resultant was centrifuged and washed with deionized water and a 5% HCl solution repeatedly. Lastly, the product was dried at 60 ^{0}C. After the preparation of the solutions is mixed according to the following ratios (x=0.2, 0.4, 0.6 and 0.8) ml where x represents the ratio of Graphene Oxide.

The resulting solution was stirred for about (10-20) minutes to be homogenized. Thin films were prepared by using this mixture. FTO glass slides (15 mm ×15 mm) were washed by using detergents and then dried ultrasonically. Spray pyrolysis technique has been used to deposit a thin film on the heated substrate at (70 °C) with spray time 4s for each minute and deposition time 12 minutes is schematically presented in scheme1. Shimadzu 6000 XR diffraction was used for XRD analysis. The absorbance of thin films were distinguished by using Shimadzu 1800 UV spectrometer. A Keithley model 2400 source meter and HIOKI3532-50 LCR meter were used for measurement I-V and C-V characterization respectively.

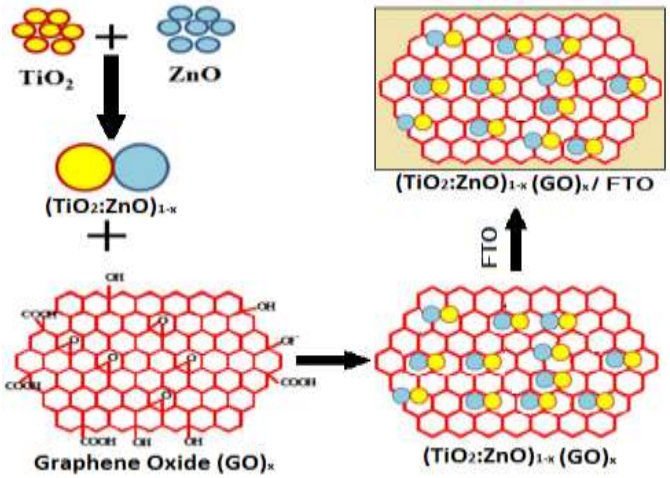

Schematic1. Illustration for the synthesis of $(TiO_2:ZnO)_{1-x}(GO)_x$/ FTO thin films.

3. Results and Discussion

The TiO_2, ZnO, and Graphene Oxide (GO) XRD findings are shown in Fig.1. TiO_2 which exhibits a moral crystallinity and a 2θ peak values at 25.06^0, 37.98^0 48.35^0, 54.33^0, and 55.57^0 can index to (101), (004), (200), (015) , and (211) planes in that order. It is good settlement with (JCPDS No. # 52-6932). It is also found ZnO peak values at 31.85^0, 34.51^0, 36.35^0, 47.57^0 and 56.6^0 with planes (100), (002), (101), (012) and (110) according to (JCPDS No. # 900-8878). Graphene Oxide (GO) shows a peak at 11.32^0 indexed to (001) plane.

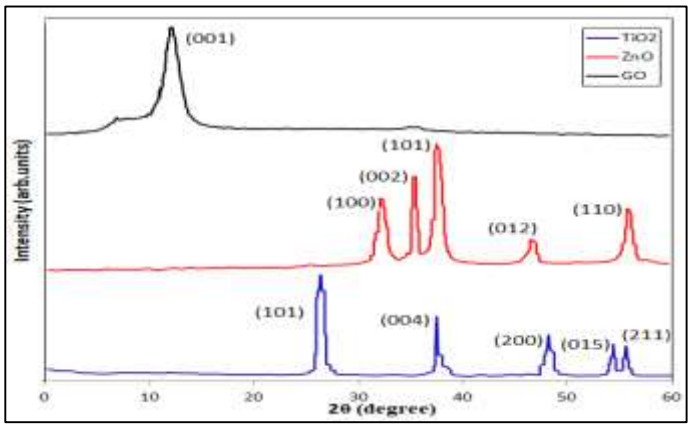

Figure 1.XRD patterns of the TiO_2, ZnO and GO nanosheets.

Current-Voltage (I-V) characteristics of prepared films are tested electrically by using a two-point probe, the first probe is contact $(TiO_2: ZnO)_{1-x}$ $(GO)_x$ thin films and the other probe on FTO, with sweeping voltages at (-2 V to 2 V). It indicates that well-ohmic contact formed between the electrodes and the prepared films. The current varies exponentially with voltage for all the prepared films we notes form the forward bias the increase of applied voltage leads to increase current value, but in the reverse bias the current value increases and gives a gradual breakdown voltage, this behaviour is one of general traits in symmetric heterojunction type (isotope) that I-V characteristics shown in Figure 2. The values of the rectification ratio (it is the ratio between the forward bias current and the reverse bias current at a particular voltage(1V)) of the prepared thin films are increases because of reduction in the depletion layer as in Table (1). The Ideality factor (β) determined by taking slope of the linear region of the forward bias (ln I – V) curve through the relation[27]:

$$\beta = \frac{q}{KT}\left[\frac{dV}{d(\ln I)}\right] \qquad (2)$$

Where q is the charge of the electron, k is the constant of the Boltzmann and T is the temperature in Kelvin. We found increasing in ideality factor value that's mean the recombination current dominates when the ideality factor (β > 1) as in Table1, and this factor correlates between the processes of recombination that happen at the interlayer surface and the mismatch the materials lattice constants.

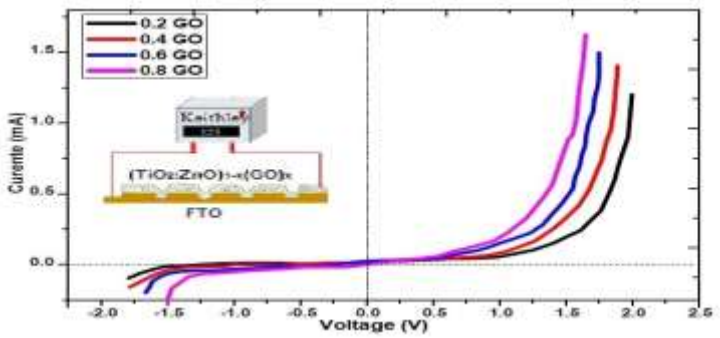

Figure 2. The I-V characteristics of $(TiO_2: ZnO)_{1-x}(GO)_x$ thin films.

Figure 3 Shows the capacitance of the heterojunction changed with the reverse bias voltage in frequency range100KHz at room temperature. It is clear from the results the capacitance decreased with the bias voltage. Also the value of capacitance has become almost constant at high reverse bias voltage.

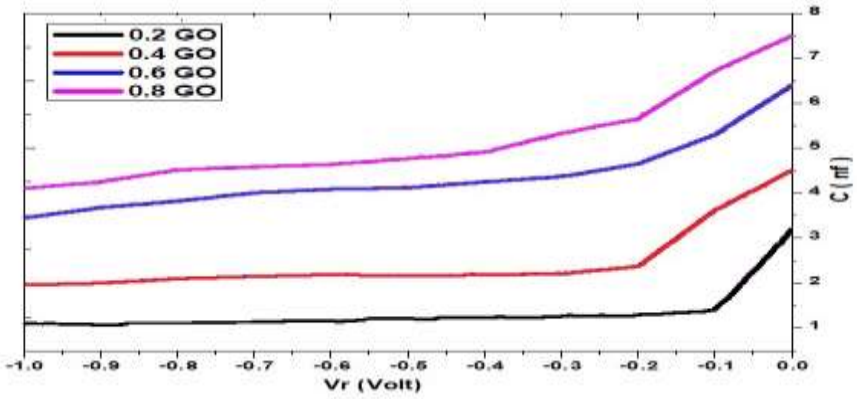

Figure 3. Capacity as a function of back voltage of thin films $(TiO_2: ZnO)_{1-x}(GO)_x$.

Figure 4. Shows the plot between $1/C^2$ and reverse voltage V_r. It can be seen that these curves are an abrupt type. From the slope of the fitted line of this plot and the equation[28]:

$$\frac{1}{C^2}=\frac{2}{q\varepsilon_s N_D S^2}\times\left(V_{bi}\text{-}V\text{-}\frac{kT}{q}\right) \qquad (3)$$

Where V_{bi} is the built-in voltage, ε_s the dielectric constant of the semiconductor, ε_0 is the dielectric constant of vacuum(8.85×10^{-12}F/m), N_D is the concentration of ionized donors and S is the thin film area ,V_{bi} can be calculated from intercept fitted line on the voltage axis at ($1/C^2=0$). The slope value gives the net doping concentration (N_D). The depletion-layer capacitance per unit area (ω) calculated by [28]:

$$\omega=\frac{\varepsilon_0\varepsilon_s S}{C_0} \qquad (4)$$

Where C_0 is the capacitance value at V_r= zero. From the obtained value we can calculate E_F value for the structures by using following relation[29].

$$E_F=\frac{KT}{q}\ \mathrm{Ln}\left(\frac{N_C}{N_D}\right) \qquad (5)$$

Here N_C is the effective density of states for electrons in the semiconductor conductivity bands (E_c) which can be calculated from the relation:

$$N_C=4.82\times10^{15}\times T^{\frac{3}{2}}\left(\frac{m_e^*}{m_0}\right)^{\frac{3}{2}} \qquad (6)$$

m_e is the effective mass ($3.36m_0$) and m_0 the rest mass of electron (9.1×10^{-31}kg). then we can calculate the barrier height by the relation[30.]

$$\emptyset_{B,C-V} = q\left[V_{bi} + \frac{KT}{q} Ln\left(\frac{N_C}{N_D}\right)\right] \qquad (7)$$

Table 1 shows decreased built-in voltage and the height of the barrier resulting from decreases in the depletion layer w due to the graphene oxide ratio leading to the injection of majority carriers, which in effect reduces the Fermi stage. These results improve the electrical properties of the prepared thin films.

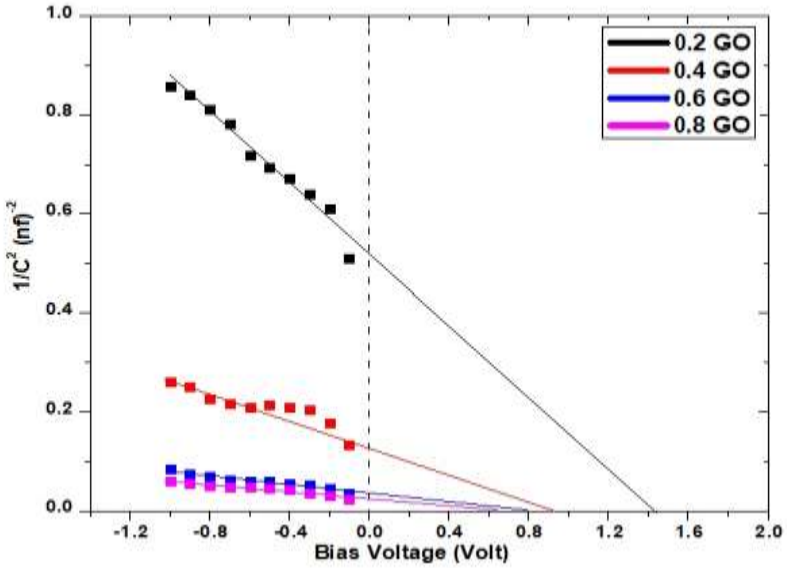

Figure 4. Shows the plot between $1/C^2$and reverse voltage V_r.

Table 1: I-V and C-V parameters for $(TiO_2: ZnO)_{1-x}(GO)_x$ thin films.

X ml	R.R	β	V_{bi} (volt)	$N_D\times10^{17}$ (cm^{-3})	C_0 (nf)	ω (nm)	E_F (eV)	$Ø_B$ (eV)

0.2	3.66	1.63	1.42	0.30	3.2	127	0.20	1.62
0.4	5.42	1.93	0.92	0.38	4.5	90.3	0.20	1.12
0.6	10	2.18	0.79	1.37	6.4	63.5	0.17	0.96
0.8	14.88	2.48	0.65	3.34	7.2	56.4	0.14	0.79

4. Conclusion

$(TiO_2: ZnO)_{1-x}(GO)_x$ / FTO thin films prepared using the technique of spray pyrolysis form heterostructured junctions with specific electrical properties depending on the GO ratio.The (I–V) and (C–V) characteristics showed that the heterojunction from symmetric type (isotope), The GO ratio leads to injecting majority carriers this in turn leads to decrease each of the barrier height , Fermi level, built-in voltage, and depletion layer. These results improved the electrical properties of the prepared thin films and indicated that graphene oxide acts as a semiconductor and can be used for flexible and transparent optical-electronic and detection devices.

References

[1]. N.M. Dimitrijevic, Z.V. Saponjic, B.M. Rabatic and T. Rajh 2005 *J. A. C. Society* 127 1344-1345.
[2]. B.M. Rabatic, N.M. Dimitrijevic and R.E. Cook 2006 *Adv. Materials*, 18 1033-1037.
[3]. S.J. Liao, D.G. Huang, D.H. Yu, Y.L. Su and G.Q. Yuan 2004 *J Photochem. and Photobio A* 168 7-13.
[4]. R. Comparelli, E. Fanizza, M.L. Curri, P.D. Corri, G. Mascolo and A. Agostiano 2005 *Appl Catalysis B* 1-11.
[5]. M.Muruganandham and M.Swaminathan, *Solar Energy Mat. and Solar Cells* 2004 81 439-457.
[6]. L.Q. Jing, B.F. Xin, F.L.Yuan, B.Q. Wang, K.Y. Shi and W.M. Cai *Appl Cat. A* 2004 2475 49-54.
[7]. G M´onica Morales Mas´ıs, M.Sc thesis 2007 Wright State University, Dayton-Ohio .
[8]. Ziad T. Khodair, Ph. D. Thesis, Department of Physics 2001 Baghdad University,Iraq.
[9]. C. R. Gorla, N. W. Emanetoglu, S. Liang,W. E. Mayo, Y. Lu, M. Wraback and H. Shen,1999 *J Appl.Phys. 85 2595* .
[10]. T. Minami, T. Yamamoto and T. Miyata 2000 *Thin Solid Films*,63 366.
[11]. D. C. Look 2001 *Eng. B-Solid State Mat. for Adv. Tech.* 80 383 .
[12]. C. Klingshirn 2007 *physica status solidi (b)* 244 3027.
[13]. H. Zhang, X.Lv ,Y.Li ,Y.Wang, J.Li 2010 *ACS Nano 4 380-386* .

- [14]. G. Venugopal, K.Krishnamoorthy, R.Mohan, S.J.Kim 2012 Mat.Chem.and Phy. 29 33.

[15]. J.W.Suk,R.D. Piner ,J.An, R.S. Ruoff, 2010 *ACS Nano 4* 6557- 6564.
[16]. X. Mu,X.Wu,T.Zhang,D.B.Go,T.Luo 2014 *Scientific reports* 4 1-9,4.
[17]. A. C. Ferrari, J. C. Meyer, V. Scardaci, C. Casiraghi, M. Lazzeri, F. Mauri,S. Piscanec, D.Jiang, K. S. Novoselov, S. Roth, and A. K. Geim 2006 *Phy. Rev. Lett.* 97 187401 .
[18]. M. Haluška, D. Obergfell, J. C. Meyer, G. Scalia, G. Ulbricht, B. Krauss, D. H. Chae, T.Lohmann, M. Lebert, M. Kaempgen, M. Hulman, J. Smet, S.Roth, and K. von Klitzing 2007 *phy. Stat. Sol B* 244, 4143.
[19]. P. Cheng, Z. Yang, H. Wang, W. Cheng, M. Chen, W. Shangguan, and G.Ding 2012 *Int. J of Hyd. Eng* 37 2224 .
[20]. G. Williams, B. Seger, and P. V. Kamat 2008 *ACS Nano* 2 1487 .
[21]. J. T.-W. Wang, J. M. Ball, E. M. Barea, A. Abate, J. A. Alexander-Webber,J. Huang, M.Saliba, I. Mora-Sero, J. Bisquert, H. J. Snaith, and R. J.Nicholas 2014 *Nano Letters* 14 724.
[22]. K. Park and K.Y. Ko 2007 *J. Alloys and Compounds* 430 200-204.
[23]. Y. Gui, S. Li, J. Xu and C. Li 2008 *Microelectronics Journal* 39 1120-1125.
[24]. C.W. Zou, X.D. Yan, J. Han, R.Q. Chen, J.M. Bian, E.Haemmerle and W. Gao 2009 *Chemical Physics Letters* 476 84-88.
[25]. S.M.Sabnis, Prakash A. Bhadane and P. G. Kulkarni 2013 *J. Appl. Phy.*4 7-11.
[26]. Cattin L, Reguig BA, Khelil A, Morsli M, Benchouk K and Bernede JC 2008 *Appl. surface science* 254 5814-5821.
[27] Lintu Rajan,C. Periasamy and Vineet Sahula 2016 *Perspectives in Science* 8 66-68 .
[28]. Sze S M 1969 *Physics of Semiconductor Devices* (New York: Wiley–Interscience).
[29] S. Nezhadesm-Kohardafchahi,S. Farjami-Shayesteh,Y. Badali, Ş. Altındal,M.A. Jamshidi-Ghozlu and Y. Azizian-Kalandaragh 2018 *Mat. Sci.Semi. Pro.* 68 173–180.
[30] Christos Tsiarapas, Dimitra Girginoudi and Nikolaos Georgoulas 2014 *Mat. Sci.Semi. Pro*. 2 199.

Experimental investigation of uranium content in urine samples of cancer patients in Al-Diwaniyah Governorate, Iraq

Zahraa Q. Rahman1, Anees A. Al-Hamzawi1*

1Department of Physics, College of Education, University of Al-Qadisiyah, Al-Diwaniyah-Iraq
* E-mail: aneesphys@gmail.com; anees.hassan@qu.edu.iq

Abstract. In the current study, the neutron activation technique of the nuclear track detectors (CR-39) has been applied to determine the content of uranium in human urine samples. This study involved two groups of male and female subjects, the first group is cancer patients and the second group is healthy subjects. The urine samples of cancer patients and healthy subjects have been collected from *Al- Diwaniyah* governorate, southern Iraq. The maximum concentration of uranium for cancer patients was 5.52 μg/l to male, 35 years old, from AL-Hamzah, infected with leukemia, and the minimum concentration was 2.34 μg/l to male, 56 years old, from Al-Sudair, infected with the stomach cancer. In the healthy subjects, the maximum uranium content was 4.63 μg/l to male, 35 years, from Shamiya, and the lower uranium content was 1.02 μg/l to female, 43 years, from Sumer. Uranium content has been found to be significantly higher in cancer patients than those of the healthy subjects. The influence between the concentration of uranium and gender, smoking habit was studied.

1. Introduction

Uranium is primal radioactive element ubiquitously current in the earth, is accessible in the crust of earth near a depth of 2900 km at an average concentration of 0.76 pg per gram of soil [1, 2]. The uranium isotopes that are normally measurable in nature are ^{234}U, ^{235}U, and ^{238}U with abundances (%) of 0.0055, 0.72, and 99.27 respectively, used for the nuclear applications [3]. The uranium is an element widely distributed in the environment. It takes at many forms of gas, liquid or solid compound [4, 5]. Exposure for uranium occurs through mining, milling, and chemical processing. Uranium can entrance to the human body by inhalation, digestion food or drinking water. The uranium absorbed by human body system (like skeleton, kidney, and liver) and after that excreted, in part, during urine [6, 7], it is weakly absorbed in the gastrointestinal tract, and the urine eliminates most from that which is absorbed [8]. Many reports studied the uranium concentration in the urine due to its importance of the subject on health and the environment .Uranium has great ability to causes contamination of the environment and leading to big problems especially in areas that exposed to uranium weapons, which occurred especially after Gulf Wars during (1991-2003) in southern Iraq region [9, 10]. Several reports detected a relationship between uranium present and cancer patients [9 – 11]. The solubility of uranium varies depending on certain compounds, this solubility determines how quickly and efficiency of the body absorbing them through the lung and intestines respectively. Uranium

deposited inside the bones and different organs is in the end returned again into the blood flow, which reasons many healthiness issues, starting from most cancers for kidney failure, skin diseases, respiratory disorders, and other nameless diseases [10]. In the present study, the urine samples were collected from different subjects in hospitals of Al-Diwaniyah governorate with various ages for both male and female. The study aims to investigation the content of uranium in human urine of the cancer patients and healthy subjects by using the fission track analysis technique of solid state alpha track detector.

2. Material and method

2.1 samples collection

In the current investigation, sixty urine samples are taken from two groups, the first group consist from (30) samples from the cancer patients, were collected from the hospitals in Al-Diwaniyah governorate southern Iraq, this city was one of the sites of military activities during the Gulf wars. The second group included (30) samples from the healthy group that collected from several regions of the governorate as shown in Fig.1. The volunteers from these groups had no previous history of occupational exposure to uranium. The basic questionnaire of the volunteers such as age, gender, and smoking habit is shown in table 1.

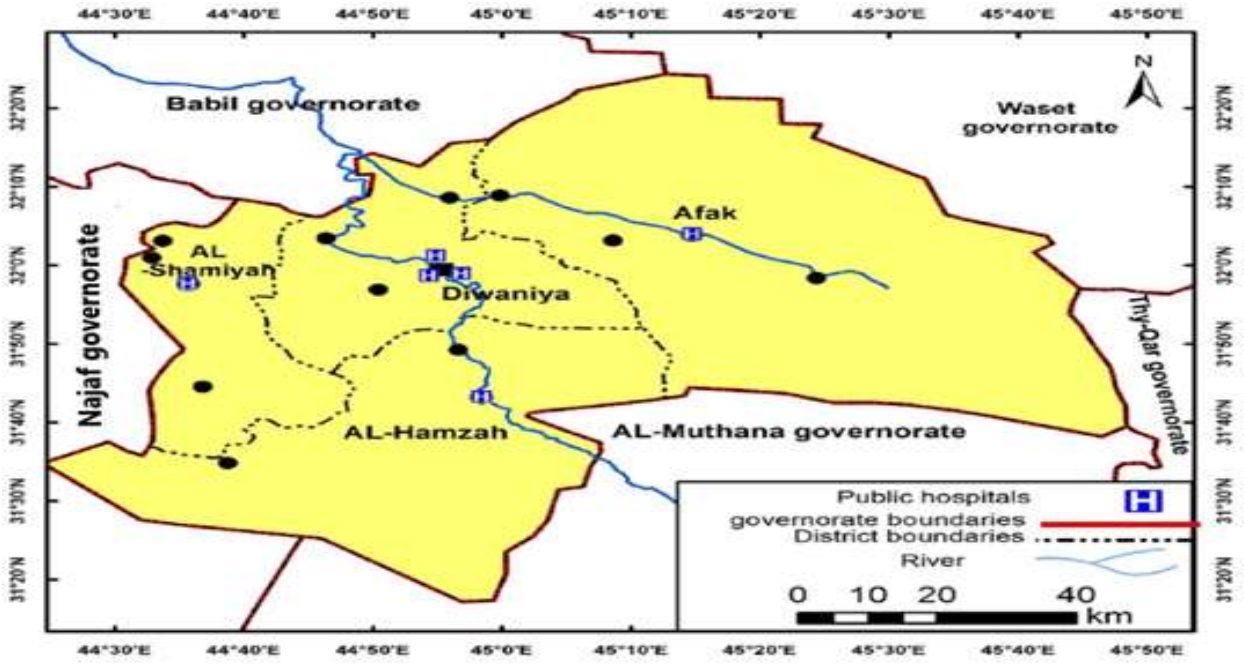

Figure1. Map showing the study location of Al- Diwaniyah governorate

Table 1. Statistical description of the two groups involved in the study

Basic information	Cancer patients group	Healthy group
Number of males	14	14
Number of females	16	16
Age range/years	19-95	19-90
Average age/years (Males)	57.21	55.64
Average age/years (Females)	43.62	42.81
Average age/years (Total)	49	48.8

2.2 Experimental method

The experimental technique that was developed to determine the uranium concentration in human urine samples is the same as that published elsewhere [12, 13]. The samples of urine were primarily stored in cold boxes with the code of the sample and then kept in the refrigerator until the time of investigation. Two drops of urine with volume equals to 100 μl were left drying on a square area of CR-39 alpha detector in an environment without dust at room temperature for 24 hours. A non-volatile substance was put on a thin film of the detector and covered by another piece of CR-39 as shown in Fig 2. Samples of urine and detectors were exposure to a beam of thermal neutrons from (Am-Be) neutron source with a total flounce of (3.024×10^9) n cm^{-2} for seven days in order to cause latent damage to the detector due ^{235}U (n, f) reaction. The irradiation process was carried out in nuclear physic laboratory department of physics college of education Baghdad university. After irradiation process, CR-39 detectors were etched in 6.25 N of sodium hydroxide (NaOH) liquid at 60 ˚C for five hours then rinsed in water [14 – 16]. Densities of the induced fission tracks were recorded by using Olympus optical microscope with magnification of 400×. The concentration of uranium in human urine samples was measured by comparing between the densities of track registered on CR-39 detectors of the unknown samples and that of the standard samples by the following expression [9, 14]:

$$U_x\ (\mu g/l) = U_s\, \rho_x / \rho_s \qquad (1)$$

Where: ρ_s and ρ_x are fission tracks densities for the standard samples and unknown samples, respectively. U_s and U_x are the uranium concentration for the standard samples and unknown samples, respectively.

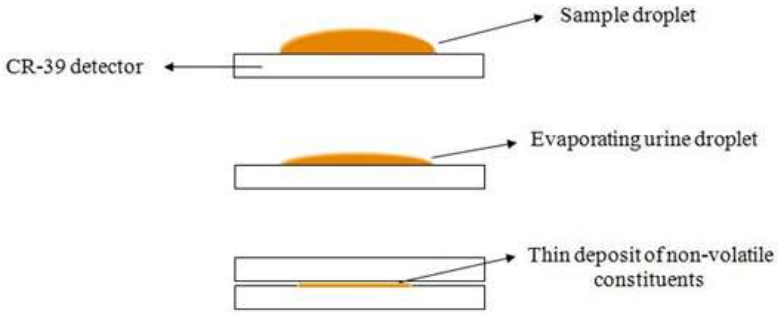

Figure 2. Preparation the droplet of urine samples to determine the uranium content

2.3 Statistical analysis

The results of the present investigation were analyzed by using Statistical Package of the Social Sciences (SPSS) program. Independent sample t Test was used to estimate the significance of the probability level (P) between the studied groups.

3. Result and discussion

Table 2 shows the uranium content in the samples of urine for cancer patients group. The highest value of uranium concentration was 5.52 µg/l for male, 35years, from Al-Hamzah suffering from leukemia, while the lower was 2.34 µg/l to male, 56 years, from Al-Sudair suffering from stomach cancer. The mean of uranium concentration in urine for this group was 4.017 µg/l.

Table 2. Concentration of uranium (µg/l) in urine samples of the cancer patients group

Sample code	Age (Year)	Gender	Cancer Type	Smoking habit	Location	Uranium content ± Sd. Error
P1	35	M	Leukemia	Yes	AL-Hamzah	5.52 ± 0.21
P2	35	F	Breast	No	Sumer	3.81 ± 0.25
P3	63	M	Lymphoma	No	AL-Badair	3.98 ± 0.18

P4	52	M	Lymphoma	No	Diwaniyah	3.62 ± 0.16
P5	50	F	Breast	Yes	Diwaniyah	3.81 ± 0.16
P6	47	F	Lung	Yes	Sumer	4.94 ± 0.18
P7	58	F	pancreatic	No	Diwaniyah	4.31 ± 0.16
P8	55	F	Breast	No	AL-Hamzah	4.66 ± 0.18
P9	48	F	Leukemia	No	Diwaniyah	2.83 ± 0.19
P10	55	F	Lymphoma	No	AL-Hamzah	3.23 ± 0.20
P11	53	M	Brain	Yes	Shamiyah	4.97 ± 0.20
P12	74	M	Leukemia	Yes	Sumer	3.21 ± 0.17
P13	70	M	Bladder	Yes	Diwaniyah	4.42 ± 0.18
P14	30	F	Leukemia	No	Sunni	4.81 ± 0.20
P15	61	M	Spinal	No	Diwaniyah	3.88 ± 0.14
P16	50	F	Cervical	No	AL-Hamzah	3.20 ± 0.20
P17	56	M	Stomach	No	Al-Sudair	2.34 ± 0.19
P18	40	F	Breast	No	Diwaniyah	3.17 ± 0.14
P19	19	M	Leukemia	No	Diwaniyah	2.85 ± 0.16
P20	33	F	Breast	No	Shamiyah	3.34 ± 0.12
P21	47	F	Breast	No	Diwaniyah	3.41 ± 0.16
P22	24	F	Lymphoma	No	Shamiyah	3.87 ± 0.10
P23	73	M	Lung	No	Diwaniyah	3.67 ± 0.17
P24	95	M	Prostate	Yes	Diwaniyah	5.36 ± 0.21
P25	62	F	Breast	No	Diwaniyah	4.11 ± 0.15
P26	34	F	Stomach	No	Sunni	5.06 ± 0.21
P27	30	F	Lymphoma	No	Sunni	4.52 ± 0.11
P28	67	M	Liver	Yes	Diwaniyah	4.01 ± 0.15

P29	42	M	Leukemia	No	Diwaniyah	4.98 ± 0.20
P30	41	M	Lung	No	Diwaniyah	4.49 ± 0.22
Mean ± Std Error						**4.017 ± 0.17**

Urinary uranium of the healthy group is shown in table3, from this table the results ranged between 4.63 µg/l for male, 36 years, from Al-Shamiya and 1.02 µg/l for female, 43 years, from Sumer .The mean of uranium level in urine for this group was 2.01 µg/l. Tables 2, 3 illustrate the mean value of urinary uranium of the cancer patients group was two times higher than the healthy group. This finding indicates that the cancer patients exposed to high level of uranium by inhalation or ingestion air and food contaminated with uranium due to the military and human activities. Statistically significant difference in urinary uranium levels between healthy subjects and cancer patients group was observed by independent sample test ($P < 0.001$).

Table 3. Concentration of uranium (µg/l) in urine samples of the healthy subjects

Sample code	Age (Year)	Gender	Smoking habit	Location	Uranium content ± Std. Error
H1	36	M	Yes	Shamiyah	4.63 ± 0.19
H2	35	F	No	Al-Hamzah	1.84 ± 0.10
H3	63	M	Yes	Shamiyah	2.02 ± 0.15
H4	53	M	Yes	Sunni	2.07 ± 0.12
H5	50	F	No	Diwaniyah	2.13 ± 0.13
H6	48	F	No	Diwaniyah	2.01 ± 0.16
H7	57	F	No	Diwaniyah	1.69 ± 0.15
H8	56	F	No	Diwaniyah	1.22 ± 0.15
H9	43	F	No	Shafei	1.14 ± 0.18
H10	57	F	No	Shamiyah	1.52 ± 0.13
H11	52	M	Yes	Sumer	2.95 ± 0.18

H12	75	M	Yes	Afak	2.20 ± 0.15
H13	70	M	No	Diwaniyah	1.92 ± 0.12
H14	25	F	No	Sunni	1.35 ± 0.17
H15	50	M	No	Diwaniyah	1.03 ± 0.16
H16	49	F	No	AL-Hamzah	1.70 ± 0.17
H17	56	M	Yes	Diwaniyah	2.01 ± 0.16
H18	44	F	No	Diwaniyah	1.66 ± 0.15
H19	19	M	No	Diwaniyah	1.64 ± 0.13
H20	32	F	No	Diwaniyah	1.41 ± 0.11
H21	43	F	No	Sumer	1.02 ± 0.15
H22	23	F	No	Diwaniyah	1.66 ± 0.14
H23	70	M	Yes	Al-Hamzah	2.57 ± 0.18
H24	90	M	No	Diwaniyah	2.94 ± 0.19
H25	63	F	No	Al-Sudair	2.10 ± 0.16
H26	33	F	No	Diwaniyah	2.11± 0.14
H27	27	F	No	Daghara	1.83 ± 0.16
H28	63	M	No	Al-Hamzah	2.07 ± 0.15
H29	41	M	Yes	Diwaniyah	3.40 ± 0.13
H30	42	M	Yes	Sumer	2.63 ± 0.16
Mean ± Std Error					**2.01 ± 0.15**

Table 4 shows the average of uranium content in human urine depending on the gender of volunteers. The mean value of uranium level in urine of males and females cancer patients group is 4.09 ± 0.18 μg/l and 3.94 ± 0.16 μg/l respectively, while the mean value of urinary uranium of males and females healthy subjects is

2.43 ± 0.15 μg/l and 1.64 ± 0.14 μg/l respectively. The results reveal that the uranium levels in urine samples of men cancer patients and healthy subjects are more than women of the study groups. The case behind this result can be attributed that the males ingested more uranium through food and water where they drink water in sufficient amounts during long working hours or maybe the exposure to the uranium from the working place, therefore the adult male showing a higher urinary uranium than female. [12]. The mean value of uranium concentrations in urine samples of the study groups as a function of the smoking habit plotted graphically in Figure 3. As presented in this figure the mean value of uranium concentration of smokers and non-smokers of cancer patients group is 4.60 ± 0.18 μg/l and 3.67 ± 0.17 μg/l respectively, while the mean value of uranium content of smokers and non-smokers of healthy subjects is 2.92 ± 0.15 μg/l and 1.74 ± 0.14 μg/l respectively. The mean values of urinary uranium for smokers of cancer patients and healthy subjects are higher than those for non-smokers of cancer patients and healthy subjects. This is because people who smoke have a higher dose of uranium in their bodies than non-smokers due to uranium in tobacco get in the body by the smoking. Many studies reported high levels of alpha emitters and uranium in different organs of the human body of smokers such as tooth, blood, hair and soft tissues [9, 17].

Table 4. Concentration of uranium (μg/l) in urine samples as a function of gender

	Gender	No. of subjects	Mean ± Std Error
Cancer patients	Male	14	4.09 ± 0.18
group	Female	16	3.94 ± 0.16
Healthy group	Male	14	2.43±0.15
	Female	16	1.64±0.14

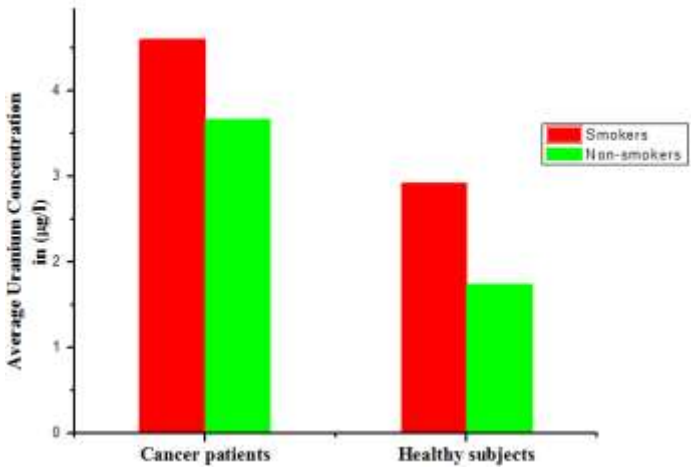

Figure 3. Uranium concentrations in urine sample as a function of smoking habit

Table 5 represents the comparison of the present results with the results of other researchers for the different countries. The results of the present investigation show that the urinary uranium concentrations of cancer patients and healthy subjects are 4.017 ± 0.17 µg/l and 2.01±0.15 µg/l, respectively. These values are higher than those that found in other countries. On other hand, the results of the study groups are about a factor of 4 to 8 higher than ICRP references mean value of urinary uranium 0.5 µg/l [18]; this indicates that the Iraqi environment has been badly polluted due to continuous wars since Gulf war up to now.

Table 5. Uranium concentration (µg/l) in urine samples for different countries

country	uranium content	References
Jordon	0.32	[1]
India	0.017 ± 0.014	[6]
Iraq, Al-Anbar	1.31 ± 0.001	[11]
ICRP	0.5	[18]
USA	0.035	[19]
Finland	2.64	[20]
Iraq, Al-Diwaniyah Cancer patients	4.01 ± 0.17	Present work
Healthy subjects	2.01± 0.15	

Conclusion

The present results exhibited that the uranium levels in urine samples of the cancer patients are higher than those of the healthy subjects. In addition, it reveals a direct relation between the uranium exposure and cancerous disease. The results of the present investigation are higher than ICRP references mean value of urinary uranium 0.5 μg/l.

Acknowledgements

The authors are thankful the main hospitals in Al-Diwaniyah governorate for providing the urine samples from the cancer patients, and to the volunteers that made possible this work. This study is supported from department of physics, college of education, university of Al-Qadisiyah is gratefully acknowledged.

References:

[1] Al-Jundi J, Werner E, Roth P, Höllriegl V, Wendler I and Schramel P 2004 Thorium and uranium contents in human urine: influence of age and residential area *Journal of environmental radioactivity.* 71(1) 61-70.

[2] Welford G A and Baird R 1967 Uranium levels in human diet and biological materials *Health Physics.* 13(12) 1321-1324.

[3] Trešl I, De Wannemacker G, Quétel C R, Petrov I, Vanhaecke F, Moens L and Taylor P D 2004 Validated measurements of the uranium isotopic signature in human urine samples using magnetic sector-field inductively coupled plasma mass spectrometry *Environmental science & technology.* 38(2) 581-586.

[4] Iversen B 1998 Determination of uranium in urine by inductively coupled plasma mass spectrometry with pneumatic nebulization *Journal of Analytical Atomic Spectrometry.* 13(4) 309-313.

[5] Al-Hamzawi A A, Jaafar M S and Tawfiq N F 2014 The measurements of uranium concentration in human blood in selected regions in Iraq Using CR-39 track detector *In Advanced Materials Research.* (925) 679-683

[6] Dang H S, Pullat V R and Pillai K C 1992 Determining the normal concentration of uranium in urine and application of the data to its biokinetics *Health physics.* 62(6) 562-566.

[7] Aswood M S, Al-Hamzawi A A and Khadayeir A A 2019 Natural radionuclides in six selected fish consumed in south Iraq and their committed effective doses *SN Applied Sciences.* 1(1) 21.

[8] Ting B G, Paschal D C and Caldwell K L 1996 Determination of thorium and uranium in urine with inductively coupled argon plasma mass spectrometry *Journal of Analytical Atomic Spectrometry.* 11(5) 339-342.

[9] Al-Hamzawi A A, Jaafar M S and Tawfiq N F 2015 Concentration of uranium in human cancerous tissues of Southern Iraqi patients using fission track analysis *Journal of radioanalytical and nuclear chemistry.* 303(3) 1703-1709.

[10] Al-Hamzawi A A, Jafaar M S and Tawfiq N F 2014 The relationship between uranium contamination

and cancerous diseases of Southern Iraqi patients *Pensee.* 76(3).
[11] Al-Hamzawi A A and Al-Gharabi M G 2019 Heavy metals concentrations in selected soil samples of Al-Diwaniyah governorate, Southern Iraq *SN Applied Sciences.* 1(8) 854.
[12] Saleh A F, Elias M M and Tawfiq N F 2013 Determination of uranium concentration in urine of workers in an Iraqi phosphate mine and fertilizer plants *Journal of radioanalytical and nuclear chemistry.* 298(1) 187-193.
[13] Battawy A A, Jaafar M S, Munem E A, Tawfiq N F, Mahde M S and Salih N F 2012 Uranium concentration in urine using fission track etch technique *International Review of Physics.* 6(4).
[14] Al-Hamzawi A A, Jaafar M S and Tawfiq N F 2014 Uranium concentration in blood samples of Southern Iraqi leukemia patients using CR-39 track detector *Journal of radioanalytical and nuclear chemistry.* 299(3) 1267-1272.
[15] Al-Gharabi M G and Al-Hamzawi A A 2019 Investigation of uranium concentrations in selected soil samples of Al-Diwaniyah governorate, Iraq using CR-39 detector *In Journal of Physics: Conference Series*. IOP Publishing 1234 (1) 012061.
[16] Al-Hamzawi A A, Tawfiq N F, Aswood M S and Najim F A 2019 Determination of radon concentrations near mobile towers in selected cities of Babylon governorate, Iraq *In Journal of Physics: Conference Series.* IOP Publishing 1234 (1) 012026.
[17] Almayahi B A, Tajuddin A A and Jaafar M S 2014 Radiobiological long-term accumulation of environmental alpha radioactivity in extracted human teeth and animal bones in Malaysia *Journal of environmental radioactivity.*129140-147.
[18] ICRP, *International Commission on Radiological Protection* 1975 ICRP Publication 23, UK.
[19] Ting B G, Paschal D C, Jarrett J M, Pirkle J L, Jackson R J, Sampson E J and Caudill S P 1999 Uranium and thorium in urine of United States residents: reference range concentrations *Environmental research* 81(1) 45-51.
[20] Karpas Z, Paz-Tal O, Lorber A, Salonen L, Komulainen H, Auvinen A and Kurttio P 2005 Urine, hair, and nails as indicators for ingestion of uranium in drinking water *Health physics.* 88(3) 229-242.

Structural, Morphological and Electrical properties of PVDF/lithium Iron Oxide nano-composites

Ruqaya Fouad Kadhim and Zainab Raheem Muslim

University of Baghdad, College of Science, Physics Department
Ruqia.f.k@gmail.com

Abstract: Lithium iron oxide, $LiFeO_2$ (LFO) powder has been successfully prepared by sol-gel method. The structure, morphology electrical and dielectric properties were investigated, cubic structure for LFO was characterized by X-ray diffraction (XRD). AFM result shows a nano LFO powder. PVDF polymer was added to the LFO is prepare composites with different percentages (1,2,3 and 4) wt.%. The results show that A.C. conductivity is found to increase with the increasing frequency. The dielectric properties reveal that the C value decreases with the increasing frequency. The values of the ε_1 and ε_2 are found to decrease with the increasing frequency.
Key Words: PVDF, LFO, dielectric properties.

Introduction

In view of the structural properties of the ceramic semiconductor nanoparticles, the researchers mainly focused on treating and synthesizing them in different ways, specifying and applying them widely in many technological fields. When a ceramic material minimizes to the nanoscale level, a severe change in chemical and physical properties is realized and due the large surface area, it is very useful for to technological applications [1].

$LiFeO_2$ (LFO) have been shown various crystalline polymorphs, One main hurdle of lithium ferrites as electrode materials the outcome their low cycling efficiency and low operating voltage. Iron-based compounds have attracted much attention as active materials for rechargeable Li batteries. LiFeO2 has many structural forms, such as α-, β- and γ-conjugated forms. Lithium ferrite ($LiFeO_2$) with a theoretical capacity of 282 MA Hg^{-1} has important advantages compared to LiCoO2 and LiNiO2 for practical use, because it is non-toxic, environmentally friendly, and contains the most abundant and low-cost metal available in the world. LFO can be used as a novel cathode material in lithium-ion batteries, with significant advantages in terms of environmental safety issues, high capacity, good cycling stability, and high-rate capability [2-3].

Dielectric materials, commonly referred to as electrical insulators, have received much attention owing to their strong electron bonding, good support of electric fields, and low energy loss. In particular, the polarization and depolarization that occur in dielectrics as a result of an external electric field have been

investigated as a means to efficiently charge and discharge electricity. This capability is very useful when applied to capacitors. Dielectrics have also been widely used in many applications, such as transistors, photovoltaic devices, and electrical insulation [4].

PVDF $(-CH2\text{-}CF2-)_n$ is a semi-crystalline polymer with at least four different crystal structures including the α-, β-, γ- and δ-phases. PVDF, a dielectric polymer, has been investigated because of its many good properties such as a good piezoelectric/pyroelectric response, chemical resistance, high dielectric permittivity and low acoustic impedance, so that it has been considered as one of the most widely studied dielectric materials in mechanical energy harvesting technologies. In particular, it can be formed in a variety of nanostructures, such as nanowires, nanofibers, and nanotubes, and can be flexible; therefore, the use of PVDF has been successfully demonstrated in a number of devices, such as capacitors, sensors, and TENGs. In addition to altering effective properties, nanoparticles can have an impact on the morphology and also crystallinity of semi-crystalline polymers. PVDF is a polymorphic semi-crystalline polymer which exhibits crystalline phases [4-6].

2. Experimental Techniques

Synthesis of LiFeO2 powder were prepared by sol-gel method. Firstly, weights (1:1:2) of $LiNO_3$, $Fe(NO_3)_2.6H_2O$ and citric acid were dissolved in (50ml) deionized water which were used as precursor agent. The mixture was heated under stirring at (70-80) °C for several hours, which made the mixture denser and formed the gel. The gel was heated at (150) °C in the air for 6 hours so that all the distilled water gets evaporated. The dried gel was calcined in air at (750) °C for two hours.

3. Results and Discussion

A. X-ray diffraction analysis

XRD patterns of the powdered samples were obtained with an X-ray diffractometer using Cu Ka radiation. The X-ray diffraction spectra for $LiFeO_2$ synthesis by the sol - gel method is reported in Fig 1. it is noted that the LFO show the characteristics diffraction peaks which indicates the formation of cubic (JCPDS NO. 96-100-8637), corresponding to the planes (111), (311), (222), (400), (440), (622), (444) and (800). Some additional minor peaks are observed close to characteristics peak and maybe due indicates the presence of the impurity phase attributed of $LiFeO_2$ are the limiting members of the solid solutions formed by the replacement of Fe^{2+} by $Li+Fe^{3+}$ in Fe_3O_4 [7].

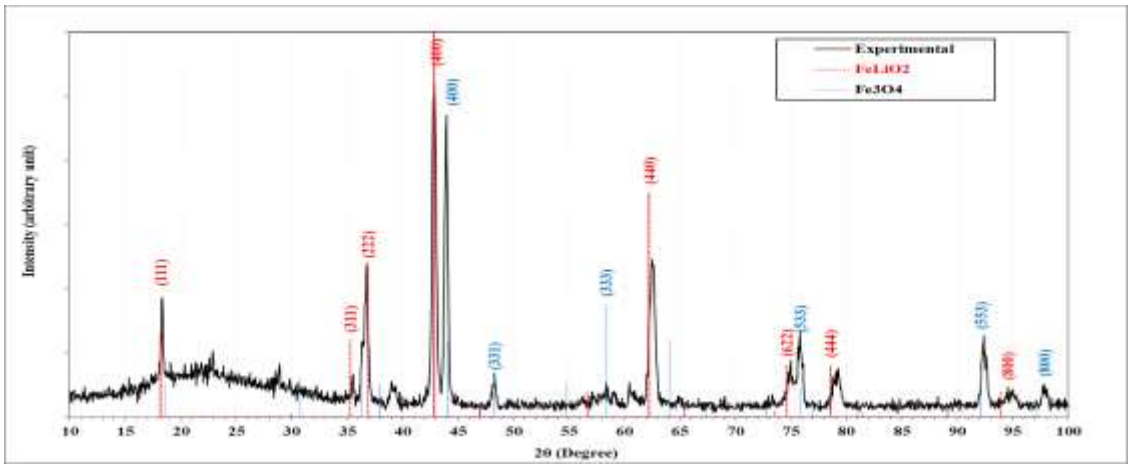

Fig. 1. X-ray diffraction spectra of $LiFeO_2$

B. Electrical properties

The measurement of A.C electrical conductivity ($\sigma_{a.c}$), and its variation with frequency was carried out using an LRC meter IA (impedance analyzer) (2494A Agilent) over a frequency range (50 Hz -5MHz). The samples of (1.2 cm) in diameter and (0.25 cm) in thickness for a shape of a pellet were employed for this study. The angular frequency (ω) is determined through the equation:

$$\omega = 2\pi f \qquad \ldots\ldots (1)$$

Where f is the linear frequency of the applied field.

The variation of capacitance with angular frequency at room temperature for pure PVDF, and PVDF doped $LiFeO_2$ with different ratio (1%, 2%, 3%, and 4%) wt. Fig. 2 shows the capacitance of the PVDF and PVDF: LFO composites. It can be seen from this Figure that the capacitance of the composites decreases with increasing content of LFO doped in the PVDF.

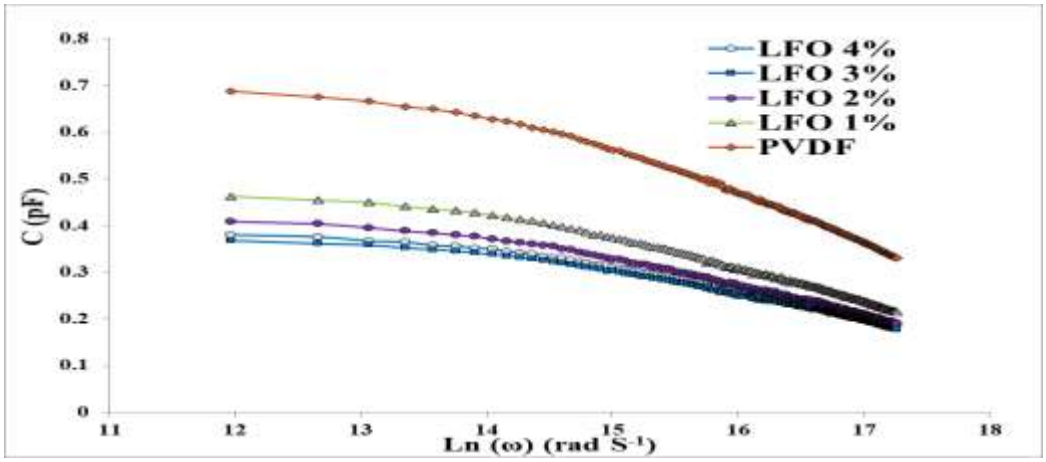

Figure (2): Variation of capacitance (C) with frequency for pure PVDF, and PVDF doped $LiFeO_2$

The variation of A.C electrical conductivity as a function of frequency over a frequency range 50Hz to 5MHz at room temperature for pure PVDF, and PVDF doped $LiFeO_2$ with different ratio (1%, 2%, 3%, and 4%) wt. are shown in Fig. 3. The $\sigma_{a.c}(\omega)$ for all samples were found to increase with increasing frequency. The value of $\sigma_{a.c}$ is calculated using the formula,

$$\sigma_{a.c} = \varepsilon_o \varepsilon_r \omega \tan \delta \qquad \ldots\ldots (2)$$

where ε_o is the permittivity of free space, ε_r is the relative permittivity, ω is the angular frequency and $\tan \delta$ is the dielectric loss. It is observed that conductivity increases with increase in the amount percentage of LFO [8].

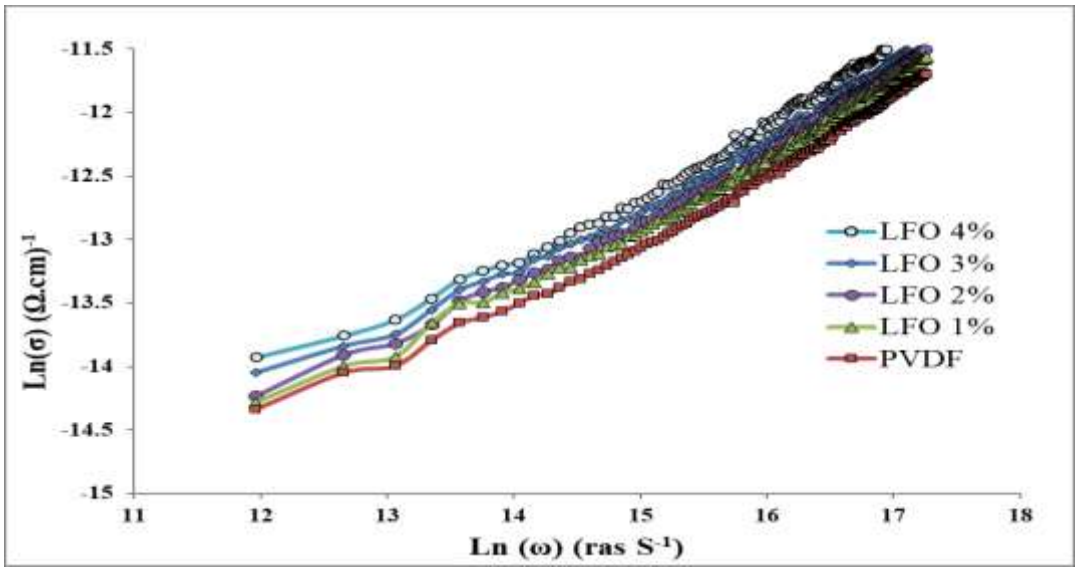

Figure (3): Variation of A.C conductivity with frequency for pure PVDF, and PVDF doped $LiFeO_2$

The variations of dielectric permittivity (ε_1) and imaginary parts (ε_2) of dielectric constant with frequency are described at 50 Hz to 5 MHz at room temperature for various concentrations of pure PVDF, and PVDF doped $LiFeO_2$ with different ratio (1%, 2%, 3%, and 4%) wt. have been shown in Fig. 4 and 5. These observations prove that the electric properties of the polymer improve by adding LFO. These results indicate that the introduced ceramic fillers and interface areas have positive influences on the structure of the polymer matrix and contribute to the enhancement of the dielectric responses and energy storage properties of the nanocomposites.

It is clear that the real part (ε_1) of the dielectric constant decrease with the increase in frequency and reach constant value at high frequencies for all samples, the high value of ε_1 at low frequency was attributed to the presence of blocking electrodes which are unable to permit to the transfer of mobile ions as a result ions are accumulated near the copper electrodes and produce the bulk polarization effect in the material. It is observed from Fig. 4, that the magnitude of dielectric loss decreases with increase of frequencies. The dielectric constant decreased gradually due to the enhancement of the mobility charge carrier; this behaviour is for polar dielectric material. The dielectric relaxation is a result of dipoles in metal-ion chains which shows a peak in ε_2 spectra.

The dielectric loss is found to be very large at low frequency region due to free charge motion within the material. The magnitude of dielectric loss can be regarded as the contribution of three different effects such as DC conductivity, interfacial polarization and the dipole orientation.

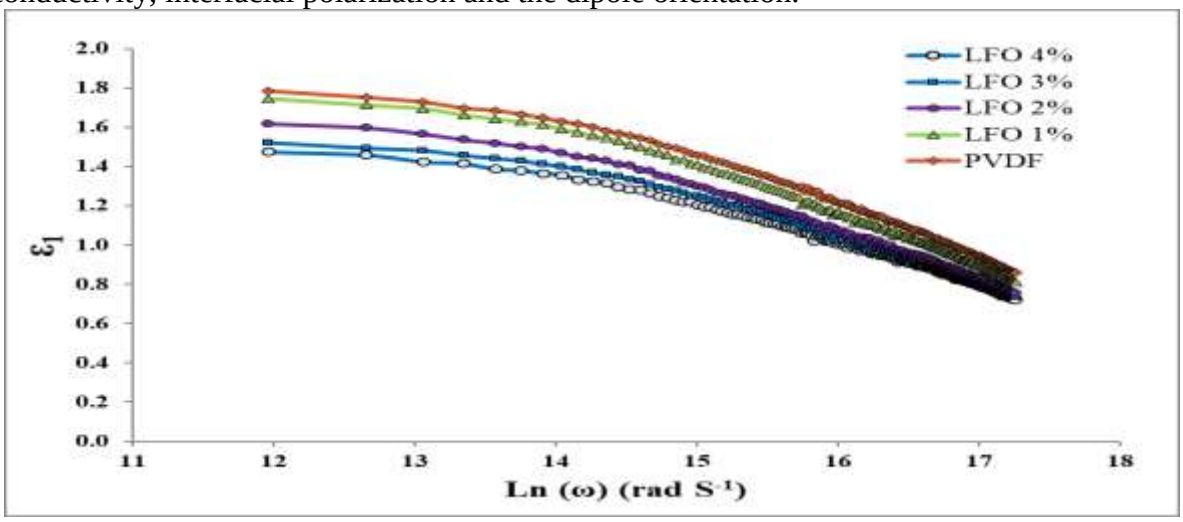

Figure (4): Variation of real part (ε_1) of dielectric constant with frequency for pure PVDF, and PVDF doped $LiFeO_2$

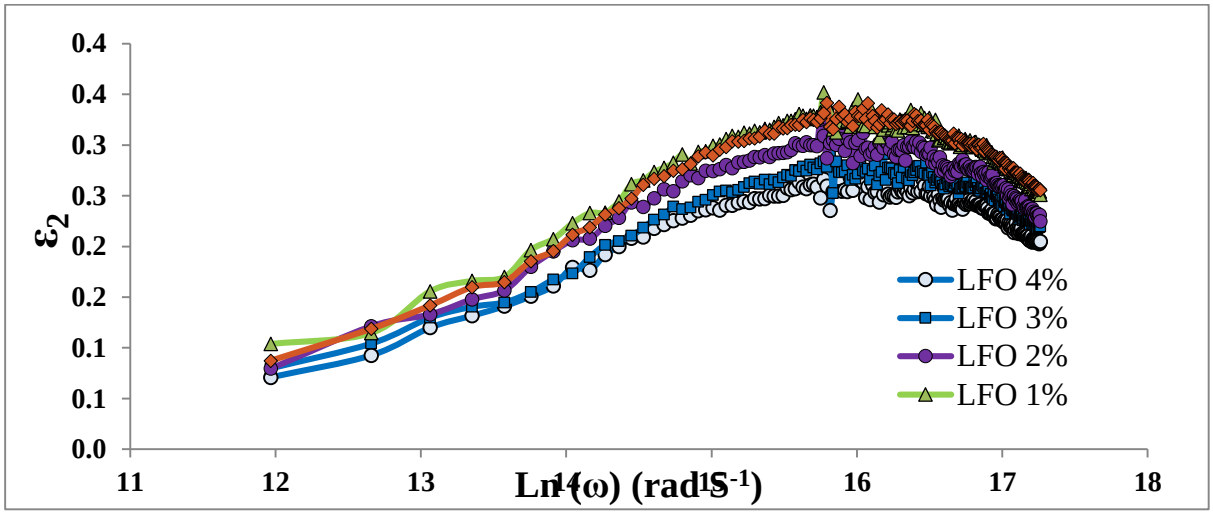

Figure (5): Variation of real part (ε_2) of dielectric constant with frequency for pure PVDF, and PVDF doped $LiFeO_2$

The Cole-Cole plots in materials with multiple relaxation process will be semicircles with centres below the real axis. The semi-circular Cole-Cole plots for different percentages of LFO: PVDF (1%, 2%, 3%, and 4%) wt. is given in Fig. 6. The semicircles drawn are the simulated ones and the curved line the experimental one.

The imaginary part of dielectric constant is a measure of energy spent during polarization. As the amount of LFO increases the dipoles can easily align with the field and hence the maximum value of the imaginary part of dielectric constant decreases.

The Cole-Cole plot in materials ($\varepsilon_2\ vs.\ \varepsilon_1$) is a strong tool for materials retaining one or more well-detached relaxation operation with analogous magnitudes and conform the Cole-Cole formalism, it will be semicircles with centres below the real axis. The plot includes the variation of the loss of dielectric with the storage of dielectric component at constant temperature and figuration of typical semicircle show the presence of single relaxation time.

Figure 8 shows a depressed semi-circular arc due to broad relaxation region and maximum loss occurs at the midpoint of the semicircle, while the dielectric values are read from right to left with an increase of frequency. One interesting conclusion is observed, that at a dielectric constant of infinite frequency ($\epsilon\infty$) and static dielectric constant (ϵs) there will be no loss [49]

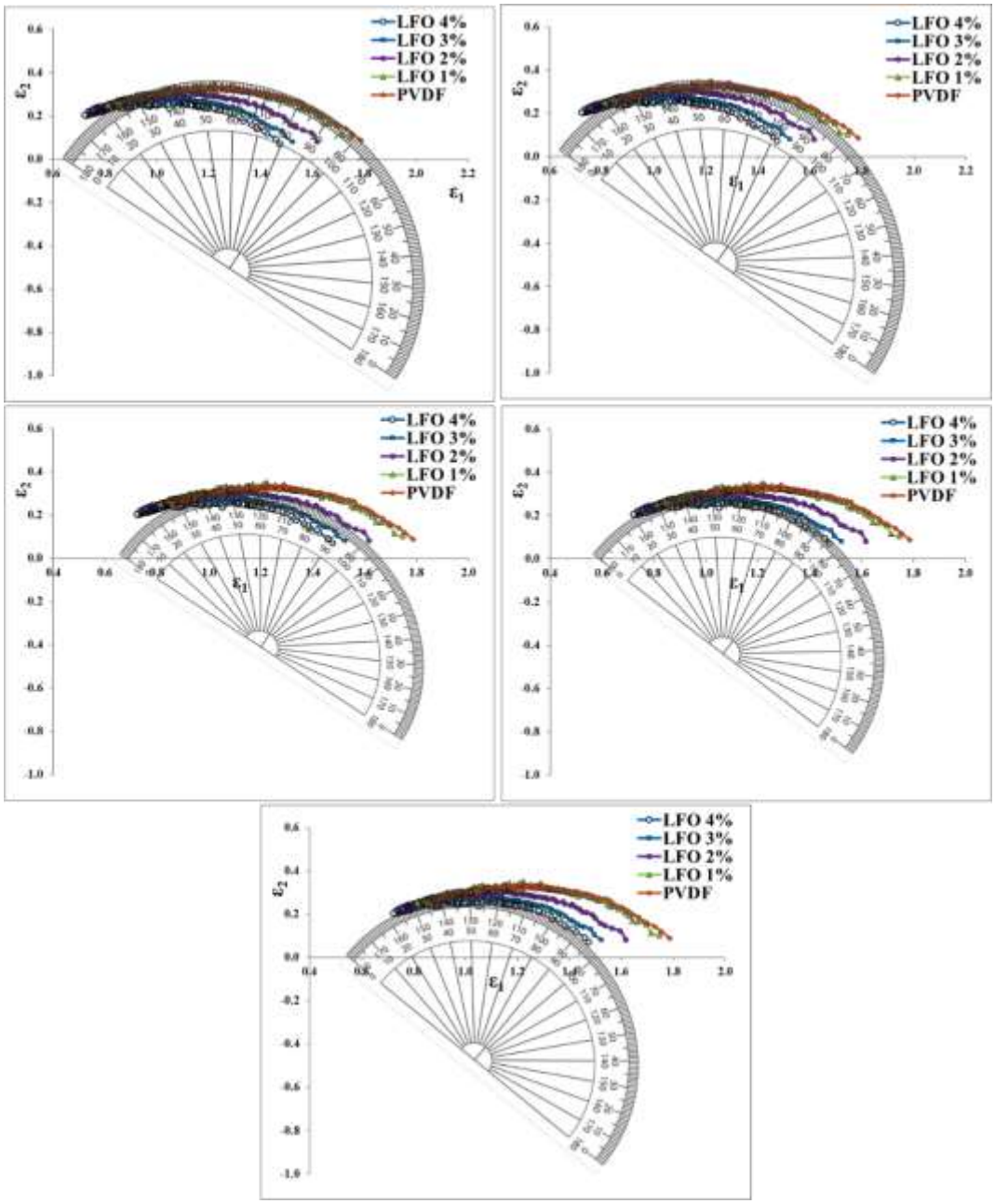

Fig. 6: Cole-Cole diagram of PVDF: LFO with different percentage

Conclusion:

Lithium iron oxide has been successfully prepared by sol-gel. $\sigma_{a.c}(\omega)$ was found to increase with increasing frequency, which is mean that a large number of free electrons exist and the relaxation time τ, i.e. the average time between collisions, is long. The decrease in ε' and ε'' with the increasing frequency is explained by the fact that as the frequency is raised, the interfacial dipoles have less time to orient themselves in the direction of the alternating field. As the frequency increases, charges can no longer follow the field and their contribution to the dielectric constant ceases. The LFO powders in PVDF improved the dipole-dipole interaction among powders and hence the effective dielectric constant of the composites was enhanced.

Structural Properties and Characterization of Lithium Olivine Compounds

Z R Muslim[1] and A Q Kadhum[2]

[1] University of Baghdad, College of Science, Department of Physics, Iraq
[2]Ministry of Industry, Al-Rasheed Factory, Baghdad, Iraq
Zainabraheem2018@yahoo.com

Abstract. Lithium Nickel Phosphate LiNiPO4 and compounds were prepared by addition of some metals precursors like Silver, Carbon and Aluminum to be doped in net powder using "sol-gel "process. The analysis of structural peak intensity with morphology of powders was studied by" XRD, EDX, AFM and SEM". Heat treatment for materials was performed in temperature in (800) C° in several hours. XRD reveal the olivine structure of $LiNiPO_4$ .Morphology were done using SEM photo images, this assisted by AFM test. .EDX shows the elements of Ni, O, C, Ag and Al.

1. Introduction

The technology of batteries are increasing now days depending on specific properties like high energy density and high voltage has important because of the development in many devices such as portable devices [1]. Li -ion battery sources are one of the important power density systems for advanced technology. These Li ion batteries supply the source for high capacity [2]. . Many researchers study and improve the batteries properties like higher operating voltage, long cycle life and safety [3] and [4].

Lthium ion rechargeable batteries are important due to their high voltage about 4V and energy density used in space applications [5-7]. Cathodes are made typically from phosphates and oxides using many methods, these undergo oxidation [8]. The choice of cathode depends on factors like cost, safety, cycle of life and power [9].

2. Process

"$LiNiPO_4$, LiNiPO4doped carbon, and doped Ag and Al "were synthesis using "sol-gel process". Nitrate of "lithium, Nickel, Aluminum and silver"with."$NH4H_2PO_4$" and" citric acid "were used as precursors. Resulted LiNiPO4 powder was mixed with equal amount of above precursors by addition of DI water (table1,). These precursors mixed by applying heat at(80)°C for 24 hrs.', until the mixture will be dense to get the gel using hot plate with raising temperature to (100) °C in air for 8 hrs.

The gel dried and heat treated in air oven to (800) °C for 2 hrs.LiNiPO4/C compounds was synthesized in the same procedures by addition 3 more times weight of citric acid to get the carbon as added material with the aid of metal precursors the resulted LiNiPO4/C/M, (M=Al and Ag) compounds The final powder show yellow color for all compounds, as it shown in 'Figure 1' as the result obtained by [10].

Table 1. Materials used and chemical formula.

Material	Chemical formula	Purity (%)	Supplier
Lithium nitrate	$LiNO_3$	98	Fluka, India
Nickel nitrate	$Ni(NO_3)_2.6H_2O$	97	HAMEDIA ,India
Nickel acetate	$Ni(CH_3COO)_2.4H_2O$	98	Central Drug House, India
Aluminum nitrate	$AlNO_3$	99.9	Fluka, India
Silver nitrate	$AgNO_3$	99.9	Fluka, India

Figure1. Colors of (a) $LiNiPO_4$, (b) $LiNiPO_4$ doped carbon, (c) $LiNiPO_4$ doped carbon and silver and (d) $LilNiPO_4$ doped carbon and Aluminum powders.

3. RESULTS AND DISCUSSION

Crystallinity for lithium nickel and compounds are shown in 'Figure 2' the crystalline peak intensity and height is based on the standard card of analysis '. It shows a narrow and sharp crystalline peak of the

orthorhombic olivine structure, as the result obtained by [3]. The similar peaks reveal many other phases included with the origin compound [4]. The aluminum is not invisible in the peaks behavior this is due to the construction in structure and radius of the "Al "added of $LiNiPO_4$ or due to the variation in structure. SEM images of powders were in 'Figure 3 respectively. The 'Figure 3a' shows the regions of agglomeration of tiny spherical particles, 'Figure 3'show the carbon addition which tend to minimize the agglomeration and growth in particles for $LiNiPO_4$ doped carbon. $LiNiPO_4$/C doped Al particles are found of regular shapes, 'Figure 3c'. Aluminum have varied the morphology, due to the change in the radius of added metal precursors [11]. The morphology for $LiNiPO_4$/C doped silver shown in 'Figure 3d'; it shows a different size due the addition of silver to the compound. Roughness and surface analysis for $LiNiPO_4$ and compounds are all involved and contributed in 'Figure 4. The improvement of uniformity analysis can be expressed by the co addition of metal ions 'Figure 4'b, c and d) the substantial and interstitial of metal a nano graen size for $LiNiPO_4$ doped carbon ,$LiNiPO_4$/C doped Al and $LiNiPO_4$/C doped Ag, respectively.

The roughness of powders were increased according to type of added metal for $LiNiPO_4$ doped carbon, $LiNiPO_4$/C doped Al and $LiNiPO_4$/C doped Ag, respectively. The elemental ratios of powders were characterized using EDX, 'Figure 5'. The result analysis of spectrum resulted peak intensity, which depend on ratios of metal included in the compounds, which shows mutually consistent with researches [12].

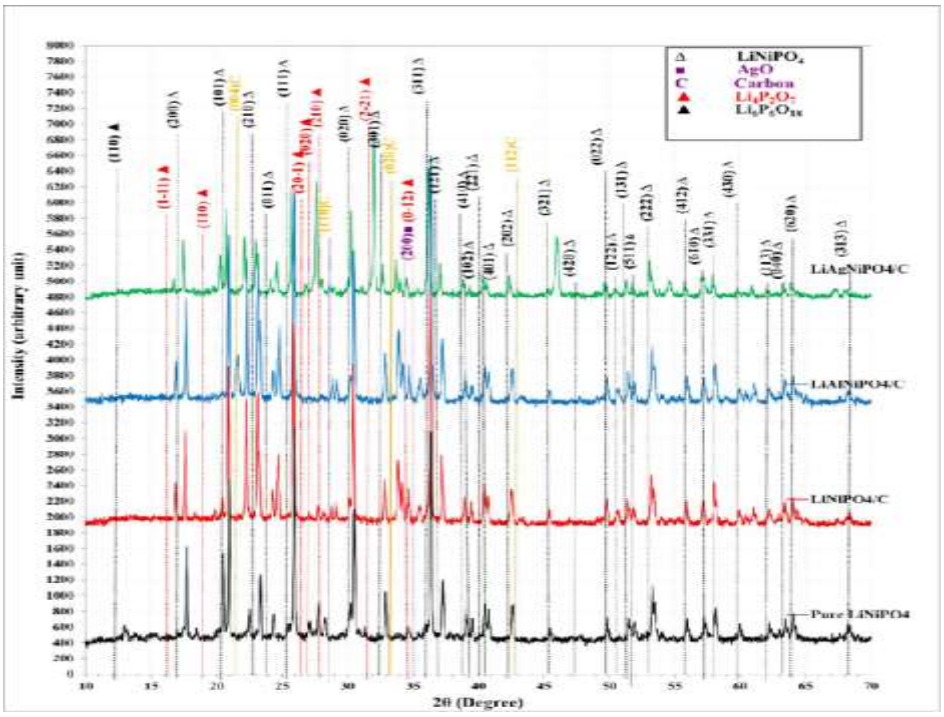

Figure 2. Structural characterization of pure $LiNiPO_4$, $LiNiPO_4$ doped carbon, $LiNiPO_4$/C doped Aluminum and $LiNiPO_4$/C doped silver.

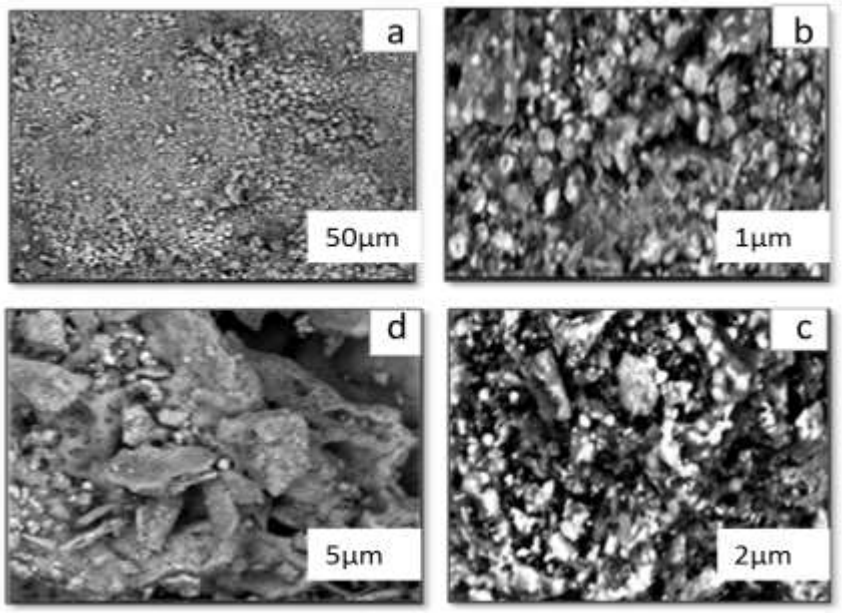

Figure 3. Morphology for images yielded of (a) $LiNiPO_4$; (b) $LiNiPO_4$ doped carbon (C) $LiNiPO_4$/C doped Aluminum and (d) $LiNiPO_4$/C doped silver.

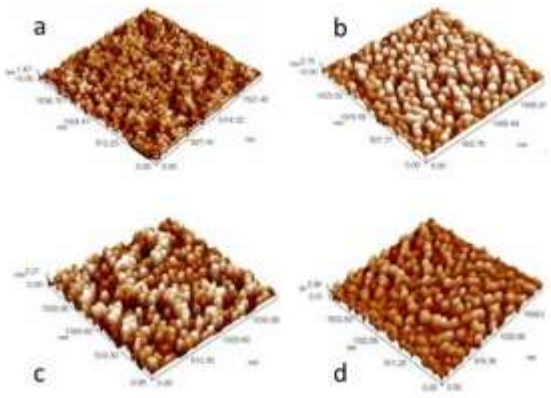

Figure 4. Uniformity analysis of surface for (a) pure $LiNiPO_4$, (b) $LiNiPO_4$ doped carbon, (c)$LiNiPO_4$/C doped Aluminum and (d) $LiNiPO_4$/C doped silver.

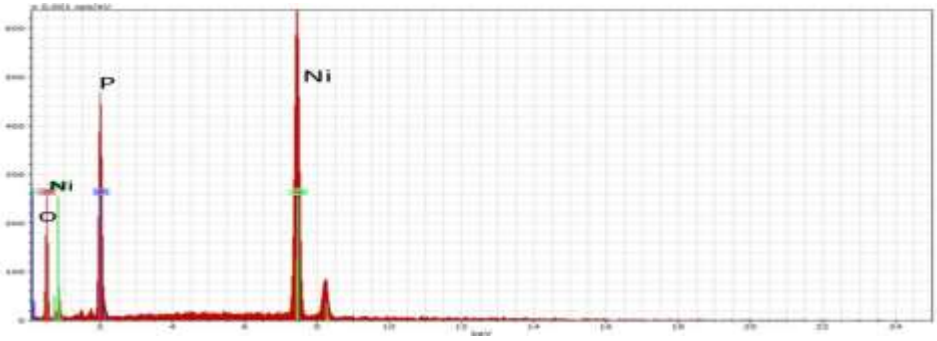

Figure 5a. EDX for $LiNiPO_4$

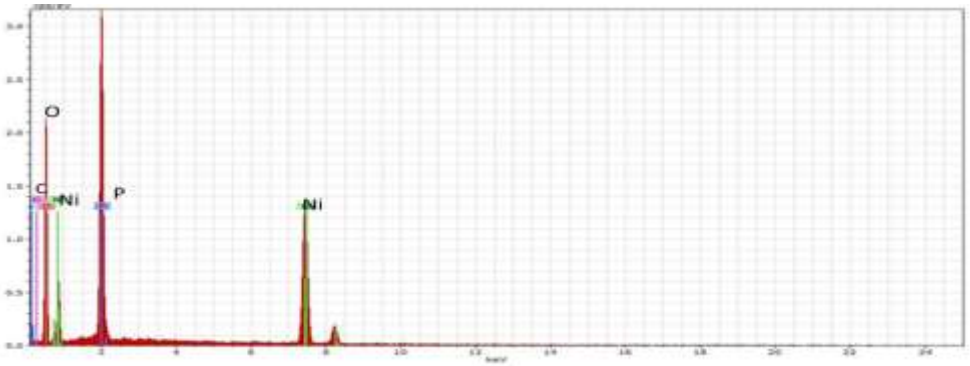

Figure 5b. EDX for $LiNiPO_4$ doped carbon

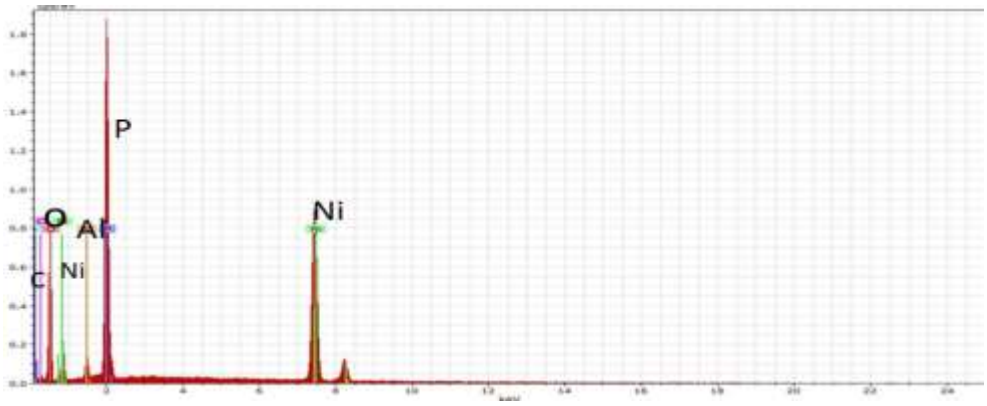

Figure 5c. EDX for $LiNiPO_4$/C doped aluminum.

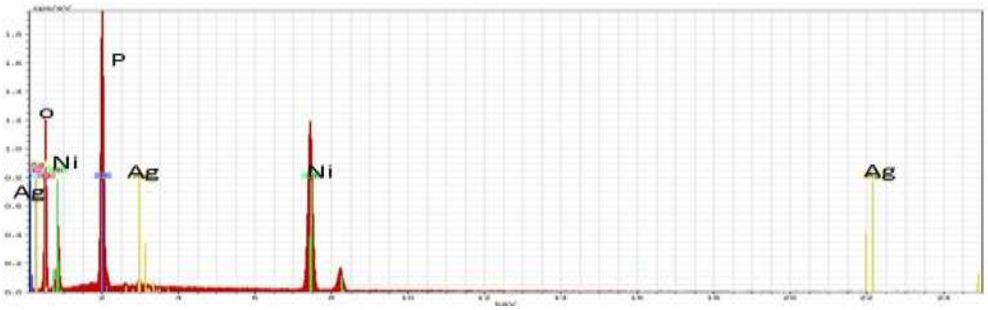

Figure 5d. EDX for $LilNiPO_4$/C doped silver

4. CONCLUSIONS

Olivine's shows sharp crystalline peaks with the indications of different peak intensity changes with all compounds, near-surface region images reveal uniformly distributed particles for pure $LiNiPO_4$ and compounds demonstrate more uniform distribution using the additives compounds. EDX spectrum peaks indicate to the concentration of elements used in the prepared compounds.

5. REFERENCES

[1] Chung H L, Hsuan H C and Chi Y, *2004, Reverse* Microemulsion synthesis and electrochemical properties of $LiNiO_2$ Powders. *Tamkang Journal of Science and Engineering, 7(4):199_204.*

[2] Jürgen G C K and Dyer P T, Moseley Z O D A. J and Rand B S, 2009,.Encyclopedia of Electrochemical Power Sources. Elsevier: Kurzweil, P.4538.
[3] ZHANG Y, PAN Y, LIU J, WANG G and CAO D, 2015, Synthesis and electrochemical studies of carbon-modified $LiNiPO_4$ as the cathode material of Li-ion batteries, Chem. Res. Chin. Univ., January, Vol. 31, P. 117—122
[4] Lucangelo. D, Dirk B, Christina S, Wolfram .J, 2012, Investigation of graphitic carbon foams/$LiNiPO_4$ composites, Solid State Electrochem, July 20; Vol, 12, P.3791–3798.
[5] Yangyang F, Huijuan Z, Ling F, Ya O, Yu W, 2015, Designed synthesis of a unique single- crystal Fe-doped LiNiPO4nanomesh as an enhanced cathode for lithium-ion batteries. Mater. Chem. A, Vol.3 (31):15969-15976.
[6] Peter G. B, Bruno S, and Jean M T,2008, Nanomaterials for rechargeable lithium batteries.Chem, Int.Ed, Vol. 47: 2930–2946.
[7] Satyavani, A. Srinivas Kumar and P.S.V. Subba Rao. Methods of synthesis and performance improvement of lithium iron phosphate for high rate Li-ion batteries. , Engineering science and Technology.2016; 19(1):178-188.
[9] Rui Q, Ming C Y, Ying S M and Wolfgang S. 2013,Synthesis of $LiNixFe1{-}xPO_4$ solid solution as cathode materials for lithium-ion batteries. Electrochimica Acta, Vol.108, P. 827-832.
[10] Subramanya H, Ellis P, Coombs N and Nazar L F, 2004,Nano-network electronic conduction in iron and nickelolivine phosphates. Nature materials, February 22, Vol.3, P.147-152.
[11] Martin R, Roald H, and Ashcroft N W, 2016, Atomic and ionic radii of elements 1–96. Chem. Eur. J, Vol. 22, P. 14625 – 14632.
[12] khalfaouy R E, knidri H E, Belaabed R, Addaou A, Laajeb A, Lahsini A,2016, Synthesis and characterization of $LiMnPO_4$ material as cathode for Li-ion batteries by a precipitation method and solid-state blending. *J. Mater. Environ. Sci. Vol.7 (1):40-49.*

Structural,Optical and Sensing Properties of ZnO:Cu Films Prepared by Pulsed Laser Deposition

Saleem A Hussain1 , Awatif J Radi1,2 , Firas A Najim1 , Mohamed A Shaheed1

Saleem.hussain@qu.edu.iq
1Department of Physics , College of Education ,University of Al-Qadisiyah, Diwaniyah ,Iraq
2 Babylon Education Directorate , Babylon , Iraq .

Abstract. This research aims to study the effect of deformation on the structural, optical and allergic properties of ZnO films prepared by pulsed laser deposition technique were deposited on glass substrate. ZnO were deformed with a copper element in different ratios (3%, 7%, 9%) due to changing the environment temperature at 275°C and annealed to 400°C. The X-ray diffraction shows that all films have polycrystalline structure with hexagonal shape due to annealing process, and they have a high permeability of 80% with energy gap 3.35eV. The best sensitivity was clear at (7%) ratio..

Key words: Zinc oxide, Pulse laser deposition, X-ray diffraction, Optical properties, Electrical resistance, gas sensing

1.Introduction

Zinc oxide is a semiconductor of the second-hexagonal group (II-IV) with a polycrystalline hexagonal structure [1]. It has large exciting binding energy and wide direct band gap of (3.3eV), so that excitonic emission processes can persist at or even above room temperature [2-3]. Pure zinc oxide is a white solid, nontoxic, not soluble in water or alcohol. Zinc oxide is an amphoteric substance because it dissolves in acids such as acetic acid, mineral acids, ammonia, ammonium carbonate and alkaline hydroxides [4].The crystal structure of zinc oxide including three types as shown in fig. 1 The crystal structure is more stable. It has a unit cell with constants (a = 3.24 Å) and ((c = 5.19 Å), cubic crystal structure which is divided into: a- Rock salt cube , b-Zinc blende and c-Wurtzite. The ZnO crystallizes in the wurtzite structure.[5] Zinc oxide is utilized in many applications including transistors, transparent electrodes for laser diodes, solar cell aggregates, radiation shielding, microwave applications, dilute magnetic semiconductor and it is suitable for optoelectronic applications [7]. Copper is one of the most important substances in semiconductor and used for doping the elements of the group (II-VI), when exposed to a thermal effect that will increases propagation inside the material to increase resistance of material [8,9]. The copper element depends on the location it occupies in the host material, either as an impurity donor (or as an acceptor), so that it is either in interfacial sites or in compensatory sites within the crystal structure of the added material depending on the diameters between the copper and the material.

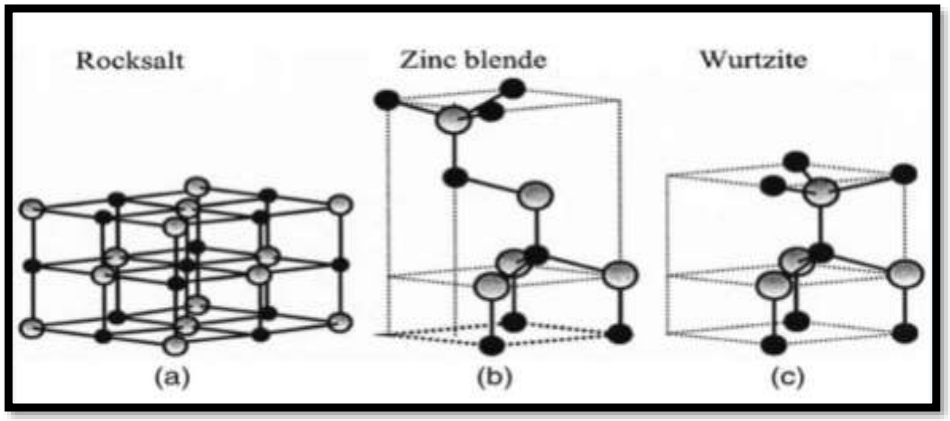

Figure1. Types of Zinc Oxide Crystalline Structure : a- rock salt b- zinc blende c- wurtzite [5-6]

2.Experimental Work .

The pulse laser deposition (PLD) technique is similar to the mechanism of growth of thin films, in this way with other methods of techniques for the preparation of thin films in terms of the formation of the substances, the formation of multiple layers will increasing the cohesion and coherence of layers. The formation of layer will change, as the power density of pulse laser increasing it will lead to changing the thickness of the layer, that mean the particles with high-energy will hit surface target of material. The multiplicity of the particles at the collision area will growth the thickness area of the sample [11]. The collision area is a source of all of kinds particle condensation. The thermal equilibrium is obtained when the particle condensation ratio is greater than the particle precipitation on the collision area, and the film grows on the surface of the substances. Thin films of pure ZnO and ZnO:Cu were prepared at different doping ratios (3%, 7%, 9%) when the substrate temperature (Ts= 275°C) and the number of pulses (300) pulses where all films have thickness approximately (125nm).

3.Result &Discussion :

3.1 X-Ray diffraction

Copper doping ZnO prepared with ratios (3%, 7%, 9%) with substrate Temperature 275°C and annealed to 400°C. The X-ray diffraction showed a hexagonal structure. Polycrystalline structure, the reflections magnitude showed at (100) (002) (101) (102) (110) accompanying with the angles (31.68 °) (34.34 °) (36.16 °) (47.46 °) (56.52 °).These results showed a good matching with ICDD card as in figure (2).

3.2 Atomic Force Microscope :

Atomic force microscopy (AFM) diagnosis of ZnO:Cu doping ratio(3%, 7% , 9%). The results showed that the pure and doping films were homogeneous through 2D and 3D diagnostics with no grouping observed. Irregular material or voids on the surface of the films are homogeneous and vertical heights of the peaks of the material as shown in the images of the atomic force microscope in Figure (3).

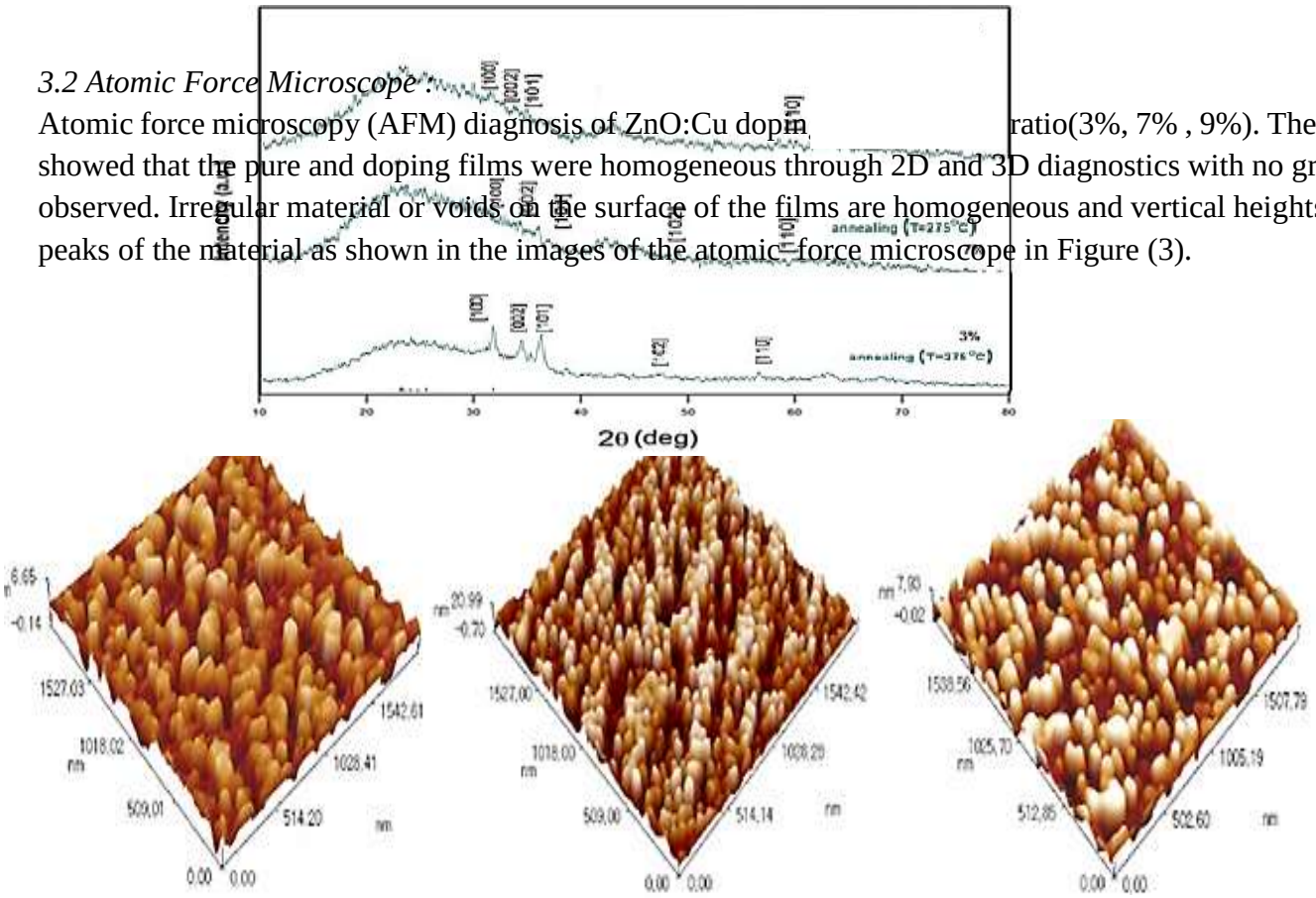

Figu . Atomic force microscopy in of ZnO:Cu thin films doped v a:3%, b: 7%, c: 9%)

3.3 Optical absorption spectrum

Optical absorbance defined as the ratio of the intensity of light falling upon a material and the intensity transmitted. The figure (4) shows the optical absorption spectrum of copper doping ZnO films in different ratios and with substrate temperature (R.T. and Ts= 275°C). The results show that the absorption decreases for all films with increasing wavelength and increasing due to increasing the deformation .

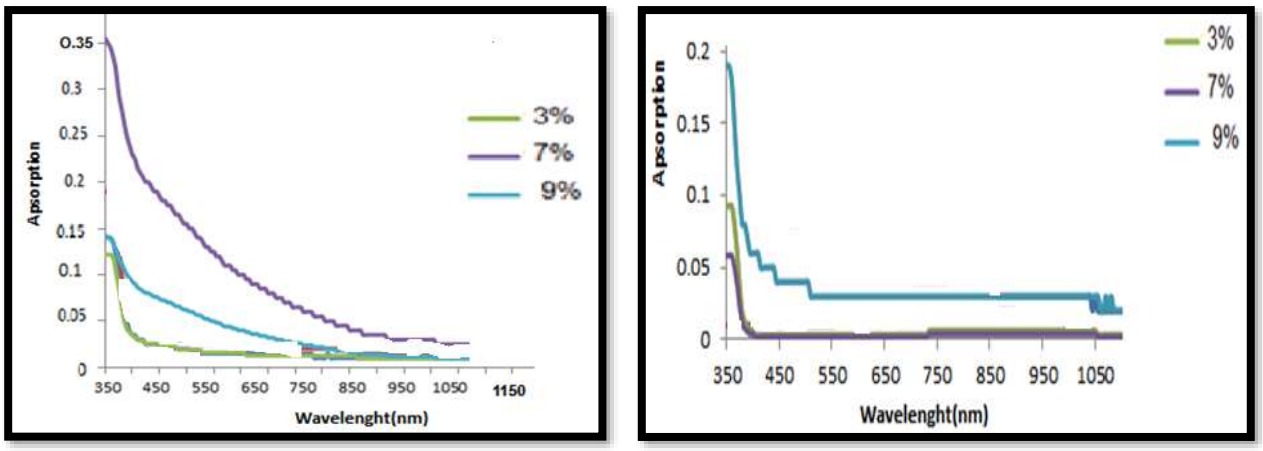

Figure 4. shows an Optical absorption spectrum for ZnO:Cu thin films doped with (3%, 7%, 9%) prepared at R.T. and at Ts=275 ˚C and annealed at (400 ˚C) .

3.4 Optical transmittance spectrum .

Optical transmittance is the ratio between the intensity of the incident radiation from the material to the initial intensity of the radiation falling on the material. The transmittance spectrum depends on the thickness. Surface imperfections and surface roughness also affect the amount of permeability as they work to disperse the incident beam and thus reduce the permeability of the prepared films. Wavelength will decreases with increasing deformation ratio as shown in figure (5).

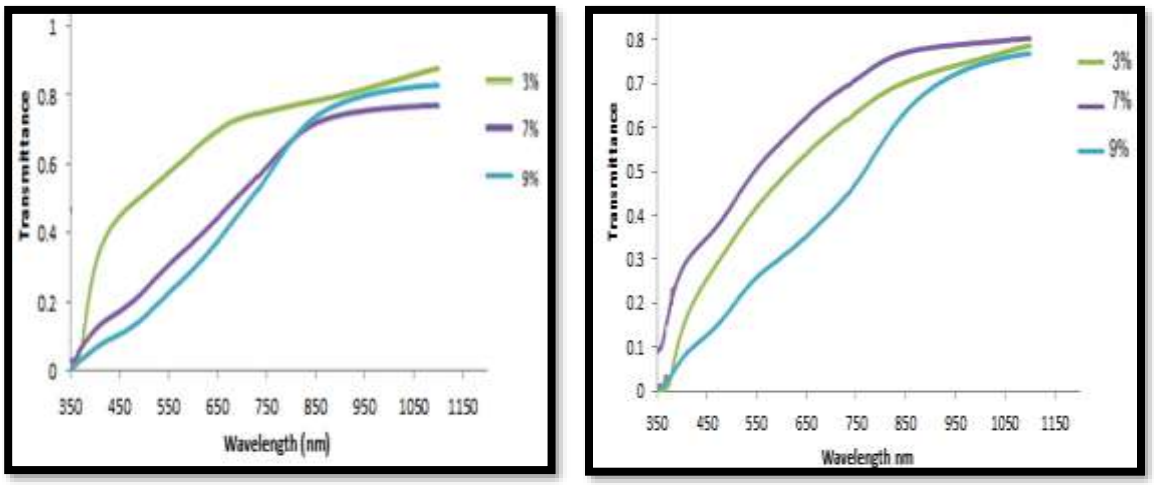

Figure 5. Optical transmittance spectrum of ZnO:Cu thin films doped with (3%, 7%, 9%) prepared at R.T. and at Ts=275◦ and annealed at 400◦C

3.5 Optical Energy Gap.

The energy gap was calculated in the allowable direct electronic transfer at (400ºC). The plot shows relationship between $(\alpha h\upsilon)^2$ and the energy of the incident photon ($h\upsilon$)as in figure (6). The straight line of the curve and intersect it with the photon energy axis at point $(\alpha h\upsilon)^2=0$ where the intersection point shows the energy gap value is given for the allowed direct transitions of doping films, and the amount of the energy gap ranges between (2.95-3.26 eV). These results are consistent with [11] and [12].

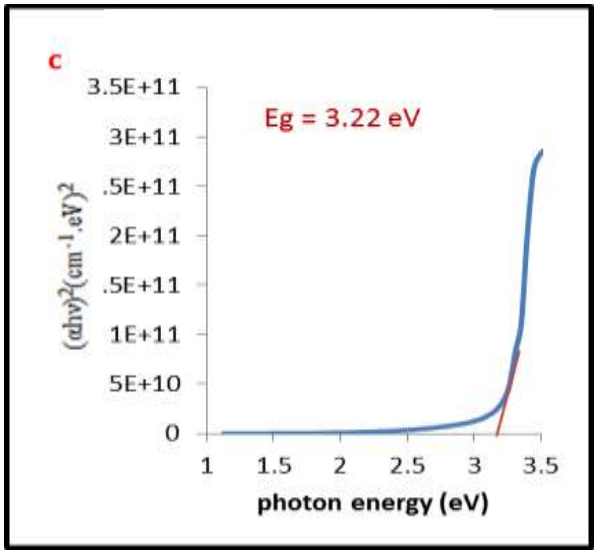

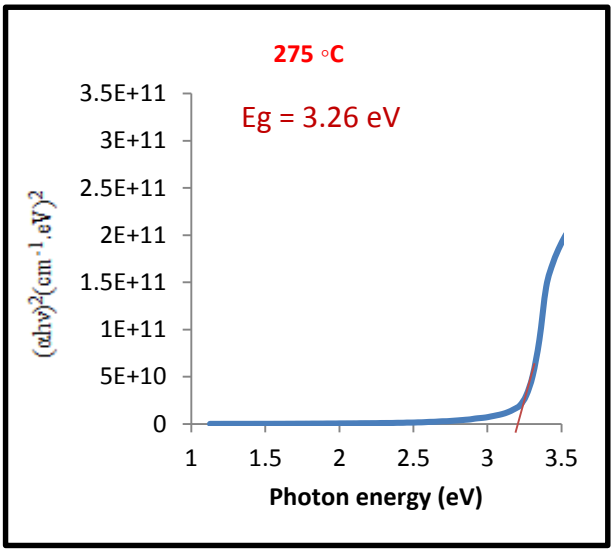

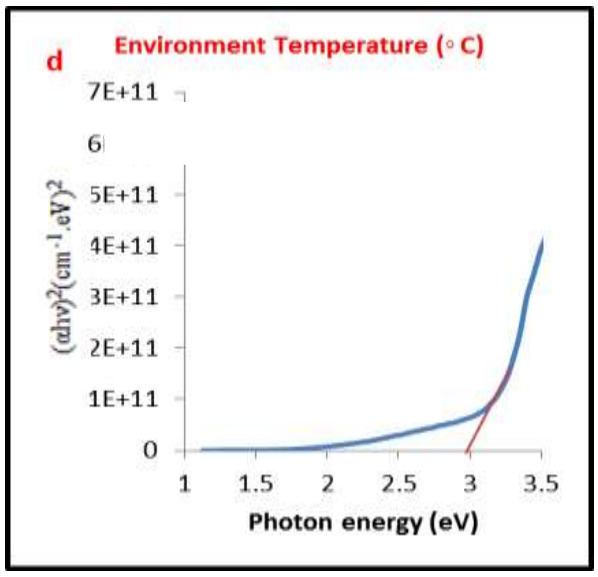

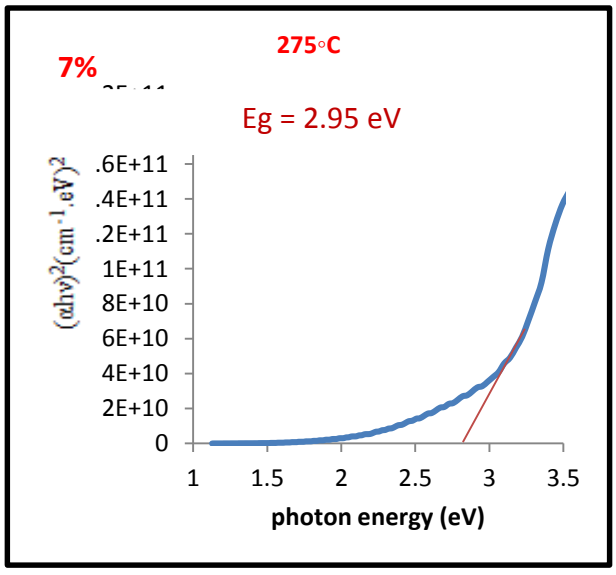

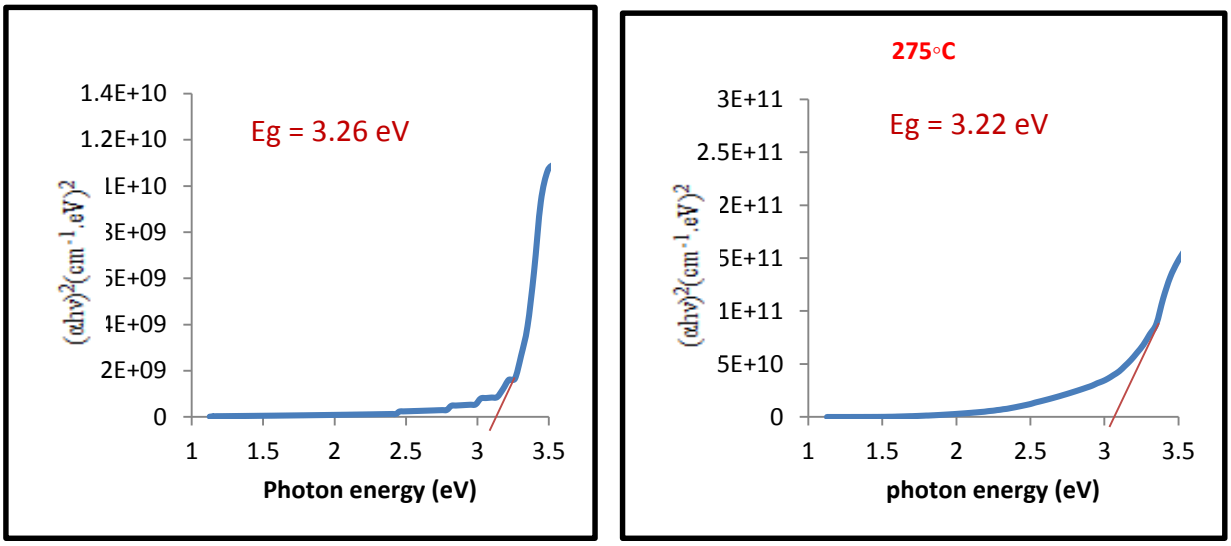

Figure 6. Direct energy gap values for thin films ZnO:Cu doped with (3%, 7%, 9%).

3.6 Sensing properties

3.6.1 Electrical resistance of ZnO:Cu films

The electrical resistance (R) of pure ZnO and ZnO:Cu films doping with different ratio (3%, 7%, 9%) was measured as a function of time with constant temperature and then the resistance was measured at different operating temperatures (35°C (R.T), 100°C ,200°C , 300°C), Sensing reactions appeared at all these degrees except 35°C(R.T), there was no response to the films at this temperature. The film prepared from pure ZnO observed that the resistance increases with increasing temperature. The figure (7) shows the relation between time in minute and the electrical resistance and as we seen that the prepared films moved from the n-type to p-type because of annealing operation.

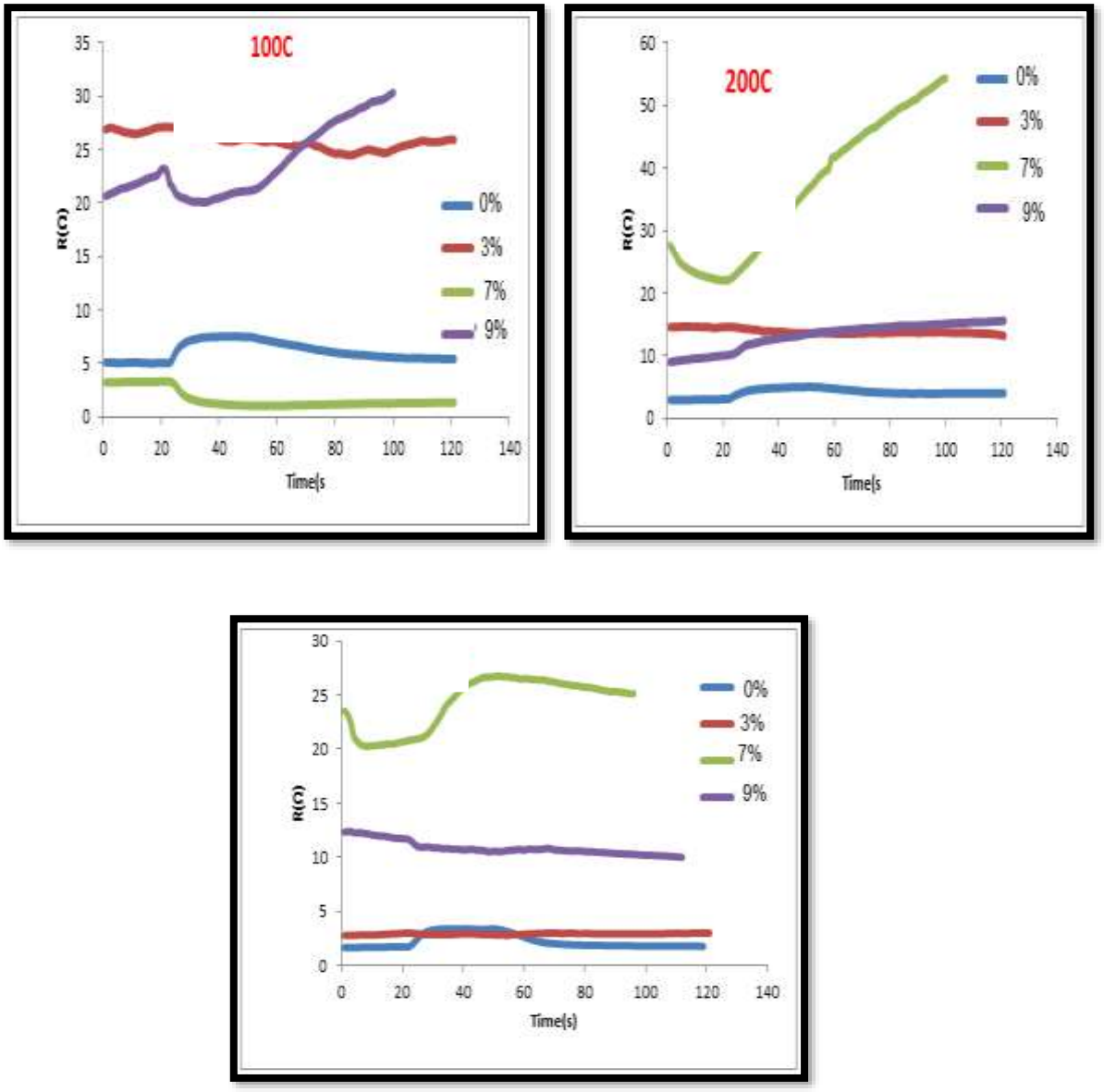

Figure 7. Resistance as a function of time at different operating temperatures for pure ZnO and doped ZnO:Cu films with (3%, 7%, 9%) ratio at (100°C, 200°C, 300°C).

3.6.2 Operating temperature and latency response .

The response time (Tres) is defined as the time at which the gas response occurs and returns to the initial state. Figure (8) shows the response and recovery time of pure ZnO and ZnO:Cu films with different ratios (3%, 7%, 9%).

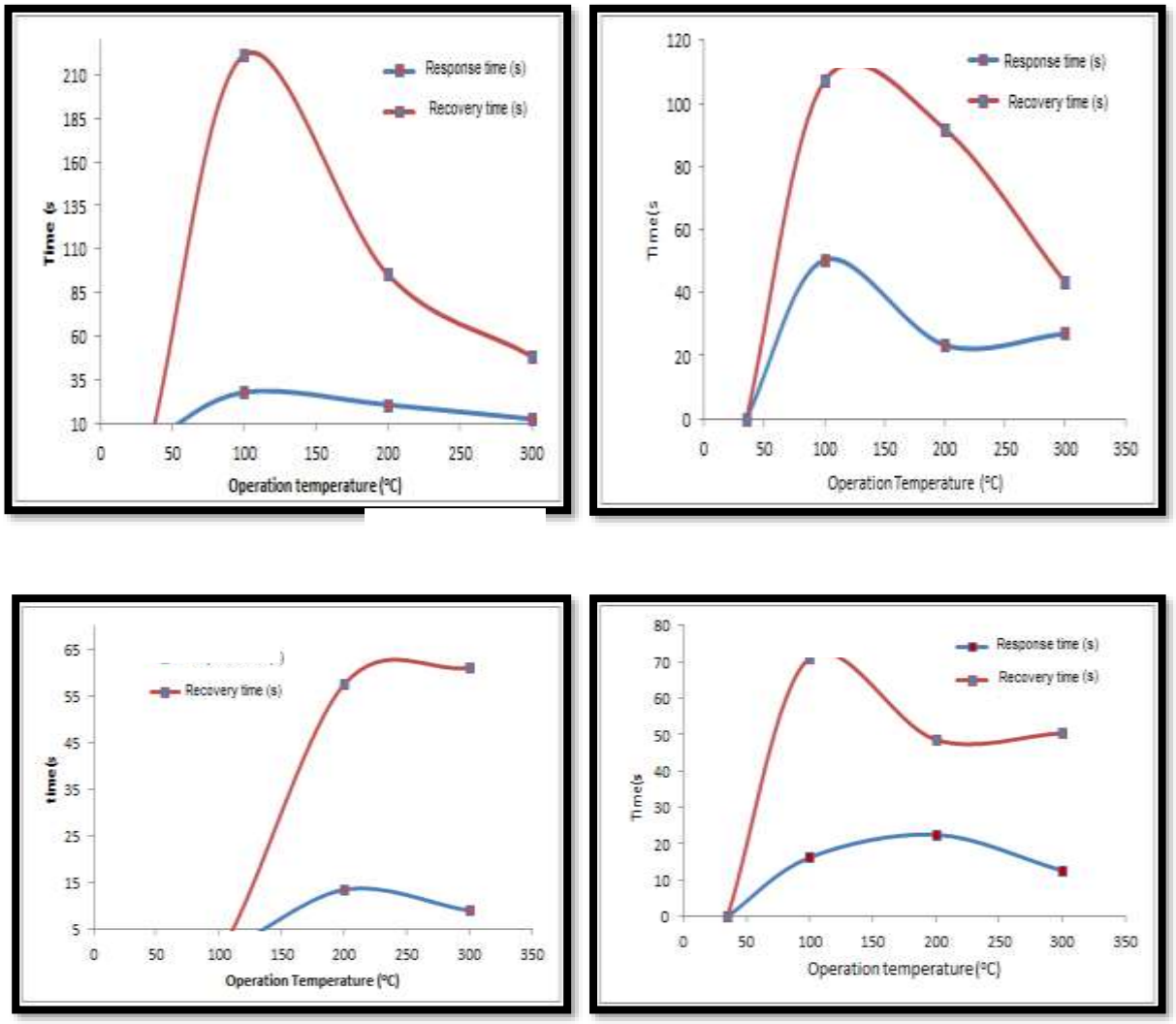

Figure 8. Response and recovery time as a function of the operating temperature of the prepared films for pure ZnO and ZnO:Cu doping with (3%, 7%, 9%)

3.6.3 Sensitivity

The sensitivity of pure and copper doped ZnO films was calculated in different ratios (3%, 7%, 9%) were deposited on glass substrates. After the film resistance was measured with the presence of NO2 gas and its absence as a function of time of the relationship (1). The maximum sensitivity of the films was found in the pure ZnO (98.2456%) with an operating temperature (300°C), which is the suitable operating temperature to sensitize the films. While the operating temperature for the doped thin films decreases and reaches 100oC for the doped films with ratio (3%).The sensitivity calculated from equation (1) to show the relation between an operating temperature and sensitivity as in figure (9) and the table1 shows different values of sensitivity and resistance for pure copper and for different ratios[13].

$$S = \left|\frac{R_{gas}-R_{air}}{R_{air}}\right| \times 100\% \qquad (1)$$

Where : R_{air} , R_{gas}: the values of electrical resistance by air and gas, respectively.

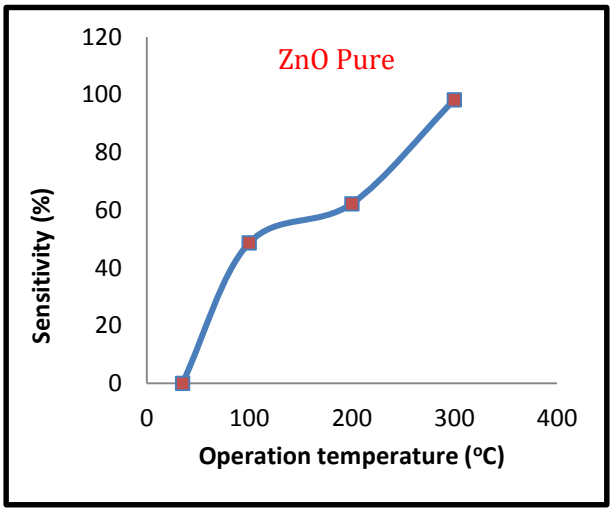

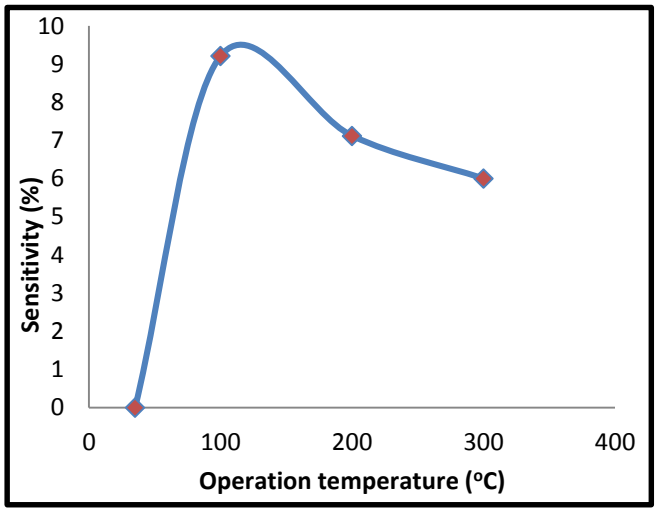

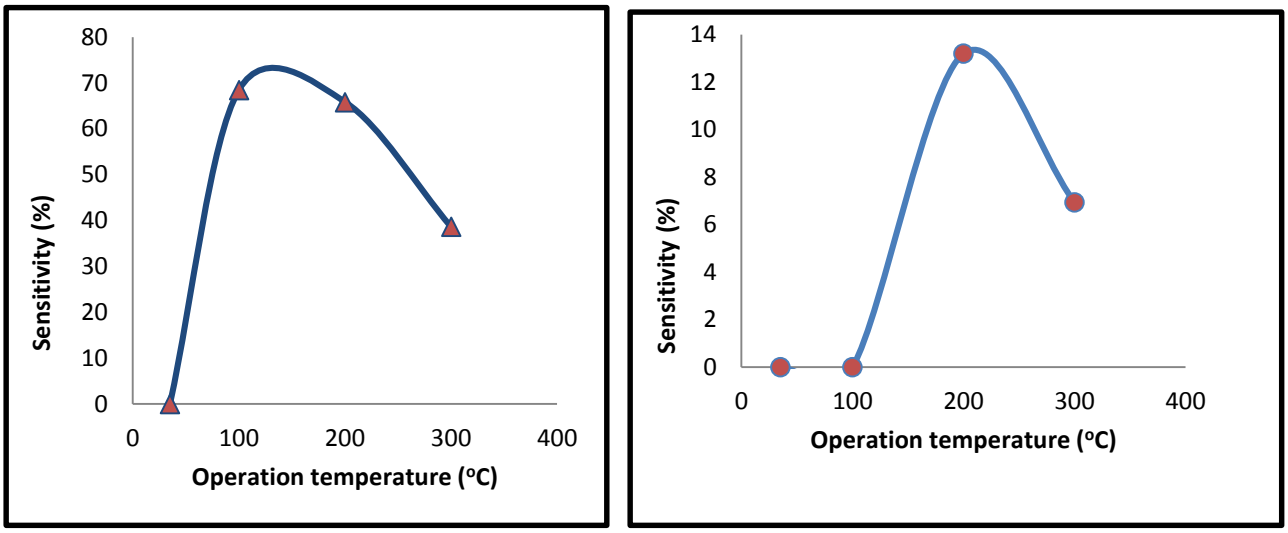

Figure 9. Shows the sensitivity as a function of the operating temperature of prepared films.

Table 1. Represents the response and recovery time of pure ZnO and ZnO;Cu films in different ratios, sensitivity and resistance values when R is (On) and R is (off).

Sample	**Tgas °C**	**t gas**		**Tgas recover**	**Response time(s) T_{res}**	**Recovery time (s) T_{rec}**	**R(Ω)**		**S%**
		On	**Off**				**On**	**off**	
Pure	35°C	0	0	0	0	0	0	0	0
	100°C	23	41	120	16.2	71.1	5.06	7.52	48.6166
	200°C	21	46	100	22.5	48.6	3.07	4.98	62.2149
	300°C	20	34	90	12.6	50.4	1.71	3.39	98.2456
	35°C	0	0	0	0	0	0	0	0

3%	100°C	25	81	200	50.4	107.1	27.1	24.6	9.2114
	200°C	22	48	150	23.4	91.8	14.6	13.5	7.1184
	300°C	22	52	100	27	43.2	3	2.82	6
	35°C	0	0	0	0	0	0	0	0
7%	100°C	23	54	300	27.9	221.4	3.3	1.04	68.4848
	200°C	21	44	150	20.7	95.4	66.7	22.7	65.8620
	300°C	22	36	90	12.6	48.6	33.1	20.3	38.6356
	35°C	0	0	0	0	0	0	0	0
9%	100°C	0	0	0	0	0	0	0	0
	200°C	21	36	100	13.5	57.6	23.1	20.1	13.2067
	300°C	22	32	100	9	61.2	11.6	10.8	6.9349

4. Conclusions.

In this research, the pulsed laser deposition method was successfully used to prepare thin films of pure zinc oxide and copper-induced zinc oxide in three different proportions. It was found that by increasing the deformation ratios, the film crystallization decreased, and the optical measurements showed that the value of the optical energy gap of the prepared films was within (2.95-3.26 eV). Sensitivity measurements of the prepared films showed no response at room temperature, and the increased resistance of the prepared film when increasing the temperature was also shown. The maximum sensitivity of the films was found in the pure ZnO (98.2456%) with an operating temperature (300°C), which is the suitable operating temperature to sensitize the films. While the operating temperature for the doped thin films decreases and reaches 100oC for the doped films with Cu at ratio (3%).

5.References

[1] H. Czternastek , and M. Jachimowski ,"Aluminum-Doped ZnO Films Prepared by DC Reactive Magnetron Sputtering", Proc. of 19-th Conference of ISHM Poland, Porabka - Kozubnik, vol. 75, p. 78, (1995).

[2] P. Sagar, M. Kumar, and R. M. Mehran, "Electrical and Optical Properties of sol-gel derived ZnO:Al thin films", Material Science -Poland, vol. 23 no. 3, P. 685, (2005).

[3] Bagnall D M, Chen Y F, Zhu Z, Yao T, Koyama S, Shen M Y and Goto " Optically pumped lasing of ZnO at room temperature" J Appl. Phys. Lett. 70, 2230,(1997)

[4] H. L. Hartnagel, A. L. Dewar, A. K. Jain, and C. Jadish,“ Semiconducting Transparent Thin Films” , Institute of Physics Publishing, Bristol , (1995).

[5] T. Nguyen, H. Hartmann, Robert N., "Structural Order of nano crystalline ZnO films". Journal of Physical Chemistry B, 103 (21): pp. 4264-4268, (1999).

[6] S. Ben, “Solid State Electronic Devises”, Hall International, Inc, USA, (1990).

[7] T. K. Subramanyam , B. Srinivasulu, and S. Uthanna , "Physical Properties of Zinc Oxide Films Prepared by dc Reactive Magnetron Sputtering at Different Sputtering Pressures", Crystal Research and Technology, vol. 35 no. 10, p. 1193, (2000).

[8] W. D. Callister “ Materials Science and Engineering” 4th Edition , (1997).

[9] J. T. Moon and H.B.IM “Effects of Copper doping on the Electronic Properties of CdS Films Sintered with CdCl2” Journal of Materials Science, Vol.23, No.10,pp 34-45. (1988).

[10] A. Bakin, A. Waag, "ZnO Epitaxial Growth", Comprehensive semiconductor Science and Technology Encyclopaedia, Volume 3,(2011), pp 368- 395

[11] S. Metev, "Process Characteristics and Film Properties in Pulsed Laser Deposition" Plunumm press, New York (1994).

[12] T.J. Goodwin, V.L. Leppert, S.H. Risbud, "Pulse Laser Deposition" J.Appl Phys, Vol.10, P. 3122 ,(1997) .

[13] G. Korotcenkov," Handbook of Gas Sensor Materials", Springer LLC, NewYork (2013).

Distribution of Radon Concentration in Farmland Soil Samples in Al-Shamiyah City, Al-Qadisiyah, Iraq

Amer Y. Kadhim[1, 2], Khalid H. Al-Ataya1, Murtadha Sh. Aswood[*2]

1Department of Physics, College of Science, University of Babylon.
2Department of Physics, College of Education, University of Qadisiyah
*Corresponding author e- mail: murtadhababylon@gmail.com

Abstract. Radon concentration has determined in 46 samples collected from farmland soil of Al- Shamiyah city, Al-Qadisiyah, Iraq with alpha-emitters records their out of radon in nuclear track detector (CR-39). The results showed the maximum concentration of radon is 13.02 Bq/m^3 and the minimum concentration of radon is 0.12 Bq/m^3, with a mean value of 6.48 ± 0.77 Bq/m^3. Results reveal that the exhalation radon mass varied from 4.271 to 6.004 mBq/kg.h. The results explained the radon concentrations in farmland soil were less than 200 Bq/m^3 that it is recommended by UNSCEAR. On the other hand, the results observed that the samples do not create any impact on humans.

Introduction:

Natural radionuclides are typically long- lived for more than a hundred million years. They exist in varying amounts in the air, water, vegetables, animals, soil, rocks and in the human body itself [1-4]. Soil is important to humans and their health. It provides a resource that can be used as a shelter and for food production. Terrestrial radionuclides series for example (U-238, U-235 and Th-232) have been indicted in every level of the state in the world. Terrestrial radionuclides and their daughters represent the major contribution of radiation doses are given human beings [5-7]. Activities of human in the soil can change the concentration of radioactivity. Natural radionuclides exist in phosphate fertilizers, and thus the application of fertilizers leads to changing the properties of the soil [8]. Chemical fertilizers have been used in all kinds of farming systems. Consequently, the determined of natural radioactivity is a dangerous on the humankind. The major supplier of radiation is radon (Rn-222). Radon and its progeny doses have been the high levels of reasons for lung cancer [1**].** The decay scheme of radon products from the isotope of radium (Ra-226) presents in soil and rock in all its kinds. The **radon atoms** product are transiting to air filled pores after that move by diffusion and advection in the space by the exhale through the atmosphere [9]. There are many studied to estimate the radon concentration in the world [10-12]. The aim of this study is to measure **the concentration of** radon and **the exhalation radon rate (mass and area)** in **farmlands soil of Al-Shamiyah city, Al-Qadisiyah, Iraq by** nuclear track detector (CR-39)**.**

2. Materials and Methods:

2.1. Description of Study Area

The study area lies in Al-Shamiyah city (180 Km) south of the capital Baghdad, which has an area of (948) km^2 on both sides of the Shatt al- Shamiyah (a branch of the Euphrates River), at Latitude (31.96 36 11^o) north, longitude (44.59 88 89^o) east [13]. In this study, the samples were collected from farmland soil in different villages for 10 different regions are includes the villages as, Al-Joboor, Abo Kofoof, Al-Hadadi, Tabar Al-Zaweed, Al-Filahi, Al-Chalakh, Al-Najaria, Al-Giratia, Al-Hafar and Nodaiba, as shown in figure 1.

Figure 1. Qadisiyah Governorate and sample sites [13].

2.2 CR-39 detector

CR-39 is a clear, colorless, rigid plastic, with a density of 1.30 g/cm^3.The sensibility of CR-39 is such that it is physically able to register low energy alphas. Its high degree of reproducibility from batch to batch ensures the correct determination of the "background signal", giving an accurate estimate of the actual radon concentration [14].

2.3 Tube-Technique (PVC)

PVC tube is a plastic cylinder, made from PVC (polyvinylchloride in the form of a cylinder of 2 mm thickness, a diameter of 3 cm and 11 cm long, used in this work to determine the radon concentration in the soil samples [15].

2.4 Calculated Concentration of Radon

Determination of the particles of alpha out of radon found in samples of soil concentrations were introduction using CR-39 detector with thickens (500×10^{-6} m) and area is (1cm×1 cm). These samples were collected from different regions in Al- Shamiyah city, Qadisiyah, and then crushed it to small pieces to get powder of samples with diameter (200×10^{-6} m). After that, the sample was weighted (5g) then stored for 60 days in a sealed cup as shown in Figure 2. After then the detectors were prepared for etched by solution (NaOH) for normality (6.25 N) for temperature of (60 ºC) for a while (7 h). To record the tracks ware and used an optical microscope to calculate the tracks density of alpha emitted from. Equation 1and 2 used to calculate the density of the tracks (ρ) and radon concentration respectively [16].

$$\rho = \frac{N}{A}$$

where N is the mean of track, A area of field view.

$$C_{Rn} = \frac{\rho}{K \times T}$$

where T is exposure time. K is calibration factor of CR-39 (0.024 tr.cm^{-2} per Bq/m^3.d) [17].

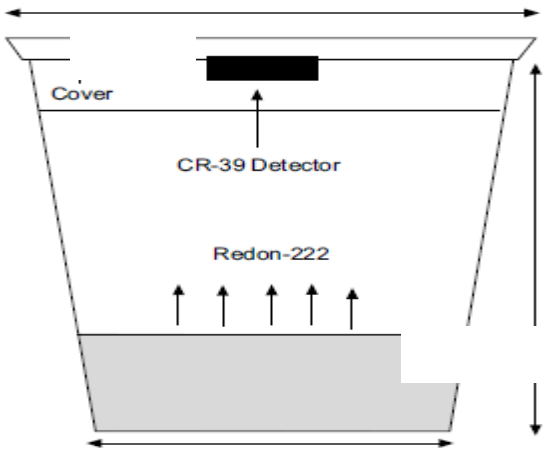

Figure 2. Sealed-cup technique.

2.5 Radon exhalation rate

As shown in Figure 2, the can technique was used to measure radon exhalation. Each 5 g soil sample was divided into separate plastic cans and closed. The detectors from all the cans were repossessed after 60 days of exposure. At several conditions, the detectors were etched as explained above. By an optical microscope with a 400X objective lens to find out the track density, 50 fields were scanned for each detector. The radon exhalation rate was measured in terms of mass and area [11, 16].

$$E_M\,(mBq/kg.h) = \frac{CV\lambda TlM}{T + 1\frac{1}{\lambda}(e^{-\lambda T} - 1)}$$

$$E_A(mBq/m^2.h) = \frac{CV\lambda TlA}{T + (e^{-\lambda T} - 1)}$$

where E_M and E_A are the mass and surface area exhalation rate, C the integrate radon exposure, T the exposure time (60 days), V the volume of the can (77.72 cm^3), M the mass of the soil samples (5 gm), λ the decay constant of ^{222}Rn, A the surface area of soil samples (177.75 cm^2) and k is the factor of calibration.

3. Results and Discussion:

3.1. Concentration of Radon

In this study, the radon concentration has measured in farmland soil samples collected from Al- Shamiyah, which it famous for the production of agricultural crops, especially cereals of rice and wheat. The estimated values of radon concentration are tabulated in Table 1. The maximum concentration of radon was found in Al-Filahi is 13.02 Bq/m^3, and the minimum radon concentration is 0.12 Bq/m^3 collected from Al-Hadadi, with an average of 6.48 Bq/m^3. The average value of the radon concentration is below the world average value of (200 Bq/m^3) as recommended by the United Nations Scientific Committee on the Effects of Atomic Radiation (UNSCEAR) [1]. All the results were compared with other studies in the world, the present study is shown the concentration of radon is indicted the lower than in the radon concentration in Brazil**,** Egypt**,** India**,** Libya and Pakistan as shown in Table 2. The results indicated that the concentration varied from country to country due to the differences in the geological nature of the soil.

Table 1. Radon concentration (C_{Rn}) for Farmland soil samples collected from Al-Shamiyah**.**

Sample code	**Region**	**C_{Rn} (Bq/m^3)**		
		Min.	Max.	Mean
S01	Al-Joboor	3.95	12.33	8.31±2.09
S06	Abo Kofoof	0.35	09.19	4.70±0.19

S11	Al-Hadadi	0.12	12.56	5.84±0.39
S16	Tabar Al-Zaweed	0.23	07.56	5.30±0.06
S21	Al-Filahi	2.33	13.02	8.00±0.81
S26	Al-Chalakh	0.93	06.51	4.674±0. 7
S31	Al-Najaria	2.09	09.77	6.49±0.46
S36	Al-Giratia	4.77	09.07	8.49±1.02
S41	Al-Hafar	6.05	09.77	8.07±2.02
S46	Nodaiba	0.35	08.02	4.95±0.03
Average				6.48±0.77

Table 2. Radon concentrations compared with the values reported for other countries.

Country	**C_{Rn} (Bq/m^3)**			**References**
	Min.	**Max.**	**Mean**	
Brazil	4	404	69	[18]
Egypt	3130	6970	5110	[19]
India	177.5	583.4	330.5	[20]
Libya (Benghazi)	31.1	469	220.3	[21]
Libya (Al-Marj)	59.3	515.8	325.5	
Pakistan	-	-	261.67	[11]
Al-Shamiyah city	0.12	13.02	6.48	Present study

3.2. Radon exhalation rate

Table 3 is indicated the values of radon exhalation (for mass and surface area) in the soil samples collected from the different regions of Al-Shamiyah city. The radon exhalation in terms of mass ranges from 4.27 to 6.19 mBq/kg h and the radon exhalation of the area ranges from 0.10 to 1.83 mBq/ m^2 h. The exhalation rate depends on some of parameters that behave in a stochastic and independent fashion. The mean radon exhalation rates measured in terms of mass and area of the soil samples are 5.16 mBq/kg.h and 1.04 mBq/m^2 h, respectively. Table 4 shows the values of radon exhalation rates compared with other references in the world. The mean radon exhalation rates are higher than the concentration of radon exhalation in Pakistan and below the concentration of India and Malaysia.

Table 3. Radon exhalation in the soil for Farmland samples collected from Al-Shamiyah city.

Sample code	**Region**	**E_M(mBq/kg h)**	**E_A(mBq/m^{2}h)**
S01	Al-Joboor	4.40	0.91

S06	Abo Kofoof	5.17	0.30
S11	Al-Hadadi	4.27	0.10
S16	Tabar Al-Zaweed	5.64	1.03
S21	Al-Filahi	6.19	1.83
S26	Al-Chalakh	5.50	0.81
S31	Al-Najaria	4.81	1.80
S36	Al-Giratia	5.11	1.72
S41	Al-Hafar	6.01	0.90
S46	Nodaiba	4.47	1.06
Mean		5.16	1.04

Table 4. A comparative study of the concentration of Radon exhalation ((mBq/kg h) with other worldwide published data.

Country	**Radon exhalation**	**References**
Pakistan	1.56-3.33	[22]
Odisha, India	4.2-13.7	[23]
Erasaima, India	648	[24]
Tusham, India	11.54	[25]
Seberang Paria, Malaysia	4.526	[16]
Al-Shamiyah city	5.16	Present study

4. Conclusions

The radon concentration has measured in farmland soil samples collected from Al- Shamiyah, which it famous for the production of agricultural crops, especially of rice and wheat. The average value (0.12 Bq/m^3) of the radon concentration is below the world average value as recommended in UNSCEAR. All the results were compared with other studied in the world, the present study are shown the radon concentrations represented lower than the concentration in other countries. On the other hand, the mean radon exhalation rates are higher than the concentration of radon exhalation in Pakistan and below the concentration of India and Malaysia

Acknowledgments

I would like to introduce my thanks to all members of the staff of Physics Department, Education College, and University of Al-Qadisiyah.

References:

[1]United Nations Scientific Committee on the Effects of Atomic Radiation Sources and effects of ionizing radiation (UNSCEAR) 2000 New York United Nations

[2]Aswood M S, Jaafar, M S and Salih, N 2017 Estimation of annual effective dose due to natural radioactivity in ingestion of vegetables from Cameron Highlands, Malaysia. Environmental Technology & Innovation, 8, 96-102

[3]Aswood M S, Abojassim, A A and Al Musawi, M S A 2019 Natural radioactivity measurements of frozen red meat samples consumed in Iraq. Radiation Detection Technology and Methods, 3(4), 57

[4]Showard A F, and Aswood M S 2019Measuring of Alpha particles in Blood samples of Leukemia patients in Babylon governorate, Iraq. In Journal of Physics: Conference Series IOP, 1234 (1) 12062

[5]United Nations Scientific Committee on the Effects of Atomic Radiation (UNSCEAR) 1988 Report to the General Assembly. Exposures from Natural Radiation Sources, New York

[6]IAEA, International Atomic Energy Agency (1989). Measurement of Radionuclides in Food and Environmental Samples. Technical Report Series No. 295 Vienna, Austria

[7]Al-Hamzawi A A, Tawfiq N F, Aswood M S and Najim F A 2019 Determination of radon concentrations near mobile towers in selected cities of Babylon governorate, Iraq. In Journal of Physics: Conference Series IOP. 1234, (1) 012026

[8]Aswood M Sh, Jaafar MS and Bauk S 2014 Measuring Radon Concentration Levels in Fertilizers Using CR-39 Detector Advan. Mater. Res. 925 610-613

[9]Salih N F, Aswood M S and Hamzawi A A 2019 Effect of porosity on evaluation of radon concentration in soil samples collected from Sulaymania governorate, Iraq. In Journal of Physics: Conference Series IOP. 1234 (1) 012024

[10] Ismail A H and Jaafar M S 2010 Hazard assessment of radon exhalation rate and radium content in the soil samples in Iraqi Kurdistan using passive and active detecting method. Journal world academy of science engineering and technology 46, 473-476

[11] Rafique M, Rahman S U, Mahmood T, Rahman S and Rehman S U 2011 Radon exhalation rate from soil, sand, bricks, and sedimentary samples collected from Azad Kashmir, Pakistan. Russian Geology and Geophysics. 52(4) 450-457

[12] A l-Jarallah M I and Abdalla K 2008 Comparative study of short-and long- term indoor radon measurements. Radiation Measurements. (43) S471-S474

[13] Zahraa M A 2011 Characteristics of the Shamiyah soil and its effect on the production of major cereal crops, MS.c thesis, University of Al- Qadisiyah, Iraq

[14] Enge W 1980 Introduction to plastic nuclear track detectors Nuclear Tracks 4(4) 283-308

[15] Salih N F and Jaafar M S 2013 Novel method to assessing and the impact of alpha emitter's concentration of the uterus on women fertility in Iraqi Kurdistan region. Journal of Radioanalytical and Nuclear Chemistry. 298 (2) 755-761

[16] Aswood M S, Jaafar M S and Salih N F 2018 Determination of radon and heavy metals in soil samples from Seberang Perai, Malaysia. Pollution Research, 37, 646-651
[17] Al-Nafiey M Sh Jaafar S M and Bauk S B 2012 Design and Fabrication of New Radon Chamber for Radon Calibration Factor of Measurement. International Journal of Scientific Engineering Research. 3 (10) 1-6
[18] Binns D A C, Figueiredo N, Melo V P and Gouvea V A 1998 Radon-222 measurements in a uranium-prospecting area in Brazil. Journal of environmental radioactivity. 38(2) 249-254
[19] Abd-Elzaher M An 2012 Overview on studying ^{222}Rn Exhalation Rates using Passive Technique Solid-State Nuclear Track Detectors. American Journal of Applied Sciences. 9(10) 1653-1659
[20] Mahur A K, Gupta M, Varshney R, Sonkawade R G, Verma K D and Prasad R 2013 Radon exhalation and gamma radioactivity levels in soil and radiation hazard assessment in the surrounding area of National Thermal Power Corporation, Dadri (UP), India. Radiation Measurements. (50)130-135
[21] Saad A F, Abdallah R M and Hussein N A 2013 Radon exhalation from Libyan soil samples measured with the SSNTD technique. Applied Radiation and Isotopes. (72) 163-168
[22] Rahman S 2006 Studying ^{222}Rn exhalation rate from soil and sand samples using CR-39 detector. Radiation Measurements. 41 (6) 708-713
[23] Mahur A K, Khan M S, Naqvi A H, Prasad R and Azam A 2008 Measurement of effective radium content of sand samples collected from Chhatrapur beach, Orissa, India using track etch technique. Radiation Measurements. (43) S520- S522
[24] Kumar R, Mahur A K, Rao N S, Sengupta D and Prasad R 2008 Radon exhalation rate from sand samples from the newly discovered high background radiation area at Erasama beach placer deposit of Orissa, India. Radiation measurements. (43)S508-S511
[25] Harmanjit S, Joga S, Surinder S and Bajwa B S 2008 Radon exhalation rate and uranium estimation study of some soil and rock samples from Tusham ring complex, India is using SSNTD technique. Radiation Measurements. 43: 459-462